Complementary Use of Electrochemical Testing Techniques to Study Corrosion Processes of HVOF Inconel 625, CoNiCrAlY and WCCoCr Coatings

By

Akbar Niaz

A thesis submitted for the degree of Philosophy

Department of Mechanical, Materials and Manufacturing Engineering

University of Nottingham

January, 2013

PREFACE

This thesis work is submitted for the degree of Doctor of Philosophy at Department of Mechanical, Materials and Manufacturing Engineering, University of Nottingham, UK. The research work was carried out under the supervision of Dr. K. T. Voisey in Faculty of Engineering and Dr. D. A. Walsh in School of Chemistry University of Nottingham. I hereby certify that the work presented in this thesis is original, and suitable references are made to any work from literature or carried out elsewhere.

To date following publications have been produced from the work contained in this thesis:

- L. Johnson, **A. Niaz**, A. Boatwright, K.T. Voisey, and D.A. Walsh, *Scanning electrochemical microscopy at thermal sprayed anti-corrosion coatings: Effect of thermal spraying on heterogeneous electron transfer kinetics.* J. Electroanal. Chem., 2011. 657(1–2): p. 46-53.
- Bakare, M. S., **Butt, A. N**, Voisey, K. T and McCartney, D. G, *Microstructural Modifications and Corrosion Behaviour of HVOF sprayed Coatings Using Laser Surface Melting-Inconel 625 and FeCrAlY. In Proceedings of Materials Science and Technology* (MS&T) 2010 p. 296-306

ACKNOWLEDGEMENTS

I would like to thank my supervisors Dr. Katy Voisey in Faculty of Engineering and Dr. Darren Walsh in School of Chemistry for their invaluable support, advice and mentoring during three years of doctoral research. I learnt to be critical to thoughts, progress logically through investigation and think rationally from working with them. I have been benefitted immensely from their comments and suggestion throughout my PhD studies.

I am also thankful of senior colleague Dr. K. Lovelock, Dr. A. Boatwright and Dr. L. Johnson for their help and advice in understanding practical aspects of electrochemistry. I am also thankful to Dr. M. S Bakare and Dr. N. Ahmed for their comments and suggestion in the experimental work of the project. I never felt short of their help thorough out my three years studies.

I acknowledge the help and support offered by technical staff at Wolfson building including, Keith Dinsdale and Tom Boss for general lab training, Dr. Nigel and Juile Thornhill for SEM training, Martin Roe for XPS experiments and analysis. I am also thankful to Dr. Sami Hassan for his generous time and valuable comments during writing thesis.

I must appreciate my sponsor Islamic development bank for their financial support. My heartily felt thank to Amman Gee Balqees, wife Riffat and son Rehan for their continual support and love.

ABSTRACT

The purpose of coating is to get a blend of unique properties at low cost which is not possible from other manufacturing processes. High velocity oxygen fuel (HVOF) is one of the most commonly used thermal spraying processes to produce wear and corrosion resistant coatings. Alongside wear and corrosion resistant properties the HVOF thermally sprayed coating process also induces microstructural heterogeneities which decreased the corrosion resistant properties. Considerable research has been reported on corrosion testing of the HVOF sprayed coatings by using electrochemical techniques. Some electrochemical techniques give area average results whilst other allows the effect of different features to be determined. The complementary use of basic electrochemical techniques with more advance techniques is missing in most of the previous research. In this research work potentiodynamic polarization testing, electrochemical impedance spectroscopy and scanning electrochemical microscopy were used to see if the combined results could provide a broader picture of corrosion processes taking place at HVOF coatings. Three HVOF coatings of different microstructural complexity i.e. γ-phase Inconel 625, γ + β-phase CoNiCrAlY and WC-CoCr cermet coating were tested.

Potentiodynamic polarization results gave overall current response of the applied potential which included the current responsible for chemical reaction and current for charging and discharging of the double layer. The general corrosion ranking of different materials was established by measuring corrosion potential, corrosion current density and passive current density from polarization curves. The analysis of the polarization curves revealed that

without careful consideration of experimental details significant errors can be introduced. Improved procedures for potentiodynamic polarization testing were demonstrated by deliberately altering experimental parameters. The localized corrosion due to chloride ions and Cr-depleted regions was also studied by potentiodynamic polarization testing. The correlation between individual microstructural features and their electrochemical response was established by EIS including equivalent circuit modelling. The impedance spectroscopy results also revealed the electrochemical changes due to immersion time and polarization. The electrochemical activity at high resolution was studied by more sophisticated spatially resolved SECM. The SECM imaging and heterogeneous electron transfer rate constant studies in feedback mode pin point the regions of different electrochemical activity. The SECM imaging and SECM feedback approach curves at stainless steel and bulk Inconel showed negative feedback all over the surface. The Inconel 625 coating showed both positive and negative feedback from the surface. The positive feedback regions correspond to less electrochemically active and negative feedback regions correspond to electrochemically active regions. The comparison between SECM images and microscopy images confirmed that the splat boundaries were the most active regions in the HVOF Inconel 625 coating. The heterogeneous ET kinetic study determined higher rate constant values at positive feedback regions and lower rate constant values at negative feedback regions.

Table of Contents

LIST OF FIGURES

LIST OF TABLES

NOMENCLATURE

a	*Radius of microelectrode*
AC	*Alternating current*
$ASTM$	*American society for testing and materials*
B	*Stern-Geary coefficient*
b	*Tafel slope*
b_a	*Anodic Tafel slope*
b_c	*Cathodic Tafel slope*
C	*Capacitance*
C	*Concentration*
C_{dl}	*Double layer capacitance*
CE	*Counter electrode*
CPE	*Constant phase element*
C_R	*Corrosion rate*
CV	*Cyclic voltammogram*
D	*Diffusion coefficient*
d	*Tip offset distance*
DC	*Direct current*
DOS	*Degree of sensitization*
E	*Applied potential*
E^0	*Standard electrode potential*
$E^{0'}$	*Formal potential*
E_{break}	*Breakdown potential*
ECM	*Equivalent circuit model*
E_{corr}	*Corrosion potential*
E_{dl}	*Electrical double layer*
EDS	*Energy dispersive spectroscopy*
EIS	*Electrochemical impedance spectroscopy*
E_{pa}	*Anodic peak potential*
E_{pc}	*Cathodic peak potential*
E_{qw}	*Equivalent weight*
F	*Faraday's constant*
f	*Frequency*
$FcOH$	*Ferrocenemethanol*
FW	*Forward scan*
HIT	*Hilbert transform*
HRS	*High resolution spectra (XPS)*
$HVOF$	*High velocity oxygen fuel*
i_p	*Peak current*
i_{pa}	*Anodic peak current*
i_{pc}	*Cathodic peak current*
$i_T/i_{T\infty}$	*Normalized tip current*
$i_{T\infty}$	*Tip current at infinite distance*
i_T	*Tip current*
j_0	*Exchange current density*
j_a	*Anodic current density*
j_c	*Cathodic current density*
$j_{charging}$	*Charging current density*
j_{corr}	*Corrosion current density*
$j_{faradaic}$	*Faradaic current density*
$j^{negative}$	*Current density with reverse scan*
j_{pass}	*Passive current density*
$j^{positive}$	*Current density with forward scan*
k	*Heterogeneous electron transfer rate constant*
k^o	*Standard heterogeneous electron transfer rate constant*
KK	*Karmers-Kronig*

KSCN	*Potassium thiocyanate*
*L**	*Inductor*
L	*Normalized tip distance*
LPR	*Linear polarization resistance*
ME	*Microelectrode*
n	*Exponent of CPE*
OCP	*Open circuit potential*
P	*Capacitance parameter CPE*
ppm	*Parts per millions*
Q	*Charge*
R	*Resistance*
r_a	*Pt-wire radius*
RE	*Reference electrode*
r_g	*Radius of the glass sheath*
R_g	*Tip geometry constant* (r_g / r_a)
R_P	*Polarization resistance*
R_u	*Solution resistance*
RV	*Reverse scan*
SC	*Substrate collection*
SCE	*Saturate calomel electrode*
SECM	*Scanning electrochemical microscopy*
SEM	*Scanning electron microscopy*
SG	*Substrate generation*
T	*Temperature*
t	*Time*
TC	*Tip collection*
TG	*Tip generation*
TGO	*Thermally grown oxide*
UME	*Ultra microelectrode*
V	*Volts*
W	*Warburg diffusion element*
WE	*Working electrode*
XPS	*X-ray electron photoelectron spectroscopy*
XRD	*X-ray diffraction*
Y_0	*Inductance of component*
YSZ	*Yttria stabilized zirconia*
Z	*Impedance*
Z'	*Real impedance*
Z''	*Imaginary impedance*
Z_c	*Impedance of capacitor*
Z_{CPE}	*Impedance of constant phase element*
Z_L	*Impedance of inductor*
Z_R	*Impedance of resistor*
α	*Transfer coefficient*
δ	*Thickness of diffusion layer*
ΔE_p	*Difference between cathodic and anodic peak potential*
$\eta = (E - E^{0'})$	*Overpotential*
η_a	*Anodic overpotential*
η_c	*Cathodic overpotential*
θ	*Phase angle shift*
ρ	*Density*
τ	*Time constant*
υ	*Scan rate*
ω	*Radial frequency*

1 Introduction

1.1 Background

High velocity oxygen fuel (HVOF) coating is one of the family of thermal spray processes commonly used to deposit a wide range of coatings for numerous applications including wear and corrosion resistance. HVOF coatings share the distinctive microstructure of all thermally sprayed coatings, consisting of a lamellar structure that may feature pores, oxides and unmelted particles. The known performance gap between thermally sprayed coatings and the equivalent bulk alloys is attributed to this microstructure [1, 2]. This issue is addressed by microstructural study of the HVOF coating loosely linked with electrochemical testing by different researchers [1, 3-5].

One of the heterogeneities that may be present in HVOF coating microstructure is interconnected porosity [3, 4], which allows the electrolyte to pass through the coating thickness and damage the underlying substrate by combined crevice and galvanic corrosion [6]. However, N. Ahmed et al. showed even when interconnected porosity is not present there is still a performance gap between sprayed and equivalent bulk material [2, 7]. They suggested that the local variation in the composition and microstructure are the main reasons for poor corrosion performance of the HVOF coatings. The corrosion performance improvement by laser surface melting of the HVOF Inconel 625 coating is also reported by M.S. Bakare et al. [8]. The passive current density measured by potentiodynamic polarization curve is predominantly used to gauge corrosion performance of the HVOF coatings.

However, a few researchers have used electrochemical impedance spectroscopy as well [9-11].

In this work a set of thermally sprayed coatings with different levels of microstructural complexity were studied by using potentiodynamic testing, electrochemical impedance spectroscopy and scanning electrochemical microscopy. As well as understanding the links between microstructural features and electrochemical behaviour, the results from the different techniques will be considered together in order to determine how best these different techniques can be combined to increase the understanding of the overall process.

1.2 Aims and objectives

- The main objective of this project is to use potentiodynamic polarization, EIS and SECM to get broader picture of the corrosion processes taking place at the HVOF coating surfaces.
- The interpretation issues related with potentiodynamic polarization testing are studied by altering the different parameters (potential scan rate, holding time etc.) and recording the change in the shape of polarization curves.
- Use EIS including equivalent circuit modelling to establish correlation between microstructural features to their electrochemical response.
- Use spatially resolved SECM imaging and ET kinetics study to identify regions of different electrochemical activity.

1.3 Methodology

The project methodology is presented as in ***Figure 1-1***. The electrochemical testing, microstructural characterization and X-ray photoelectron spectroscopy (XPS) were the main components of the project. The HVOF Inconel 625, CoNiCrAlY and WCCoCr coatings of different level of microstructural complexity were the main set of samples. The potentiodynamic polarization, EIS and SECM have been used on coating samples. The bulk Inconel 625, stainless steel and platinum were used for some tests to give additional, reference data for comparison. All potentiodynamic polarization tests were carried out with reference to open circuit potential (E_{oc}), where E_{oc} is the potential difference between working electrode and reference electrode just before the potential scan started.

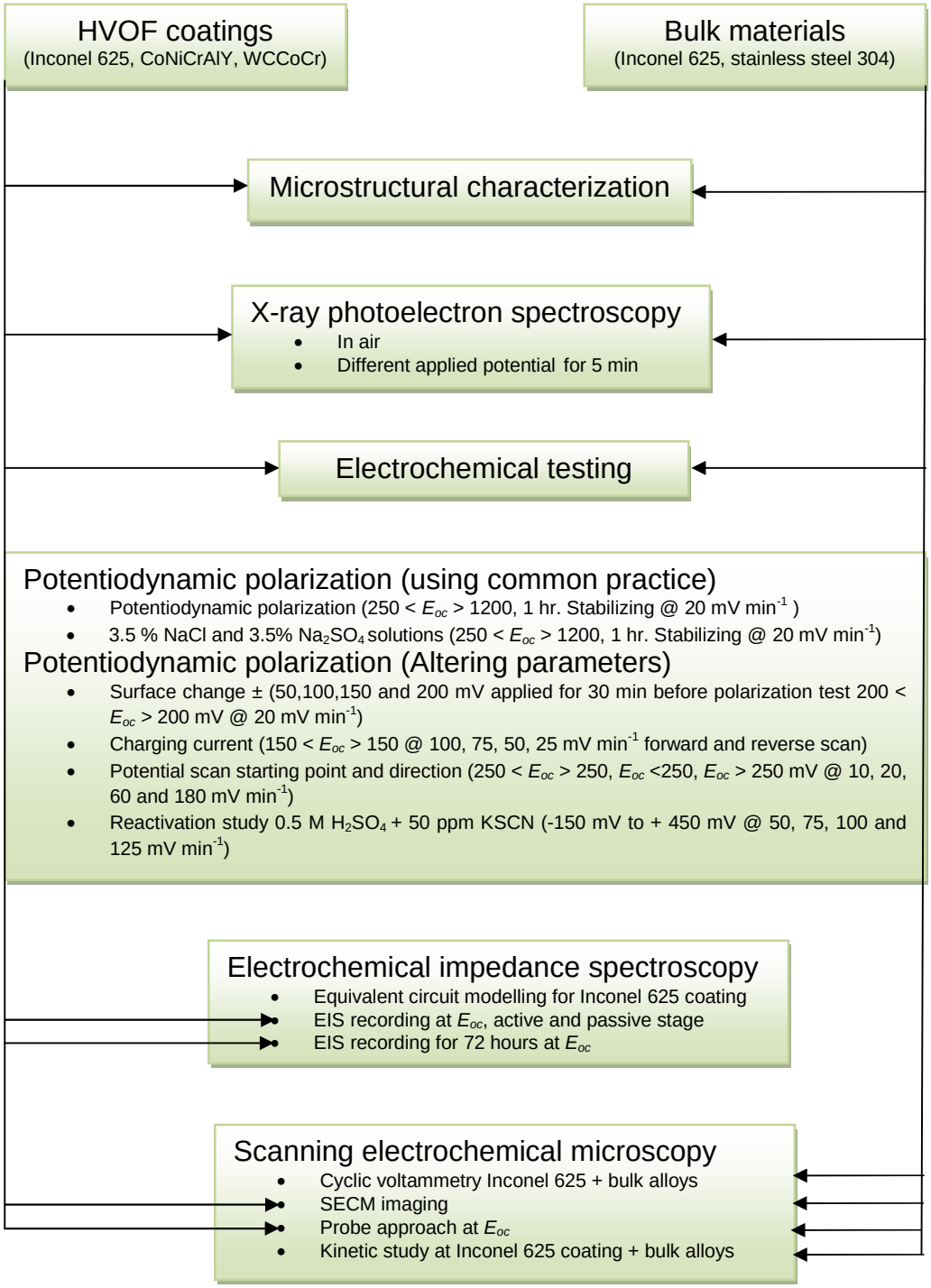

Figure 1-1: Experiments performed on coating and bulk materials

1.4 Thesis structure

This thesis is composed of eight chapters including this introduction as chapter one. A brief overview of these chapters is given below;

Chapter two presents literature review which contains a summary of previous work carried out in the field as well as the basics of corrosion and its types, electrochemical nature of corrosion, high velocity oxygen fuel coating process, corrosion testing and monitoring with more emphasis on electrochemical corrosion testing. Detail of three electrochemical methods used in the project i.e., potentiodynamic polarization testing, electrochemical impedance spectroscopy and scanning electrochemical microscopy is given in chapter three. The information extracted from the literature survey will be used throughout the thesis.

Chapter four presents experimental details which include: material used, methods employed, equipment used and procedures for conducting different experiments.

Results and discussion of the experiments are presented in chapter five, six and seven. This includes potentiodynamic polarization testing and X-ray photoelectron spectroscopy in chapter five, electrochemical impedance spectroscopy in chapter six and scanning electrochemical microscopy in chapter seven. The summary, conclusions of the project and recommendation for future work are given in chapter eight.

2 Literature review

2.1 Introduction

This literature review chapter covers the background knowledge of corrosion process, corrosion protection by HVOF coatings, electrochemical corrosion testing techniques and previous research in the field of electrochemical corrosion testing. The centre of the literature review is on the three electrochemical testing techniques particularly used in this work i.e., potentiodynamic polarization, electrochemical impedance spectroscopy (EIS) and scanning electrochemical microscopy (SECM) testing of the Inconel 625 coating, the CoNiCrAlY and the WCCoCr coatings produced by HVOF process.

2.2 Corrosion and its types

Corrosion is generally defined as the destructive disintegration process in which a metal is gradually destroyed by electrochemical reaction with the environment [12-14]. There is no hard and fast rule to classify corrosion but generally can be divide into two main groups called uniform and localized corrosion [12, 15]. In uniform corrosion, the damage occurs on entire surface at uniform rate. In localized corrosion damage occurs on localized spots due heterogeneities in material microstructure (galvanic, intergranular, de-alloying) and environment (crevice, hydrogen damage). The localized stress (stress corrosion cracking, corrosion fatigue, fretting) and geometry of the closed chemical fluid flow systems parts (erosion, cavitation) also cause localized corrosion damage [16, 17]. The corrosion damage depends on the extent of particular factor i.e. aggressive ions, stress amplitude. ***Figure 2-1*** shows the comprehensive view of different types of corrosion takes place in different industrial environments [13].

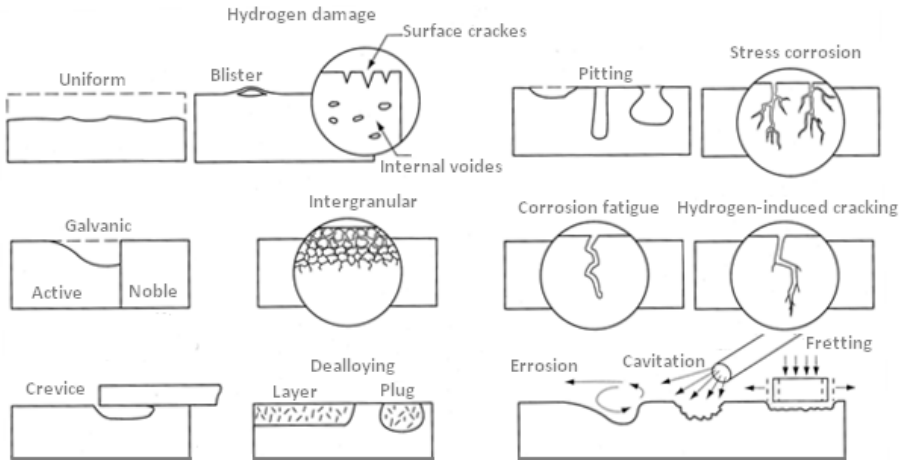

Figure 2-1: Types of corrosion in different industrial environments[13].

2.3 Electrochemical nature of corrosion

Corrosion of engineering metals and alloys in aqueous environment is an electrochemical process [17, 18]. There are at least two reactions taking place in electrochemical corrosion, one being anodic and other one cathodic [19]. The anodic reaction is dissolution of metal to form ions and release electrons as given in ***equation 2.1.***

$$M \xrightarrow{Metal\ oxidation} M^{+} + ne^{-} \qquad \textbf{2.1}$$

The main cathodic reaction is oxygen reduction (***equation 2.2***) in neutral or alkaline environments [20].

$$O_2 + 2H_2O + 4e^{-} \xrightarrow{Cathodic\ reaction\ (Neutral\ \&\ alkaline)} 4OH^{-} \qquad \textbf{2.2}$$

The overall corrosion reaction in neutral or alkaline environment is given in ***equation 2.3***.

$$M(s) + O_2(g) + H_2O(l) \xrightarrow{Corrosion(neutral\ \&\ alkaline\ sol.)} M(OH)_n \qquad \textbf{2.3}$$

In acidic environments the anodic reaction is dissolution of metal to form ions as in neutral environment but the dominant cathodic reaction is hydrogen evolution (***equation 2.4***).

$$2H^{+} + 2e^{-} \xrightarrow{Cathodic\ reaction\ (Acidic)} H_2 \qquad \textbf{2.4}$$

The overall corrosion reaction in acidic environment is metal dissolution to form ions and evolution of H_2 gas (***equation 2.5.).*** Metal ions can further react with anions to form metal salts or oxides [18].

$$M(s) + H^{+}(l) \xrightarrow{corrosion(acidic\ sol.)} M^{+}(l) + H_2(g) \qquad \textbf{2.5}$$

During electrochemical corrosion the anodic and cathodic reactions proceed simultaneously. The tendency of metal to corrode is defined by the standard electrode potential, the more negative the standard electrode potential the greater the tendency to corrode [14, 21]. ***Figure 2-2*** shows the electrochemical nature of corrosion by a drop of water on a metal surface. The dissolved oxygen is consumed and more rapidly replenished at the periphery of the drop via diffusion as compared to the centre of the drop. Therefore the centre of the drop acts as anode and periphery as cathode. The metal dissolution takes place at the centre and oxygen reduction at the periphery of the drop. The metal ions further react with OH^- ions to form metal hydroxide, which if insoluble precipitates at the surface. The surface of the metal changes from centre to periphery due to corrosion product. The metal hydroxide can further react with oxygen to form more stable corrosion product (e.g. oxides) [22, 23].

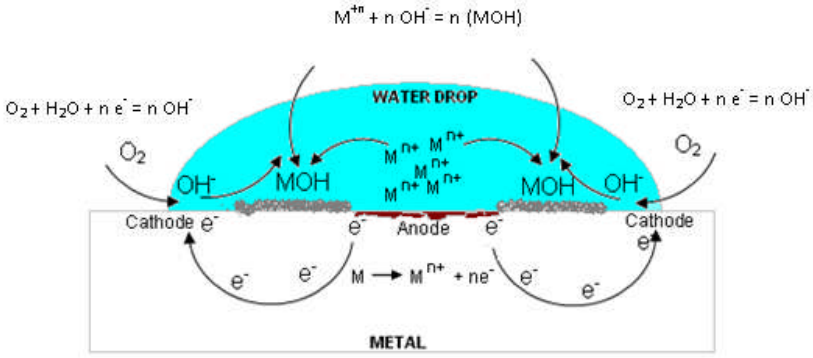

Figure 2-2: Corrosion by oxygenated water drop on metal surface

2.4 Economic aspects of corrosion

Corrosion has a huge economic and environment impact on world infrastructure like highways, bridges, oil/gas industries, chemical processing,

water and waste water systems [24]. Corrosion can't be fully eliminated but its effect can be minimized by using different protection and prevention methods [25]. The direct cost attributed to corrosion damage has been estimated to be of the order of 3 to 4 % of industrialized countries gross national product (GNP) [26]. According to National Association of Corrosion Engineers (NACE) in 2001 the corrosion cost to the world by direct and indirect loss was $US 552 billion [27], which increased to $US 1.3 trillion in 2009 [28]. The direct and indirect damage to and environment is huge if corrosion related problems are overlooked in sensitive oil/gas industries and nuclear power plants, e.g. radiation and poisonous gas leakage due to severe pitting at nuclear plant can put workers health at risk [29].

2.5 Corrosion protection and monitoring

Corrosion measurement and prevention covers a large field of technical activities which includes corrosion rate measurement, controlling physical parameters like temperature, pH, pressure stress, corrosion protection like cathodic, anodic protection [30, 31], chemical dosing, and prevention by material selection or organic/inorganic coatings [32]. Corrosion rate measurement by weight loss, is one of the commonly used corrosion testing method in the past and still in use [12]. A material is exposed in the environment where it need in service for a prolonged time (90 days). The corrosion rate is measured from the net weight loss per unit time i.e., difference of weight between before and after the exposure divided by exposure time. In this way corrosion damage can be assessed for future by extrapolating the weight loss results. With advancement in the electrochemical

sensor technology, different sort of resistance probes, linear polarization resistance probes and H_2 evolution probes are used for monitoring the corrosion system [33]. Metallic and non-metallic coating along with cladding or surface modification are also some of the most commonly corrosion prevention methods. Their effective use depends on careful selection and regular in service monitoring for corrosion. Corrosion prevention, monitoring and testing can save billions of dollars along with minimizing the hazards [25].

2.6 Thermal spray coating for corrosion protection

In thermal spray coating process, the metallic or non-metallic materials of the desired properties are deposited on the substrate material. The coating material is heated to molten or semi molten state in a heating torch/gun and accelerated in a gas stream to project against the substrate [34]. Upon impaction the coating material adheres to the substrate predominantly by mechanical interlocking. Thickness of the coating can be varied by depositing multiple layer of coating material. The heating torch design and fuel source varies with the coating process or coating material. A wide variety of materials can be coated, and worn parts can be re-coated easily by thermal spray coating [9, 35]. The limitation of the thermal spray coating process include restriction of maximum coating thickness to a few millimetres, thin machine parts where holding of the part is problematic and the surfaces at narrow/awkward places where coating torch can’t reach. Thermal spray coatings are used in almost every manufacturing industry including aerospace, agriculture, automotive and chemical industries. The flame spraying, electric arc spraying, plasma

spraying, detonation gun spraying and high velocity oxygen fuel are the main types of thermal spray coating processes [36, 37].

2.7 High velocity oxygen fuel coating

HVOF process was invented in 1958 by Union Carbide and bring significant development in the field of thermal spray coating for the last 3 decades [37, 38]. Updates include modification of the equipment design, automation of process and modelling to estimate particle velocity and melting [39-41]. In HVOF coating process, the fuel (mixture of kerosene, acetylene, propylene and hydrogen) is mixed with oxygen and burned in the combustion chamber. In some other HVOF coating processes liquid kerosene stream is combusted with air to heat the coating material. The combustion product is allowed to expand through a nozzle where the gas velocities may become supersonic. The coating material is injected into, heated and accelerated by the gas stream. The fully or partially melted powder particles of 20-50 μm size reach speeds of the order of 550 m/s, which produces compact coatings [42]. The coatings produced by HVOF process show low porosity and oxidation (<2%) [43] due to fast travelling and high impaction of the powder particles to the substrate surface [44, 45]. The controlled heating, supersonic impaction of particles and bonding produces more compact and less oxidized coatings than plasma and flame spraying process.

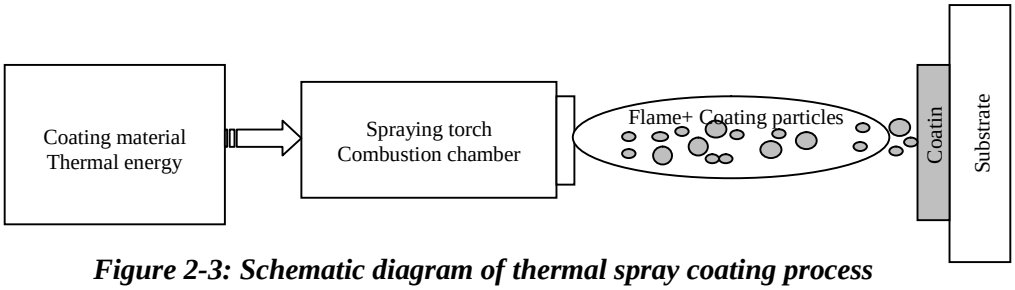

Figure 2-3: Schematic diagram of thermal spray coating process

2.7.1 Microstructure of HVOF coating

The coating produced by HVOF processes is characterised as lamellar structure embedded with solid particles, oxide and inclusions (residue at the surface from shot blasting or surface cleaning process) [46, 47]. The schematic in ***Figure 2-4*** shows the main components of HVOF coating. Molten or semi molten particles deform when they hit the substrate. Deformed particles in the coating are called splats, have a thickness of approximately 1-20 µm. The fast striking speed of particles produces compact coating but still some voids/pores are formed at the surface and inter-lamellar particle boundaries [43]. The impaction of the solid particles at fast speed also adds the strength due to peening effect (tensile stress relieving or adding compression by low level mechanical stresses). The high temperature and presence of oxygen in the environment also causes formation of oxides. The adherence between substrate and coating is predominantly by mechanical interlocking.

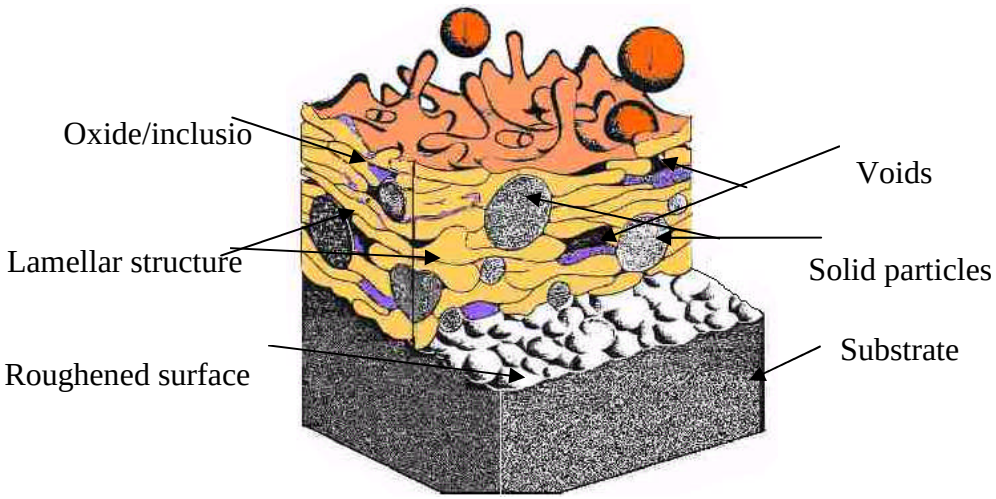

Figure 2-4: Schematic showing typical microstructure of a HVOF coating [37]

2.7.2 Uses of thermally sprayed coatings

Thermally sprayed coatings are used in wide variety of applications in engineering and manufacturing to impart different surface characteristics such as heat resistance, wear resistance and corrosion resistance [37]. The coating application area includes gas turbine, aerospace industry, process industry and automotive. Thermally sprayed coating can be used in the thermal barrier coating. The aerospace industry is the biggest users of thermal barrier coatings both at original equipment manufacturing stage and repair stage. Thermal barrier coatings and super-alloy coatings are applied in combustors and nozzle guide vanes to protect against extreme heat. The gas turbine mainly consists of suction, compression and combustion chamber where severe operating conditions exist. Almost every component of the gas turbine engine has some type of coating to prevent the damage due to high temperature and wear [48]. The super-alloy Inconel 625 along with MCrAlY coatings are used where operating temperature reaches more than 1400° C [49, 50]. Other applications of Ni-based super alloys include marine and nuclear industries. Wear resistant coatings are used in aircraft landing gear, pistons and implants used in forming industries. Thermally sprayed coatings are also used in surgical implants such as replacement hips, rolls used in paper and printing industries and thread guided components in textile industry [51].

2.8 Previous electrochemical corrosion study of HVOF coating

Electrochemical techniques have been extensively used to characterize corrosion of different HVOF coatings. The general trend is to modify the coating composition, surface, microstructure, HVOF process and record their impact on the corrosion performance. Measurement of E_{oc}, potentiodynamic polarization and impedance spectroscopy results combined with structure characterization by scanning electron microscopy (SEM) and X-ray diffraction (XRD) are reported by different researchers. In this section the previous research in the field of electrochemical testing with emphasis on measurement of E_{oc} vs. time, potentiodynamic polarization, EIS and SECM of Inconel 625, CoNiCrAlY and WC10Co4Cr coatings will be presented.

2.8.1 Microstructure modification and corrosion study

The motivation behind metallic sprayed coating is to achieve a combination of good surface properties at low cost [45]. One of the important concerns of the corrosion scientists is to improve corrosion performance and enhance the service life of a material. There is a performance gap between sprayed coatings and the equivalent bulk material due to porosity and splat boundaries [3, 52]. The porosity allows the electrolyte to penetrate in the coatings, which leads to crevice corrosion due to difference of oxygen concentration inside and outside of the pore. If pores in the coatings are interconnected, the electrolyte can reach the substrate [3]. When electrolyte reaches the substrate, intense corrosion takes place at the substrate due to different oxygen concentration and

galvanic corrosion (substrate material is generally less corrosion resistant). The galvanic corrosion is further enhanced by the small anode (inside pore) and large cathode area (coating surface). The galvanic corrosion may also exist between different areas of the microstructure of the coatings [3]. In splats the area adjacent to the oxides is depleted in chromium as compared to core of the un-melted powder particles [53-55]. The difference in electrochemical activity of these regions within the microstructure of the coatings can cause galvanic corrosion [3, 6].

The performance gap between HVOF coatings and equivalent bulk material has been reported by different researcher using different approaches [1, 52, 56]. D. Zhang et al. [2] carried out their research on Ni-based super-alloy Inconel 625 coatings produced by HVOF process. The coatings were deposited by a liquid-fuelled and gas fuelled guns. Their work showed that the coating deposited by liquid fuel gun gives 10-20 times lower current density than the coating deposited by gas fuelled gun. They attributed this improved corrosion resistance to reduced extent of melting and high speed of the liquid fuelled gun which reduced the interconnected porosity and low oxidation. Their work also highlights that Cr_2O_3 was the principle oxide formed during spraying process. The amount of Cr_2O_3 was directly linked with the extent of melting. The higher speed of the powder particles stream in HVOLF allow less melting, hence lower oxidation. The relative oxidation of the coatings produced by HVOLF and HVOGF was also tested by XPS analysis. The amount of Cr_2O_3 was < 0.1 wt. % for the coating produced by liquid fuel gun as compared to 6.3 wt. % for the coating produced by gas fuelled gun [2]. They also reported that

average powder particle size affected the oxide content and porosity. The coating produced from 33 µm average size powder contained a higher amount of oxide as compared to the one produced from 46 µm average size powder [2]. The greater extent of porosity was linked with the greater average powder particle size. It was also suggested in their work that variation in the feedstock particle sizes can change the extent of oxide and porosity 5 to 20% [2].

P.H. Suegama et al. [57] also sprayed SAE 4140 stainless steel powder on mild steel to test the corrosion properties of the HVOF coatings. They suggested that porosity, presence of micro-cracks and un-melted particles strongly influenced the corrosion performance of the HVOF stainless steel coatings. Their work also suggested that for the higher energy flames the distance between the flame and substrate material is very important to produce a compact and adherent coating.

N. Ahmed et al. [58], in their work on Inconel 625 sprayed coatings and equivalent bulk alloy, suggested that performance gap still exists in the absence of any interconnected porosity effect. They suggested the performance gap is due to localized variations in the composition and microstructure. They verified their point by increasing the porosity to 12% in sintered samples and modifying the microstructure by laser surface treatment. The 12% increment in the porosity only increases the passive current density by a factor of two. However, the microstructure modification of the Inconel 625 sprayed coated samples by laser surface treatment which replaced the lamellar microstructure of the coating gives the current density same as Inconel 625 bulk alloy.

The superior corrosion performance of the bulk Inconel 625 was also confirmed by A. J. Sturgeon et al. [59]. They further suggested that oxygen to fuel ratio, total gas flow rate and length of the combustion chamber significantly influence the oxide content in the coating. The oxygen to fuel ratio equivalent to 80 % stoichiometric value produces low oxidation. The powder of narrow particle size range 15-45 µm and small percentage of 50 µm sized powder produces coatings with optimum properties. Their results also showed that minimum oxidation occurs when combustion chamber length was 12 mm and gas flow rate at 337 L min^{-1}. The oxides present in the coating were Cr_2O_3 and spinel $NiCr_2O_3$ They also found Ni-rich grains in the coatings i.e. Cr-depleted regions.

Bakare's [8] work covers the effect of microstructure modification on corrosion resistance along with using SECM to visualize the localized activity at the Inconel 625 sprayed coating surface. His work also suggested that during electrochemical polarization the oxides present in the passive film depends on the applied polarization potential. Z. Liu, et al. [60] carried out their research on improving corrosion performance of Inconel 625 and WC-Inconel 625 coating by laser surface treatment. Microstructural, composition and phase analysis were conducted on as coated and laser alloys before and after the potentiodynamic polarization tests. They conclude that laser surface treatment significantly improved the corrosion properties by elimination of splat boundaries, reducing micro-crevice and porosity.

A Neville et al. [1] carried out work on corrosion performance of HVOF Inconel 625 coating and bulk alloy. They conduct testing on both materials in static saline conditions at 18^0 C and 50^0 C by potentiodynamic polarization and impedance spectroscopy. The HVOF sprayed Inconel 625 coatings suffer more extensive localised corrosion than bulk alloy. Furthermore, even conducting coating process in vacuum i.e., completely eliminating oxidation during deposition did not improve the HVOF coatings. The cold spray Inconel 625 coating followed by laser surface melted was also done by P. Poza et al. [61] they also found that microstructure and mechanical properties of the laser treated Inconel 625 coating are improved as compared to as coated samples.

A. Boudi et al. [62] tested the Inconel 625 coatings used in the power industry to improve the service life of the parts. Mild steel and stainless steel samples were coated with Inconel 625 and tested in 0.1N H_2SO_4 + 0.05N NaCl solution. They found that the coating was of layered structure and segregated, with the presence of a slightly darker contrast phase presumed to be oxide. The bonding strength of the coating marginally reduced after 3 week times. A study on the Cr-depleted region in Inconel 600 bulk alloys was carried out by W. Tsung et al. [63]. They used electrochemical reactivation to characterize sensitization. The improvement in corrosion performance by laser surface modification in Inconel 625 was also reported by K. P. Copper et al. [64]. They compared laser surface melted Inconel 625 samples with the Inconel coating injected with tungsten carbide and titanium carbide in sea water environment. Both particle injected samples showed the corrosion damage and significantly change in the composition due to oxidation of the tungsten and titanium

carbide phase. The dendritic structure of Inconel 625 showed nominal corrosion in sea water. The inter-lamellar boundary characterization of Inconel 718 sprayed coating was carried out by R. Molins et al. [43]. They reported that the globular oxide formed during particle flight consist of an outer spinel oxide (Ni, Fe) Cr_2O_3 and an inner nano-crystalline $CrNbO_4$ structure.

It has been demonstrated that microstructure of the coating changes the overall corrosion performance of the HVOF in terms of passive current density and lower impedance. The interconnected porosity, regions of different compositions in a coating and different phases are largely responsible poor corrosion performance of the coating. Although it is evident from different research work that microstructure does contribute in overall corrosion and its modification improves the corrosion resistance but still a trade off is necessary between microstructure optimizing cost and corrosion performance.

2.8.2 HVOF process modification and corrosion study

Improvement in corrosion performance by changing different process parameters or modifying coating material composition is reported. P. H. Suegama et al. [65] deposited 75% Cr_3C_2 and 25% NiCr by HVOF process on mild steel at gun transverse speed of 500 to 1000 mm/s for different samples. The corrosion performance was later tested by E_{oc} vs. time, impedance spectroscopy and microscopy. The corrosion potential of the coating deposited at 1000 mm s^{-1} gun transverse speed was 100 mV more positive than the coating deposited at 500 mm s^{-1} gun transverse speed [66]. The impedance values for the coating at higher transverse speed were more than the coatings at lower transverse speed. The improved corrosion performance was probably

due to particle compaction and less exposure time of molten particles in air during processing [66].

The role of coating thickness for corrosion properties of the coatings was studied by J.M. Guilemany et al. [3]. The Cr_3C_2–NiCr was deposited on mild steel samples and electrochemical corrosion was carried out by E_{oc} vs. time, polarization resistance, cyclic voltammetry, and impedance spectroscopy. The electrolyte passed through very thin and very thick coatings [3]. In case of thin coating the electrolyte passed through interconnected porosity while in thick coatings, thermal stresses induces crack which allowed the electrolyte to penetrate into the coatings. For producing thick coatings, thermal stresses must be removed before adding more layers to the coated surface.

The speed of the powder particles stream hitting the target material, transverse speed of the spraying gun, oxygen fuel ratio greatly contributes into resultant microstructure of the coating. The larger exposure of the coating materials at high temperature before deposition at the substrate material causes greater oxidation and microstructural heterogeneities. The variations in the microstructure in return give low corrosion resistance of the HVOF coating.

2.8.3 Corrosion study of HVOF thermal barrier coatings

Thermal barrier coatings are high temperature and corrosion resistant materials used at high temperature environment. Thermal barrier coatings generally consist of three layers i.e. a top ceramic layer, a thermally grown oxide layer and metallic bond layer. The ceramic layer is yttria stabilised zirconia (YSZ) which have very low thermal conductivity, the thermally grown oxide layer is

stable layer of Al_2O_3 and metallic bond layer is MCrAlY (M = Co or Ni) [67-70]. The oxide thickness growth with temperature and types of the oxides has been extensively studied in the past by thermal cycling and subsequent electrochemical testing. In our work, the research is limited to electrochemical corrosion testing of the base coat of thermal barrier coating i.e. the CoNiCrAlY coatings deposited by thermal spraying.

Electrochemical impedance spectroscopy supported with scanning electron microscopy and energy dispersive X-ray spectrometry (EDS) analysis was used by M.S. Ali et al., to characterize the corrosion properties of thermal barrier coating bond coat [109]. The NiCrAlY bond coat was deposited on Haynes-230 alloy and samples were heated from 700 to 1200° C for different intervals of time. The structural composition and compound formation analysis were carried out before and after thermal cycling. The change in electrical properties, resistance, and capacitance was related to the microstructure and microchemistry of the thermally grown oxide (TGO). In the early stage of thermal cycling, the impedance increased due to formation of thermally grown Al_2O_3 and reached to maximum value after 100 hours. With further thermal cycling the TGO changed from Al_2O_3 to a mixture of Cr_2O_3, (Ni, Co) (Cr, $Al)_2O_4$ spinel oxide. The spinel oxide is porous and although thermal cycling increased the thickness of oxide, impedance decreased.

To enhance the amount of alumina during thermal cycling of CoNiCrAlY, F. Tang et al. [50] used commercially available CoNiCrAlY with 2% alumina powder (≤40 μm) and cryo-milled in liquid nitrogen. The cryo-milled CoNiCrAlY powder was sprayed on mild steel to produce an approximately

100 µm thick coating. Polished and as coated samples were heated at 1000°C for a 1 to 24 h. The polished sample formed almost pure alumina while a spinel-oxide was formed at the as received sample. It was suggested that the oxides produced during the spraying process promoted the formation of spinel oxide structure. The low oxide formation during the coating process reduced the undesirable, fast growing non-alumina oxides. F. Tang et al. [71] also studied the effect of different oxygen-fuel gas ratios on oxide formation, a dense oxide scale mainly consisting of alumina was formed with low oxygen content while a mixed spinel oxide was found when higher concentration of oxygen was used. The characterization was carried out by SEM, XRD and energy dispersive spectroscopy. The fact is linked with the greater oxidation during the coating process at higher oxygen content which speeds up the formation of spinel oxide during thermal cycling. Oxide growth as a function of thermal cycling, changing process parameters of HVOF and comparing with other coating was also studied by EIS [110-115].

2.8.4 Corrosion study of carbide coatings

Carbide coatings offer a combination of abrasion, erosion and corrosion resistant properties that solves the wide range of wear and corrosion problems. Tungsten carbide embedded in the metal matrix (Co, Ni), produced by HVOF process are generally used as wear and corrosion resistant coatings. The good wetting of the WC by the metal binder results in tough, strong and wear resistant coatings [72]. The focus of research in this thesis work is electrochemical corrosion testing, the previous work in the field of electrochemical testing of the carbide coatings will be highlighted here. The

performance of the carbide coating has been reported by the tribo-corrosion. The corrosion damage in tribo-corrosion is due to combined action of friction, lubrication, wear and abrasion processes.

Wear resistant coatings were tested by electrochemical methods by N. Espallargas et al. [73]. They deposited Cr_3C_2 and WC-Ni coatings on stainless steel substrates to find a replacement for hard chrome coatings for erosion corrosion resistance. Structural characterization along with XRD was used to detect the compounds present before and after the corrosion. Impedance spectroscopy was used to study corrosion behaviour under different conditions. It was found the erosion corrosion performance of the thermal spray coatings was widely influenced by the ceramic phase composition, the size of ceramic particles and composition of the metallic binder [4]. The wear resistance of the tungsten carbide coating was found high at greater loading while Cr_3C_2 Ni-Cr showed high wear resistance under lower loading [73]. It was also found the erosion corrosion properties of the thermal sprayed coatings improved by surface finish [73].

The electrochemical corrosion study of the cermet coating was also carried out by V. A. D. Souza et al. [5]. They deposited WC-CrC and WC-Cr-Ni coatings on mild steel and stainless steel. The structure composition and compound formation was tested by SEM, EDS and XRD before and after the corrosion. The corrosion testing was carried out by potentiodynamic polarization, galvanic corrosion, critical pitting temperature testing. It was found at all temperatures corrosion occurs at faster rate for WC-Cr-Co coatings than for WC-Cr-Ni coatings. The galvanic test was carried out between coating and

substrate materials by immersing in the solution and measuring the galvanic current flow. The WC-Cr-Ni coating and stainless steel form a passive layer and very low galvanic current flow, the larger current were generated in case of WC-Cr-Co on mild steel due to higher galvanic current [4]. There was no well-defined critical pitting temperature where current rapidly increased. The WC, Co and Cr rich phases of the coating oxidized during anodic polarization but their percentage in overall corrosion product was dependent on electrochemical cell temperature. The WO_3, Cr_2O_3 and Co_3O_4 were the main components of corrosion product [74]

The coating produced by the powder mixed with nano-powder was carried out by L. Fedrizzi et al. [75]. The main purpose was to replace hard chromium coatings with new HVOF cermet coatings. The tribo-corrosion was tested with a load of 5-80 N at a specimen with a revolving speed of 200 rpm. The electrochemical testing was carried out by E_{oc} vs. time, potentiodynamic polarization and impedance spectroscopy under free and wearing conditions. The test coatings were further put in cathodic protection to see improved corrosion performance. The coatings with nano-powder displayed a markedly smaller weight loss than the coating produced from a conventional HVOF coating process.

The corrosion resistance of the cermet coating is reported by tribo-corrosion testing where stress, rotation and chemical reaction with the environment is considered. The electrochemical study reported for the cermet coating showed that coating suffered localized corrosion due to predominant attack on WC phase along with others phases. The particle size of the WC phase and

composition of the binder phase also contribute into overall corrosion performance of the cermet coatings.

2.8.5 Kinetic and localized corrosion testing by SECM

To study ET kinetics at alloy surface by SECM technique is relatively new in the field of corrosion. Previous work at the University of Nottingham by M. S Bakare et al. He did some work on spotting regions of different electrochemical activity at Inconel 625 alloy by imaging the surface in feedback mode [76]. Regions of different electrochemical activity were further confirmed by current distance SECM feedback approach curves on specific spots. This kinetic study of the coating and quantification of the electrochemical activity has not reported by any other research group [77-80]. Furthermore the SECM images were compared with microscopic images to correlate the electrochemically active spots to the splat boundaries [81]. Some researchers reported corrosion kinetic study by SECM on surfaces showing simple oxidation [82]. Mirkin at al. carried out heterogeneous electron kinetics study at stainless steel surface in 0.2M KNO_3 containing 1mM $Ru(NH_3)_6Cl_3$ and reported the k^0 approximately 10^{-3} cm s^{-1} which is three orders of magnitude lower than the platinum and gold electrodes [82].

V. Edgar et al. found the presence of ferrous ions in localized corrosion of tin plated mild steel [77]. They studied the Fe^{+2} formed on the tin plated mild steel sample by scanning tip of platinum electrode. The localized electron transfer activity at aluminium covered with 2-3 nm thick alumina layer was reported by S. Henry [83, 84]. The local activity at the oxide surface was revealed by SECM imaging which showed 1-10 μm radii size defects showing higher

current than the rest of the surface. After correlation between EDX analysis and SECM imaging the defects were identified as Cu and Fe rich regions. The electron transfer at Al-alloys 2024-T3 surface by SECM was studied by M.B. Jensen et al. [85]. They applied potential to drive oxidation and reduction at substrate and recorded the feedback current. The alloy contains Al-Cu phases which showed higher electron transfer rates as compared to the rest of the surface. The Cu-rich phase was also confirmed by SEM/EDS analysis and SECM imaging.

The effect of stress on kinetics of heterogeneous ET was studied by P. Sun et al. [86]. The combined effect of stress and corrosion was studied in this work. Reactions at stainless steel electrode as a function of applied mechanical stress was measured in $Ru(NH_3)_6Cl_3$. The current vs. distance SECM feedback approach curves were obtained at different applied potential and stress. The kinetic parameters were extracted from the Tafel plots, which showed good linearity. This indicates that valid kinetics can be performed by using SECM. The localized corrosion initiation and propagation was studied by K. Fushimi [87-90]. He fabricated a chloride injection tip by polarizing in the HCl for deliberately initiating chloride ions at the iron surface. The tip of the microelectrode was kept 40-60 µm away from the substrate. The chloride ions were released from the tip by applying a negative potential. The change in tip current was recorded to reveal different stages of pitting i.e. initiation, propagation and pit formation.

The SECM has not been reported as a routine electrochemical corrosion testing technique as potentiodynamic polarization and impedance spectroscopy

possibly due to intricate nature of the experimental setup and analysis. Some of the researchers used SECM for imaging of the Al, Ti alloys to find the defects in the surface oxides. These alloys form a uniform oxide layer; therefore the hotspots can be located with ease on the surface. The chloride injection by the SECM tip to deliberately enrich the regions high in chloride concentration is also reported by one group but detail of the processes taking place has been left unanswered. The ET kinetics study of the materials have regions of electrochemical activity within the narrow difference has not been reported.

2.8.6 Complementary use of electrochemical techniques

The electrochemical testing combined with microstructural characterization was used in the past to rank the corrosion resistance of HVOF coatings. Complementary use of electrochemical techniques, where shortcomings of one technique are addressed by another electrochemical technique is missing in the previous research. For example more positive value of E_{oc} vs. time plot of one material as compared to other indicate that former is more corrosion resistant. But establishing material corrosion performance ranking from only E_{oc} vs. time plot may lead to some wrong conclusion as the higher positive potential of the material may be influenced by the extent of surface preparation, microstructure or environment variation. In this case, the E_{oc} vs. time results supported by potentiodynamic polarization curves give better assurance for corrosion ranking of a material.

The potentiodynamic polarization curves give the average corrosion performance of the material with some limitations of charging current and ohmic drop [91-93]. In particular corrosion study, if electrochemical response

of the different microstructure and only chemical reaction are the main interest, it is not possible to get the desired results from potentiodynamic polarization testing. Electrochemical impedance spectroscopy will be a better candidate method to acquire the desired corrosion parameters. The usefulness of the EIS ends where corrosion measurements are required at steady state, the non steady state in corrosion process adds errors into final EIS results [94-96].

It is possible to study complex corrosion study by EIS and correlate individual microstructural features to their electrochemical response but precise identification of regions of different electrochemical activity and their quantification cannot be done by EIS. If it is desired to spatially resolved the regions of different electrochemical activity and quantify them, SECM is probable the only option to chose. The regions of different electrochemical activity can be correlated by SECM and microscopy imaging while the quantification of the electrochemical activity can be done by heterogeneous ET kinetic study [97]. Hence complementary use of electrochemical techniques can enhance the better understanding of corrosion processes.

2.9 Summary

The corrosion of engineering metals and alloys occur in most of the industrial environments and it cost billions of dollars. Therefore spending resources on corrosion prevention and protection is a rational approach. The purpose of coating is either to get a blend of unique surface properties at low cost. This can be done either coating expensive materials on cheap substrates instead of using bulk alloys. The superior corrosion/wear resistant properties while keeping the tougher substrate properties can also be achieved by HVOF

thermally sprayed coating process. Despite improved properties by use of HVOF coatings compared to substrate, the corrosion performance of the coating is generally lower than its equivalent bulk material. Researchers have made efforts to improve corrosion performance of the coating by modifying different process parameters, stress relieving and surface modifications. Some of the techniques improve the corrosion performance but modifying coating further adds to processing cost. Considerable research has been reported on the use of electrochemical testing techniques for corrosion testing. Some electrochemical techniques give area average results whilst other allows the effect of different features to be determined. The complementary use of basic electrochemical techniques (e.g. potentiodynamic polarization, E_{oc}, and EIS) with more advanced techniques (e.g. SECM) is lacking which is tried to address in this work to get deeper insight of corrosion process taking place at HVOF coatings

3 Electrochemical testing methods

3.1 Introduction

In this chapter the details of three electrochemical corrosion testing methods used in this project i.e. potentiodynamic polarization, electrochemical impedance spectroscopy and scanning electrochemical microscopy are given. The theory of the above three electrochemical testing methods, test protocols, data analysis and interpretation are included in the chapter.

3.2 Electrochemical testing of corrosion

A potentiostat attached with three electrode electrochemical cell is generally used for electrochemical corrosion testing. The cell consists of working electrode (WE), counter electrode (CE) and reference electrode (RE) in a test solution called the electrolyte. In electrochemical testing anodic and cathodic reactions can be separated on WE or CE by controlling the potential difference (PD) between WE and RE

The schematic in ***Figure 3-1*** shows the main components of an electrochemical cell attached with the potentiostat. The potentiostat applies the potential difference (PD) between WE and RE while current is measured in the circuit between WE and CE [14]. A saturated calomel (SCE) is commonly used as a RE in corrosion testing. The WE is the sample tested, e.g. a piece of metal whose corrosion behaviour is of interest. A platinum wire (diameter 5mm) or strip (1 × 5× 5mm) is commonly used as CE [98]. Electrochemical corrosion testing techniques are fast (corrosion rate by linear polarization resistance (LPR) takes few min), sensitive (can measure 10^{-15} amps with some limitations), easy and results are reproducible within the limit of 5-10% [99, 100].

A variety of equipment and techniques are available to study corrosion mechanisms in different fields of research and applications. To cover all electrochemical corrosion testing is beyond the scope of this project. Only open circuit potential (OCP), potentiodynamic polarization, electrochemical

impedance spectroscopy (EIS) and scanning electrochemical microscopy (SECM) are covered here.

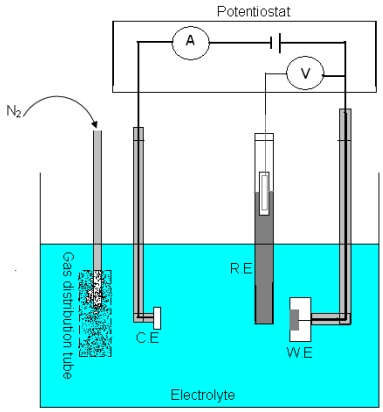

Figure 3-1: Three electrode electrochemical cell

3.2.1 Open circuit potential vs. time

The open circuit potential (OCP) is defined as the PD between WE and RE in a solution [14, 26]. One or more anodic or cathodic reactions are taking place but the current flow due to anodic reactions is equal to the current flow due to cathodic reactions. The term E_{oc} is interchangeable with corrosion potential, rest potential and freely corroding potential [17]. The E_{oc} measurement is the easiest test in electrochemical testing but provides the least information about the mechanism of corrosion. The equipment required to perform E_{oc} test includes a stable RE and a potentiostat or RE and high impedance potentiometer [101]. The E_{oc} measurements can be made over a period of time to determine how long is taken for it to reach a stable value. The basic use of the E_{oc} vs. time experiment is to achieve a stage where E_{oc} become approximately constant with time [16]. The E_{oc} often increases with time for passive materials and decreases when localized corrosion begins [21]. Based on the information obtained from E_{oc} alone it is not possible to draw

conclusions about the mechanism of corrosion, hence the E_{oc} test is normally combined with polarization resistance or other electrochemical techniques.

3.2.2 Potentiodynamic polarization curves

Potentiodynamic polarization is commonly used to study the mechanism and rate of corrosion reaction [15]. Information about corrosion rate, pitting susceptibility, passivity can be determined and the results obtained are averages representative of the area exposed [102]. Potentiodynamic polarization is sweeping the half cell potential away from the E_{oc} to more positive and more negative potentials. Polarization curves are also known by the name of famous scientist Ulick. R. Evans as Evan's diagram for his work on aqueous corrosion. In cathodic polarization electrons are supplied while in anodic polarization electron are drained by the potentiostat [15]. The reaction taking place at working and counter electrode depends on the applied potential between working electrode and reference electrode. An applied potential more positive than the open circuit potential will drive dominant anodic reactions at working electrode and dominant cathodic reactions at counter electrode. ***Figure 3-2*** shows the anodic reaction at working electrode and cathodic reaction at counter electrode.

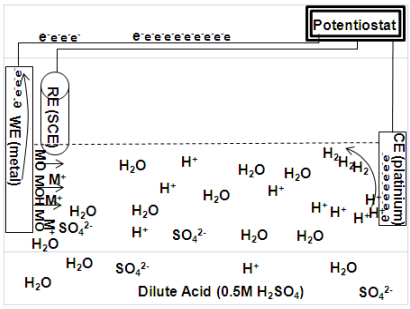

Figure 3-2: Controlled electrochemical reactions in a corrosion cell

3.2.2.1 Features of potentiodynamic polarization curves

The potentiodynamic polarization data is commonly presented in a semi logarithmic graph of potential and current or current density (*E vs. logj*) to show all current potential trends in one graph [18, 103]. The corrosion behaviour of the material is predicted from the shape and analysis of these polarization curves [104]. The schematic in ***Figure 3-3*** shows the main features of a potentiodynamic polarization curve for a material that passivates, such as stainless steel. Three distinct regions in potentiodynamic polarization schematic are; active, passive and transpassive. The region AO to OB, in ***Figure 3-3*** is the active region. In this region the exponential increase in current with overpotential (η) gives a linear behaviour on log scale which is also referred as the Tafel region (where $\eta = E\text{-}E_0$, E is applied potential and E_0 = no applied potential also called formal potential (equivalent to E_{oc}). In this region the Tafel equations are obeyed, the ET reaction is controlling the overall reaction rate across the electrode-electrolyte interface. The straight line portions below and above the point O are called cathodic and anodic Tafel region respectively. The intersection point of the anodic and cathodic Tafel line is called corrosion potential (E_{corr}) on the Y-axis and corrosion current (j_{corr}) on the X-axis. The j_c and j_a within the Tafel regions can be calculated by the Tafel equation given in ***equation 3.1.***

$$E - E_0 = b \log \frac{j}{j_0} \qquad \textbf{3.1}$$

($E\text{-}E_0$) = η (Overpotential), b is Tafel slope, j is current at any given potential, j_0 is current at $\eta = 0$. The Tafel equation for anodic and cathodic reaction can be rewritten as ***equation 3.2*** and ***equation 3.3***. The Tafel region is

schematically illustrated in ***Figure 3-4.*** At E_{corr} the anodic and cathodic current densities are equal i.e., $j_a = j_c$. The Tafel slopes can be calculated from cathodic and anodic branch of the Tafel plot [21].

$$\eta_c = \frac{2.303RT}{1-\alpha} log\ \frac{j_c}{j_0} \qquad \textbf{3.2}$$

$$\eta_a = \frac{2.303RT}{\alpha nF} log\ \frac{j_a}{j_0} \qquad \textbf{3.3}$$

η_c and η_a are cathodic and cathodic overpotential, n is the number of electron release in the reaction and T is the temperature. α is called transfer/symmetry coefficient obtained from intersection of the potential energies profiles for the reactants and products during ET reaction. The value of α can be from 0-1, α approximately 0.5 defines the symmetry of potential energies profile of reactants and products [105, 106]. The approximately vertical line labelled B-C in ***Figure 3-3*** polarization schematic is the passive region. In passive region, a corrosion product such as an oxide is formed on the surface which form a barrier [107], inhibiting the anodic reaction. Due to this restriction, current does not increase with potential in passive region. The region labelled C-D in polarization schematic is the transpassive region. In transpassive region, the current increases rapidly with potential due to break down of the passive layer. In stainless steel and chromium bearing nickel alloys, the transpassive region appears at a potential more positive than the oxygen evolution potential, where the chromium rich passive film is unstable [13]. Results from the potentiodynamic polarization method are used to determine instantaneous corrosion rate, pitting propensity [108], intergranular corrosion, chromium

depleted regions, as well as current densities for cathodic and anodic protection [109-114].

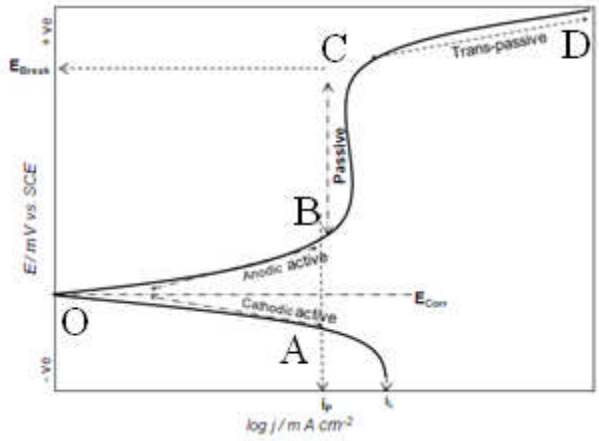

Figure 3-3: Schematic diagram for different regions of potentiodynamic polarization curve

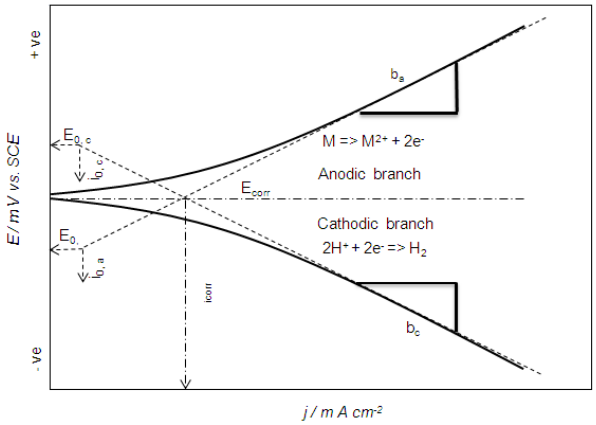

Figure 3-4: Schematic diagram for showing kinetic regions of polarization curve

3.2.2.2 Test Protocol for potentiodynamic polarization curve

There are number of corrosion standards available that are relevant to recording potentiodynamic polarization curves. These standards are internationally recognized and used to study the desired corrosion property. The American society for testing and materials (ASTM) describes most of the operating and interpretation issues related with corrosion characterisation. ASTM G1-03 and G31-72 describe the sample preparation, surface cleaning

before/after corrosion test and electrolyte purity issues. The solution and electrolyte specifications given in ASTM G1-03 and ASTM G31-72 are standardised for immersion test and weight loss test (corrosion rate measurement methods) but these specifications can also adopted for electrochemical tests [115]. The high purity of electrolyte and water are recommended for the test solution. Other main issues described by these standards are proper specimen marking, the sample/test solution, no sharp edges, surface finish and cell operating temperature [116]. The ASTM G3-89 describes the convention to represent the electrochemical data along with describing different regions. The standard also describes the complete polarization curve with its different regions i.e. active, passive and transpassive. The current density at active passive transition point is called the critical current density and the current density in the region where current does not increase with potential is called the passive current density [117]. ASTM G59-97 is used for conducting potentiodynamic polarization tests. The standard is also used for verification and calibration of the test equipment. In this method a small potential ±30 mV with respect to corrosion potential is applied at a scan rate of 0.6 V/h and resultant currents are recorded. The current density related with the polarization resistance is calculated by the Stern-Geary equation given in ***equation 3.4***.

$$i_{corr} = \frac{B}{R_P} \qquad \textbf{3.4}$$

$$B = \frac{b_a \times b_c}{2.303(b_a + b_c)} \qquad \textbf{3.5}$$

$$C_R = \frac{3.27 \times 10^{-3} \times i_{corr} \times Eq_w}{\rho} \quad \textbf{3.6}$$

In ***equation 3.4***, the i_{corr} is in amps cm^{-2}, R_p is polarization resistance when reaction is under activation control, presented in units of Ω cm^{-2} and B is the Stern-Geary coefficient in Volts. The Stern-Geary coefficient is related to the anodic (b_a) and cathodic (b_c) Tafel slopes and calculated by the ***equation 3.5***. Measuring corrosion rate is also one of the important aspects of corrosion testing. The corrosion rate, C_R, in thickness loss can be calculated by using the ***equation 3.6*** where Eq_w is equivalent weight in grams/equivalent, ρ is density of material in g cm^{-3}[118, 119]. The ***equation 3.6*** is only applicable for uniform corrosion not for localized corrosion, it is also only applicable for free corrosion at E_{oc} since it does not take any passivation or mass transfer limitation effects into account. The ASTM G5-94 is standard test method for making potentiostatic and potentiodynamic anodic polarization measurement. Some of the operational parameters and equipment of G5-94 overlap with the above standards, i.e. preparation of the sample, electrochemical cell, nitrogen gas flow 150 cm^3/h, operating temperature, reference and counter electrode [100]. Although those standards are devised to perform potentiodynamic polarization tests researchers have generalized experimental parameter for their convenience.

3.2.2.3 General practice for potentiodynamic polarization test

The surface of the working electrode was polished on different grades of polishing wheels. The main aim was to get an average surface roughness below <1µm surface finish [104]. An exposed surface area of $1cm^2$ was used

for carrying out electrochemical testing. The edges (metal-epoxy interface) of the metal surface are covered with the non-conducting lacquer to avoid initiation of corrosion by edge effects. If this is allowed to occur it may lead to crevice corrosion (type of localized corrosion) [115]. It is common practice to purge the electrolyte with high purity nitrogen gas for 30 min before inserting the sample; this removes any absorbed oxygen from the electrolyte. A steady flow of nitrogen in the solution is maintained throughout the experiment [103, 104, 108]. The potentiodynamic work reported for the materials that do not passivate use a shorter potential range i.e. ±20-40 mV while some other polarize to a larger range ±250 mV with reference to E_{oc} [103]. A scan rate of 20-50 mV/min is generally applied for potentiodynamic polarization test with the scan starting from a potential more negative than E_{oc} and scanning to a more positive potential [116, 117].

3.2.2.4 Variants of potentiodynamic polarization testing

The potentiodynamic polarization is also used with some variations. The cyclic polarization is the modified form of potentiodynamic polarization to study pitting and crevice corrosion in stainless steel and Ni-CO base alloys. In cyclic polarization the potential scan is reversed from the transpassive region. The changes between forward and reverse scan indicate the material pitting or crevice corrosion tendency. The ASTM standard G61-86 is a standard protocol to conduct cyclic polarization test for stainless steel and Fe-Ni-Co base alloys. The electrochemical cell setup is the same as described by G5-94 with purity and cleaning comments matching with G1. The ASTM G61-86 test protocol recommends using 3.5% NaCl solution at 25^0 C. The test sample

should be immersed in the electrolyte for 1 hour before the potential scan. The E_{oc} is measured immediately before the potential sweep. The scan is started from E_{oc} towards positive direction at a scan rate of 60 mV h^{-1} until current reaches 5 mA. The scan is then reversed until it reaches starting E_{oc} [120]. If the polarization curve from forward and reverse scan overlaps each other, material is not prone to localized corrosion. The overlap of the polarization curve in reverse scan indicates the passive film instantaneous heal and re-passivate, contrary to that if E_{corr} shift to more negative value indicates that the passive film do no re-passivate. The greater the E_{corr} shift to more negative potential in the reverse scan, the greater is the probability of localized corrosion, i.e. susceptibility to pitting [108, 121]. Another variant of potentiodynamic polarization is reactivation, commonly used for evaluating sensitization of Ni-Cr alloys [122, 123]. The chromium depleted regions around the grain boundaries formed due to high temperature processes (welding, hot rolling) [124]. The process of chromium depletion at grain boundaries is called sensitization. The ASTM G108-98 describes the standard test method for electrochemical reactivation for detecting sensitization of AISI type 304L [125]. Some other researchers use the same standard method (ASTM G108-98) for detecting sensitization in Ni-Cr super alloys [126, 127]. A small amount of potassium thiocyanate (KSCN) i.e. 50-100 ppm in 0.5 M H_2SO_4 is used as test solution. The small amount of KSCN reactivates the chromium depleted region on reverse scan [127]. The sample is passivated for 2-3 min at 450 mV constant potential. A potential is scanned from passivated potential to 950 at a scan rate of 150 mV min^{-1} in forward and reverse direction. The hysteresis between forward and reverse current peak indicates

the degree of sensitization of a material. There are some other equivalent standards available to conduct potentiodynamic polarization tests e.g. BS EN ISO 17475 [128]. The potentiodynamic polarization method and its variants reported by researchers are very diverse.

3.2.2.5 Factors affecting potentiodynamic polarization results

The response current due to applied potential in potentiodynamic polarization consists of faradaic and non-faradaic current or charging current. The current flow due to redox reactions is faradaic and that due to charging of the electrode-electrolyte interface is non-faradaic current [129]. The electrode-solution interface becomes an electrical double layer (E_{dl}) when potential is applied from potentiostat.

The schematic in ***Figure 3-5*** shows the main components of an electrical double layer. When potential is applied to the metal immersed in electrolyte the excess charge moves to the surface (metal side of the double layer). Ions and molecules interact at the metal surface to neutralize this charge (solution side of the double layer). The solution side of the double layer consist of sub-layers called inner Helmholtz (2), outer Helmholtz (3) and diffuse layer (4). The inner Helmholtz is a mono-layer of solvent molecules and specifically adsorbed ions. The solvated cations next to inner layer are non-specifically adsorbed (long range electrostatic forces) and form the outer Helmholtz layer. Next is a three dimensional solvated cations layer, this is less compact than inner layer and is called diffuse layer.

As soon as potential is applied to a metal immersed in solution, ions and molecules interact with metal surface to neutralize the excess charge. Two

types of processes occur at metal electrolyte interface, one involves electron transfer across metal-electrolyte interface (redox) and the other involves charging/discharging of the double layer [130, 131].

Information about an electrochemical system is often gained by applying a potential and recording the resultant current. As stated by Faraday's law, the amount of chemical reaction by flow of current is proportional to the amount of electricity passed. A corrosion system is neither ideally polarised nor fully reversible hence the applied potential partially contributes to both redox reactions and to charging/discharging of the double layer. In continuously increasing potential techniques (e.g. potentiodynamic polarization), a charging current always flows because each incremental step of the potential scan changes the charge stored at metal-electrolyte interface [18, 131].

The charging current cannot be fully eliminated but can be minimized by using a slower scan rate during potentiodynamic polarization. The slow scan rate decreases the rate of charging of the double layer therefore decreasing the charging current. The charging current is therefore a smaller proportion of the measured current which thereby better relates the redox reaction [132].

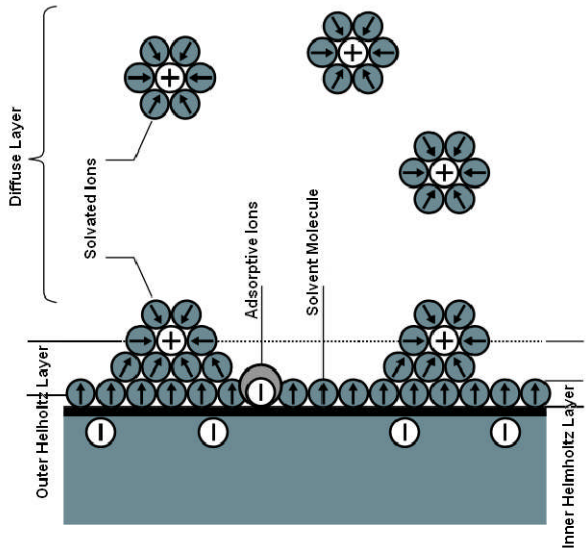

Figure 3-5: Schematic diagram of Electrical double layer

The behaviour of the double layer is analogous to a capacitor and is governed by the ***equation 3.7***, where q is the charge stored at the capacitor (in coulombs), E is potential difference across the capacitor (in Volts) and C is the capacitance (in farads). Farad is the charge in coulombs stored in a capacitor when potential of 1 volt is applied. The applied potential across a capacitor will allow the charge accumulation at electrode surface until q satisfies the ***equation 3.7.*** The charging current flows in the electrochemical cell due to charging/discharging of the double layer [133].

$$C = \frac{q}{E} \qquad \textbf{3.7}$$

For example, if 1 V is applied across a double layer with 30 µF of capacitance, the current will flow until a charge of 30 µC accumulates at the metal-electrolyte interface. The charge is generally presented in charge per unit area called charge density. In potentiodynamic polarization test the continuously changing electrode potential, changes the charge density stored at electrode

electrolyte interface. The change in the charge stored density causes charging current to flow all the time in potentiodynamic polarization test.

The current of interest is usually Faradaic current which depends on kinetics of ET and rate at which the redox species diffuses to the surface. The diffusion dependent faradaic current increases with the square root of the scan rate. The charging current increases linearly with the scan rate [129]. Due to the different dependencies of charging and faradaic current on scan rate, there will be some scan rates where the charging current is so large that it swamps the Faradaic current. The direction of the potential scan also effects the distortion due to flow of the charging current [91]. In positive scan the same direction of charging current and anodic current causes corrosion potential *(E_{corr})* to shift more negative potentials and in negative scan direction the charging and cathodic current cause E_{corr} to shift more positive potentials [91, 134].

3.2.3 Electrochemical impedance spectroscopy (EIS)

The history of the EIS is as old as electrochemistry and used for different electrochemical studies e.g., dielectric properties (Carter, 1925), Smith-chart impedance diagram (Smith, 1939-1944), semiconductors and ionic systems (Randles, Jaffe 1947-1952) etc [94]. The real power of the EIS technique was discovered by different electrochemists and materials scientists with advancement in data acquisition and statistical analysis for studying complicated systems [94].

EIS is a non destructive method for characterising corrosion study at the surface and through thickness without damaging the tested part [135]. Any process which involves the change in electrical characteristics of the system

can be studied by EIS. The corrosion of the steel bars embedded in concrete is unknown until rust stains appear on the structure. In compact, non-defective concrete structure the highly alkaline environment (pH > 13) maintains the passivation around the steel bars. Unfortunately during the service life concrete structures different processes involve (weathering, stress, chemical species) which changes the passivation environment surrounding the steel bars. The de-passivation process further leads to oxidation of the steel bars, which causes volume expansion surrounding the steel bars. The process of volume expansion builds up micro-cracks which allow the corrosion product to appear on the concrete surface. The EIS can detect the corrosion in concrete at very early stage (depassivation) before it appears on the surface [136]. Different processes in organic paint coatings i.e. water uptake, blister formation, corrosion under paint and paint rupture can be studied by impedance spectroscopy [137]. Other applications includes quality control of anodized layer, characterizing porous electrodes, working efficiency of fuel cells and the state of the charge of batteries [95, 138].

The electrode study by potentiodynamic polarization test involves applying a large perturbations and measuring the transient currents. In impedance spectroscopy a small AC-signal is applied to study the system response at the steady state. In a DC circuit the resistance is the ability of circuit element to offer hindrance to electron flow. The ideal resistor can be defined by Ohm's law and is independent of frequency. However in real circuits elements behave in a much complex way. A more general parameter, impedance is use instead of resistance. Impedance can be generally considered as the resistance offered in the current flow when alternating potential is applied. As the applied

potential is sinusoidal the current response will also be sinusoidal. The applied excitation signal is expressed in ***equation 3.8***, where *V (t)* is the potential at time *t*, V_0 is the amplitude of the signal, and ω is radial frequency. In linear systems the response signal has a change in amplitude and a phase shift *(θ)*, where θ = Phase angle between *V (t)* & *i (t)* (***equation 3.9***). The impedance can be expressed by Ohm's law as in ***equation 3.10***. The magnitude of the impedance is generally divided into real and imaginary parts (***equation 3.11***). The conversion of angular frequency *(ω)* to radial frequency *(f)* is defined by, $\omega = 2\pi f$, [94, 138].

$$Applied\ potential = V(t) = V_0 \sin(\omega t) \qquad \textbf{3.8}$$

$$Response\ current = i(t) = i_0 \sin(\omega t + \theta) \qquad \textbf{3.9}$$

$$Impedance = V(t)/i(t) = V_0 \sin(\omega t)/i_0 \sin(\omega t + \theta) \qquad \textbf{3.10}$$

$$Total\ Impedance = Real\ impedance + Imaginary\ impedance \qquad \textbf{3.11}$$

$$[Z] = Z' + Z''$$

As sinusoidal signal is applied periodically at different frequencies, it is common practice to analyse the response by Laplace or Fourier transform equations integrated in EIS software [139]. EIS is a powerful diagnostic tool to measure the electrode, electrolyte and interface responses when a small sinusoidal voltage (10mV) is applied over a range of frequencies (mHz to MHz). The measured spectrum is the combined response of all circuit elements over a range of frequencies.

3.2.3.1 Application of EIS in corrosion testing of coatings

The electrochemical impedance spectroscopy testing offers an advanced method of evaluating the performance and barrier properties of metallic and organic coatings [10, 140]. Electrochemical impedance spectroscopy technique does not accelerate the corrosion reaction and is non-destructive. The technique is very sensitive to resistive-capacitive nature of the coating and electrochemical interface. The electrochemical impedance spectroscopy can distinguish between resistive properties of the coatings or passive film because of its ionic, electronic capacitive nature and thickness [99]. Different process taking place over a period of time for metallic and organic coating can also be tested by EIS [141, 142].

The thermally sprayed coatings may contain regions of different composition, oxide, pores and cracks. Depending on the amount of these defects in the coatings, defects display a characteristic appearance in the impedance spectra. The corrosion begins at coating electrolyte interface, which lead to galvanic corrosion due to different phases or penetration of solution/ions to the substrate [94]. The rate of corrosion at coating substrate depends on the transport of corrosion species through the coating. All above process make the corrosion process more complex, hence EIS is sometimes preferred over other DC electrochemical technique to study and distinguish different corrosion processes taking place in a system [135, 138, 143, 144].The EIS previously been used to study oxide growth as a function of temperature, evaluation of paint coating and corrosion processes taking place due to interconnected

porosity. In our work, we used the EIS to correlate the microstructure features of the coatings to their electrical response.

3.2.3.2 EIS Data presentation

EIS data is presented either in the Bode plot or the Nyquist plot (***Figure 3-6***c) or both. The Bode plot is divided into Bode-impedance (***Figure 3-6***a) or Bode-theta plot (***Figure 3-6***b). In Bode plot, impedance and theta can be plotted on the common frequency axis or impedance and theta on separate plots. The Nyquist plot is presented between real and imaginary components of the impedance. Each part of the impedance spectra is representative of the specific feature of the system response. A horizontal line in the Bode impedance plot indicates that the system impedance is dominated by a resistor. Increase and decrease in impedance with decrease in frequencies represent capacitor and inductor behaviour respectively. These properties can also be defined from the Bode theta plot i.e. output current stays in phase for resistor while a 90^0 lead and lag occurs in capacitor and inductor respectively. A semi circle appearing in the Nyquist plot means there is only one process involved in the investigated frequency range. More than one semi circle appear when more process with sufficiently different time constants are involved. The ***equation 3.12*** gives the time constant for electric circuit have one resistance and capacitance components.

$$Time\ Constant = \tau = RC \qquad \textbf{3.12}$$

The semi circle is generally depressed, indicating that capacitive behaviour is non-ideal. The non ideal capacitor is attributed to surface roughness, heterogeneous corrosion or presence of more than one polarization mechanisms.

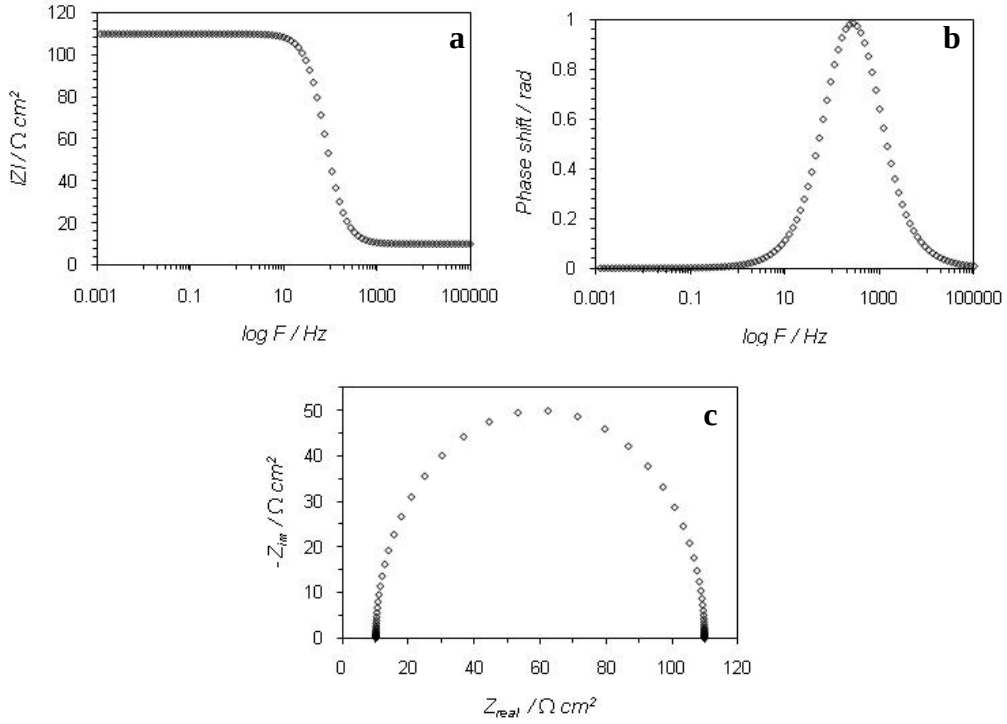

Figure 3-6: IS data presentation, a) Bode impedance, b) Bode theta, c) Nyquist plots

3.2.3.3 EIS data analysis by electrochemical equivalent circuit modelling

Impedance spectra produced from an electrochemical system requires the interpretation of the data with the help of suitable models. Electrochemical equivalent circuit modelling (ECM) is the most common method to analyse EIS spectra. Electrochemical equivalent circuit is a theoretical representation of the sample being tested. Electrochemical equivalent circuits consist of a number of electrical components i.e. resistors, capacitors, inductors and some specialized electrochemical elements like Warburg diffusion elements and

constant phase elements. Each component has a specific behaviour over the range of frequencies. The first step is an educated guess which may be based on prior knowledge of the system and observing the experimental impedance spectra to predict the components involved in the electrochemical system. Next step is to combine these circuit elements into logical series and parallel combinations to construct an equivalent circuit [145]. A simple Randles model used for bare metal in an electrolyte is shown in ***Figure 3-7***; this consists of a solution resistance R_u capacitance of the double layer C_{dl} and a polarization resistance R_p. The solution resistance is a significant factor in highly resistive electrolytes. The 3-electrode electrochemical cell minimises the solution resistance between CE and RE by increasing the counter electrode area and placing CE and RE in close vicinity to each other. However the solution resistance between reference electrode and working electrode must be considered in highly resistive electrolytes. The resistance of a solution depends on ionic concentration, type of ions, temperature and the area in which current is carried. Most electrochemical cells do not have uniform current distributions throughout area; hence calculating solution resistance is big problem. With EIS modelling the solution resistance can be directly determined from the higher frequency results because all of the current has to pass through solution at higher frequencies [94, 146].

In an electrochemical system the double layer forms on the surface due to excess of charge at electrode surface and corresponding attraction of ions from the solution ***(See section 3.2.2.5)***. The double layer is analogous to a capacitor, the associated; double layer capacitance is referred as C_{dl}. The separation of the charge between two layers is on the orders of angstroms which typically

generate a capacitance of 20 to 60 µF for every 1cm^2 area [105, 106]. The value of the double layer capacitance depends on applied potential, surface roughness, oxide layer and impurity adsorption [105]. More complicated equivalent circuit models can be used for representing complex electrochemical systems.

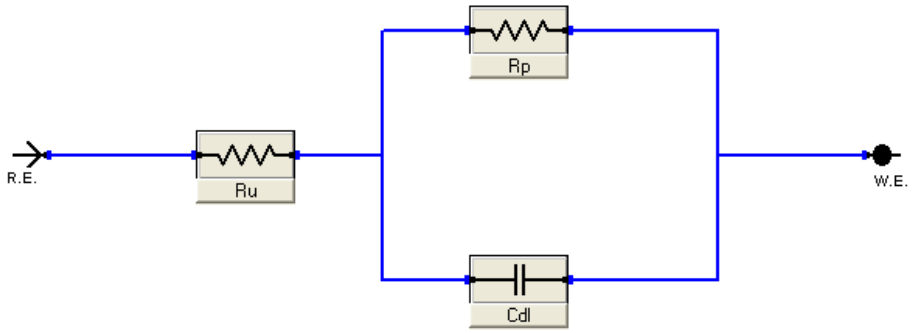

Figure 3-7: Simple Randles model

3.2.3.4 Interpretation of circuit components and calculating seed values

Each component of electrochemical equivalent circuit has physical meaning and justification to be in the circuit [95]. The fit between experimental and ECM can be improved by increasing the number of circuit components but this is generally only of real value when a sound physical argument can be given [38, 138]. The seed values of the circuit components are the starting values to fit the theoretical model with experimental spectra [94]. The impedance of the resistance remains constant at all frequencies and no change in the phase angle (θ). The common resistors in the equivalent circuit are R_u and R_p which represent solution resistance and polarization resistance [136, 140]. The solution resistance is not very significant for conductive solutions but for less conductive solutions, higher solution resistance can add errors into overall

resistance [147, 148]. The inverse of polarization resistance can be used for measuring corrosion rate. The impedance of a resistor show plateau in impedance spectra and the seed value can be calculated by the ***equation 3.13***. The capacitor component in the equivalent circuit represents the double layer [94]. The impedance of the capacitor increases at low frequencies and current lead the voltage by 90^0 (phase shift is 90^0). The seed value for capacitor can be calculated from ***equation 3.14***. The inductor in the equivalent circuit model represents the adsorption process at low frequencies and artifacts (inductance of wires or surrounding instruments) at high frequencies [96]. The impedance of the inductor decreases at low frequencies and current signal lag the voltage by 90^0 (phase shift is -90^0). The seed value of an inductor can be calculated from ***equation 3.15***. The constant phase element represents the rough or inhomogeneous surface or scattered electrochemical reactivity at electrode surface [95, 148]. The constant phase element (CPE) is also called as impure capacitor. The CPE consist of parameter (P), called capacitance and the exponent (n) where $0 < n < 1$. The seed value can be calculated by the ***equation 3.16***. The Warburg impedance is a diffusion resistance and the seed value can be calculated by the ***equation 3.17*** [148].

$$Resistor\ impedance\ =\ Z_R = R \qquad \textbf{3.13}$$

$$Capicitor\ impedance =\ Z_C = \frac{-j}{\omega C} \qquad \textbf{3.14}$$

$$Inductor\ impedance = Z_L = j\omega L \qquad \textbf{3.15}$$

$$Constant\ phase\ element\ impedance = Z_Q = \frac{1}{Y_0(j\omega)^n} \qquad \textbf{3.16}$$

$$Warburg\ resistor\ impedance = Z_W = \frac{1}{Y_0\sqrt{(j\omega)}} \qquad \textbf{3.17}$$

The fitting of the EIS data requires the seed values to be within a factor of 10 to 100 of the final values [149]. The fitting software minimises the deviation between simulated and experimental values of impedance spectra. The generally accepted error limit for the EIS result is 10% but researchers have also published their work with errors in excess of 20% [146, 150].

3.2.3.5 EIS data validity

The impedance data is validated by different methods namely Kramers-Kronig (KK) and Hilbert transforms (HIT) [151]. The real impedance is calculated from the imaginary part and compared with experimental values and vice versa with imaginary part. Most of the computer based EIS softwares have this built in function for data validity [152, 153]. Full compliance of the data with the KK transfer is only attained if physical conditions of the systems are fulfilled i.e. causality (response signal only related to perturbation applied), linearity (response remain linear within the applied potential perturbation), stability (no physical or chemical change with the time) and continuity (data valued from 0 to ∞ frequencies) [94, 151, 153]. As corrosion is a continuous degradation process and the surface condition changes all the time, data does not follow the KK transform [152]. Impedance data acquired from corrosion systems that do not comply with KK still can yield useful information via analysis of their variation over time and the use of an equivalent circuit model [151].

3.2.4 Scanning electrochemical microscopy

Scanning electrochemical microscopy (SECM) was introduced by Allen J Bard's group in 1989 to study the chemistry at high resolution near interfaces. In SECM the current flows through a small electrode (micro or ultra-micro electrodes 1-25 μm diameter) which is used to characterize processes and structural features at the substrate as electrode tip is scanned in close proximity to a surface [154]. The SECM has been used in a wide range of fields including corrosion study, reaction rate kinetic study, micromachining, biological systems study and measuring potential across membrane [155].

3.2.4.1 Basic components of SECM

SECM apparatus includes high resolution electrode positioning device, micro electrode, bi-potentiostat, electrochemical measurement cell, vibration isolation table and a video microscope. The schematic diagram in ***Figure 3-8*** shows the main components of a SECM apparatus.

3.2.4.1.1 High resolution electrode positioning device

Accurate and reproducible positioning of the microelectrode in three dimensions is an important design element of the SECM. It is also required that movement in one direction does not produce movement in other directions [156]. The stepper motor positioner in conjunction with a closed loop 3-dimensional piezo positioner is an integral part of the SECM equipment [157]. The piezo-positioner provides a movement of sub-nanometre resolution. Two motors assembled perpendicular to each other provide scanning in X and Z plane while the third one attached with microelectrode provides the movement

in Y plane. The resolution of the piezo-motor is much higher than required in most SECM measurement. The stepper motor mechanism provides a quick three dimension movement of the microelectrode [105].

3.2.4.1.2 Microelectrode and ultramicroelectrodes

The microelectrodes have the characteristic dimension from tens of microns to hundreds of microns while ultramicroelectrodes (UMEs) are electrodes which have the characteristic dimension of few microns. The characteristic dimension of the electrode is the surface allowing electrochemical reaction to occur. Microelectrodes were invented around 1980, and are one of the most important parts of the SECM apparatus [158].

The main advantages of the UMEs are faster double layer charging, reduced ohmic resistance and high mass-transport rates which makes the fast kinetic study feasible in variety of environments. The invention of microelectrodes played a significant role in application of analytical chemistry to small volume, fast and spatially resolved measuring techniques [159-161]. The application of microelectrodes to study micro-electrochemical systems is spread across fields in material engineering, fuel cells, biotechnology, medicine, electrochemical sensors and micromachining [79].

3.2.4.1.3 Electrochemical measurement cell

A small size measurement cell capable of holding few millilitres of electrolyte is generally used in SECM measurements. The electrochemical cell housing three electrodes is fixed on a stainless steel working stage. The working stage can be made precisely flat by up and down movement of the micro-screws provided under the working stage. The micro-positioning is important in

imaging to correct surface tilt and avoiding microelectrode tip crash. A Faraday cage and vibration free work place for SECM measurements are also beneficial [154].

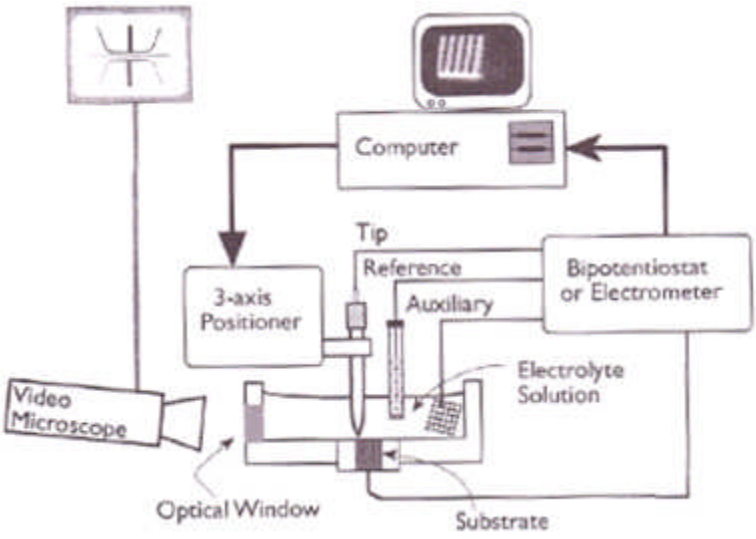

Figure 3-8: Schematic showing all components of SECM setup [78]

3.2.4.2 SECM principle

The quantitative aspect of measurement by SECM is based on movement of the microelectrode from an infinite distance in solution to the close proximity of the substrate. There are different shapes of microelectrodes used but disc shaped microelectrodes are commonly used due easy fabrication and polishing procedures [162]. When feedback current (***see section 4.7.3.5***) is measured at microelectrode, the potential of the microelectrode is set to a value so that the current is diffusion limited at tip-electrolyte interface. Ferrocenemethanol was used as redox mediator in our work, and tip was kept at 0.6 V to allow diffusion limited current at tip-electrolyte interface. The tip current at infinite distance can be calculated by the ***equation 3.18.***

$$i_{T\infty} = 4naFDC_0 \qquad \textbf{3.18}$$

$i_{T\infty}$ is the tip current at infinite distance, *4* is the tip geometry constant for disc shape for the tip R_g > 10. The tip geometry constant (R_g) is a ratio between radius of the glass sheath *(r_g)* and radius of the platinum wire *(r_a)* as shown in ***Figure*** 3-9. For a tip where of 1.1 < R_g <100, a 0.2% diffusion from back of the tip also comes into action. This applies a correction factor of β (where $\beta = 4 + [1 + 0.1380 / (R_g\text{-}0.6723)^{0.8686}]$).The *n* in ***equation 3.18*** is number of electrons transferred during redox reaction, *F* is Faraday's constant, *D* is diffusion coefficient of the oxidized/reduced species, *C* is bulk concentration and *a* is radius of the microelectrode. The SECM current distance feedback approach curves can be recorded when the microelectrode tip at diffusion limited current is brought to a distance of < 4*L* from the substrate surface. (where *L* is normalized tip distance = *d/a*, *d* = tip substrate distance and *a* is radius of the metal wire of the microelectrode) [154].

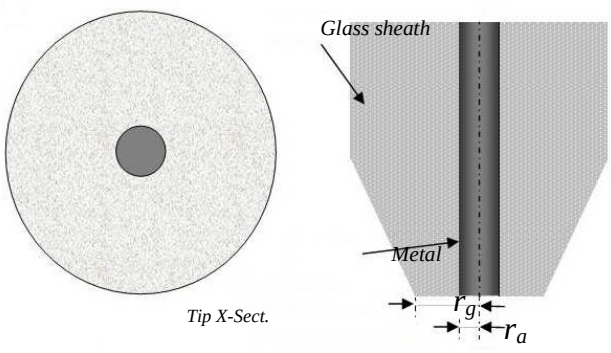

Figure 3-9: Microelectrode tip geometry

3.2.4.3 Different modes of SECM

The SECM is generally used in feedback mode and generation/collection modes [158, 163, 164]. In our study we used SECM in feedback mode for imaging and kinetics of heterogeneous ET, so only detail of the feedback mode is given here.

3.2.4.3.1 The feedback mode

In amperometric feedback mode the tip current of the microelectrode is perturbed by the substrate surface. The schematic in ***Figure 3-10*** shows the three possible situations in the feedback mode. The current at the tip at infinite distance from the substrate can be defined by the ***equation 3.18***. The tip in solution at unknown tip substrate height is called infinite tip distance.

At infinite distance from the substrate surface in the bulk solution, the oxidized species is reduced at the tip produces a steady-state current that is limited by hemispherical diffusion. As the tip approaches a conductive substrate in the solution, the reduced species formed at the tip get oxidized at the conductive surface, resulting in an increase in the current, producing positive feedback. The opposite effect is observed when probing insulating surfaces, the oxidized species cannot regenerate at the insulating surface and diffusion to the electrode is inhibited by the physical obstruction as the tip approaches the substrate, producing a negative feedback and decreasing the tip current less than the steady state current [165]. The SECM feedback mode can be used for surface imaging and to study the kinetics of heterogeneous ET across electrode electrolyte interface [78, 166].

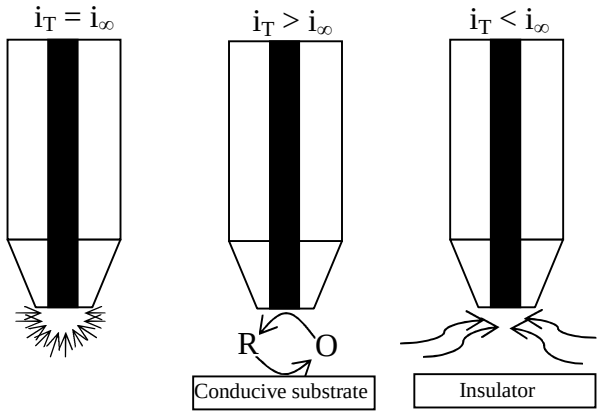

Figure 3-10: a). Microelectrode tip at infinite tip-substrate distance, b) Positive feedback near conductive surface, 3) Negative feedback near insulator surface

3.2.4.3.2 SECM imaging in feedback mode

The topographic or imaging in feedback mode is one of the important features of SECM. The surface image can be obtained by scanning the microelectrode tip over the substrate surface in X-Y plane at constant tip height (within the feedback) and measuring the current as a function of tip location. The SECM imaging has been used to study membranes, leaves, artificially patterned biological and corrosion systems [78, 158, 167-170]. ***Figure 3-11*** show the SECM image which was recorded in 0.1M KNO_3 containing 1mM hexaammineruthenium III chloride ($Ru(NH_3)_6Cl_3$) as redox mediator. The tip substrate distance was 2µm, this was done by tip approaching the substrate from un-known distance in solution to zero tip-substrate distance (i.e. tip touched the substrate surface). From zero distance the microelectrode tip was moved up to 2µm in the electrolyte. An area of 100×100 µm was scanned by the microelectrode tip at a lateral scan rate of 5µm s^1. The image shows the different electrochemical activity at boron doped electrode, the red spots show the highest and blue the lowest current values [171]. The regions were reported to have different electrochemical activity at the surface [171].

The resolution of the SECM image depends on the tip size and tip-substrate distance. The resolution increases with use of the sub-micrometer tips but with a tip size <100 nm it is very difficult to image due to stray vibration, surface irregularities and surface tilt [80, 166]. The SECM imaging was used in our work to locate regions of different reactivity in HVOF coatings.

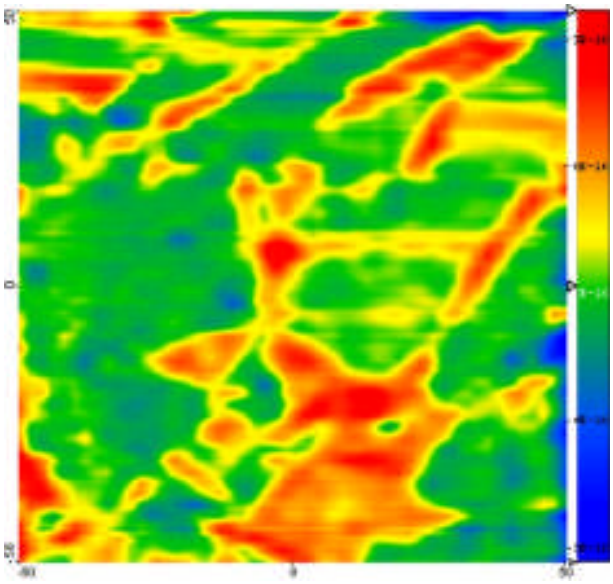

Figure 3-11: Different electrochemical activity at boron doped diamond electrode by using 2 µm Pt UME, 1mM $Ru(NH_3)_6Cl_3$ redox mediator, tip-substrate separation approximately 2µm, area scanned 100×100µm and lateral scan rate 5µm s^{-1} [171].

3.2.4.4 Heterogeneous ET kinetics study by SECM

A typical electrochemical process at electrode-electrolyte interface involves three successive steps i.e. diffusion of reactants to the electrode surface, heterogeneous ET and diffusion of products into the solution. The kinetics parameters are standard heterogeneous ET rate constant (k^0) and transfer coefficient (α) [86]. There are two main categories of measuring kinetic parameters of electrochemical reactions called transient and steady state methods [105]. In transient methods the electrochemical equilibrium is

perturbed by applying small potential and recording the current. Main difficulties involved in transient methods are charging current and solution resistance. The linear sweep, cyclic and AC voltammetry techniques are examples of transient methods [105, 158, 164]. The charging current and solution resistance problems are overcome by steady state processes which include rotating disc electrodes, thin layer electrochemical cells, electrochemistry at microelectrodes and SECM [105]. The SECM process combines the features of microelectrodes and thin layer cells, which minimize the effect of charging, quickly acquire steady state and minimize the solution resistance [105].

There are two well established techniques for measuring standard heterogeneous ET reaction rate constant, k^0, by using SECM i.e., k^0 measurement at the UME and at the substrate [164, 167]. For measuring the k^0 value either at tip or substrate one process should be diffusion controlled. The first technique is used for conductors which have an ET rate comparable to mass transport rate. In this method UME is held at different *L (d/a)* values with constant substrate potential (diffusion limited process at substrate) while performing cyclic voltammetry at the tip to obtain kinetics of ET at the tip. These cyclic voltammograms are compared with theoretical curves to get rate constant values [172]. In the second case UME is held at constant positive potential to get diffusion limited mass transfer at the tip and kinetics controlled process at the substrate. The process of oxidation and reduction were driven at the substrate by providing a small range of positive and negative potentials around formal potential. 4-6*L* distance away from the substrate in solution the tip process is at diffusion limited steady state and mass transport rate is ~ *a/D*

(a radius of the tip in cm, D is diffusion coefficient in $cm^2\ s^{-1}$) [130]. Approaching the substrate in close vicinity (<1L) the mass transport rate at the tip become ~ d/D (d tip height from substrate in cm). By monitoring the diffusion controlled process at the tip kinetic information at the substrate can be obtained from SECM current distance feedback approach curves. Fitting the resulting normalized current (i_T/i_∞) vs. normalized distance *(d/a)* curves to well established SECM current distance feedback theory [173] reaction rate constant can be determined. With varying substrate potentials it is possible to obtain a value of k at different over-potentials. The fitting procedure used here is based on SECM theory for finite substrate heterogeneous kinetics [173], using the following equations to extract the first order rate constant (only concentration of one reactant e.g. FcOH involved in reaction with one ET).

$$I_T^k = I_S^k\left(1 - I_T^{ins}/I_T^c\right) + I_T^{ins} \qquad \textbf{3.19}$$

Where I_T^c, and I_T^{ins} describe the normalised tip currents for diffusion controlled regeneration and insulating substrate kinetics respectively, and I_S^k is the kinetically controlled substrate current given below [162].

$$I_T^c = \frac{0.78377}{L} + 0.3315\,exp(\frac{-1.0672}{L}) + 0.68 \qquad \textbf{3.20}$$

$$I_T^{ins} = 1/[0.15 + \frac{1.5358}{L} + 0.58\,exp(\frac{-1.14}{L}) + 0.0908\,exp(\frac{L-6.3}{1.017L})] \qquad \textbf{3.21}$$

$$I_S^k = \frac{0.78377}{L(1+1/\kappa)} + [0.68 + 0.3315\,exp\left(\frac{-1.0672}{L}\right)]/[1 + \frac{7.3+11/L\,\kappa}{110-40\,\kappa}] \qquad \textbf{3.22}$$

L is the normalised tip-substrate distance and $\kappa = kd/D$, where k is the heterogeneous rate constant ($cm\ s^{-1}$). Tafel graphs were plotted from the

extracted log of the reaction rate constant vs. over potential (i.e. *log k vs. (E - E^{o})*). Extrapolation of the Tafel plots to the equilibrium potential gives heterogeneous ET reaction rate constant k^{o} at equilibrium conditions. The accurate and reproducible k^{o} results obtained by SECM measurements extend its applications to study transport across membranes, adsorption-desorption, corrosion processes, living cells and charge transfer at liquid-liquid interfaces [174-177].

The accuracy of the ***equation 3.19*** is claimed by the authors as within 1-2% for $0.1< L <1.5$ and $0.01\ k <1000$ for a disk microelectrode with $R_g = 10$ [86, 158, 162]. Finding the exact R_g value and zero tip-substrate distance is a difficult task and errors in these parameters contribute to errors in rate constants. Until now the ***equation 3.19*** was extensively used for fitting the experimental data for rate constant study without the consideration of exact R_g value. A new analytical approximation ***equation 3.23*** is proposed by Lefrou et al. [178, 179] which is R_g specific and can be used for any R_g value. They also reported that previously reported analytical ***equation 3.19*** produce an error values of 5-10% as the authors have overlooked the error sources in zero tip-substrate distance, real R_g values and errors in steady state current. They addressed these issues in their research and claimed the accuracy of their ***equation 3.23*** within ±2.5% for any kinetics in the condition of $L > 0.1$ for disk microelectrode with $R_g< 20$ [178-181]. In our work we have used both old and new analytical equation to check the difference in k^{0} value.

$$Ni_T(L,\kappa,R_g) = Ni_T^c\left(L+\frac{1}{\kappa},R_g\right) + \frac{Ni_T^{ins}(L,R_g)-1}{\left(1+2.47R_g^{0.31}L\kappa\right)\left(1+L^{R_g-0.113}\kappa^{-0.0236R_g-0.91}\right)} \quad \textbf{3.23}$$

$$Ni_T^{ins}(L,R_g) = \frac{\frac{2.08}{R_g^{0.358}}\left(L-\frac{0.145}{R_g}\right)+1.585}{\frac{2.08}{R_g^{0.358}}\left(L+0.0023R_g\right)+1.57+\frac{LnR_g}{L}+\frac{2}{\pi R_g}Ln\left(1+\frac{\pi R_g}{2L}\right)} \quad \textbf{3.24}$$

$$Ni_T^c(L,R_g) = \alpha(R_g)+\frac{\pi}{4\beta(R_g)ArcTan(L)} + \left(1-\alpha(R_g)-\frac{1}{2\beta(R_g)}\right)\frac{2}{\pi}ArcTan(L) \quad \textbf{3.25}$$

$$\alpha(R_g) = Ln2 + Ln2\left(1-\frac{2}{\pi}ArcCos\left(\frac{1}{R_g}\right)\right) - Ln\left(1-\left(\frac{2}{\pi}ArcCos\left(\frac{1}{R_g}\right)\right)^2\right) \quad \textbf{3.26}$$

$$\beta(R_g) = 1+0.639\left(1-\frac{2}{\pi}ArcCos\left(\frac{1}{R_g}\right)\right) - 0.186\left(1-\left(\frac{2}{\pi}ArcCos\left(\frac{1}{R_g}\right)\right)^2\right) \quad \textbf{3.27}$$

The terms κ, k, k^0, and L used in ***equations 3.23***, ***3.24*** and ***3.25*** are the same as used by Bard and co-workers. The values of the $\alpha(R_g)$ and $\beta(R_g)$ values were calculated separately by using ***equations 3.26*** and ***3.27***. The term normalized tip current used differently in the Bard equations. The normalized tip currents in the Bard equations were not corrected for small R_g values. The $i_{T\infty}$ for the R_g < 1.1 can add approximately 10% errors in the normalized tip current. An error factor of the zero distance from the tip-substrate distance and errors in the

steady state current as compared to the SECM feedback approach curve starting point should also be included while fitting the experimental data with theoretical curves extracted from the analysis of the approximation curves.

3.3 Summary

The above details of the three electrochemical testing method show that each testing method has its limits of application and information extracted from the acquired data. It is expected that their usefulness in understanding corrosion process at HVOF coating can be enhanced by their complementary use, where results extracted from one electrochemical testing technique aid interpretation of data obtained from other methods and produce a clearer understanding of the overall process.

4 Experimental

4.1 Introduction

In this chapter the detail of the materials and equipment used for producing and characterizing HVOF coatings is given. The experimental procedures of the potentiodynamic polarization, electrochemical impedance spectroscopy and scanning electrochemical microscopy testing techniques and data analysis are also included in the chapter.

4.2 Materials used

4.2.1 Coating materials

The gas atomized Inconel 625 powder (Ni-328-5/T1265F) with nominal size range -53+20, the gas atomized CoNiCrAlY powder (Co-210-24) with nominal size range -45+20 µm and the sintered WCCoCr powder (WC-731/1350VF) with a nominal size of -38+10 µm were purchased from William Rowland Ltd. (Sheffield, UK). The compositions of the powders were tested by using optical emission spectroscopy (Foundry-Master UV, Oxford Instruments Bucks, UK) and given in the ***Table 4-1.***

Table 4-1: Composition of the powders used for producing HVOF coatings

Inconel 625 powder					
Element	Ni	Cr	Mo	Nb	-
Weight %	65	22	9	4	-
CoNiCrAlY powder					
Element	Co	Ni	Cr	Al	Y
Weight %	38.5	32	21	8	0.5
WCCoCr powder					
Element	W	Co	Cr	C	-
Weight %	80.8	10	4	5.2	-

4.2.2 Wrought alloys

The 6 mm thick Inconel-625 bulk alloy sheet was purchased from Special Metals Corporation (Hereford, UK), mild steel and stainless steel AISI304 were purchased from Smith Metals Ltd. (Bugleweed UK). The composition of the materials were tested by using optical emission spectroscopy (Foundry-Master UV, Oxford Instruments Bucks UK) and given in ***Table 4-2.***

Table 4-2: Compositions of the bulk alloys used as substrate

Wrought Inconel 625					
Element	Ni	Cr	Mo	Nb	Fe
Weight %	63.29	20.9	9.13	3.41	3.27
Stainless steel 304					
Element	Fe	Cr	Ni	Mn	Si
Weight %	72.31	17.8	8.31	1.24	0.34
Mild steel					
Element	Fe	C	Si	S	Cr
Weight %	99.57	0.11	0.20	0.02	0.10

4.2.3 Microelectrode wire and chemicals

The 25µm diameter platinum wire was purchased from Goodfellow Ltd. (Cambridge, UK). All chemicals used for experiments were bought from Sigma Aldrich with highest purity (> 99%) and used as received. All electrolyte solutions were prepared using Milli-Q (18.2MΩ) deionised water.

4.3 High velocity oxygen fuel coating

The HVOF Inconel 625, CoNiCrAlY and WCCoCr coatings were deposited on previously grit blasted 60 × 25 × 6 mm mild steel samples. The Met-Jet III equipment made by Metallization limited, Dudley, West Midland, UK was used for coating with previously optimized spraying parameters [7]. A sectioned schematic of the gun is given in ***Figure 4-1.***

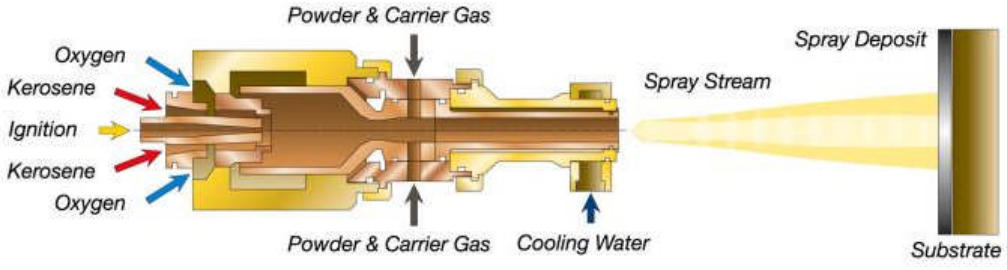

Figure 4-1: Schematic of the HVOF Met-Jet III gun and different parts [182].

The gun is fuelled with premixed kerosene and O_2 to burn in the combustion chamber. The combustion chamber is 100-200 mm long to allow the full combustion of the premixed fuel. The geometry of the combustion chamber is designed to give the desired pressure and acceleration to the powder stream. The stream of the powder is introduced radially outside the combustion chamber to avoid overheating of the powder. The gun also accommodates the cooling water supply to avoid the overheating damage of the gun. Coatings of the different materials were produced on the coupons mounted on the sample holder moving at 80 rpm. The spraying processes parameters for different coatings are summarized ***Table 4-3***

Table 4-3: Spraying process parameters for different coatings

Sample	O_2 flow rate (L/min)	Fuel flow rate (L/min)	N_2 flow rate (L/min)	Nozzle length (mm)	Spray distance (mm)	Powder feed rate (g/min)	Number of passes
Inconel 625	910	0.48	4.6	100	350	78.7	24
CoNiCrAlY	890	0.47	5.5	100	356	70	30
WCCoCr	915	0.33	7	100	355	75	15

4.4 Surface roughness measurement

4.4.1 Sample preparation

The coating coupons were cut into small size of 10 ×10 × 6 mm by abrasive wheel. Samples were mounted in conductive epoxy for microscopy and non conductive epoxy for electrochemical testing. The grinding and polishing was carried out by 240 grit size grinding paper to 1µm polishing wheel to get < 1 µm surface finish. The samples were washed with de-ionized water before and after each grinding step to avoid scratching and contaminations.

4.4.2 Surface profile

Before conducting electrochemical experiments the surface profile of the samples were measured by Talysurf CLI 1000-3D system from Taylor Hobson Ltd., UK. An area of 5×5mm was scanned by a 2µm radius stylus at 500µm s^{-1}. The average surface roughness (R_a) profile was 0.43 µm, 0.48 µm, 0.68 µm and 0.52 for stainless steel, bulk Inconel-625 and Inconel-625 coating and CoNiCrAlY coating respectively.

4.5 Etching and Microscopy

Substrate surfaces were etched with different etchants to reveal the microstructure features. The stainless steel and coated sample were etched in 2% nital (2% nitric acid in ethanol) for 10-15 s and bulk Inconel-625 was etched with aqua regia for 5-10 sec (1 part conc. HNO_3 and 3parts conc. HCl acids). The Phillips model XL30 Scanning Electron Microscope fitted with energy X-ray dispersive spectroscopy analysis was used for microstructural characterisation. The elemental composition analysis was done by INCA software.

4.6 Micron and sub-micron electrode preparation

4.6.1 Microelectrode preparation by heat sealing glass

The microelectrode was prepared by heat sealing 1.5cm long, 25µm diameter platinum wire in soft borosilicate glass. The electrical connection between the copper and platinum wire was achieved by soldering. The copper wire was fixed in place by a drop of non conductive epoxy. The tip of probe was

bevelled to give the correct ratio of glass to wire diameter (R_G value) with object of obtaining a value below 10 [183]. Fine sharpening of the tip was carried out on micropipette beveller fitted with diamond polishing wheel. A value of R_g of approximately 7 was measured by microscopy and fitting current distance feedback curves with theoretical curves extracted from the processing of the analytical approximation equations. The flow sheet diagram in ***Figure 4-2*** shows the major steps in fabrication of a 25 µm glass sealed microelectrode.

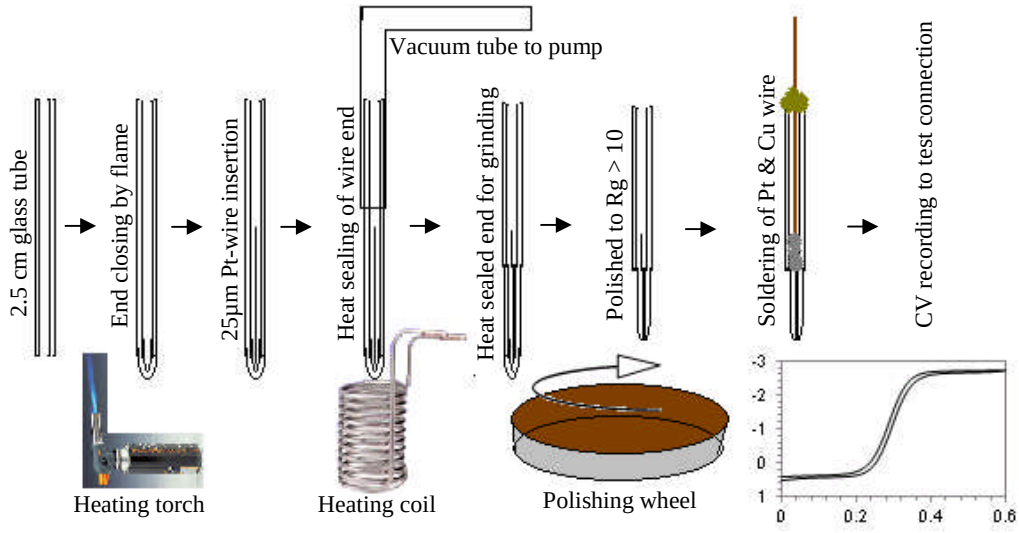

Figure 4-2: Flow sheet diagram of different steps in microelectrode fabrication.

4.6.2 Ultramicroelectrode preparation by laser puller

The ultramicroelectrodes were prepared by using P-2000 laser puller from Sutter instruments shown in ***Figure 4-3***. The main steps involved in submicron electrode preparation are shown in flow sheet diagram ***Figure 4-5*** include: straightening of 25µm diameter × 1.5 cm long Pt-wire, inserting into 1mm diameter × 10 cm long glass tube, tapping the Pt-wire into centre of the glass tube, mounting the glass tube on laser puller, air removal by vacuum pump.

After steady negative pressure the previously optimized heating and pulling parameters [172] were used to pull the glass tube containing Pt-wire. Three cycles of heating and one cycle of pulling were used for pulling each 10 cm long glass tube. The process was repeated until the glass tube pulled into two pieces. The laser heats the middle of the glass tube to 900° C for 40 seconds followed by 10 seconds cooling. In pulling cycle the glass tube was heated to 875° for 40 seconds followed by pulling until the glass tube break into two parts. Once the microelectrodes were pulled the connection with the external circuit was established by soldering between Pt and Cu wire. The grinding was carried out on BV-10 microelectrode beveller supplied by Sutter instruments shown in ***Figure 4-4.***

Figure 4-3: Laser ultramicroelectrode puller [184].

Figure 4-4: Micro beveller for polishing of the microelectrodes[185].

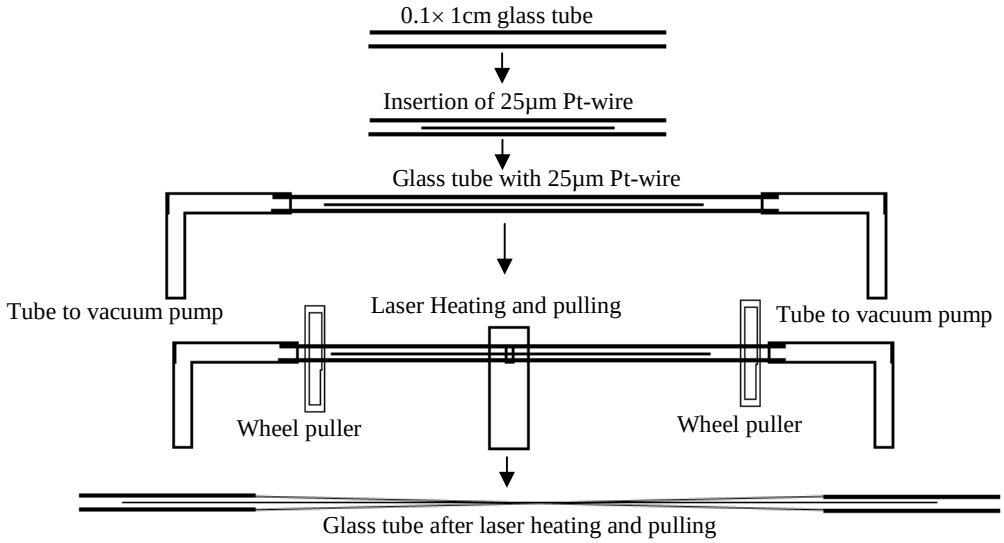

Figure 4-5: Flow sheet diagram of sub-micron electrode fabrication

4.6.3 Measuring ratio between glass and Pt-wire (R_g)

The R_g is the ratio between glass r_g and radius of the Pt-wire r_a. Measuring R_g value of the tip is an important step of the SECM as the current measurements at the tip affected by this. The R_g values were measured by taking microscopy and subsequent measurements by Image-J analyser and fitting with the positive and negative feedback curves.

Figure 4-6 shows the working end of the microelectrode, 50 µm line of the micrographs was used to calibrate the as scale of the Image-J. The maximum and minimum external diameter of the tip was 206 µm and 160 µm respectively. The diameter of the micro wire was 25 µm. The maximum and minimum R_G values were 8.24 and 6.4 producing the average R_G value as 7.32.

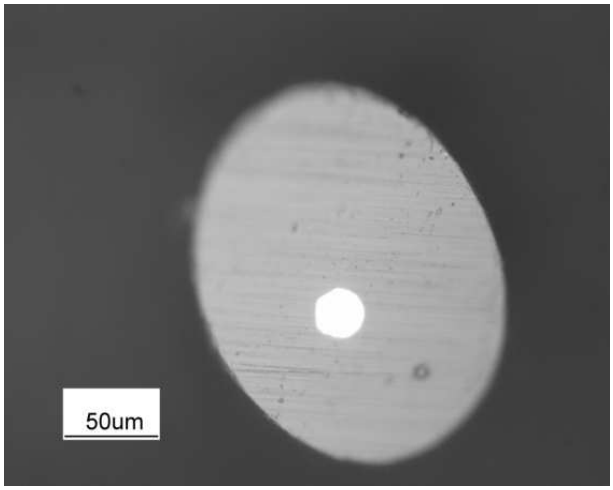

Figure 4-6: Micrograph of the 25µm microelectrode tip after grinding and bevelling

In second method of R_g measurement, SECM feedback approach curves were recorded with the tip in 0.5M K_2SO_4 solution containing 1mM ferrocenemethanol as redox mediator. The current distance SECM feedback approach curves were recorded at Pt-electrode for positive feedback and at PTFE for negative feedback. The experimental curves were fitted with the theoretical curves generated from the analytical ***equations 4.1, 4.2***. The theoretical curves for different R_g values were generated by using constants values in ***Table 4-4*** for positive feedback and ***Table 4-5*** for negative feedback. The experimental SECM feedback approach curves were overlaid on the theoretical curves. The positive SECM feedback approach curves fit with the theoretical curve of R_g value of 5.10 and the negative SECM feedback

approach curves fit with a theoretical curve of R_g value 8.13 producing an average value of 6.6 which was approximately same as analysed from the micrograph of the tip i.e. 7.3.

Positive feedback $$i_T(L) = k_1 + \frac{k_2}{L} + k_3 \exp\left(\frac{k_4}{L}\right) \qquad \textbf{4.1}$$

Table 4-4: Constants for the pure positive feedback at conductor surface [162, 164]

R_G	k_1	k_2	k_3	k_4	Error (%)	L validity range
1002	0.7314	0.77957	0.26298	-1.29017	< 0.2	0.1-200
10.2	0.72627	0.76651	0.26015	-1.41332	< 0.3	0.1-200
5.09	0.72035	0.75128	0.26651	-1.62091	< 0.5	0.1-20
1.51	0.63349	0.67476	0.36509	-1.42897	< 0.2	0.1-200

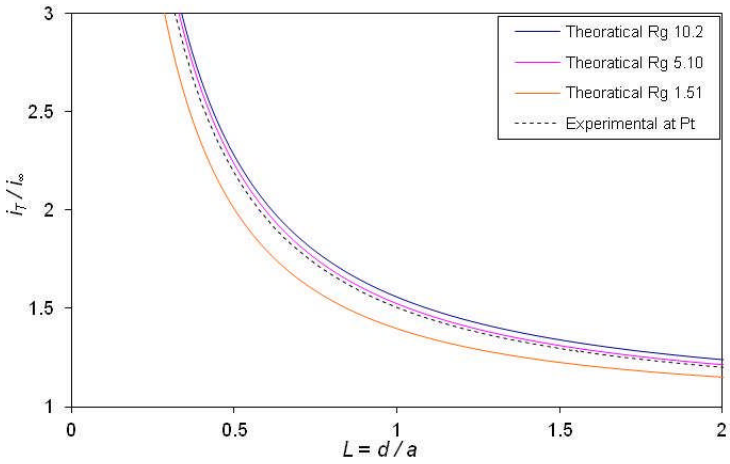

Figure 4-7: The curve fitting for positive feedback to find Rg. Values of k_1, k_2, k_3 and k_4 for different R_g values, given in Table 4-4 were used in equation 4.1to produce theoretical curves. The pure positive SECM feedback approach curve was obtained by using 25µm size disc shaped Pt-tip and 3mm size substrate. The SECM feedback approach curve was recorded in 0.5M K_2SO_4 contianing1mM FcOH. The Rg was obtained from the best fit between theoretical and experimental curves.

Negative feedback $$i_T(L) = \frac{1}{k_1 + \frac{k_2}{L} + k_3 \exp\left(\frac{k_4}{L}\right)} \qquad \textbf{4.2}$$

Table 4-5: Constants for pure negative feedback at insulator surface [162, 164]

R_G	k_1	k_2	k_3	k_4	Error (%)	L validity range
1002	0.13219	3.37167	0.8218	-2.34719	< 1	0.3-20
100	0.27997	3.05419	0.68612	-2.7596	< 1	0.4-20
50.9	0.30512	2.6208	0.66724	-2.6698	< 1	0.4-20
20.1	0.35541	2.0259	0.62832	-2.55622	< 1	0.4-20
15.2	0.37377	1.85113	0.61385	-2.49554	< 1	0.4-20
10.2	0.40472	1.60185	0.58819	-2.37294	< 1	0.4-20
8.13	0.42676	1.46081	0.56874	-2.28548	< 1	0.4-20
5.09	0.48678	1.17706	0.51241	-2.07873	< 1	0.2-20
3.04	0.60478	0.86083	0.39569	-1.89455	< 0.2	0.2-20
2.03	0.76179	0.60983	0.23866	-2.03267	< 0.15	0.2-20
1.51	0.90404	0.42761	0.09743	-3.23064	< 0.7	0.2-20
1.11	-1.46539	0.27293	2.45648	8.995E-7	< 1	2-20

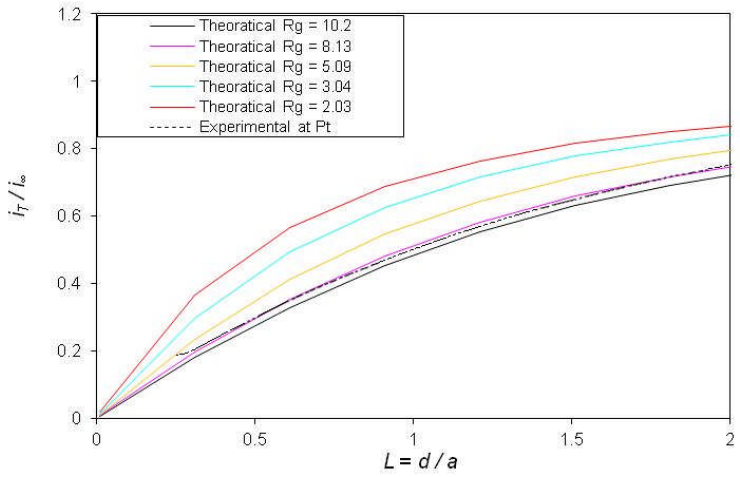

Figure 4-8: The curve fitting for negative feedback to find R_g. Values of k_1, k_2, k_3 and k_4 for different R_g values, given in Table 4-5 for were used in equation 4.2 ***to produce theoretical curves. The pure negative SECM feedback approach curve was obtained by using 25µm size disc shaped Pt-tip and PTFE insulator substrate. The SECM feedback approach curve was recorded in 0.5M K_2SO_4 contianing1mM FcOH. The R_g was obtained from the best fit between theoretical and experimental curves.***

Figure 4-9 shows the curve fit for pure negative feedback by using platinum at insulator surface. The curve fitting was carried out by using ***equation 3.24*** to find the tip of R_g value [179]. The minimum tip substrate distance was taken as $L = 0.1$ to incorporate the errors of tip geometry. The best fit between theoretical and experimental data was obtained at R_g value of 8, therefore the R_g value is well correlated with the one obtained from above procedures [162].

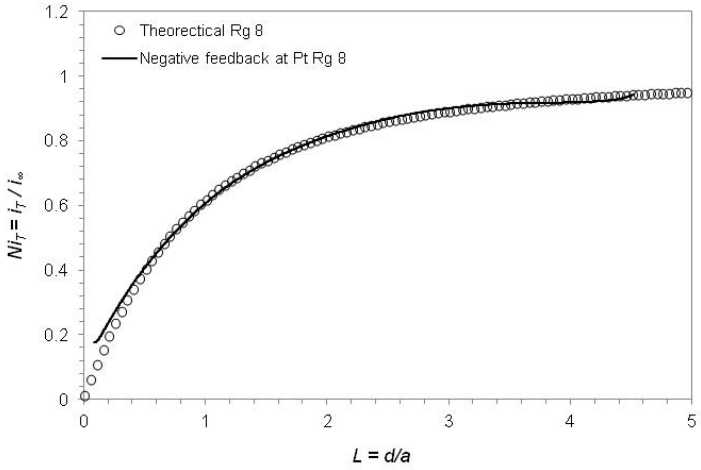

Figure 4-9: The curve fitting for negative feedback by using analytical equation 3.24 to find the Rg value. The minimum tip substrate distance was conservatively taken as 0.1L. The pure negative SECM feedback approach curve was obtained by using 25µm size disc shaped Pt-tip and PTFE insulator substrate. The SECM feedback approach curve was recorded in 0.5M K_2SO_4 contianing1mM FcOH. The R_g value was varied until the best fit obtained between theoretical and experimental curves. The best fit value of the tip was used as R_g value.

4.7 Electrochemical Testing

The potentiodynamic polarization testing and electrochemical impedance spectroscopy were carried out in conventional 3-electrode configuration where metal surface to be tested was used as working electrode, 0.5 × 5 × 5 mm Pt-strip was used as counter electrode and calomel electrode was used as reference electrode. The detailed functioning of the cell components is given in chapter 1 (***see section 3.2***).

The SECM experiments were carried out in 4-electrode cell where the tip of the microelectrode used as working electrode-1, substrate surface used as working electrode-2. The 3mm Pt-wire was used as counter electrode and Ag/AgCl was used as reference electrode. ***Figure 4-10*** shows the working set-up of SECM.

The crocodile clips attached with different electrodes completes the circuit between potentiostat and working cell. The electrodes are represented with the standard colours i.e., white for RE, green for WE_1, yellow for WE_2 and red for CE. The tip is mounted in tip holder attached to the fixture which allowed the three directional movement of the working electrode. The white container of the working stage is working cell, which contained few ml of electrolyte and accommodate 4 electrodes. In our testing, we removed the white electrolyte container and place the epoxy coating sample on the working stage. A big drop of electrolyte was poured on the surface to carry out the SECM imaging and current distance SECM feedback approach curves.

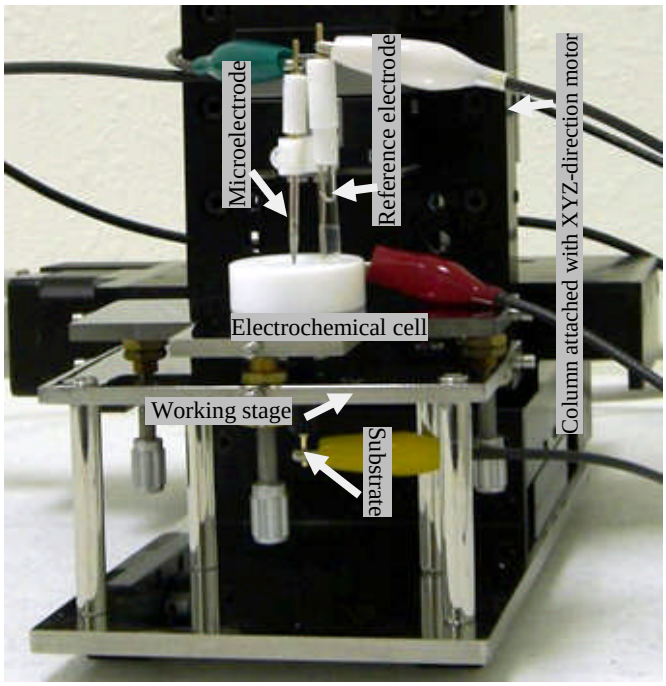

Figure 4-10: SECM working stage mounted with electrochemical cell [157].

4.7.1 Sample preparation

For electrochemical testing samples of 1 × 1cm of stainless, steel, bulk Inconel 625, Inconel 625 coating, WCCoCr coating and CoNiCrAlY were embedded in nonconductive epoxy. The diameter of the epoxy embedded sample was 2.5cm and thickness of 1.5cm. Connection of the embedded metal piece was obtained by drilling a hole in the sample until the drill bit (2.6mm) slightly entered into metal surface. Internal screws were made (3.2mm tap); a 3 mm diameter threaded rod was screwed in to establish connection of the metal piece to external circuit. The threaded metal rod was covered with flexible insulating tube to avoid contact with solution. The interface between non-conductive resin and flexible insulating tube was sealed with quick-set epoxy to avoid entering of electrolyte to the substrate. Electrical connection was verified by using a multi-meter. All substrates were ground and polished to 1 µm final finish. The metal surface was covered with acid resistant lacquer where metal meets the mount. This was done to avoid corrosion starting at the edges of the metal sample.

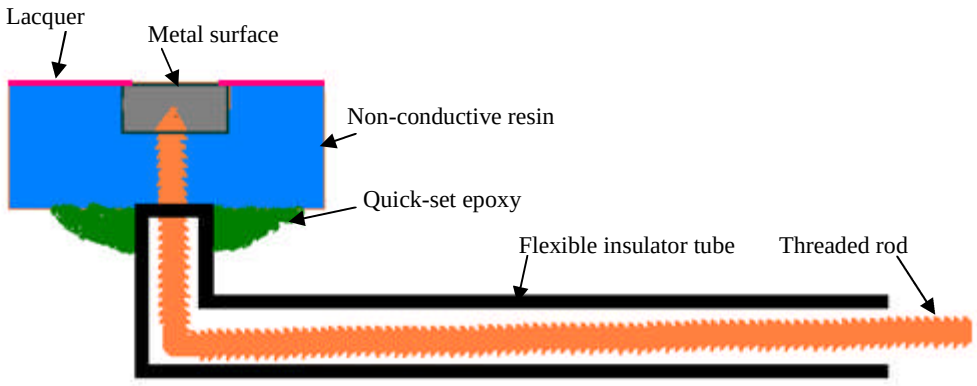

Figure 4-11: Working electrode for potentiodynamic and EIS testing

The sample preparation was same for the SECM experiments, except a shorter threaded rod was used.

4.7.2 Reagents and equipment

The potentiodynamic and EIS experiments were performed in 0.5M sulfuric acid, diluted in demineralised water from lab scale 99.5% concentrated sulfuric acid. The potentiodynamic and EIS testing were carried out with ACM Gill-8 potentiostat with V-2 software package. The EIS data was converted into the desired format of EIS Spectrum analyser a free ware EIS analyser available on the net.

The cyclic voltammogram and kinetics of heterogeneous ET reaction rate constant were studied in 0.1 M K_2SO_4 containing 1mM ferrocenemethanol as redox mediator. The CH910B potentiostat with software version 6.28 was used CV and SECM experiments.

4.7.3 Electrochemical testing procedures

4.7.3.1 Potentiodynamic polarization testing

The potentiodynamic and EIS tests were performed in a multiport corrosion cell contained in a Grant-Sub28 water bath at 30°C. The dissolved oxygen in 0.5 M H_2SO_4 was removed by nitrogen purging for 15-20 min. During testing the porous end of the N_2 gas distribution tube was kept above the electrolyte surface to avoid any stirring effects. The ASTM G5-94 was followed to perform potentiodynamic polarization test along with ASTM G1-03 and ASTM G31-72 for sample and solution preparation.

- The potentiodynamic polarization tests to find the corrosion potential,

passive current density, active, passive and transpassive regions were carried out by commonly used testing parameters i.e. 1 hour cell settle time, potential scan started from -250 mV more negative than E_{oc} to 1250 more positive than E_{oc} at a scan rate of 20 mV min^{-1}.

- The pitting propensity tests were carried out in 3.5% sodium chloride and 3.5% sodium sulphate. The potential scan was started from -250 mV more negative than E_{oc} to 1250 mV more negative than E_{oc} at a scan rate of 20 mV min^{-1}. The experimental set-up was same as the potentiodynamic polarization testing
- The effect of small positive and negative potential was carried out by applying small constant potential before recording polarization curve. 4 polarization curves were recorded after applying a constant potential of 50, 100, 150 and 200 mV respectively positive to E_{oc}. The potential scan was started from -200 mV < E_{oc} to 200 > E_{oc} at a scan rate of 20 mV min^{-1}. The same procedure was used to record 4 polarization curves after applying 50, 100, 150 and 200 mV constant potentials negative to E_{oc}. The procedure was repeated for all materials.
- The polarization curves to calculate the charging current were recorded in separate forward and reverse scan at 25, 50, 75 and 100 mV min^{-1}. The forward potential scan was started from 250 mV more negative than E_{oc} to 250 mV more positive than E_{oc}. The reverse scan was started from 250 mV more positive than E_{oc} to 250 mV more negative than E_{oc}. The Tafel extrapolation method was used to measure the positive and negative current before calculating charging current
- The partial and complete polarization curves were carried out at a scan

rate of 10, 20. 60 and 180 mV min^{-1}. The complete polarization curves were started from -250 mV more negative than E_{oc} to 250 mV more positive than E_{oc}. The partial polarization curves were started from E_{oc} to 250 mV more positive and negative potential.

- The potentiodynamic polarization reactivation tests were carried out in 0.5 M H_2SO_4 containing 50 parts per million KSCN. A complete forward and reverse scan was recorded at a scan rate of 50, 75, 100 and 125 mV min^{-1}. The potential was scanned from -150 mV to 450 mV to forward and reverse direction.

4.7.3.2 Polarization curve analysis for linear polarization resistance and Tafel extrapolation methods

The polarization curves in ***section 5.3.3*** were used to extract the corrosion current, i_{corr}, and corrosion rate, C_R, by using linear polarization and Tafel extrapolation methods. The log current axis of the polarization curves were converted into linear axis and slope of the graph gives linear polarization resistance, R_p. This R_p value was later used in the Stern-Geary equation (***see section 3.2.2.2***) to calculate the i_{corr}. The Stern-Geary coefficient was calculated from the anodic and cathodic Tafel slopes. The i_{corr} value was later used to calculate the corrosion rate by using ***equation 3.6***. The *E-log i* curves were used to obtain the anodic (i_a) and cathodic (i_a) currents at zero overpotential. The average of both currents produces the i_{corr}, which was later used to calculate the corrosion rate. The equivalent weight and density of the materials were calculated from the percents of different elements present in the alloys.

4.7.3.2.1 Stability check of the reference electrode

Most of the experiments in this work were carried out for extended time, hence it was vital to check the stability of the reference electrode. The stability of the reference electrode was checked by recording cyclic voltammogram at platinum electrode in 0.5 M H_2SO_4 for consecutive 10 days as shown in ***Figure 4-12***. The reference electrode was kept in the test solution all the time during 10 days. Platinum electrode reacts with acids and gives bulk hydrogen evolution at 0 V with reference to hydrogen electrode. The SCE is a secondary electrode and its standard electrode potential is -244 mV with reference to standard hydrogen electrode. The CVs recorded at platinum electrode over a period of 10 days approximately overlap each other and show bulk hydrogen evolution around -250 mV. The approximately reproducible CV and hydrogen evolution around -250 mV indicates that the potential at reference electrode stayed constant during a period of 10-days.

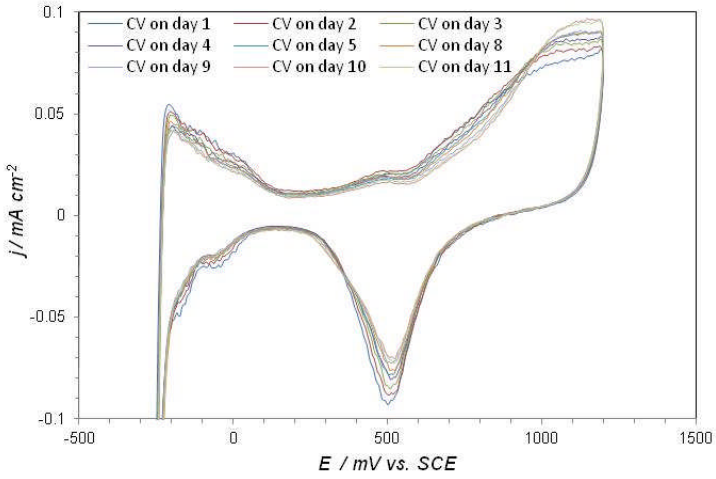

Figure 4-12: Cyclic voltammograms recorded at 10×10×0.5 mm platinum strip in 0.5 M H_2SO_4. The potential was scanned from -250 mV< E_{oc} to 1250 > E_{oc} at a scan rate of 60 mV min^{-1}. One CV was recorded each day while keeping the platinum electrode and reference electrode in the solution all the time for 11 consecutive days. All CVs overlap each other very well proving stability of reference electrode.

4.7.3.3 Electrochemical impedance spectroscopy

The electrochemical impedance spectroscopy experiments were carried out in 0.5 M H_2SO_4 by using the same multiport electrochemical cell. A 10 mV sinusoidal signal was applied over a frequency range of 0.1 Hz to 10000 Hz. The data was converted into desired format of EIS Spectrum analyser. The experimental data was fitted with proposed model by 4-5 iteration until the minimum errors between % of errors was attained. The long term EIS experiments were carried out by setting up the potentiostat sequencer take the EIS readings after set intervals of time.

4.7.3.3.1 EIS data validity

The consistency of the practical data was also tested by Karmers-Kronig (KK) check available in the software. The KK-check calculates the real part of the spectrum function from the imaginary and vice versa [151]. The software automatically compares the calculated part of the function to the experimentally measured values and finds the percentage error. If the error is more than 2 %, the EIS data is considered to have failed the KK-check. The KK-check performed on Inconel 625 impedance data and a simulated smooth data are presented in ***Figure 4-13***. The % residual values for the Inconel 625 coating were found more than from simulated smooth graph. The % residual is the difference of percentage difference between experimental values and the one calculated theoretical from it. The experimental EIS data does not pass the KK-check due to electrochemical instability but still the results produced by comparing with equivalent circuit was within the acceptable limit of error i.e. <10% [186].

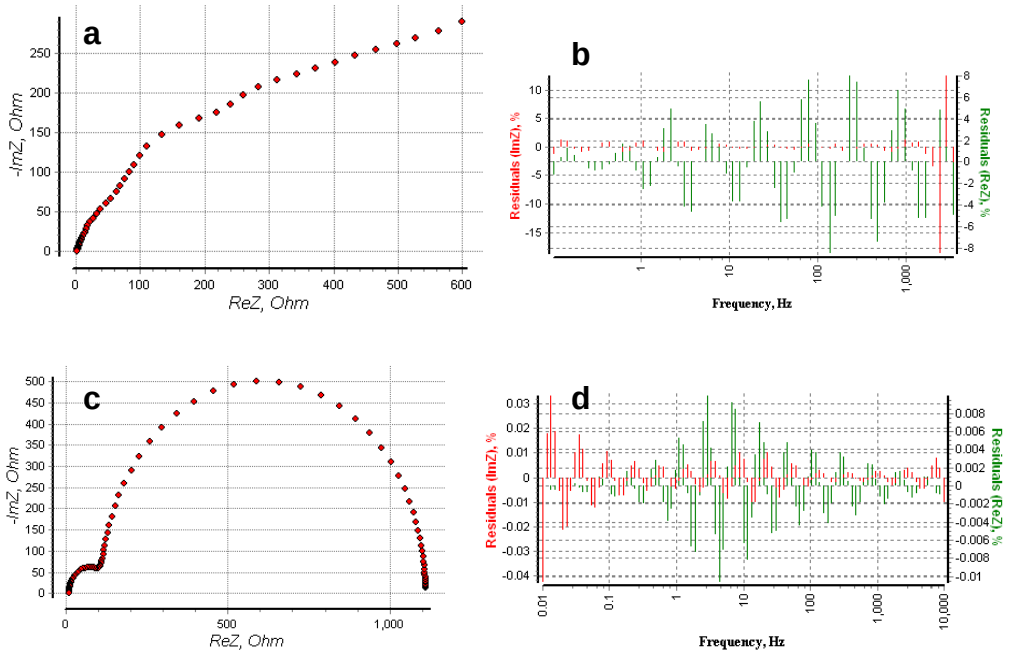

Figure 4-13: The KK- check on Inconel 625 coating impedance data and smooth simulated data. a, b) Nyquist plot and KK-check for Inconel 625. The experiment was performed on 1cm^2 Inconel 625 coating by applying 10mVof AC signal with a frequency range of 0.01Hz to 10000Hz in 0.5M H_2SO_4. The residual values (experimental real impedance and theoretical imaginary value and vice versa of them) were obtained as ±15%, c, d) Nyquist plot and KK-check for smooth simulated data. The plot was generated from theoretical ECM of two time constant where $RC_1 < 10RC_2$. The residual values were < 1% for theoretical ECM.

4.7.3.3.2 EIS data fitting

The EIS data acquired from the ACM-Potentiostat was in the form of total impedance [Z] (Real impedance [Z'] + Imaginary impedance [Z"]) as a function of phase angle shift in degree. The data for the EIS-analyser (software used for analysis) required the impedance data in the form of separate real and imaginary parts and the phase angle shifts in radians (rad). The real impedance (Z×COS(<rad>)) and imaginary impedance (Z×SIN(<rad>)) were generated from the raw data by using excel. The EIS data in the required format was converted into text file for comparison with equivalent circuit model in EIS-analyser.

The EIS graphs for Inconel 625 coating and bulk alloy in ***section 6.3.3*** were analysed by using the equivalent circuit model reported in the literature and the one proposed in our work. The EIS graphs in ***section 6.4*** were analysed by the Randal model without any inductor. For the CoNiCrAlY coatings the data at lower frequency was very erratic due to irreversible changes at the surface. The low frequency data from 0.01 Hz to 0.1 Hz was removed from the graph during analysis.

4.7.3.4 Cyclic voltammetry

Cyclic voltammetry experiments were carried in 0.1 M K_2SO_4 containing 1mM redox mediator at microelectrode tip and 3mm platinum electrode. The Pt-wire was used as counter electrode and Ag/AgCl was used as reference electrode. The potential was scanned from 0 V to 0.6 V in forward and reverse direction. The CVs at polished surfaces bulk Inconel 625, Inconel 625 coating and stainless steel were recorded in a 1.5-2 ml drop of electrolyte covered the exposed surface as shown in ***Figure 4-14***. The potential was scanned from -0.2 V to 0.6 V for bulk Inconel 625 and Inconel 625 coating. The potential at the stainless steel surface was scanned from -0.4 to 1.2 V. The CVs for all materials were recorded at 10, 20, 30, 40, 50, 60 and 70 mV s^{-1}. The analyses of the CVs were carried out with Excel to extract mechanistic information about the redox reaction taking place at the electrode surface.

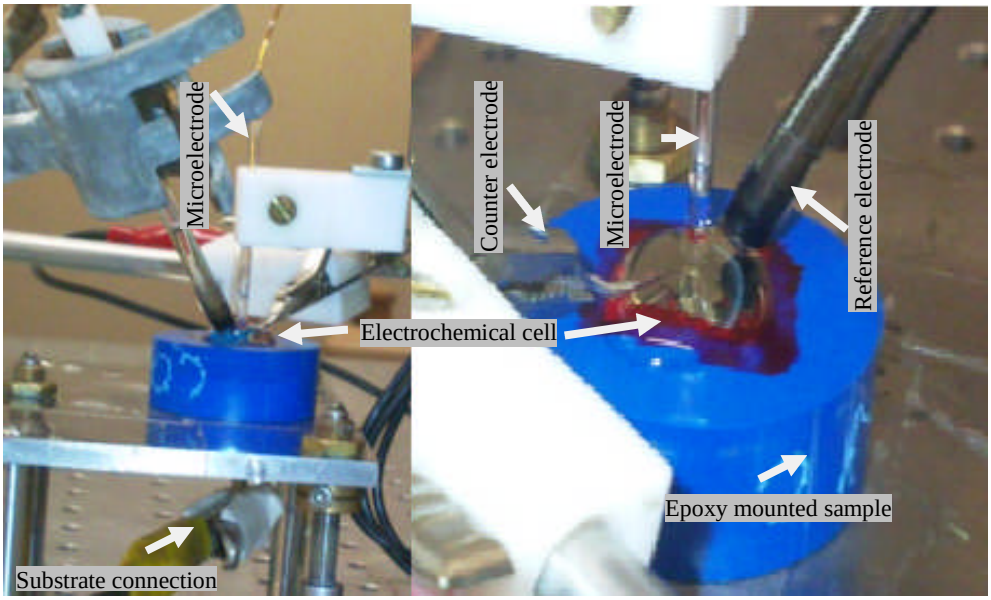

Figure 4-14: Electrochemical cell at 25mm epoxy mounted substrate sample for cyclic voltammogram and SECM testing. The SECM feedback approach curves and CVs were obtained in 2-3ml drop of 0.5M K_2SO_4 containing 1mM FcOH.

4.7.3.4.1 Comparison of CV and potentiodynamic polarization curve

Figure 4-15 is the potentiodynamic polarization and cyclic voltammogram graphs plotted from the same data for electrode in 0.5 M H_2SO_4 solution. The x-axis presents the potential with reference to SCE and y-axis the current density. The *Y-1* presents the log current density for potentiodynamic polarization curve and *Y-2* presents the current density for cyclic voltammogram. The current density for polarization curve was converted into absolute current and both negative, positive current values were plotted for CV graph. The negative part of the polarization curve is vertical flip of the CV curve due to conversion of the negative current to absolute current. In reverse sweep different processes are dominated are labelled in ***Figure 4-15***. The bulk hydrogen evolved around -240 mV and bulk oxygen around 1200 mV. The peak current 0.09 mA at around 500 mV shows the reduction of platinum oxide, labelled D in ***Figure 4-15***. The point C is the double layer region where

metal platinum oxide is reduced and hydrogen is fully desorbed. At point B the formation of the adsorbed hydrogen takes place. The same points are marked with * sign shows the same process for polarization curve. In forward potential sweep the oxidation of hydrogen and platinum takes place, the shape and occurrences of the peaks depends on the platinum surface exposes, pre-treatment of the electrode and purity of the solution [105].

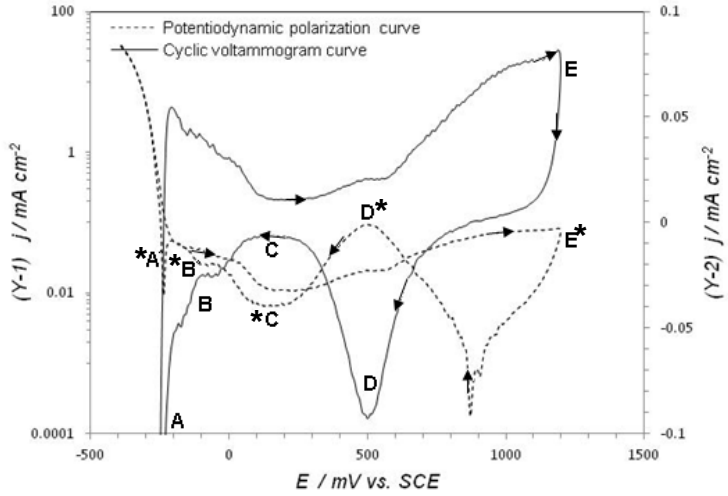

Figure 4-15: Potentiodynamic polarization curve and cyclic voltammogram plotted from the same data recorded at platinum electrode in 0.5 M H_2SO_4. The potential was scanned from -250 mV< E_{oc} to 1250 > E_{oc} at a scan rate of 60 mV min^{-1}. A) bulk hydrogen evolution, B) formation of adsorbed hydrogen, C) double layer region, D) Reduction of oxide layer, E) bulk oxygen evolution. Letters marked with * are the same points on polarization curve.

4.7.3.5 Scanning electrochemical microscopy

The SECM experiments were carried out with the same set-up as that for cyclic voltammetry except the 2nd electrode. The microelectrode was used as 1st working electrode and kept at 0.6 V to allow the diffusion controlled oxidation reaction at the tip, the substrate was used as 2nd electrode and potential at substrate was independently controlled.

- The distance between the tip of the microelectrode and substrate was adjusted by using two programs i.e. probe approach scan and probe scan curves. The tip from infinite distance to the close proximity was adjusted by probe approach curve. In probe approach curves the microelectrode travels towards substrate surface at 2 μm s^{-1} and is set to stop automatically when current at the tip become 3/4th of the starting tip current. In probe scan technique the tip of the microelectrode travel at 2 μm $s^{-1}$and manually stopped when touched the substrate surface with the substrate to get maximum feedback.
- The SECM images were recorded by crashing the tip of the microelectrode to maximum feedback at the substrate (substrate at E_{oc}), then moving back 4 μm from the surface to stay in the current feedback region. A quite time of 50 seconds was given before scanning the surface laterally in X-Y direction. The lateral scan was carried out at a forward travelling speed of 250 μm s^{-1} with transverse increment step of 5 μm. The stepper motor was used in SECM imaging and piezoelectric motor was used in carrying out SECM feedback approach curves.
- After SECM imaging the tip of the electrode was taken to regions of different electrochemical activity by using X-Y stepper motors. Once the tip reached to desired location the SECM feedback approach curve was recorded by probe scan technique until the maximum feedback was reached.
- The kinetic data to extract the heterogeneous ET rate constant reaction rate was collected by applying different potentials around formal

potential to drive cathodic and anodic reaction at the substrate. The substrate potentials were changed from negative to positive values and SECM feedback approach curves were recorded. The procedure was repeated on regions of different electrochemical activity as well as for different materials.

- The data was firstly converted into text file than normalized values of the current and distances were generated. The normalized current was achieved by dividing the tip current at particular distance with tip current at infinite distance (i_T/i_∞). The offset between tip and substrate was normalized by dividing offset to the radius of the tip (d/a). The normalized currents and normalized distances were used in the curve fitting generated from the analytical equation given in chapter 3 (***see section 3.2.4.4***), to calculate the heterogeneous ET rate constant. The radius of the microelectrode and offset were converted into cm units to equate with the diffusion coefficient values i.e. 7.8×10^{-6} cm^2s^{-1}. The heterogeneous ET rate constants were extracted from the fitting of current distance SECM feedback approach curves with theoretical curves extracted from analysis of the approximation analytical equations. The log of the heterogeneous ET rate constant was plotted verses overpotential, the plot is also called a Tafel plot. The extrapolation of the Tafel plots to zero overpotential yield standard heterogeneous ET rate constant. The same procedure was repeated for stainless steel, Inconel 625 coating and bulk Inconel 625.

4.8 X-ray photoelectron spectroscopy

The samples were polished to 1µm surface finish before conducting XPS experiments. The air exposed samples were kept in the lab environment for 24 hours before transferring into the ultra-high vacuum XPS chamber environment. General survey spectra and high resolution spectra of the principal element photoelectron peaks were collected for Inconel 625 coating, CoNiCrAlY coating, WCCoCr coating, bulk Inconel 625 and stainless steel 304. The samples were polarized to 100, 200, 500 and 1000 mV constant potential for 5 min before carrying out XPS experiment. Same samples were re-polished before polarizing to next potential. The instrument used was a VG Scientific ESCALab Mark I photoelectron spectrometer utilising non-monochromatic AlKα with excitation energy of 1486.6 eV and a vacuum pressure of approximately 1×10^{-9} mbar. The determination of the binding energy enables to get the electronic configuration and therefore the atomic species and oxidation state can be identified. The experiments measure the number of counts (intensity) versus binding energy. The charge correction was made with respect to the C 1s peak at 285 eV for all materials.

The survey spectrum covers the full range of binding energies from 0-1100 eV and the scan take approximately 10 minutes. The high resolution spectrum covers the binding energies where the particular peak of the elements appears e.g. the high resolution spectrum for Cr was recorded from 570-592 eV binding energy. The high resolution spectrum scan also takes approximately 10 minutes to complete.

The binding energies and peak shapes were used to identify the peak present in the spectrum. The peak area ratios allow determining the relative amount of element and oxides present in a particular peak. Peak decomposition was carried out using a symmetrical Gaussian Lorentzian shape and a Shirley background for Cr, Ni, Mo and Nb peaks. The fitting parameters i.e. full width half maximum (FWHM), peak position and area ratio were constrained as given in [187]. Area ratio 2:1 was used for $2p_{3/2}$:$2p_{1/2}$ in Ni and Cr and 3:2 was used for $3d_{5/2}$:$3d_{3/2}$ for Mo and Nb peaks [187]. Peak fitting of the photoelectron peaks of different materials regions were made using the Casa-XPS software package.

5 Potentiodynamic polarization

5.1 Introduction

In this chapter experimentally obtained potentiodynamic polarization results are presented for stainless steel, bulk Inconel 625 and HVOF Inconel 625, WCCoCr and CoNiCrAlY coatings. The experimental and interpretation issues with potentiodynamic polarization technique, localized corrosion study and analysis of the corrosion products by X-ray photoelectron spectroscopy are also presented in the chapter.

5.2 Microstructure characterization

5.2.1 Stainless steel 304 and bulk Inconel 625

The major phase in AISI304 stainless steel is austenite [122, 188]. The EDS analysis shows that the austenite phase contains approximately 18% chromium and 8% nickel. This is consistent with the literature and other reported work [189]. The high magnification images of stainless steel show the dark grey phase near the grain boundaries. The EDS analysis reveals the dark phase is rich in C and O. The microstructure of bulk Inconel 625 has a major γ-phase with bright particles around the grain boundaries. The EDS analysis shows the bright particles are rich in Nb. The higher concentration of Nb around the grain boundaries in bulk Inconel 625 has also been reported by other authors [55, 190]. In bulk Inconel 625 the Nb may have limited solubility in γ-phase and segregated at grain boundaries [7, 191, 192].

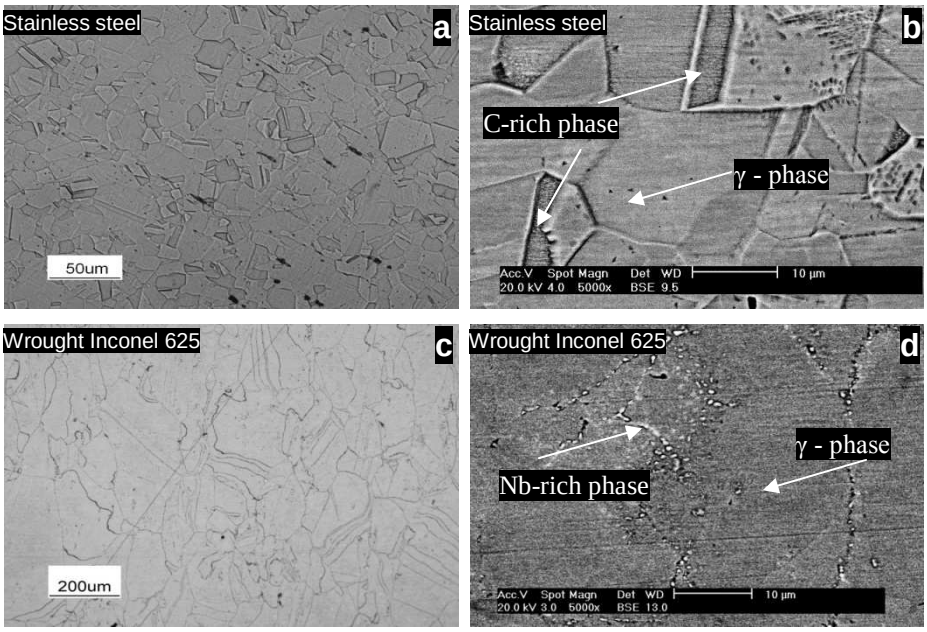

Figure 5-1: Micrographs of a, b) stainless steel and c, d) bulk Inconel 625 alloys etched in aqua regia at 20°C for approximately 30 s before imaging.

Table 5-1: EDS spot analysis for stainless steel and bulk Inconel 625

Stainless steel					
Element wt %	C	O	Cr	Fe	Ni
Average surface	3.7 ± 0.3	0.8 ± 0.4	18.3 ± 0.2	67.6 ± 0.6	8.1 ± 0.3
C-rich phase	7.3 ± 0.9	5.4 ± 0.3	17.0 ± 0.2	61.7 ± 0.8	6.7 ± 0.2
γ -phase	4.1 ± 0.3	1.0 ± 0.5	18.3 ± 0.6	67.0 ± 0.5	7.6 ± 0.8
Wrought Inconel 625					
Element wt %	-	Cr	Ni	Nb	Mo
Average surface	-	22.1 ± 1.6	59.0 ± 6.3	5.3 ± 2.1	13.7 ± 5.8
γ -phase	-	23.2 ± 0.2	63.0 ± 0.1	3.8 ± 0.3	9.9 ± 0.2
Nb-rich phase	-	20.3 ± 1.5	51.9 ± 6.9	7.7 ± 2.2	20.1 ± 6.1

The contribution of different phases in their electrochemical response depends on their percentage and nature of the constituents present. The C-rich phase in austenitic stainless steel might be martensite, a phase formed due to fast heating cooling cycle or mechanical stresses [193, 194]. In our experiments the stainless steel sample did not go through any heating/cooling process the stress induced during cutting, grinding and polishing may have formed martensite. The dark phase stress induced martensite also reported by some other authors [195]. The amount of oxygen is also higher around this phase indicating etchant attack of this phase is more extensive than for the rest of the surface.

5.2.2 HVOF Inconel 625, CoNiCrAlY and WCCoCr coatings

The ***Figure 5-2***a shows the microstructure of HVOF Inconel 625 coating, generated by repeated impaction of a stream of powder particles [2]. Within the microstructure there are splats, pores, partially melted particles and dark regions around solid particles [43, 72, 192]. The particle boundaries and solid particle phases are magnified in ***Figure 5-2***b. The particle boundaries are clearer with major grey dendrite phase and brighter inter-dendritic phase covering the grey phase. The EDS spot analyses were carried out on average

surface and different phases of the microstructure, results were presented with standard errors ***Table 5-2***. The standard error (SE) of mean is = $s / \sqrt{n}$, s is standard deviation and n is number of sampling. The dark region around the particle boundaries contain oxygen peaks, the EDS analysis show the oxygen amount of 22.6 ± 2.5%. The brighter dendrites were rich in Mo and Nb and low in Ni. The higher percentage of Nb in the brighter phase was also consistent with the previously reported work [7]. The grey phase in the brighter phase was found low in Nb and high in Cr.

Table 5-2: EDS spot analysis for Inconel 625, CoNiCrAlY and WCCoCr coatings

Inconel 625 coating					
Element wt %	O	Cr	Ni	Nb	Mo
Average surface	-	22.3 ± 0.2	63.3 ± 1.2	4.0 ± 0.9	10.1 ± 0.9
O-rich composition	22.6 ± 2.5	25.4 ± 2.5	38.9 ± 5.7	4.8 ± 0.8	8.4 ± 0.2
Bright-phase	-	21.3 ± 0.1	58.0 ± 1.2	8.2 ± 0.7	12.4 ± 0.6
Grey –phase	-	22.5 ± 0.2	64.5 ± 1.0	3.2 ± 0.4	9.9 ± 0.5
CoNiCrAlY coating					
Element wt %	O	Al	Cr	Co	Ni
Average surface	-	8.7 ± 1.4	21.4 ± 1.1	36.2 ± 3.1	31.8 ± 3.1
O-rich	18.2 ± 1.7	11.2 ± 1.2	19.5 ± 2.6	27.8 ± 2.0	23.4 ± 1.4
Al-rich phase	-	10.0 ± 0.7	21.2 ± 0.6	36.2 ± 1.1	32.7 ± 1.2
Co-Cr-rich phase	-	6.3 ± 0.6	22.5 ± 0.3	38.1 ± 0.2	33.1 ± 0.9
WCCoCr coating					
Element wt %	-	C	Cr	Co	W
Av. Surf. comp.	-	6.0 ± 3.9	7.2 ± 5.5	21.5 ± 11.9	67.6 ± 17.9
WC	-	5.0 ± 4.2	0.5 ± 0.5	0.9 ± 0.7	93.6 ± 5.0
Co-rich phase	-	3.8 ± 3.1	4.3 ± 1.4	26.7 ± 1.7	65.2 ± 3.5
Co-Cr-rich phase	-	6.5 ± 3.2	14.7 ± 0.4	29.1 ± 2.2	49.7 ± 4.6

The ***Figure 5-2***c shows the presence of pores and micro cracks in the CoNiCrAlY microstructure. As expected the CoNiCrAlY coating consists of Co, Ni, Cr and Al. No Y peak is identified in EDS analysis, probably due to its low concentration or Y may have been vaporized during HVOF process [49, 50]. There are two phases present in the CoNiCrAlY coating called γ-phase

and β-phase. The γ-phase is a solid solution of Co-Ni-Cr and β-phase is a solid solution of Co-Ni-Al [49, 196]. The grey region in the CoNiCrAlY coating microstructure is γ-phase and black phase is β-phase. The EDS analysis results of the CoNiCrAlY coating are consistent with previously reported work [197].

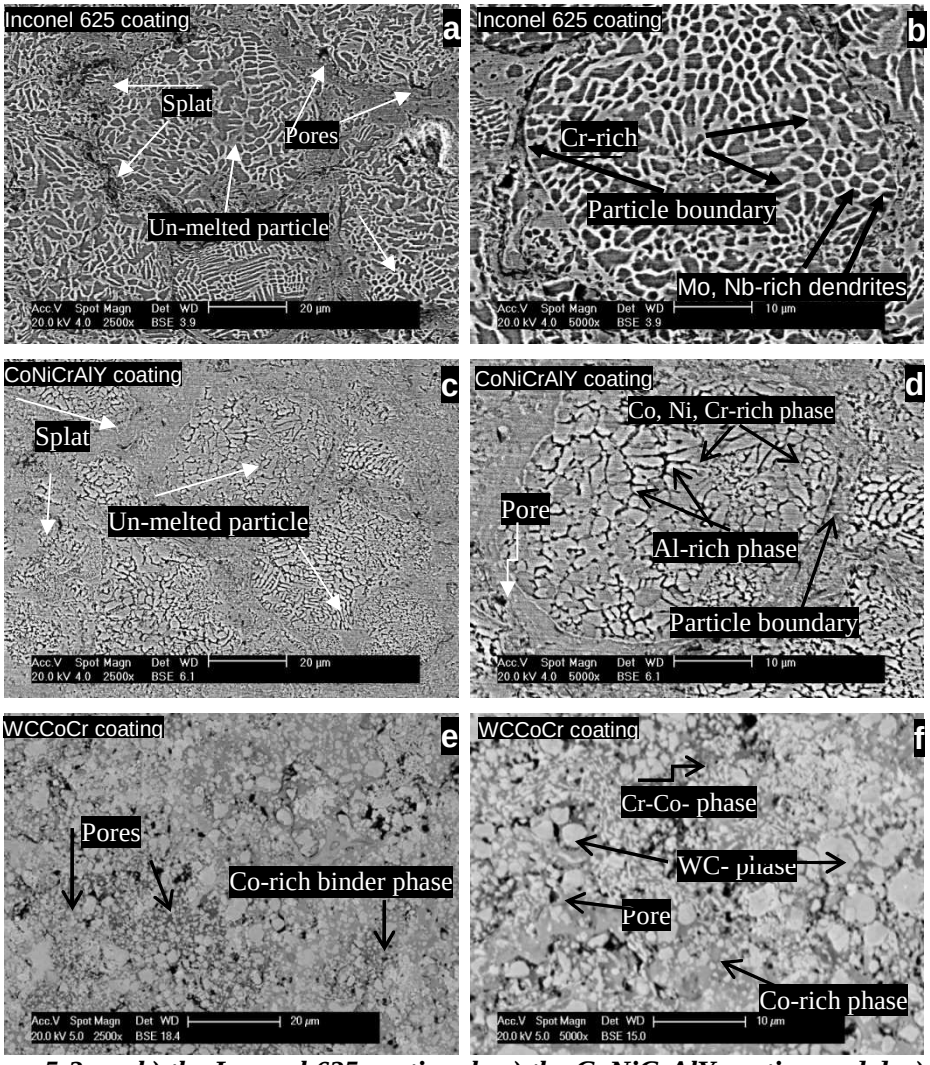

Figure 5-2: a, b) the Inconel 625 coating, b, c) the CoNiCrAlY coating and d, e) the WCCoCr cermat coating at × 1000 and × 5000 magnifications. The samples were etched in aqua regia at 20° C for approximately 30 sec before imaging.

The WCCoCr coating in ***Figure 5-2***e consists of three phases along with pores and cracks. The brighter phase is WC-phase, light grey is Co-rich matrix phase and dark grey regions are Cr-rich binder phase. The EDS analyses of different

phases in WCCoCr coating are summarized in ***Table 5-2.*** Some other researchers reported the same phases in WCCoCr coating [198].

5.2.3 Polarization curves of bulk Inconel 625, stainless steel

Three distinctive regions can be seen in ***Figure 5-3*** polarization curves of bulk Inconel 625 and stainless steel. The region AB is active, BC is passive and CD is transpassive for bulk Inconel 625 alloy. The labels in ***Figure 5-3*** with * sign represent the same regions for stainless steel. The point B, where further increase in potential decreases the current density takes place at 30 mV for bulk Inconel 625 and -89 mV stainless steel samples. The region BC where current does not increase with increase in potential is called the passive region. This current density is called passive current density. The passive current density was 3.61 ± 0.51 μA cm^{-2} for bulk Inconel 625 and 5.67 ± 1.83 μA cm^{-2} for stainless steel sample. The potential at point C where current increases exponentially is called breakdown potential. The breakdown potential is 906 ± 3 mV for bulk Inconel 625 alloy and 898 ± 5 mV for stainless steel sample. The region CD is called transpassive region, where the current increases either due to breakdown of the passive layer or bulk oxygen evolution. The potential at point A is called corrosion potential (E_{corr}). The E_{corr} value for the bulk Inconel sample is -251 mV and -307 mV for stainless steel.

In chromium bearing alloys the threshold limit to form uniform protective oxide layer is 11% [199]. The γ-phase in both stainless steel and Inconel 625 contains the Cr than the threshold limit. The uniform passive regions for both stainless steel and Inconel indicate the protective oxide layer is formed [200]. ***Figure 5-3*** shows polarization curves for bulk Inconel 625 and stainless steel.

Each experiment is repeated three times on different samples. The results for bulk Inconel 625 and stainless steel are presented with standard errors of the mean in ***Table 5-3***.

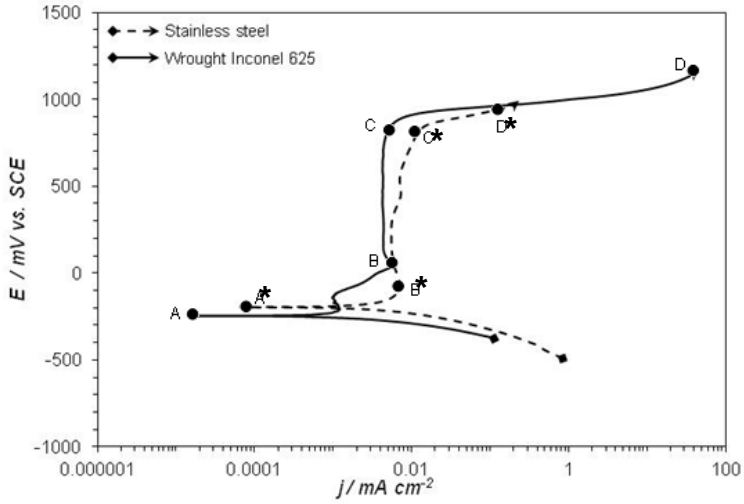

Figure 5-3: Potentiodynamic polarization curves for bulk Inconel 625 (solid line) and stainless steel (dotted line) samples. Both samples were polarized in 0.5 M H_2SO_4 from -250 more negative than E_{oc} to 1200 mV more positive than E_{oc} at a scan rate of 20 mV min^{-1}.

Table 5-3: Polarization results for bulk Inconel 625 and stainless steel

Material	E_{corr} / mV	j_{corr} / µA cm^{-2}	j_{pass} / µA cm^{-2}	E_{break} / mV
Wrought Inconel 625	-251 ± 10	0.41 ± 0.05	3.61 ± 0.51	906 ± 3
Stainless steel	-307 ± 16	0.35 ± 0.07	5.67 ± 1.83	898 ± 5

5.2.4 Using polarization curves to examine changes due to the HVOF spraying process

Figure 5-4: shows the polarization curves for Inconel 625 coating and the bulk Inconel 625 samples to identify change in the potentiodynamic polarization curves due to the HVOF process. The active to passive transition potential point is 45 mV for bulk Inconel 625 and 72 mV for Inconel 625 coating sample. The polarization curve of Inconel 625 coating shows an extra hump

below the point B^* at -60 mV. The polarization graph of bulk Inconel 625 shows the passive current density is a factor of 10 lower than that of the Inconel 625 coating. The breakdown potential is 906 mV for bulk Inconel 625 alloy and 890 mV for Inconel 625 coating sample.

The physical and chemical heterogeneity of a material surface may contribute to the overall corrosion behaviour change of the material. The pores and cracks provide the potential sites for crevice corrosion, where inside of the pore environment become different than the bulk environment at the electrode surface due to oxygen and electrolyte concentration [201]. The regions of composition gradient or phases of different electrochemical activity act as the potential source of galvanic corrosion where corrosion takes place at higher rate at active sites more than non-active site [202]. The corrosion starts around the regions of heterogeneities or electrochemically active sites. The pores and cracks at the surface provide potential source of crevice corrosion. The oxygen concentration inside the crack/pore becomes low than the bulk surface. The oxygen concentration cell established due to this situation causes the pore regions to corrode more than the rest of the surface [203]. The phases of different electrochemical activity present in the microstructure can also cause galvanic corrosion of the surface. The less electrochemical active phase corrode more than the one which is electrochemically less active [204-206]. The defect free homogeneous surface can form a uniform protective oxide layer which stops the metal from further oxidation [207]. The bulk Inconel 625 has more uniform microstructure than HVOF coating [1, 7].

Physical discontinuities like pores, cracks, splats and chemical segregations are present in the coating samples. The polarization curves in ***Figure 5-3*** shows the E_{corr} of the bulk Inconel was 42 mV more positive than the Inconel 625 coating. The more positive E_{corr} for the bulk Inconel 625 is due to the more homogeneous surface of the bulk Inconel 625 than Inconel 625 coating [1, 7, 61]. The homogeneous surface formed more uniform passive layer than the coating. In coating samples pores/cracks and composition gradients exists in the microstructure which do not allow the coating surface to form uniform layer as for the bulk alloy [7, 8]. The passive layer analysis by XPS also revealed the higher oxidation of the bulk Inconel as compared to Inconel 625 coating (***see section 5.7.1 and 5.7.4***). The corrosion current density in activation region i.e. j_{corr} and in passive region j_{pass} are lower for the bulk Inconel 625 than the Inconel 625 coating sample. The lower values of j_{corr} and j_{pass} for the bulk Inconel 625 alloy represent that the reaction is slower when metal is actively corroding as well as when a passive layer is formed.

The predominant anodic reaction takes place around splat boundaries [7, 192]. The composition at splat boundaries is significantly different than rest of the coatings [61, 200]. The current densities within pores and cracks may be higher due to above described crevice phenomenon. The second loop in ***Figure 5-4*** around B* is probably due to localized corrosion attack on active region like Cr-depleted regions around the grain boundaries than rest of the coating [109, 126, 127]. The second loop in polarization curve is less pronounced for the bulk Inconel 625 alloy. The extra hump in the polarization curve of the bulk Inconel 625 may be due to oxidation around the grain boundaries where

Nb preferentially corrodes and once Nb fully oxidized the surface starts oxidizing uniformly [1, 192]. The elimination of the hump in polarization curve by laser surface treatment of the coating is reported by some authors [1, 7, 8]. They attributed this change to the laser surface modification process which eliminates the pores, cracks and regions of different chemical compositions and make the surface homogenized [208, 209].

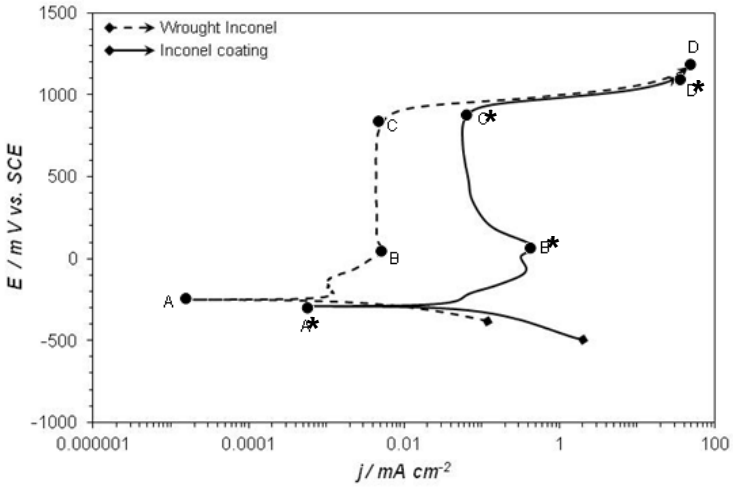

Figure 5-4: Potentiodynamic polarization curves recorded at bulk Inconel 625 (dotted line) and Inconel 625 coated (solid line) samples. Both samples were polarized in 0.5M H_2SO_4 from -250 more negative than E_{oc} to 1200 mV more positive than E_{oc} at a scan rate of 20 mV min^{-1}.

Table 5-4: Results from polarization curves of bulk Inconel 625 and coating

Material	E_{corr} / mV	j_{corr} / µA cm^{-2}	j_{pass} / µA cm^{-2}	E_{break} / mV
Wrought Inconel 625	-251 ± 10	0.41 ± 0.05	3.61 ± 0.51	906 ± 3
Inconel 625 coating	-293 ± 17	21.58 ± 3.18	34.26 ± 8.34	890 ± 5

5.2.5 Polarization curves for different HVOF coatings

The potentiodynamic polarization curves for HVOF coatings show the shift in active, passive and transpassive regions. The active, passive and transpassive regions are labelled AB, BC and CD. The passivation potential is -265 mV for the CoNiCrAlY coating, 65 mV for the Inconel 625 coating and 120 mV for the WCCoCr coating. The polarization curve of CoNiCrAlY coating shows the

lowest passive current density and corrosion potential. Polarization curve for tungsten carbide coatings shows a higher gradient in Tafel regions than the CoNiCrAlY and the Inconel 625 coatings. The polarization curves of both Inconel 625 and CoNiCrAlY coatings show a hump B^{*} around -100 mV and B^{**} around 150 mV respectively in ***Figure 5-5***. The polarization curve for the CoNiCrAlY sample shows decrease in the current density once passivation was started. The polarization curve of WCCoCr coatings shows no decrease in current density once passivation is started. The corrosion potential is -355 mV for CoNiCrAlY, - 323 mV for WCCoCr and -293 mV for Inconel 625 coatings. Results summary for the polarization curves for three coatings are given ***Table 5-5* .**

The microstructure of the coatings and their corrosion behaviour depends on the constituents from which it is made-up. The coating of soft material produces less porosity and cracks in the final product than hard material due to greater deformation of incompletely melted material on impaction [48, 49]. The microstructure of the CoNiCrAlY coating and the Inconel 625 has less porosity and cracks than the WCCoCr coatings (***see Figure 5-8***). This was probably due to hard WC structure in the WCCoCr coating [74, 198].

The passive current density of the three coatings is not very much different but the passivation of the coating reached differently. The polarization curve for the CoNiCrAlY shows a point B^{**} at around 200 mV where active to passive transition occur while a constant passivation current for WCCoCr coatings when passivation is started. In the CoNiCrAlY sample this is probably due to oxidation of Al, Co and in WCCoCr due to Cr, Co content in the coating [210].

The oxidation of different constituents in the coatings is later studied by XPS and presented in the later section of this chapter. The potential limit for the transpassive regions of different coatings was approximately same as for the bulk oxygen evolution [211, 212]. The EDS analysis shows that phases present in the coatings have different percentage of elements. The extent of oxidation of the phase depends on the elements present and their percentage in the phase [205, 206]. The phases present in three different coatings do change the appearance of their respective polarization curve shapes but increased microstructural complexity of the cermet coating did not produce an increased complexity of the potentiodynamic polarization curve.

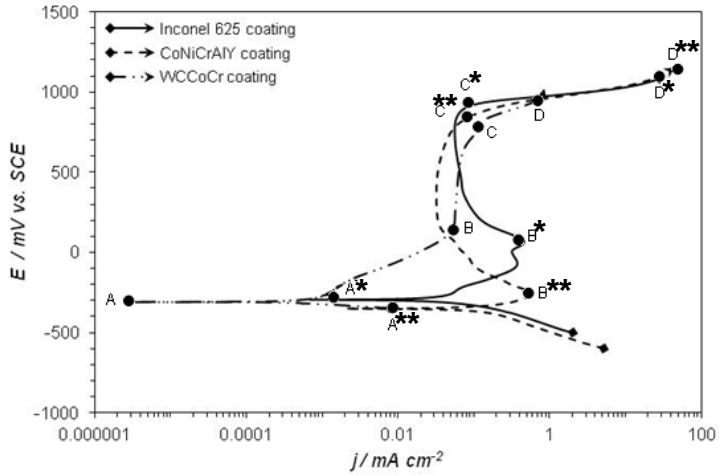

Figure 5-5: Potentiodynamic polarization curves recorded at the Inconel 625, the CoNiCrAlY and the WCCoCr coated samples. Samples were polarized in 0.5M H_2SO_4 from -250 more negative than E_{oc} ***to 1200 mV more positive than*** E_{oc} ***at a scan rate of 20 mV min^{-1}***

Table 5-5: Results from polarization curves of different coatings in Figure 5-5.

Coating material	E_{corr} / mV	j_{corr} / µA cm^{-2}	j_{pass} / µA cm^{-2}	E_{break} / mV
Inconel 625	-293 ± 17	21.58 ± 3.18	34.26 ± 8.34	890 ± 5
WC 10Co 4Cr	-323 ± 25	9.65 ± 0.80	41.25 ± 3.68	843 ± 13
CoNiCrAlY	-355 ± 23	130.00 ± 2.50	36.15 ± 3.00	910 ± 17

5.2.6 Reproducibility of polarization curves on coatings

Potentiodynamic polarization curves experiments were performed on same sample and different samples to check their reproducibility. For same sample polarization curves in ***Figure 5-6***a, one sample was used three times after regrinding the surface. For different sample polarization curves in ***Figure 5-6***b-d three different samples were used. The different sample polarization curves were recorded on Inconel 625, WCCoCr and CoNiCrAlY coatings. The polarization curves show the E_{corr} = -286 ± 9 mV for the same sample and -275 ± 16 mV for different samples of Inconel 625 coating. The polarization curves shows the j_{pass} = 16 ± 1 µA cm^{-2} for the same sample and 15 ± 3 µA cm^{-2} for the different samples. The polarization curves in ***Figure 5-6***a on the same sample overlap each either and error in the results is lower than the polarization curves in ***Figure 5-6***b-d, performed on different samples, hence reproducibility of the polarization curves performed on the same sample is higher than those performed on different samples. The higher reproducibility of the polarization results on same sample is attributed to the same microstructure and surface conditions. The corrosion potential and passive current density of the polarization curves on different samples was different due different surfaces of the samples.

The reproducibility of the polarization curves is also checked for WCCoCr and CoNiCrAlY coatings. The E_{corr} for the WCCoCr and the CoNiCrAlY is -291 ± 18 and 360 ± 10 mV respectively. The polarization curves in ***Figure 5-6*** shows the passive current density change was maximum for WCCoCr and minimum for the Inconel 625 coating when experiments were performed on the same

samples. The sample to sample variation in passive current density was 69% for WCCoCr coating, 32% for CoNiCrAlY coating and 20% for the Inconel 625 coating. The j_{pass} was even decreased to 6% for the same sample on Inconel 625 coating. The percent difference in the j_{pass} can be correlated to their microstructural heterogeneity. The WCCoCr coating shows maximum heterogeneity, the polarization curves display maximum difference in j_{pass}. The Inconel 625 coatings show minimum heterogeneity, the polarization curves display minimum difference in j_{pass}. The difference in j_{pass} become further decreased when polarization curves were recorded on the same sample. The results extracted from the polarization curves of different coatings are summarized in ***Table 5-6***.

The polarization curves are not 100% reproducible as it is hard to maintain exactly same testing and materials parameters all the time. The ASTM G5-1994 also permitted the results within the error of 10% [100]. The testing parameters include difference in apparent surface area and true geometrical surface area, time interval between sample preparation and insertion in solution, nitrogen purging and surface preparation. The material parameters are most difficult to control this include microstructural variations, different compositions in different regions and crystal planes.

The different corrosion potential and passive current density of the polarization curves on different samples is due to surface area of the samples. The surface roughness due to micro-pores cracks and splats were different from sample to sample [213, 214]. The samples with higher number of pores or cracks will show higher current density and the samples with lower number of pores or

cracks will show lower current density on their polarization curves [215]. The large number of pores and cracks increased the true exposed surface area as compared to the one have low number of pores. If pores or cracks were interconnected the polarization curve of the coating will be similar to the substrate, contrary to those samples have fewer pores or cracks will show their polarization curve more like the bulk alloy. The E_{corr} of the sample can be linked with the overall potential at the metal surface. The metal having more electrochemically active regions on the surface will show a more negative potential value than the one having less electrochemically active regions.

The E_{corr} of the metal also changes with surface roughness. The E_{corr} shifts to more negative potential value with rough surface and to more positive potential value with smooth surface. This high positive E_{corr} for smooth surface is probably due to less surface area and smooth oxide layer than the rough surface [216-218]. ***Figure 5-6***d for the WCCoCr coating results show more variation in polarization curves than Inconel 625 coating in ***Figure 5-6***b probably due to more surface heterogeneity which was also visible from the microstructure of the coatings [5, 219]. The CoNiCrAlY coating was more compact than the WCCoCr coating but the change in passive current density is attributed to Al-rich phase in CoNiCrAlY coating microstructure. Therefore the difference in CoNiCrAlY was dominant due to material type.

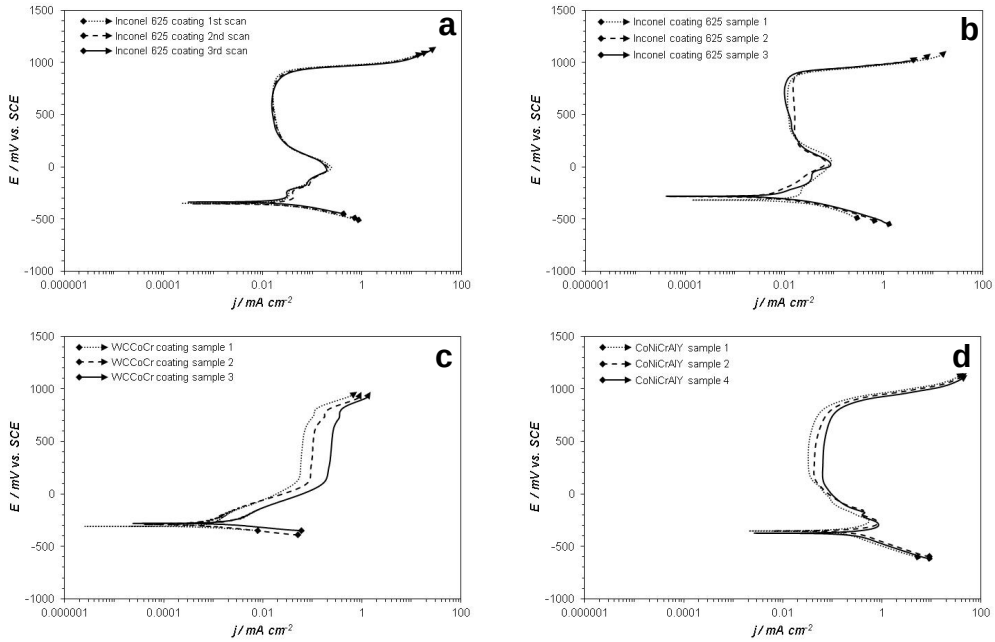

Figure 5-6: Potentiodynamic polarization for different materials in 0.5 M H_2SO_4 from -250 more negative than E_{oc} to 1200 mV more positive than E_{oc}, at 20 mV min^{-1}. a, b) Inconel 625 coating, c) bulk Inconel 625, d) WCCoCr coating, e) CoNiCrAlY coating. (Polarization curves in a repeated on same sample and b, c and d repeated on different samples)

Table 5-6: Polarization results extracted from different coating materials

j_{pass} / μ A cm^{-2} for different coatings, ^{D} = different samples, ^{S} = same sample				
	WCCoCr	CoNiCrAlY	Inconel ^{D}	Inconel ^{S}
Sample 1	60	34	11	16
Sample 2	101	46	16	17
Sample	235	65	16	15
Average	132	49	15	16
Standard deviation	91	16	3	1
% Difference	69	32	20	6
E_{corr} / mV on different coatings				
Sample 1	-312	-371	-294	-296
Sample 2	-283	-352	-264	-280
Sample	-278	-357	-268	-281
Average	-291	-360	-275	-286
Standard deviation	18	10	16	9
% Difference	6	3	6	3

5.2.7 Polarization curves for different material in 3.5% NaCl and 3.5% Na_2SO_4

Pitting is a localized form of corrosion which generally occurs due to heterogeneities in the microstructure or in chloride containing solution [113, 220]. To simulate the material pitting tendency of different materials, polarization curves in ***Figure 5-7***a-f are recorded in sodium chloride and sodium sulphate. Both solutions were used in same concentration of 3.5% to see the effect of chloride ions in pitting of the different materials.

Figure 5-7a, b show the polarization curves for bulk Inconel 625 and Inconel 625 coating in both solutions. The polarization curves of bulk and coating show passivation in sodium sulphate solution. The j_{pass} is factor of 10 lower for the bulk alloy sample than the coating. The polarization curve for the bulk alloy in sodium chloride do not show good passivation but still current around the passive region is lower than the coating sample. The polarization curve for the coating in sodium chloride did not show passivation instead current fluctuations in anodic side of the curve. The pitting in the coating sample is attributed to heterogeneity and composition gradient within the microstructure as compared to bulk alloy.

The polarization curves in ***Figure 5-7***b, f for the Inconel 625 coating and stainless steel show current fluctuations in anodic region. The fluctuation of current is due to metastable pitting, where pits form but re-passivate [107]. The polarization curves in ***Figure 5-7***b for Inconel 625 shows that meta-stable pitting starts at around 250 mV. The heterogeneities in Inconel 625 coating can

lead to defects in the oxide layer which may be more susceptible to chloride attack [13]. The chloride attack destabilises the oxide layer hence allowing pitting corrosion [221]. The polarization curve ***Figure 5-7***f for Inconel 625 coating in chloride containing electrolyte does not show any passivation, consistent with attack all over the surface. The microstructure after polarization test in ***Figure 5-8*** also show pits on the Inconel 625 coating. The critical size, pH below 3 and chloride ions in the environment were the necessary conditions for auto-catalytically growth of the pit, when these conditions were not fulfilled pit will not grow but re-passivate [222].

The fluctuation in current with increasing applied potential indicates that the pit formation and its re-passivation go side by side until the potential point where current increases exponentially [12]. The small current fluctuations in higher numbers in ***Figure 5-7***b are probably due to higher number of localized pits which cannot grow further but passivates. The sharp rise in current and slow fall of the current fluctuation in ***Figure 5-7***f represents the fast pitting and slow re-passivation of the pit [223, 224]. The slow re-passivation of the pit is attributed to accumulation of corrosion product around the active pit area [225]. The meta-stable pitting can be seen from the polarization curves of Inconel 625 coating and stainless steel in ***Figure 5-7***b, f.

Table 5-7: Results extracted from the polarization curves in Figure 5-7

Material	Solution	E_{corr} / mV	j_{corr} / µA cm^{-2}	j_{pass} / µA cm^{-2}	E_{break} / mV
Wrought Inconel 625	3.5% NaCl	-250 ± 13	0.93 ± 0.13	1.1 ± 0.3	669 ± 4
	3.5% Na_2SO_4	- 267 ± 7	0.88 ± 0.10	1.0 ± 0.10	688 ± 7
Inconel 625 Coating	3.5% NaCl	-264 ± 18	7.15 ± 1.58	-	298 ± 10
	3.5% Na_2SO_4	- 288 ± 3	8.85 ± 1.15	4.31 ± 0.42	595 ± 5
CoNiCrAlY coating	3.5% NaCl	-310 ± 21	1.42 ± 0.32	-	17 ± 12
	3.5% Na_2SO_4	-327 ± 14	9.10 ± 1.62	6.25 ± 2.53	598 ± 6
WCCoCr coating	3.5% NaCl	-498 ± 30	42.80 ± 2.32	24.50 ± 7.21	561 ± 13
	3.5% Na_2SO_4	-547 ± 26	85.90 ± 13.80	91.90 ± 5.70	576 ± 9
Platinum	3.5% NaCl	-283 ± 10	3.55 ± 0.66	3.21 ± 0.90	570 ± 10
	3.5% Na_2SO_4	-214 ± 13	9.98 ± 1.02	5.90 ± 1.82	580 ± 8
Stainless steel	3.5% NaCl	-295 ± 16	1.63 ± 0.52	-	421 ± 20
	3.5% Na_2SO_4	-310 ± 6	2.65 ± 1.32	7.82 ± 1.25	945 ± 13

The pitting in AISI304 stainless steel is previously reported due to sulphide inclusions (MnS), which act as a potential source of irregularities in the passivation film [226]. These spots provide sites for pit initiation which propagate later in the chloride containing environment. In CoNiCrAlY coating as there was Al, which form alumina on the surface which is not good resistant to pitting in chloride environment [210], hence severe pitting occurs in the CoNiCrAlY coating. The polarization curve for the CoNiCrAlY sample shows the breakdown potential around 17 mV in sodium chloride as compared to 598 mV in sodium sulphate. The stainless steel 304 sample is also prone to pitting in sodium chloride solution [108, 220]. The polarization curves of WCCoCr coating and platinum did not show any sign of pitting due to their less reactivity in both sodium sulphate and sodium chloride environments [5, 227], indicating that HVOF microstructure itself is not increasing pitting propensity for WCCoCr coating.

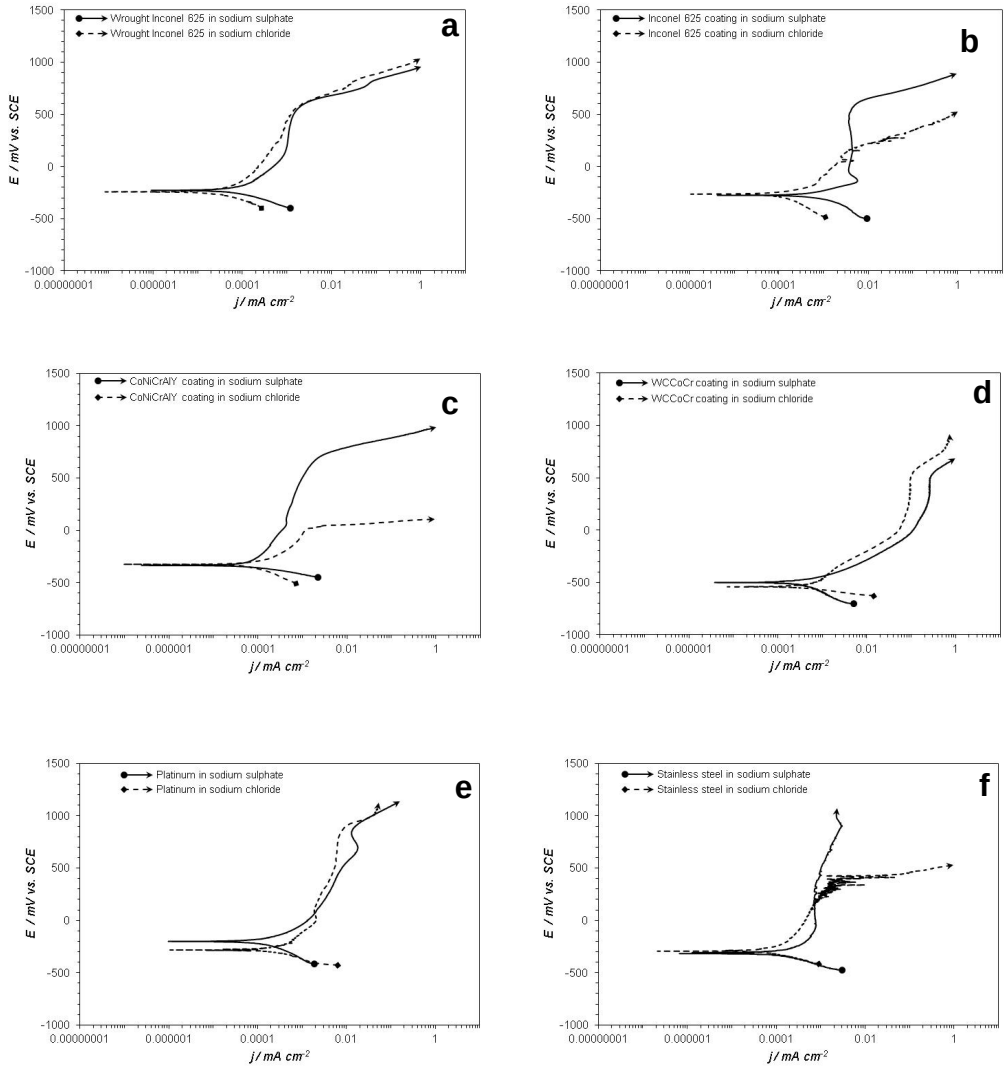

Figure 5-7: Potentiodynamic polarization curves of different material in 3.5% Na2SO4 (solid) and 3.5% NaCl (dotted). Samples were polarized from -250 more negative than E_{oc} to 1200 mV more positive than E_{oc} with a maximum current limit to 1 mA at a scan rate of 20 mV min-1. a) bulk Inconel 625, b) Inconel 625 coating, c) CoNiCrAlY coating, d) WCCoCr coating, e) platinum, f) stainless steel.

5.2.8 Microstructure changes after immersion

Corrosion of the material in oxygenated environments generally occurs due to heterogeneity in the microstructure and presence of aggressive anions like sulphate or chloride [228]. The bulk Inconel 625 is a corrosion resistant material due to air formed oxide on the surface. The micrographs for the bulk Inconel 625 did not show any corrosion attack in the water, sodium chloride

and sodium sulphate solution. The protective oxide layer on bulk Inconel 625 acts as a barrier between solutions and metal surface and does not allow oxygen or anions to attack the metal and change the microstructure.

Figure 5-8a to c shows the micrographs of bulk Inconel 625 and Inconel 625 coating after 10 days exposure in the stagnant water, 3.5% Na_2SO_4 solution and 3.5% NaCl solution. The micrographs were labelled as w for the bulk Inconel 625 and c for the Inconel 625 coatings. The micrographs of bulk Inconel 625 in water, sodium sulphate and sodium chloride did not show any corrosion damage. The Inconel 625 coating samples also remain un-attacked in water and sodium sulphate. The micrograph of Inconel 625 coating in sodium chloride solution shows black spots along the edges. The black spots were pronounced near the lacquered region than rest of the coating. We suggested that long exposure of the coatings in sodium chloride caused localized corrosion due to combine galvanic and crevice corrosion effect [108, 228]. It is possible that the electrolyte penetrate underneath the lacquer through some pores, which later established a crevice corrosion cell. The difference of oxygen between two regions increases the PD which allows the metal ions to move out and chloride ions to move in the lacquered region. The crevice corrosion initiated in the lacquered region did not slow down due to restricted availability of oxygen and movement of chloride ions in the region. The colour change of the solution and black spots were also visible on the Inconel 625 coating surface. The chloride ions contribution to crevice corrosion of the Inconel 600 alloys is also reported by some other researchers [228]. The

micrographs of all other samples do not show black spots around the lacquer region.

5.2.9 Microstructure changes after polarization test

The bulk Inconel 625 surface shown in ***Figure 5-8***a-w is homogeneous and does not have defects like HVOF coating surfaces. The only electrochemical active sites are grain boundaries hence the applied potential preferentially attack the grain boundaries and make them more visible in micrographs. The micrograph of bulk Inconel 625 also shows ***Figure 5-8***d-w some ridges or channels which is probably due to removal of small grains from the grain boundaries.

The microstructure after polarization in sodium sulphate show fewer and less dark pits than in sodium chloride solution. The less dark contrast of the pits in sodium sulphate is probably due to shallow pits and darker in sodium chloride due to deeper pits. The contribution of sulphate and chloride ions towards different kind of pitting was also consistent with other researchers work [220]. The severely etched non-melted particles evident from the micrographs of the Inconel 625 coating indicates that overall corrosion damage for the sample polarized in sodium chloride is more than sodium sulphate.

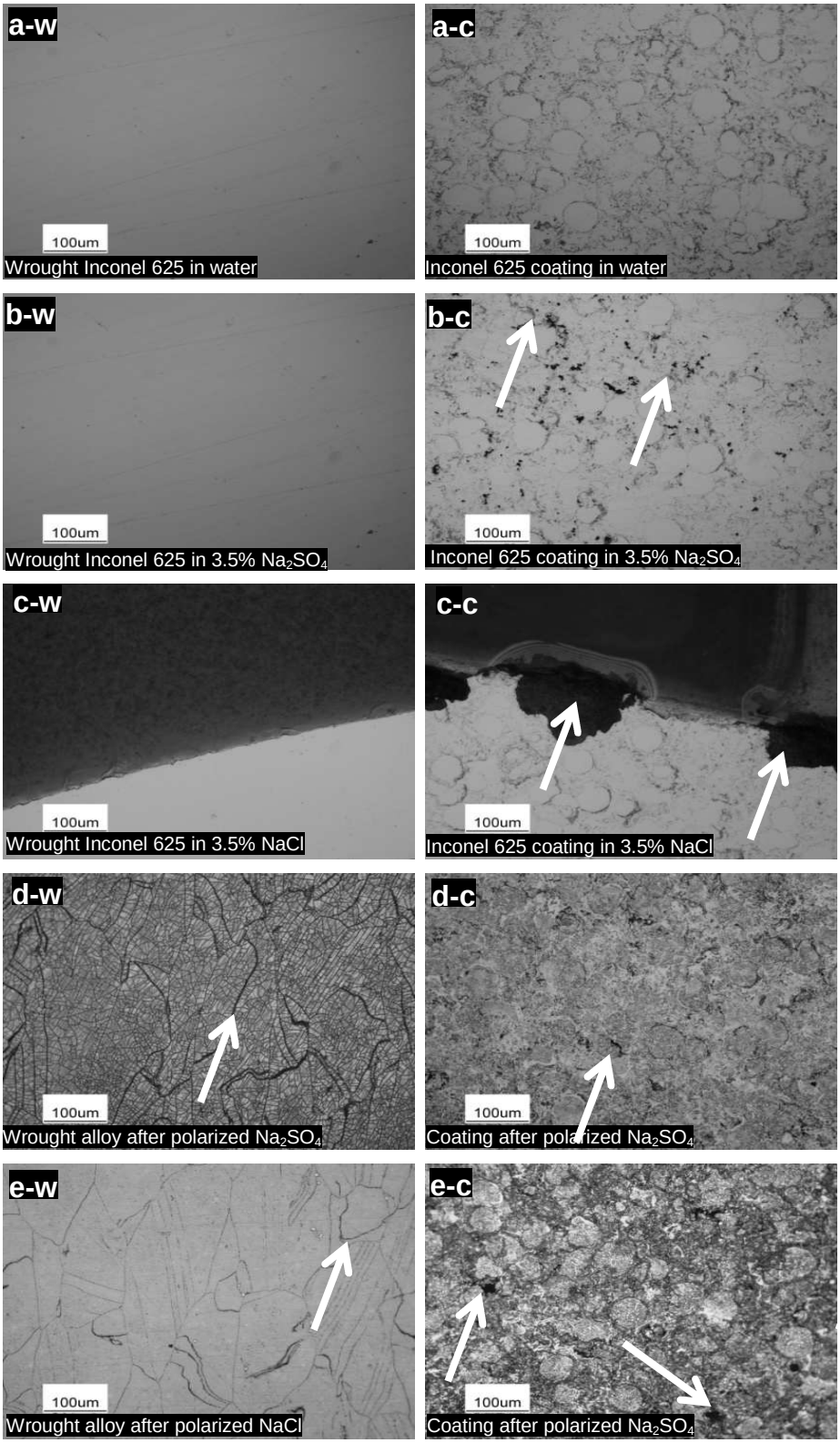

Figure 5-8: Microstructure. a-w) bulk Inconel 625 in water for 10 days, b-w) bulk Inconel 625 in 3.5% Na_2SO_4 for 10 days, c-w) bulk Inconel 625 in 3.5% NaCl for 10 days, d-w) bulk Inconel 625 after conducting polarization test in 3.5% Na_2SO_4, e-w) bulk Inconel 625 alloy after polarization test in 3.5% NaCl. The micrographs a to e with c show the same labelling for the Inconel 625 coating where bulk 'w' is replaced with coating 'c'.

5.3 Factors affecting polarization curves

The main objective of the controlled potential process is to measure the response current related with redox reactions. During polarization experiments, different processes are involved which can cause errors in the results. Careful selection of the process parameters and elimination of unwanted factors can make results more meaningful.

5.3.1 Effect of E_{oc} change with time

Figure 5-9 and ***Table 5-8*** show that the E_{oc} value changed rapidly for first 5 hours before reaching to an approximately stable value for all materials. The value of E_{oc} at the start for bulk Inconel 625 was -91 mV and changed to -8 mV after 15 hours. A more negative value of E_{oc} was measured for the coating samples and the value changed to a more negative after 15 hours. The E_{oc} values for Inconel 625, CoNiCrAlY and WCCoCr coatings were -212 mV, -214 mV and -157mV at the start of experiment and reached -266 mV, -312 mV and -291 mV after 15 hours.

The stable E_{oc} value also is known as corrosion potential. This is the potential of a corroding metal in a solution relative to a reference electrode measured under open circuit conditions. One of the requirements of the polarization testing is that the electrochemical reactions must be approximately constant during the measurement. Such a condition is identified by approximately constant corrosion potential. A big error source in the potentiodynamic polarization test is not waiting long enough for approximately stable corrosion potential before starting the potential sweep. The E_{oc} vs. time curves were

recorded to see the material tendency to reach the stable corrosion potential [104].

Increasing the stabilization time from 1h to 15 hours before starting polarization test decreased the E_{oc} change rate from 13-50 mV/h to 1-6 mV/h. The greater stabilization of E_{oc} increased accuracy of the polarization test as current voltage correlation defining polarization curve reflects the same corrosion phenomena of the curve. The higher rate of E_{oc} change adversely effect in passive systems where slight polarization upset the electrochemical process enough that the generated curve did not pass through the origin, this mean applied current will be observed at zero volt relative to the starting $E_{oc.}$

The possible reactions responsible for changing E_{oc} value at metal electrolyte interface are labelled ***Figure 5-10***. The results presented in ***section 5.3.1*** shows that corrosion potential of the bulk Inconel 625 shifts to more positive value and coatings to more negative values. The oxide film forms rapidly when a freshly prepared metal surface exposed in an oxygen including atmosphere. The few nanometre thick oxide is called native oxide [229]. The native oxide film tends to dissolve when immersed into acidic solution by oxide reduction or complex formation by hydrogen ions [230, 231]. The dissolution of the native oxide depends on the pH, temperature and film thickness. If oxide film dissolving process is dominant the E_{oc} will shift to a more negative value. In solutions containing inhibiting anions, the oxide film dissolution may be suppressed by the corrosion product and protect the surface from further oxidation.

The protective oxide layer at the surface shifts the potential to more positive values when the oxide layer is increasing during stabilization. In coating samples, the coating microstructure largely varies over the surface and sample to sample. Different regions of the surface have different potential due different oxygen concentration, compositions of material and concentration of active species in solution from one part of the corroding surface to another [232, 233]. The E_{oc} results for different materials in ***Table 5-8*** shows that change in E_{oc} for each hour is higher for first five hours before reaching to a steady state.

It can be concluded from above results and discussions that it is not straightforward to determine the relative magnitude of the E_{oc} change due to different process shown in ***Figure 5-10.*** One process may be dominant at the time than other but the E_{oc} stabilization with time is evident from E_{oc} vs. time graphs and data analysis of all materials.

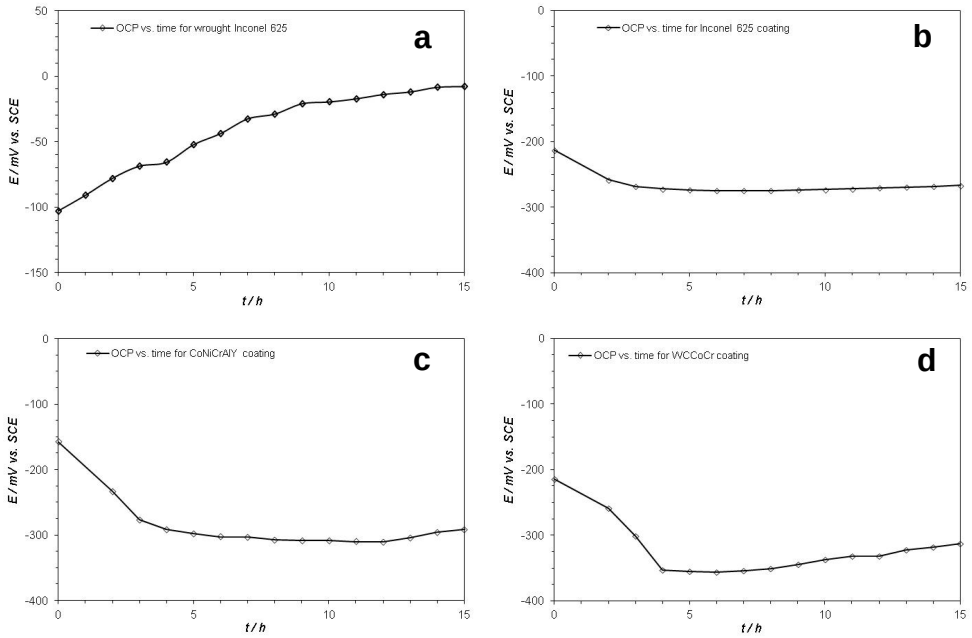

Figure 5-9: E_{oc} vs. time graphs for different materials 0.5 M H_2SO_4 a) bulk Inconel 625 alloy, b) Inconel 625 coating, c) WCCoCr coating, d) CoNiCrAlY coating

Table 5-8: E_{oc} results extracted from different materials for 15 hours

Exposure time	Inconel 625 coating		WCCoCr coating		Wrought Inconel 625		CoNiCrAlY coating	
t / h	E_{oc} / mV	ΔE_{oc} / mV	E_{oc} / mV	ΔE_{oc} / mV	E_{oc} / mV	ΔE_{oc} / mV	E_{oc} / mV	ΔE_{oc} / mV
1	-213	E_{oc1} - E_{oc2}	-158	E_{oc1} - E_{oc2}	-91	E_{oc1} - E_{oc2}	-215	E_{oc1} - E_{oc2}
2	-258	45	-233	-75	-78	13	-260	-45
3	-269	11	-277	-44	-69	9	-301	-41
4	-272	3	-291	-14	-66	3	-353	-52
5	-274	2	-298	-7	-52	14	-355	-2
6	-275	1	-303	-5	-44	8	-356	-1
7	-275	0	-303	0	-33	11	-354	2
8	-275	0	-308	-5	-29	4	-351	3
9	-274	-1	-308	0	-21	8	-345	6
10	-273	-1	-308	0	-20	1	-337	8
11	-272	-1	-310	-2	-17	3	-331	6
12	-271	-1	-311	-1	-14	3	-331	0
13	-270	-1	-304	7	-12	2	-322	9
14	-268	-2	-296	8	-9	3	-318	4
15	-267	-1	-292	4	-8	1	-312	6
ΔE_{oc} = Difference of potential between two consecutive readings								

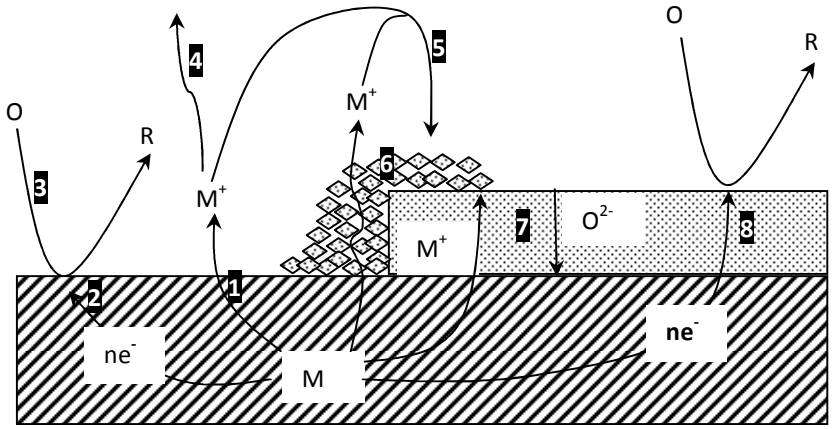

Figure 5-10: Schematic showing different process taking place during corrosion, 1) metal dissolution forming ions, 2) oxygen or proton reduction at metal surface, 3) transport of oxygen or ions to the surface, 4) metal ion transport from surface to solution, 5) precipitation of corrosion product, 6) metal ions transport through precipitates, 7) oxygen diffusion through solid corrosion product, 8) oxygen/proton reduction at solid product layer.

5.3.2 Effect of constant prior potential before recording polarization curves

The majority of the potentiodynamic polarization work reported in corrosion performance of the material used 200 to 300 mV more negative potential than E_{oc} as a starting potential [91, 104, 112, 213]. Starting from a potential more negative than the E_{oc} is generally used for cathodic conditioning or partial reduction of the air formed film [234]. To study the contribution of applied potential before the polarization different coating samples were polarized by a constant potential more positive and more negative than the E_{oc}.

The polarization curves for Inconel 625 and the WCCoCr coating did not change significantly due to the prior applied potential. This was probably due to the regions of different electrochemical activity in the Inconel 625 coating which did not from uniform oxidation of the surface within the applied

potential limit [112, 235, 236]. The polarization curves of WCCoCr coatings did not affected with the prior constant applied potentials. The range of applied potential may not be enough to damage the air formed surface oxide layer of WCCoCr coating [235]. The low oxidation at WCCoCr coating due to lower positive potential was also clear from the XPS results (***see Table 5-16***). The amount of Cr was 4 % which partially contributes in the E_{corr} shift within the positive and negative applied potentials with respect to E_{oc} due to oxide formation. The E_{corr} value increases with the more positive prior potential indicating more oxidation is taking place and covering the metal surface, this makes the corrosion potential more positive.

The shape of the polarization curve changed with the value of the constant prior potential for the bulk Inconel 625 and stainless steel was approximately the same way. The negative constant prior potentials shift the E_{corr} value to more negative values indicating that the surface was becoming electrochemically more active. The E_{corr} shift to more negative potential increases with more negative constant prior potential before the polarization test. It is suggested that partial reduction of the air formed oxide film was occurred which makes the surface more active. The E_{corr} shift with negative constant prior potential was clearer for stainless steel than the bulk Inconel 625. This is probably due to type of the oxide layer of the material, the oxide layer at the stainless steel surface is dominant in chromium oxide and the bulk Inconel 625 consist of NiO, MoO and Nb_2O_5 as shown by XPS (***see section 5.7.4*** and ***5.7.5***). Due to predominant one type of oxide, stainless steel surface provide more effective protection than that of bulk Inconel 625 alloy.

it is pertinent to mention that although the E_{corr} of the bulk Inconel 625 and stainless steel shifted to much negative values, it is believed that complete de-oxidation did not occurs as a much higher negative potential is required to reduce the existing oxides (e.g. Fe/Fe^{++} E^0 = 0.89 V, Cr/Cr^{+++} E^0 = 0.74 V etc). The positive constant prior potentials for both bulk Inconel 625 and stainless steel only slightly changes the position of E_{corr} indicating that once the oxidation occurs the surface is not changing too much. The E_{corr} shift to more positive value by oxidation is also consistent with other researchers work [237].

The E_{corr} values for different materials (after constant prior potential) in the forward scan in ***Table 5-9*** were approximately same as prior polarization results (without constant prior potential) in ***Table 5-5***. The E_{corr} values were -293, -323, -355 mV from prior polarization and -313, -334, -361 in forward scan for Inconel 625, WCCoCr and CoNiCrAlY coatings respectively. In reverse scan the E_{corr} values were 20-60 mV more positive than the polarization curves in forward scan. The shift in the E_{corr} of the reverse scan was attributed to different surface conditions and potential scan direction. The CoNiCrAlY coating was most affected by the constant prior potential and WCCoCr least affected by the constant prior potential. The Inconel 625 coating is moderately affected by both positive and negative potentials.

The negative applied potential before starting the test shifted the E_{corr} value to more negative values than the starting E_{oc} and positive applied potential before the test shifted the E_{corr} value to more positive than starting E_{oc}. The shift in E_{corr} to more negative potential value by applying negative potential was 15-40

mV for bulk alloys and 5-15 mV for the coatings. The shift in E_{corr} value to more positive value by applying positive potential was 2-4 mV for bulk alloys and 5-18 mV for the coatings. The higher negative shift in E_{corr} value for the bulk alloy by negative applied potential was attributed to partial removal of the oxide layer. The higher positive shift in E_{corr} value by positive applied potential for the coatings was probably due to increasing the potential driving force between different active and passive spots of the coatings. In bulk alloys once the oxide formed it slows down further oxidation of the surface, therefore the shift in E_{corr} value by positive applied potential was lower for bulk alloys. From these experimental results we suggest microstructure, constituents present and their percentage in the coating contribute to the over E_{corr} shift.

The schematic in ***Figure 5-11*** summarizes the changes that occur in polarization curves due to prior applied potential. Only two reactions are considered with no scale of potential/current axis to generalize the changes. The part a in the schematic, show the E_{corr} and i_{corr} where anodic and cathodic reactions are balanced. The ***Figure 5-11b*** shows the negative shift in the E_{corr} due to prior negative applied potentials. The negative prior applied potential decreases the thickness of the air formed film due to reduction of metal oxide by excess electrons or by the hydrogen evolution reaction at the surface. The hydrogen reduces the metal oxide at the oxide/solution interface. The reduction of the metal due to electrons takes place at metal/oxide interface. The reduction of the surface oxide causes a decrease in thickness, shifting the E_{corr} to more and more negative values. Contrary to that, with positive prior potential more and more oxide grows at the surface and shifts the E_{corr} to positive values as

shown in ***Figure 5-11c***. For the active-passive metals the surface quickly gets oxidized any application of prior applied potential only slightly changes the polarization curves. Such a situation is represented in ***Figure 5-11d*** where prior positive polarization slightly shifts the E_{corr} in the positive direction.

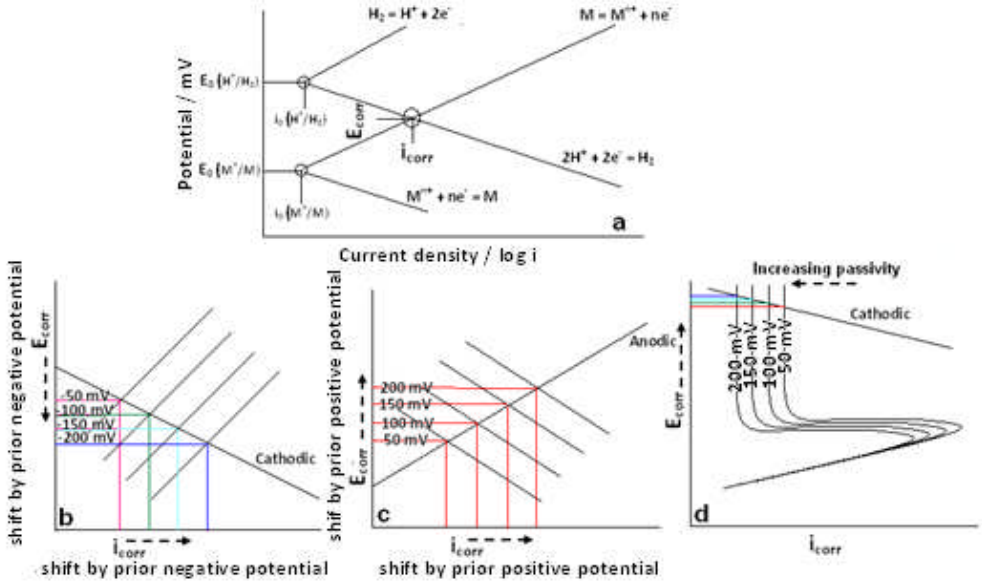

Figure 5-11: Schematic illustration of E_{corr} shift in Evans diagram due to prior applied potential. a) E_{corr} of the corrosion system involves H_2 evolution and metal oxidation, b) E_{corr} shift due to prior negative potentials, c) E_{corr} shift due to prior positive potentials, d) E_{corr} shift in passivation occurs with prior positive potentials.

The prior constant potentials -200 mV before recording polarization curves was carried out to investigate possible error sources in the existing practice of potentiodynamic polarization testing. The prior potential was kept constant for 30 minutes to simulate the time taken in polarization test to scan the potential from starting potential to the E_{oc}. It should be noted that if investigation of pit growth and healing is required a significant larger magnitude of prior positive potential should be used instead of the +200 mV or it is more appropriate to carry out experiment in galvanostatic mode. In galvanostatic mode, constant current is applied and response potential is observed. The schematic, ***Figure***

5-12 shows the polarization curve when cathodic lines are moved due to constant applied current. The material is actively corroding when applied current is in active region, i.e., line a. Line b crosses three regions of the anodic line at passive, active-passive and active region. This gives rise to multiple values of the E_{corr} [238].To be in the passive regions the applied current should exceed that at point X in the polarization curve. Once the current passes this limit passivation can be attained even at lower currents, as shown with line c. The current in the transpassive region either fully dissolves the active regions or passivates the surface. In the case of coatings pit growth may occurs leading to the rupture of the coating due to interconnected porosity. Galvanostatic mode is also a good approach when the thickness of the oxide growth and its effect on polarization curve is of interest.

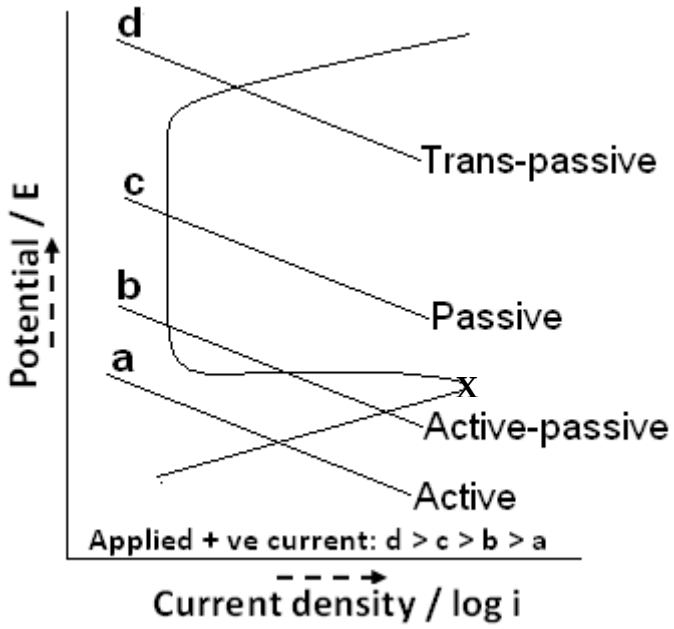

Figure 5-12: Schematic diagram where cathodic line cross different regions of anodic curve to demonstrate prior polarization extended to transpassive region.

Table 5-9: Effect of constant prior potential on E_{corr} shift for different materials

Inconel625 coating								
E	-200	-150	-100	-50	50	100	150	200
E_{corr} (FW)	-313	-312	-310	-309	-308	-308	-306	-303
E_{corr} (RV)	-275	-276	-274	-272	-263	-258	-252	-249
CoNiCrAlY coating								
E_{corr} (FW)	-361	-359	-354	-345	-330	-323	-317	-312
E_{corr} (RV)	-307	-298	-290	-284	-260	-245	-246	-241
WCCoCr coating								
E_{corr} (FW)	-334	-334	-333	-334	-332	-331	-328	-327
E_{corr} (RV)	-283	-284	-282	-281	-278	-274	-269	-260
Wrought Inconel 625								
E_{corr} (FW)	-307	-303	-296	-290	-284	-280	-278	-280
E_{corr} (RV)	-263	-260	-251	-237	-226	-217	-210	-208
Stainless steel								
E_{corr} (FW)	-319	-307	-288	-278	-273	-272	-271	-271
E_{corr} (RV)	-219	-218	-214	-212	-216	-212	-209	-206
E = Constant potential in mV with respect to E_{oc} FW, RV = Forward, reverse potential sweep								

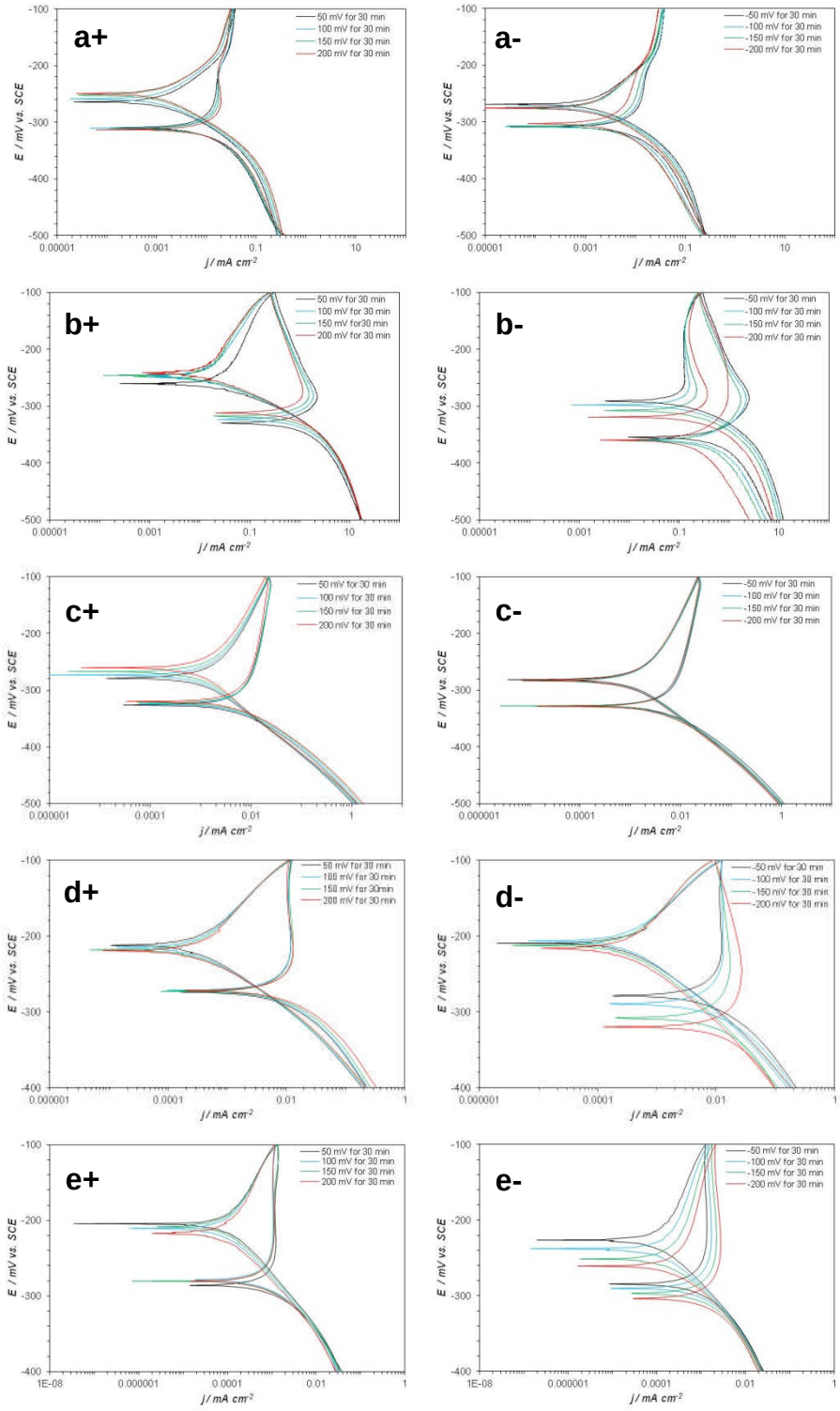

Figure 5-13: Potentiodynamic polarization curves after holding at a constant prior potential E_{oc}. A constant prior potential from -200 mV to 200 mV with an interval of 50 mV increments was used before recording each potentiodynamic polarization curve (label with + and – sign were positive and negative constant prior potentials for 30 min, potential increment from solid to thin-dotted lines). a) Inconel 625 coating, b) CoNiCrAlY coating, c) WCCoCr coating, d) stainless steel and e) bulk Inconel 625.

5.3.3 Effect of scan rate on charging current and polarization results distortion

Figure 5-14 to ***Figure 5-18*** show the polarization curves for stainless steel, bulk Inconel 625, Inconel 625 coating, CoNiCrAlY coating and WCCoCr coating in forward and reverse direction to extract the charging and faradaic current data. The stabilization time of one hour in electrolyte was given to every sample before recording the first scan. For each material the polarization curves were recorded at a scan rate of 100, 75, 50 and 25 mV min^{-1}. The potential ± 250 mV with respect to E_{oc} was swept in forward and reverse direction. The potential sweep in forward direction was started from -250 mV more negative than E_{oc} to +250 more positive than E_{oc}. The potential sweep in reverse direction was carried out on the same sample after 30 minutes of E_{oc} stabilization. The polarization curves were carried out in a sequence by starting the first potential sweep in forward direction and second in reverse direction after E_{oc} stabilization. The first set of polarization curves were carried out at a scan rate of 100 mV min^{-1} followed by polarization curves at 75, 50 and 25 mV min^{-1}. The data was extracted from the potentiodynamic polarization in forward and reverse direction curves by Tafel extrapolation. The charging and faradaic currents were separated by using ***equations 5.1*** and ***5.2***, [91] where $j^{positive}$ and $j^{negative}$ are the net currents forward and reverse scan. A region of 100 to 150 mV in the Tafel region was selected to extract the data for net currents.

$$j_{charging} = \frac{j^{positive}(E) - j^{negatve}(E)}{2} \qquad 5.1$$

$$j_{faradaic} = \frac{j^{positive}(E) + j^{negative}(E)}{2} \qquad 5.2$$

The faradaic current and charging current calculated from above equations were plotted against the scan rate. For each sample the experiment and analysis were repeated at least three times. The error bars of the data plot show standard errors for each plot. The polarization experiments were carried out within narrow potential scan limit to avoid surface change. But still the polarization curves of all materials show partial passivation of each sample.

The response current in potentiodynamic polarization test is the combination of charging and faradaic currents. The faradaic current flow in an electrochemical cell is due to redox reactions and charging current is due to charging and discharging of the double layer [105]. The continuously changing applied potential in potentiodynamic polarization test causes the charging current to flow all the time in an electrochemical cell [91, 97]. Each incremental step in potential scan changes the charge density stored at electrode-electrolyte interface [91]. The rate of change of charge density increases with scan rate. Charging current cannot be fully eliminated in potentiodynamic polarization but can be minimized by using a slow potential scan rate [91, 104].

The results show that both faradaic and charging current are material dependent and increase with the scan rate. The higher value of faradaic current can be attributed to faster corrosion reaction. At all scan rates the faradaic and charging currents are highest for CoNiCrAlY coating and lowest for bulk Inconel 625, this indicates that the CoNiCrAlY coating is least and bulk Inconel 625 is most corrosion resistant material under the used experimental conditions. The gradient of the line for charging current plot is more than the

faradaic current for all materials which indicates that charging current increases faster with scan rate than faradaic current.

The polarization curves for charging current calculation were carried out between ±250 mV to avoid passivation of the surface. However partial passivation occurs, as seen in ***Figure 5-12*** and ***Figure 5-13*** where the anodic side of the polarization curve becomes almost perpendicular near +250 mV. The polarization curves for all materials showed an E_{corr} shift of 150-200 mV between forward and reverse potential scans. This is probably due to a sulphate salt layer formed at metal solution interface. At higher overpotential the metal ions are released from the surface and react with sulphate ions in the solution to form salt which settles at the surface [205, 239]. This settling of the salt at the interface hinders the in/out diffusion of ions and oxygen, hence decreasing the corrosion rate of the same samples in reverse scan.

The effect of microstructure features on faradaic and charging current can be seen from the trend line plots of bulk Inconel 625 and Inconel 625 coating. The faradaic and charging current values were approximately a factor of 100 lower for the bulk Inconel 625 than the coating sample. The higher values for Inconel 625 coatings sample indicates that corrosion reaction was taking place at much faster rate than the bulk Inconel 625. The faradaic and charging current increases with scan rate for both sample but the difference between faradaic and charging current was greater for bulk alloy as compared to coating. The greater difference between faradaic and charging current for the bulk and coating alloy was probably due to surface change which was more predominant on bulk alloy than the coating.

It can be noted from the ***Figure 5-14, Figure 5-15*** and ***Figure 5-17*** that the polarization curves for stainless steel, bulk Inconel 625 and CoNiCrAlY coating become perpendicular in the forward scan and give a shorter Tafel region due to passivation. The shorter or improper selection of Tafel region can add errors in result calculations. The polarization curves for CoNiCrAlY show maximum offset both in forward and reverse scan. This may be the reason of larger errors as well as negative values of charging currents.

The results extracted from the different samples of the same material indicate that the faradaic and charging current trends remain the same but the trend lines show larger errors. This indicates that different samples also change the charging and faradaic current values. The variation in results is most likely dependent on the heterogeneity of the different sample. The results extracted from the polarization curves of the bulk Inconel 625 at different samples show shorter error bars than the one extracted from the Inconel 625 coating samples. The faradaic and charging current values for the bulk Inconel 625 were one decade higher than on the same sample probably due to repeated experiments on same sample.

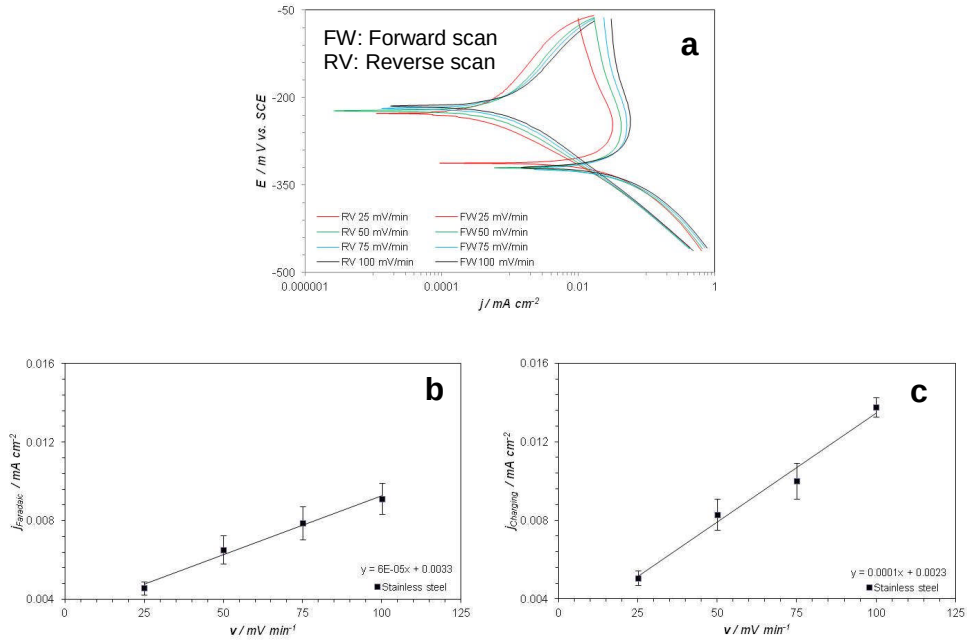

Figure 5-14: Potentiodynamic polarization curves for stainless steel in 0.5 M H_2SO_4. The potential was swept from -250 mV more negative than the E_{oc} to 250 mV more positive than the E_{oc} at a scan rate of 25, 50, 75 and 100 mV min^{-1}. The potential was swept in forward and reverse direction. a) Polarization curves at different scan rates, b) and c) the faradaic and the charging currents graphs

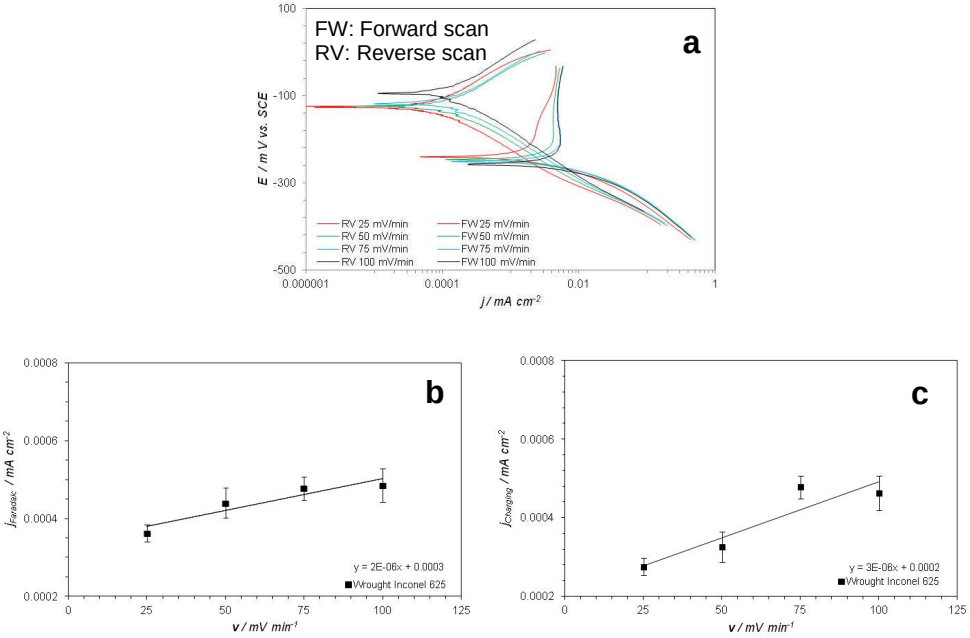

Figure 5-15: Potentiodynamic polarization curves for bulk Inconel 625 alloy in 0.5 M H_2SO_4. The potential was swept from -250 mV more negative than the E_{oc} to 250 mV more positive than the E_{oc} at a scan rate of 25, 50, 75 and 100 mV min^{-1}. The potential was swept in forward and reverse direction. a) Polarization curves at different scan rates, b) and c) the faradaic and the charging currents graphs.

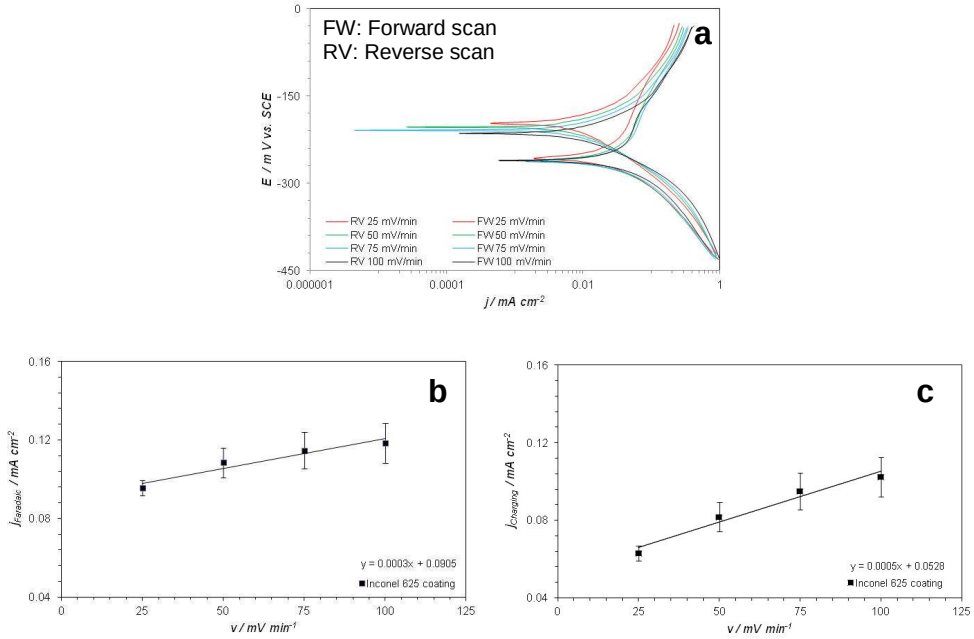

Figure 5-16: Potentiodynamic polarization curves for Inconel 625 coating in 0.5 M H_2SO_4. The potential was swept from -250 mV more negative than the E_{oc} to 250 mV more positive than the E_{oc} at a scan rate of 25, 50, 75 and 100 mV min^{-1}. The potential was swept in forward and reverse direction. a) polarization curves at different scan rates, b) and c) the faradaic and the charging currents graphs.

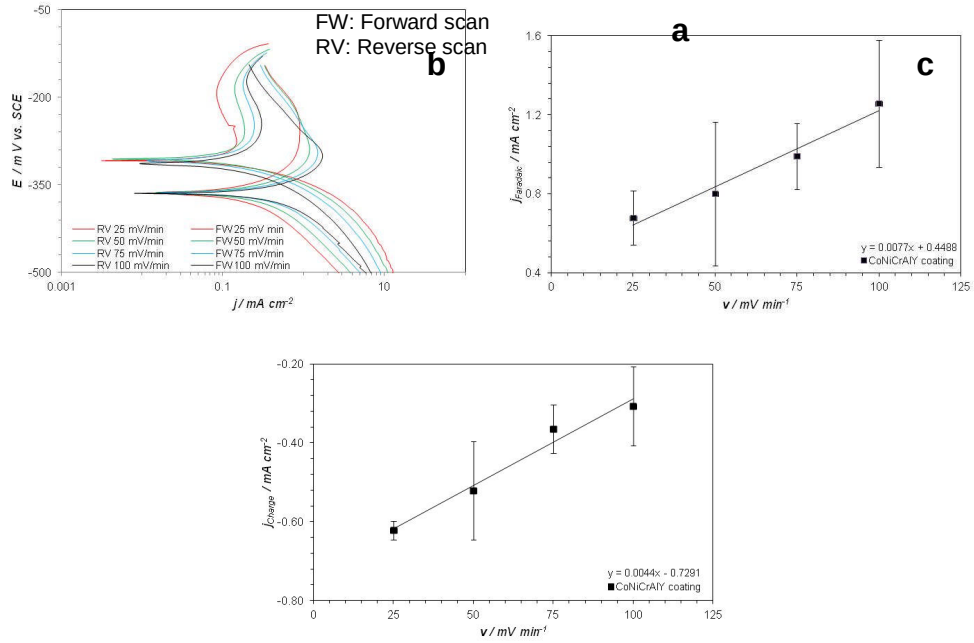

Figure 5-17: Potentiodynamic polarization curves for CoNiCrAlY coating in 0.5 M H_2SO_4. The potential was swept from -250 mV more negative than the E_{oc} to 250 mV more positive than the E_{oc} at a scan rate of 25, 50, 75 and 100 mV min^{-1}. The potential was swept in forward and reverse direction. a) polarization curves at different scan rates, b) and c) the faradaic and the charging currents graphs.

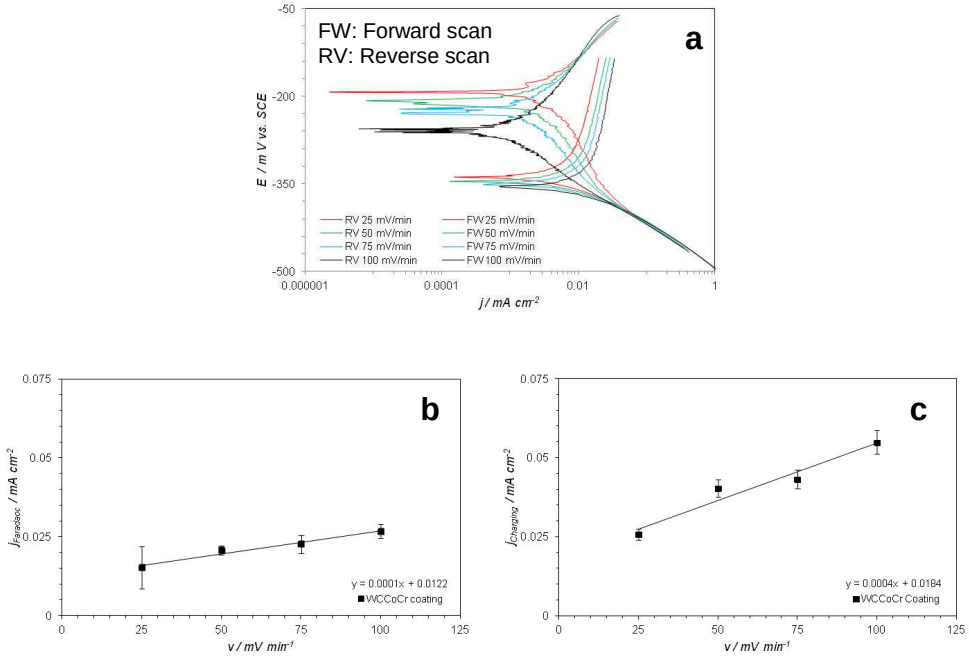

Figure 5-18: Potentiodynamic polarization curves for WCCoCr cermet coating in 0.5 M H_2SO_4. The potential was swept from -250 mV more negative than the E_{oc} to 250 mV more positive than the E_{oc} at a scan rate of 25, 50, 75 and 100 mV min^{-1}. The potential was swept in forward and reverse direction. a) Polarization curves at different scan rates, b) and c) the faradaic and the charging currents graphs.

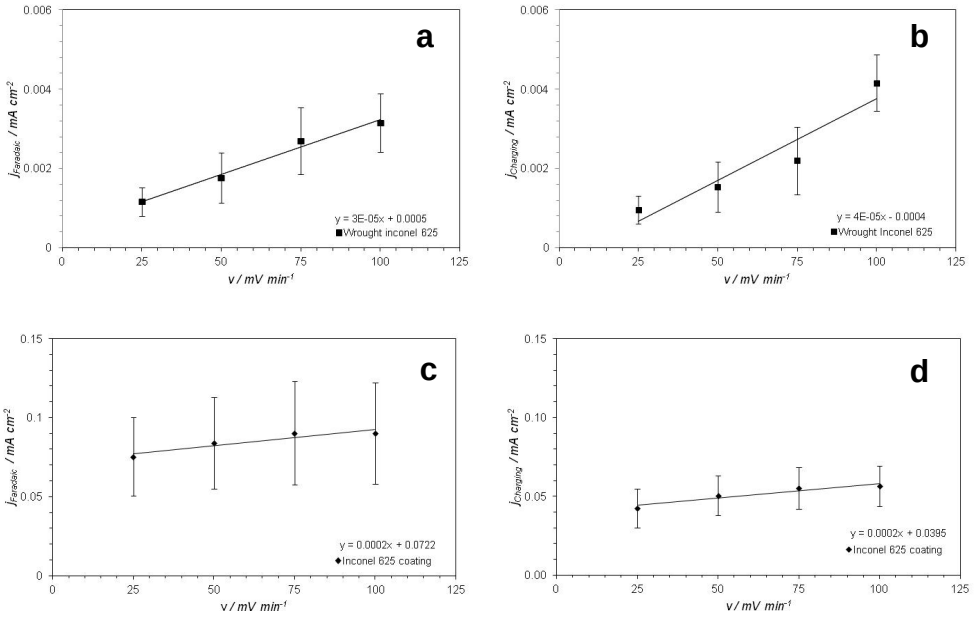

Figure 5-19: Faradaic and charging current data extracted from different samples. a), b) bulk Inconel 625, c), d) Inconel 625 coating.

5.3.4 Effect of potential sweep direction on E_{corr} shift

Most of the researchers used complete potentiodynamic polarization scan, starting from a potential more negative to E_{oc} and sweeping to more positive potential [103, 240-243] with exception of few used separate anodic and cathodic polarization scans [244, 245]. The results presented in ***section 5.3.4*** for stainless steel, bulk Inconel 625, WCCoCr coating, Inconel 625 coating and CoNiCrAlY coatings shows the complete and partial anodic and cathodic polarization curves started from E_{oc}. The partial anodic and cathodic polarization curves, starting from E_{oc} to more positive and negative potential were carried out to avoid any charge residual due to continuous scan. The time between each potential scan was kept one hour to acquire equilibrium before carrying out the next scan. A stabilization time of ten hours in solution was given to every sample before starting the first potential scan.

After 10 h of stabilization time the E_{corr} shift from the staring E_{oc} value was -4 mV from -251 mV for bulk Inconel 625, -30 mV from -307 mV for stainless steel -265 mV from -293 mV for the Inconel 625 coating, -399 mV from -355 mV for CoNiCrAlY and -318 mV from -323 mV for WCCoCr coating. The E_{corr} values after 10 hours stabilization time were more related with the passivation, i.e. the E_{corr} of the metal surface shift to positive value due to protective oxide layer at the surface [246, 247].

The electrode surface and its surrounding environment at electrode electrolyte interface changes with direction of potential sweep. The positive potential with respect to E_{oc} at the surface attracts the negative species from solution and vice versa for negative potential at the surface. The amounts of species attracted

towards electrode surface depend on the magnitude of the applied potential and its increasing or decreasing trend. The positive and negative species can either adsorb or react with the surface and change the surface temporarily or permanently. To see the effect of potential sweep direction polarization tests were carried with different potential starting point and direction.

The shift in E_{corr} value was 2-22 mV for the partial anodic and cathodic curves and 36-176 mV for the continuous polarization curves at 10, 20, 60 and 80 mV $min^{-1}$for all materials. In the continuous polarization curves the shift in E_{corr} value was 176 mV for stainless, 109 mV for the bulk Inconel 625, 32 mV for the Inconel 625 coating, 35 mV for the CoNiCrAlY coating and 30 mV for the WCCoCr coating. The shift in E_{corr} value from the partial scans was 21 mV for bulk Inconel 625, 22 mV for stainless steel, 8 mV for Inconel 625 coating, 9 mV for CoNiCrAlY coating and 2 mV for the WCCoCr coating for the same set of scan rates. The magnitude of difference in E_{corr} at 20 mV min^{-1} was 26 mV for the Inconel 625 coating, 14 mV for CoNiCrAlY coating and 22 mV for WCCoCr coating. After 10 h stabilizing time and starting potential scan from E_{oc} the difference in E_{corr} was decreased to 8 mV for Inconel 625, 10 mV for CoNiCrAlY and 4 mV for WCCoCr coatings. The shift in E_{corr} value was attributed to surface change and charging current flow.

The comparison between partial and complete polarization curves clearly shows that there is a shift in E_{corr} as well as shape of the polarization curves. The deviation between separate and continuous polarization curves increases with scan rate. The change in E_{corr} due to higher scan rate is also reported by some other researchers [245, 248]. For stainless steel sample the continuous

polarization curve approximately overlaps the separate polarization curves at 20 mV min^{-1}, this indicates that scan rate is slow enough to almost eliminate the charging current. A further slower scan rate was required (1 mV min^{-1}) to eliminate charging for bulk Inconel 625 alloy. The ***Figure 5-21*** shows distortion due to very slow scan rate, especially at higher side of the applied potential. The waviness in the polarization curve might be some surface changes due to extended time at higher applied potential. The polarization curves for Inconel 625, CoNiCrAlY and WCCoCr coatings show that the complete polarization curves overlap with the partial polarization curves at potential sweep rate of 10 mV min^{-1}. It can be established from these results that the sweep rate required to eliminate the charging current effect is material dependent.

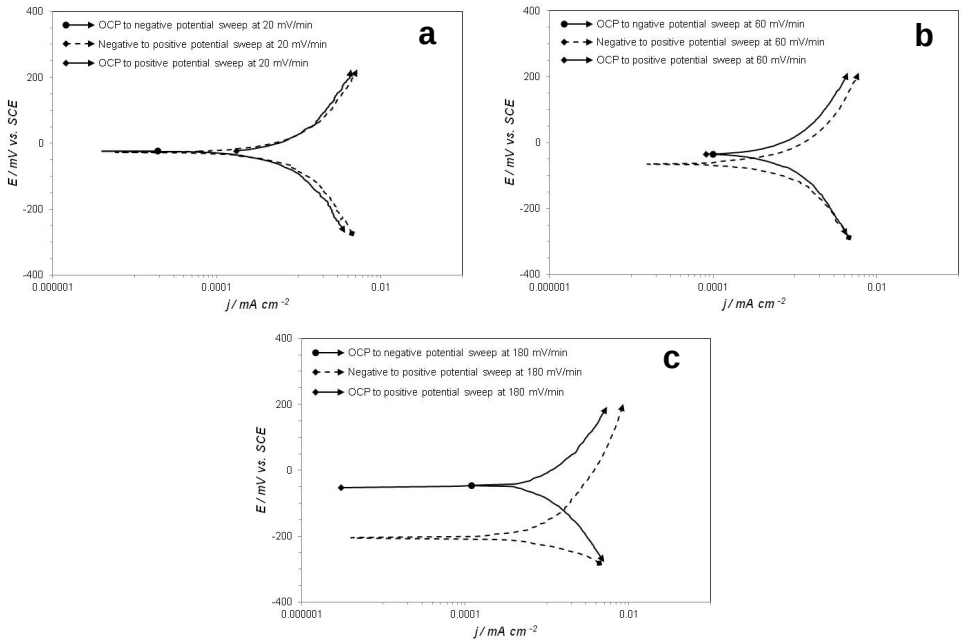

Figure 5-20: Complete potential sweep started from a potential more negative than E_{oc} to a potential more positive than E_{oc}, partial sweeps started from E_{oc} to positive and negative potentials at a scan rate of 20, 60 and 180 mV min^{-1} on stainless steel.

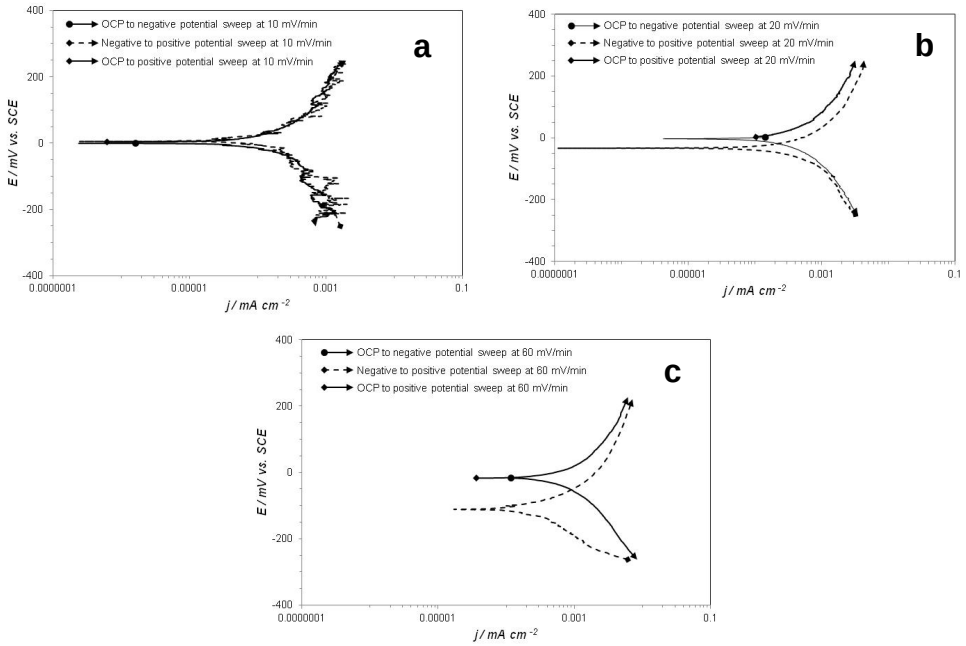

Figure 5-21: Complete potential sweep started from a potential more negative than E_{oc} to a potential more positive than E_{oc} (dotted lines), partial sweeps (solid lines) started from E_{oc} to positive and negative potentials at a scan rate of 10, 20 and 60 mV min^{1}on bulk Inconel 625.

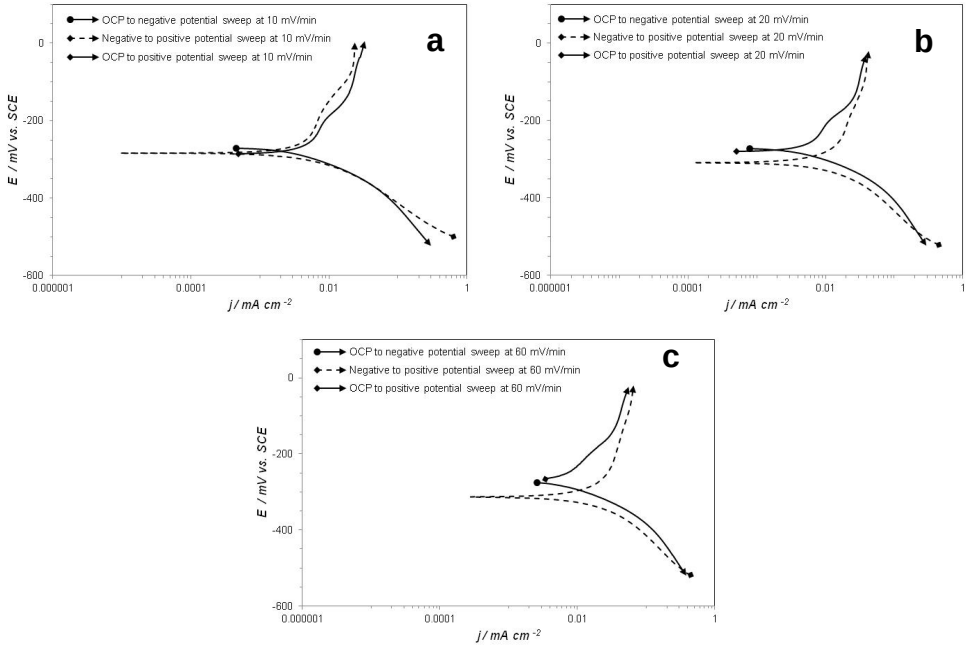

Figure 5-22: Complete potential sweep started from a potential more negative than E_{oc} to a potential more positive than E_{oc}, partial sweeps started from E_{oc} to positive and negative potentials at a scan rate of 10, 20 and 60 mV min^{-1} on Inconel 625 coating.

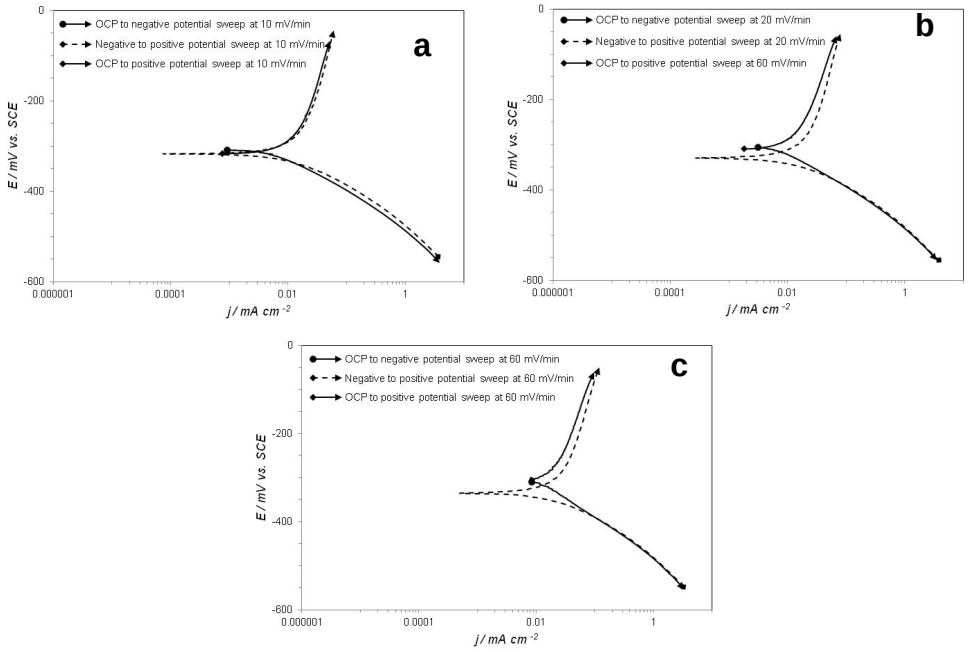

Figure 5-23: Complete potential sweep started from a potential more negative than E_{oc} to a potential more positive than E_{oc}, partial sweeps started from E_{oc} to positive and negative potentials at a scan rate of 10, 20 and 60 mV min-1 on WCCoCr coating.

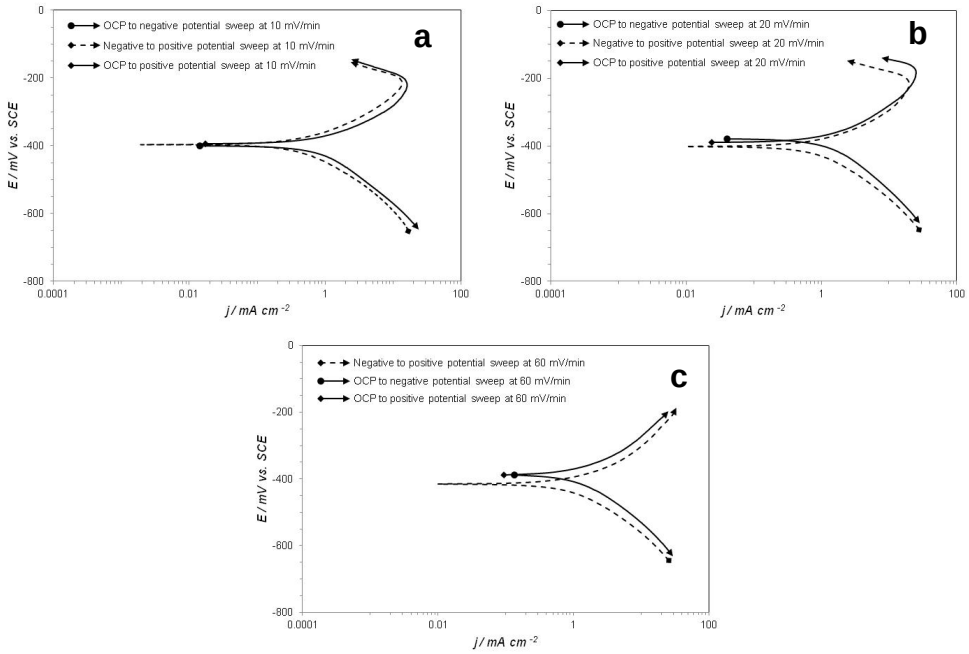

Figure 5-24: Complete potential sweep started from a potential more negative than E_{oc} to a potential more positive than E_{oc} and partial sweeps started from E_{oc} to positive and negative potentials at a scan rate of 10, 20 and 60 mV min^{-1} on CoNiCrAlY coating.

Table 5-10: E_{corr} shifts due to different starting point for different materials

Material	υ / mV min^{-1}	E_{corr1} / mV	E_{corr2} / mV	ΔE_{corr} / mV
Inconel 625 coating	10	-272	-285	13
	20	-280	-306	26
	60	-279	-311	32
	180	-280	-317	37
CoNiCrAlY coating	10	-397	-399	2
	20	-387	-401	14
	60	-386	-415	29
	180	-388	-434	46
WCCoCr coating	10	-311	-318	7
	20	-307	-329	22
	60	-303	-335	32
	180	-313	-348	35
Wrought Inconel 625	1	6	5	1
	10	-3	-32	30
	20	-4	-50	46
	60	-15	-114	99
Stainless steel	20	-25	-30	5
	60	-35	-66	31
	180	-47	-206	159

5.4 Comparison of polarization curves data in linear and log linear regimes

The polarization curves from ***Figure 5-14*** to ***Figure 5-17*** are further analysed to study the application of Butler-Volmer equation in linear polarization (Stern-Geary regime) and *E-logi* (Tafel regime) graphs. It was also of interest to compare the results from Stern-Geary equation with Tafel extrapolation results. Results are summarized in ***Table 5-11***. The encircled regions in ***Figure 5-25*** are the cathodic and anodic parts of the linear polarization regimes. At higher overpotentials of Tafel equation describe the behaviour.

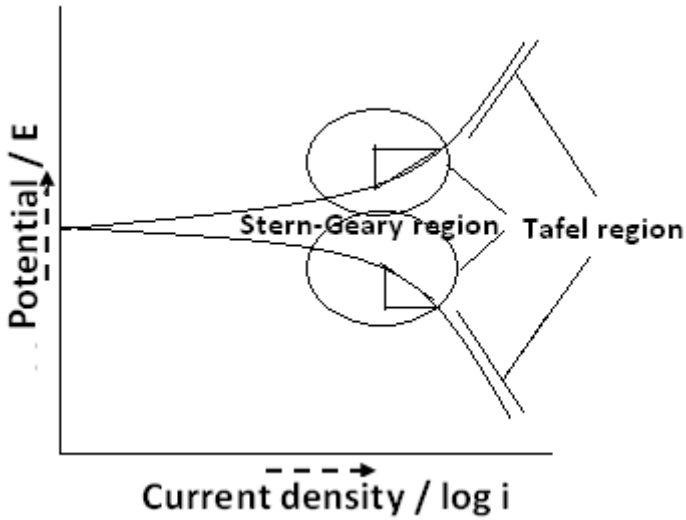

Figure 5-25: Schematic diagram shows two regions where Butler-Volmer equation deduced into Stern-Geary equation at low overpotentials and Tafel equation at higher overpotentials in Evans diagram.

The i_{corr} calculated from the Stern-Geary equation was higher than the one from intersection of anodic and cathodic curves in Tafel region. This was probably due to higher oxidation rate at low overpotentials and relatively low oxidation rate at higher overpotentials due to partial passivation. The corrosion rate calculation from both i_{corr} values also confirmed the higher corrosion rate in linear polarization than Tafel extrapolations.

The corrosion rate calculated for the Inconel 625 coating by using Stern-Geary equation was over a factor of 100 higher than for the bulk alloy, and over a factor of 10 higher by using Tafel extrapolation. The higher corrosion rate by using both methods further validates the higher overall oxidation of the coating. The corrosion rate of stainless steel was higher than the bulk Inconel 625 but less than the Inconel 625 coating when data was analysed by both Stern-Geary and Tafel extrapolation methods. It can be noted from the results table that corrosion rate from the polarization curves carried out in reverse scan was slightly lower than the forward scan. The slow corrosion rate in reverse

scan further consolidating the argue of sulphate salt formation. The change in corrosion rate in reverse scan was lower in Tafel region than linear polarization region.

Table 5-11: Data extracted from polarization curves in Figure 5-14 to Figure 5-17

*Analysis by **Stern - Geary** equation*					*Analysis by **Tafel extrapolation***				*Scan rate*
Analysis of the polarization curves carried out in forward scan for stainless steel sample									
R_P / (Ω)	b_a / mV	b_c / mV	i_{corr} / mA	C_R / mil Y^{-1}	i_a / mA	i_c / mA	i_{corr} / mA	C_R / mil Y^{-1}	υ / mV min^{-1}
919	88	94	2.16×10^{-2}	12.70	7.20×10^{-3}	2.00×10^{-2}	2.36×10^{-2}	7.99	100
703	93	99	2.97×10^{-2}	17.40	7.00×10^{-3}	2.00×10^{-2}	1.35×10^{-2}	7.93	75
628	97	99	3.40×10^{-2}	20.10	6.10×10^{-3}	1.90×10^{-2}	1.26×10^{-2}	7.40	50
648	47	96	2.13×10^{-2}	12.50	2.80×10^{-3}	1.60×10^{-2}	9.40×10^{-3}	5.52	25
Analysis of the polarization curves carried out in forward scan for Inconel 625 coating sample									
189	181	147	1.87×10^{-1}	94.00	5.10×10^{-2}	1.50×10^{-1}	1.10×10^{-1}	50.80	100
180	177	151	1.97×10^{-1}	99.10	4.90×10^{-2}	1.60×10^{-1}	1.04×10^{-1}	52.30	75
170	159	148	1.97×10^{-1}	99.10	3.90×10^{-2}	1.60×10^{-1}	9.95×10^{-1}	50.00	50
167	208	147	2.25×10^{-1}	113.00	4.60×10^{-2}	1.70×10^{-1}	1.08×10^{-1}	54.30	25
Analysis of the polarization curves carried out in forward scan for bulk Inconel 625 sample									
66000	66	94	2.57×10^{-4}	0.19	1.30E-04	2.10×10^{-4}	1.70×10^{-4}	0.13	100
88700	99	150	2.94×10^{-4}	0.22	1.40E-04	2.00×10^{-4}	1.70×10^{-4}	0.13	75
68000	87	225	4.50×10^{-4}	0.33	2.10E-04	3.50×10^{-4}	2.80×10^{-4}	0.21	50
80900	135	223	4.54×10^{-4}	0.34	2.60E-04	3.50×10^{-4}	3.05×10^{-4}	0.23	25
Analysis of the polarization curves carried out in reverse scan for stainless steel sample									
5110	83	121	4.21×10^{-3}	2.47	2.54×10^{-4}	3.10×10^{-4}	2.80×10^{-4}	0.16	100
2290	86	104	9.01×10^{-3}	5.29	2.60×10^{-4}	2.90×10^{-4}	2.70×10^{-4}	0.16	75
1790	91	99	1.16×10^{-2}	6.81	2.50×10^{-4}	2.40×10^{-4}	2.45×10^{-4}	0.14	50
1850	73	91	9.57×10^{-3}	5.62	9.30×10^{-4}	1.40×10^{-4}	1.16×10^{-4}	0.17	25
Analysis of the polarization curves carried out in reverse scan for Inconel 625 coating									
165	173	119	1.86×10^{-1}	93.50	6.40×10^{-2}	6.40×10^{-2}	6.40×10^{-2}	32.20	100
156	168	114	1.90×10^{-1}	95.60	6.10×10^{-2}	6.20×10^{-2}	6.15×10^{-2}	30.90	75
151	177	109	1.95×10^{-1}	98.10	6.30×10^{-2}	5.90×10^{-2}	6.10×10^{-2}	30.70	50
153	212	139	2.39×10^{-1}	120.00	8.30×10^{-2}	7.80×10^{-2}	8.05×10^{-4}	40.50	25
Analysis of the polarization curves carried out in reverse scan for bulk Inconel 625									
75700	186	261	6.26×10^{-4}	0.46	3.90×10^{-4}	5.10×10^{-4}	4.50×10^{-4}	0.33	100
71700	228	237	7.06×10^{-4}	0.52	4.70×10^{-4}	5.00×10^{-4}	4.85×10^{-4}	0.36	75
79100	217	231	6.16×10^{-4}	0.46	4.30×10^{-4}	4.20×10^{-4}	4.25×10^{-4}	0.31	50
77900	231	168	5.45×10^{-4}	0.40	3.90×10^{-4}	3.10×10^{-4}	3.15×10^{-4}	0.36	25

5.5 ET rate constant from polarization curves data

Polarization curves at a scan rate of 20 mV min^{-1} shown in ***section 5.3.4*** were used to extract the kinetic data for heterogeneous ET rate constant reaction for bulk Inconel 625, Inconel 625 coating, CoNiCrAlY coating and WCCoCr coating. The potential axis of the polarization curves were converted into overpotential ($E_{applied}$ - E_{oc}). The straight line portion of the anodic and cathodic side of the polarization curves were extrapolated to zero overpotential for anodic and cathodic slops (b_a, b_c in mV units) and i_{corr}. The Tafel slopes were used to calculate the Stern Geary constant in ***equation 5.3*** [119, 249].

$$\boldsymbol{R_p = \frac{B}{i_{corr}}} \qquad \textbf{5.3}$$

$$\boldsymbol{B = \frac{b_a \times b_c}{2.303(b_a + b_c)}} \qquad \textbf{5.4}$$

Polarization resistance was calculated from the correlation between Stern Geary constant and corrosion current given in ***equation 5.3***. The polarization resistance was later used in ***equation 5.4*** to calculate the exchange current density i_0 in A cm2 [250, 251]:

$$\boldsymbol{i_0 = RT/nFR_p} \qquad \textbf{5.5}$$

Where *R* is gas constant in J/mol *K*, T is absolute temperature in *K*, *n* is no or electrons involved, *F* is faraday constant which is 96500 C/mol and R_p is polarization resistance in Ω cm^2**.** The value of i_0 was used in ***equation 5.6*** to calculate the ET rate constant across electrode electrolyte interface [252]. The

k_{ET} is heterogeneous ET rate constant in cm s^{-1} and C is the bulk concentration in mol cm^{-3}. The ET rate constants calculated for different materials are summarized in ***Table*** 5-12**.**

$$k_{ET} = i_0/nFC \qquad \textbf{5.6}$$

The kinetics of ET rate constant gives the basic idea how fast or slow a particular reaction is taking place at the surface. The potentiodynamic polarization results are related with overall surface response of the applied potential and a number of different reactions take place during the potential scan. The rate constant also included the errors due to charging current and ohmic drop. The rate constant for the CoNiCrAlY coating was somewhat higher than Inconel 625 coating. The ET rate constant was a factor of 10 lower than the WCCoCr coating. The higher reaction rate constant at the WCCoCr coating is attributed to greater microstructural heterogeneity which did not allow the surface to passivate as for the bulk Inconel 625.

Table 5-12: ET rate constant extracted from potentiodynamic polarization data

Data extracted from polarization curves for calculating k^0				
Material	*b_a / mV*	*b_c / mV*	*i_{corr} / mA cm^{-2}*	*B*
Wrought Inconel	4.15×10^{1}	1.05×10^{2}	1.60×10^{-4}	1.29×10^{1}
Inconel coat	1.98×10^{2}	1.45×10^{2}	2.17×10^{-2}	3.64×10^{1}
CoNiCrAlY coat	8.23×10^{1}	1.98×10^{2}	9.33×10^{-3}	2.52×10^{1}
WCCoCr coat	3.81×10^{2}	9.33×10^{1}	1.13×10^{-1}	3.25×10^{1}
The R_p used to calculate i_0 and later k^0 calculated from i_0				
Material	*B*	*R_P / Ω cm^2*	*i_0 / A cm^{-2}*	*k^0 / cm s^{-1}*
Wrought Inconel	1.29×10^{1}	8.08×10^{4}	3.18×10^{-7}	6.59×10^{-12}
Inconel coat	3.64×10^{1}	1.68×10^{3}	1.53×10^{-5}	3.17×10^{-10}
CoNiCrAlY coat	2.52×10^{1}	2.71×10^{3}	9.49×10^{-6}	1.97×10^{-10}
WCCoCr coat	3.25×10^{1}	2.88×10^{2}	8.92×10^{-5}	1.85×10^{-9}

5.6 Localized corrosion testing by reactivation

The localized corrosion by Cr-depletion, i.e. sensitisation, is largely reported in different grades of stainless steels and some other Ni-Cr alloys when processed under fast heating and coaling cycles [53, 253]. The HVOF coating process is a high temperature process where difference of Cr-content arises between re-solidified regions and non melted regions of the coatings due to flight oxidation. The presence of chromium depleted regions can be studied by reactivation method [254]. The test solution for reactivation study consists of 0.5 M H_2SO_4 + 50 ppm of KSCN. The low concentrations of KSCN function as activator and de-passivate the Cr-depleted region on reverse potential scan [63, 122, 123].

From reactivation curves of different materials in ***Figure 5-26***, only HVOF Inconel 625 alloy show the defined forward and reverse current peak indicating some of the region may be depleted in Cr due to high temperature process of HVOF coating. The reactivation curve identifies the presence of Cr-depleted regions by degree of sensitization. The degree of sensitization (DOS) can be defined by the ratio of forward current peak and reverse current peak ($j_{forward}$ / $j_{reverse}$). The greater the ratio the greater will be degree of sensitization. The EDS analysis in the earlier section also shows that regions of different composition exist in the coatings.

The polarization curve for stainless steel does not show any peak on forward scan but show the two cathodic peaks on reverse scan, 1st at 250 mV and 2nd around 150 mV. The first peak is related with reactivation of martensite (a

metastable phase present in stainless steel) and second with the grain boundary reactivation due to galvanic effect [255]. The double peak response on reverse scan is also reported for duplex stainless steel (Cr-Ni-Mo steels) where first peak corresponds to martensite and second one with Ni-rich phases [256]. The higher % of carbon phase may be martensite which was reactivating in the reverse scan. The cathodic peak shifts at higher positive potential on reverse scan for bulk Inconel, probably due to formation of uniform passive layer which shifts the corrosion potential to more positive [63].

The WCCoCr curves show passivation around the Cr-oxidation detection peak. The reactivation curves for CoNiCrAlY show a peak on forward scan at around -100 mV, probably due to Al oxidation and a slight reactivation peak in the reverse peak can be seen around 100 mV. The bulk Inconel micrograph shows only few spots with minor attack. The noisy reactivation curve of stainless steel and bulk Inconel 625 sample as compared to coating sample was due to a more varied susceptibility to localised attack. This gives slight bursts of current, in coating the only defective area was chromium depleted one which show a defined peak in polarization curve.

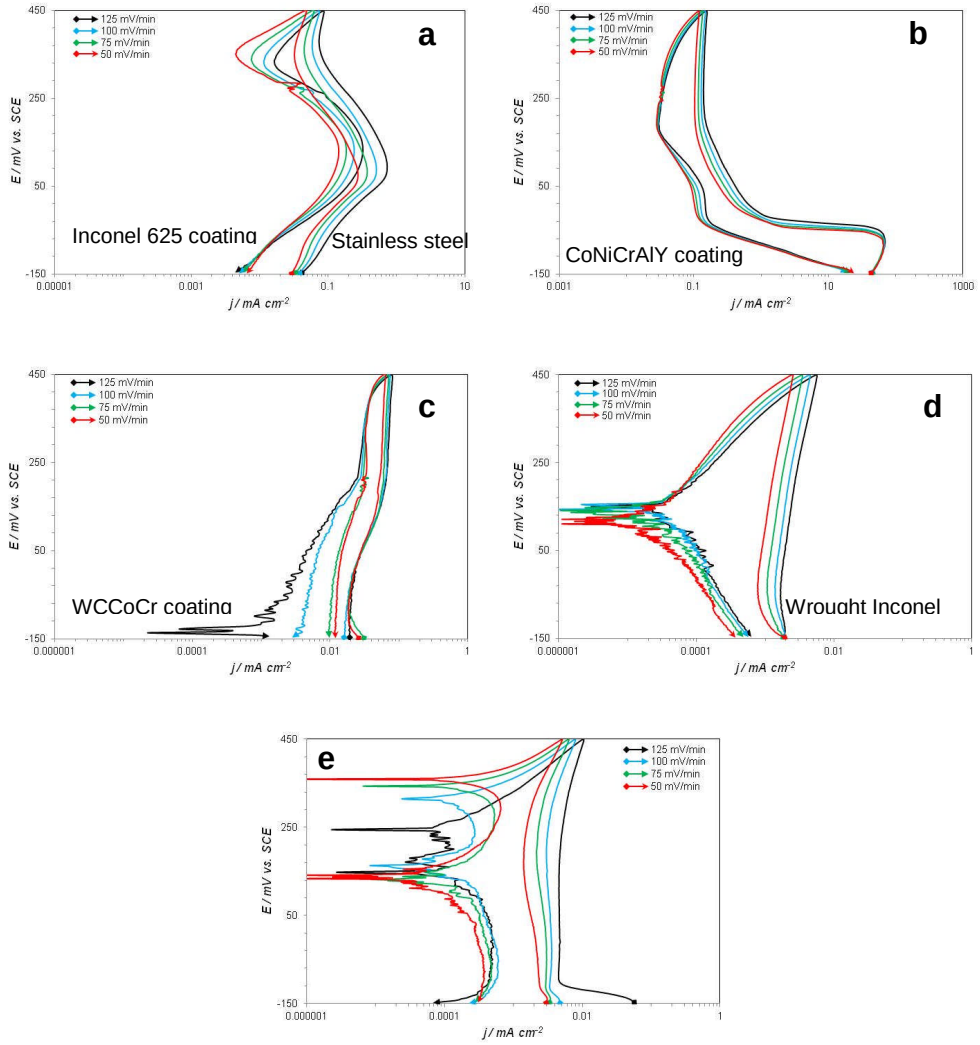

Figure 5-26: The reactivation curves for different coatings in 0.5 M H_2SO_4 containing 50 ppm of KSCN. The potential was swept from -150 mV to 450 mV at a scan rate of 50, 75, 100 and 125 mV min^{-1} on the same sample. a) Inconel 625 coating, b) CoNiCrAlY coating, c) WCCoCr coating, d) bulk Inconel 625, e)stainless steel

The corrosion attack at Cr-depleted regions was further explored by performing reactivation curves at different scan rates shown in ***Figure 5-26.*** The reverse peak potential for Inconel 625 coating sample occurs at same potential and forward potential peak shift to slightly more negative which indicates that the surface became more active after the first scan. The forward and reverse peak currents increase with the scan rate but the degree of sensitization [123, 125] is not significantly affected by the scan rate [109].

Table 5-13: Results extracted from reactivation curves of different materials

Material	υ mV min^{-1}	$E_{passivation}$ mV	j_{pass} / mA cm^{-2}	$j_{forward}$ / mA cm^{-2}	$j_{reverse}$ / mA cm^{-2}	DOS $j_{reverse}/j_{forward}$
Stainless steel	125	-96	7.7×10^{-3}	-	-	-
	100	-110	5.5×10^{-3}	-	-	-
	75	-119	4.9×10^{-3}	-	-	-
	50	-115	4.0×10^{-3}	-	-	-
Inconel 625	125	-50	1.8×10^{-3}	-	-	-
	100	-35	1.5×10^{-3}	-	-	
	75	-30	1.1×10^{-3}	-	-	-
	50	-30	0.8×10^{-3}	-	-	-
Inconel 625 coating	125	362	90.0×10^{-3}	1470.0	650.0	0.4
	100	370	70.0×10^{-3}	1010.0	480.0	0.5
	75	377	15.0×10^{-3}	750.0	360.0	0.5
	50	387	12.0×10^{-3}	550.0	280.0	0.5
CoNiCrAlY coating	125	204	178.0×10^{-3}	-	-	-
	100	220	141.0×10^{-3}	-	-	-
	75	223	129.0×10^{-3}	-	-	-
	50	218	118.0×10^{-3}	-	-	-
WCCoCr coating	125	189	80.0×10^{-3}	-	-	-
	100	216	74.0×10^{-3}	-	-	-
	75	220	62.0×10^{-3}	-	-	
	50	234	62.0×10^{-3}	-	-	-
DOS: Degree of sensitization						

No attack is evident from the micrographs of the bulk Inconel 625 alloy ***Figure 5-27***e, the coating microstructures in ***Figure 5-27***a shows attack around the particle and splat boundaries. The EDS analysis show that chemical composition of the coating varies in different regions especially in the splat boundaries. The stainless steel microstructure in ***Figure 5-27***b shows the corrosion attack around the grain. The WCCoCr coating micrograph in ***Figure 5-27***d corrosion is localized on defects and majority of the surface do not show any major corrosion attack. After reactivation test the CoNiCrAlY sample surface become black. The slight polishing the surface in ***Figure 5-27***c show

the black partially unmelted particles in the microstructure, this indicates that corrosion attack is spread all over the surface for the CoNiCrAlY coating.

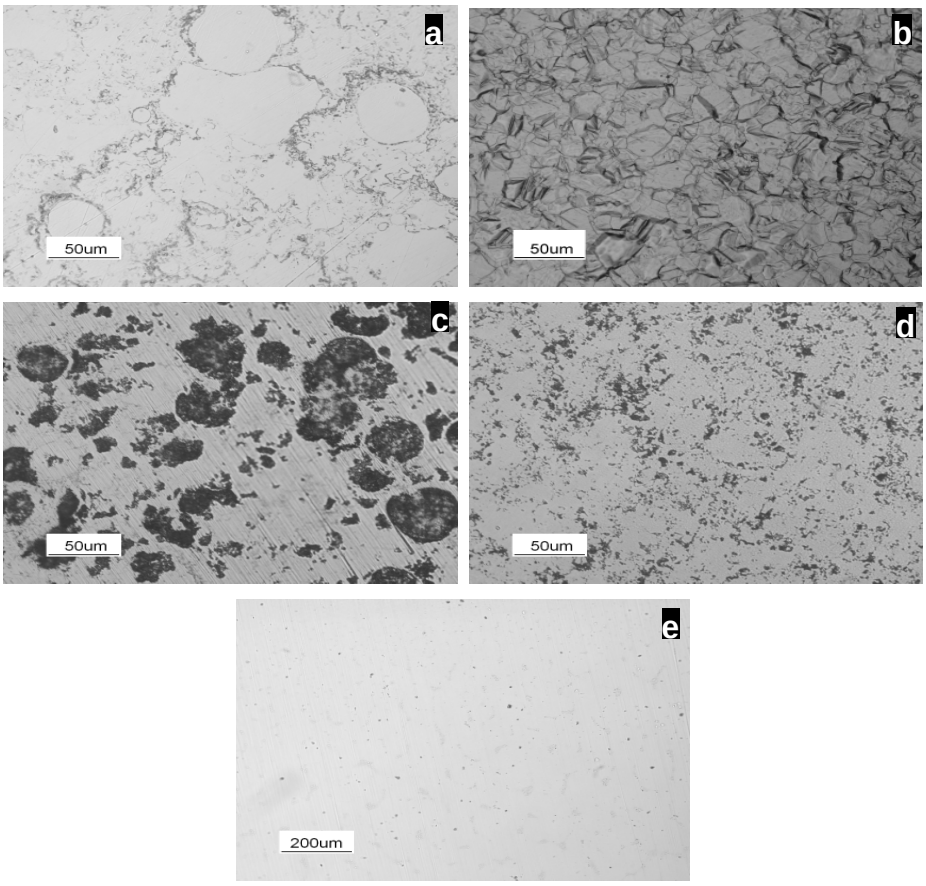

Figure 5-27: Microstructure of different materials after reactivation test. a) Inconel 625 coating, b) Stainless steel, c) CoNiCrAlY coating, e). Bulk Inconel 625 alloy

5.7 X-ray photoelectron spectroscopy results

Figure 5-28 to ***Figure 5-48*** show the XPS results for Inconel 625 coating, CoNiCrAlY coating, WCCoCr coating, bulk Inconel 625 and stainless steel. One sample of each material was kept in air for 24 hours to correlate the results with polarized samples. Each sample of different materials was polarized to different potential one by one (100, 200, 500, 1000 mV vs. E_{oc}) in 0.5M H_2SO_4 for five min. Samples were rinsed washed and dried before inserting into XPS high vacuum chamber. All samples were grinded and polished for each next set

of polarization. The polarization of the samples to 100, 200, 500, 1000 mV potentials were carried out to correlate how the type and amount of oxides change with potential increment. The significant changes in the XP spectrum were seen for the samples polarized to 100 mV and 1000 mV. Both photoelectron and auger peaks were labelled in survey spectrum. The main photoelectron peaks were further analysed by high resolution spectrum. The charge correction for all survey and high resolution spectra was carried with respect to the C 1s peak at 285 eV.

5.7.1 XPS of Inconel 625 coating

Figure 5-28a, b and c show the XPS survey for Inconel 625 after air exposure for 24 hours and polarized to 100, 1000 mV. The elements present at the surface were quantified by using photoelectron peaks of O 1s, Ni2p, Cr2p and Mo3d and represented in atomic percent (At %). The peak position of O 1s, Ni2p, Cr2p and Mo3d were 530, 852, 576 and 230 eV which were consistent with the previous work on Inconel 625 coating [8] and XPS data base [187]. The surface oxidation of a material is greatly dependent on constituents of the material and environment in which material is exposed.

The survey spectrum of the 24 hours air exposed sample shows 76% oxygen indicating presence of surface oxide. The oxidation of the surface was increased by polarizing samples to higher potentials. The high resolution spectrum of the main photoelectron peaks shows that different elements in the materials were oxidized to different extents. There was no metallic Nb remaining in the sampled volume indicating all Nb at the surface was oxidized. There may be Nb present in the depth of the sample beyond the XPS sampled

volume, generally accepted as 10nm or 20 atomic layers [257]. The oxides of Nb were identified as NbO and Nb_2O_5. This indicates the Nb can oxidize to Nb^{2+} and Nb^{5+} in air. The increment of Nb_2O_5 at higher potential also shows that oxidation was more extensive at higher potentials, i.e. there was a higher proportion of Nb in the Nb^{5+} state.

The majority of the Mo present was also found in oxide form. The oxidation of the Mo also increases with increasing the polarization potential. The main oxides peaks of the Mo were MoO_2 and MoO_3. The Nickel was found in both elemental and oxide form. The main oxide of the Ni was NiO [257] and its percentage did not significantly change when coating sample was polarized to 100, 200 and 500 mV. The peak area ratio of elemental to oxide was approximately same for air formed layer and the one polarized at 100, 200 mV. This was probably due to slow oxidation rate of the Ni element at lower positive potential as compared to Nb, Mo and Cr present in the alloy. The high resolution spectrum of Ni2p after polarization at 1000 mV shows that the elemental Ni was decreased to 10%, hence it can be established the extensive oxidation of Ni in Inconel 625 coating only occurs at higher potentials. At 1000 mV, two NiO-satellite peaks associated with $Ni2p_{1/2}$ and $Ni2p_{3/2}$ were also found which increase the overall Ni-oxide amount at the surface. The satellite peak appears in XPS of transitions metal when non-monochromatic x-ray was used. The non monochromatic X-ray causes the minor resonance lines to appear in the XPS spectra. The results of the peak fitting for Cr2p shows that more than 80% of Cr in the surface gets oxidized in air and forms Cr_2O_3. The Cr_2O_3 is considered the main oxide responsible for forming a protective

layer on Inconel 625 [200, 258]. The peak area of the Cr-oxides increases and elemental-Cr decreases with high potential polarizations [259].

Table 5-14: XPS survey and high resolution results of Inconel 625 coating

XP survey spectrum results after different constant potential polarizations for 5 min						
Constituent	Binding energy (eV)	Air for 24 h % peak area	100 mV % peak area	200 mV % peak area	500 mV % peak area	1000 mV %peak area
O 1s	530.28	75.7	77.5	88.5	74.3	81.6
Ni 2p	852.35	11.9	7.5	0	5.8	7.2
Cr 2p	575.95	8	10.5	11.5	16	6.5
Mo 3d	230.18	4.4	4.5	0	3.9	4.7
Nb 3d	202.10	0	0	0	0	0
High resolution XP spectrum results of Cr 2p						
2p3/2 Cr	573.4	9.7	9.7	5.7	7.7	6.3
2p3/2Cr_2O_3	576.13	56	55.7	55	57.8	54.4
2p1/2 Cr	582.74	8.1	5.7	8.2	5.3	5.1
2p1/2Cr_2O_3	586.08	26.2	28.9	31.1	29.2	34.2
High resolution XP spectrum results of Ni 2p						
2p3/2 Ni	852.12	35.5	38.8	42.5	45.4	27.9
2p3/2 NiO	854.96	36.3	27.7	34.3	25.2	36
2p1/2 Ni	869.26	19.1	17.4	17.4	25	16.6
2p1/2 NiO	873.08	9.1	16.1	5.9	4.5	7.7
2p3/2NiOsat	860.76	-	-	-	-	7.2
2p1/2$(NiO)_X$	875.53	-	-	-	-	4.6
High resolution XP spectrum results of Mo 3d						
3d5/2 Mo	227.46	33.6	25	15.6	15.8	18.6
3d5/2MoO_2	232.93	3.9	12.9	6	2.6	60.9
3d3/2 MoO_2	230.71	55.7	38.9	64.9	60.4	
3d3/2MoO_2	234.67	4.5	21.5	8.8	12.6	20.4
3d3/2MoO_3	235.67	2.4	1.7	4.7	8.6	
High resolution XP spectrum results of Nb 3d						
3d5/2 Nb	202.10	-	-	-	-	-
3d5/2 NbO	202.70	18.2	8.8	12.8	10.5	
3d3/2 NbO	206.18	59	65.1	63.7	63.7	58.9
3d3/2Nb_2O_5	209.29	22.8	26.1	23.4	25.8	41.1

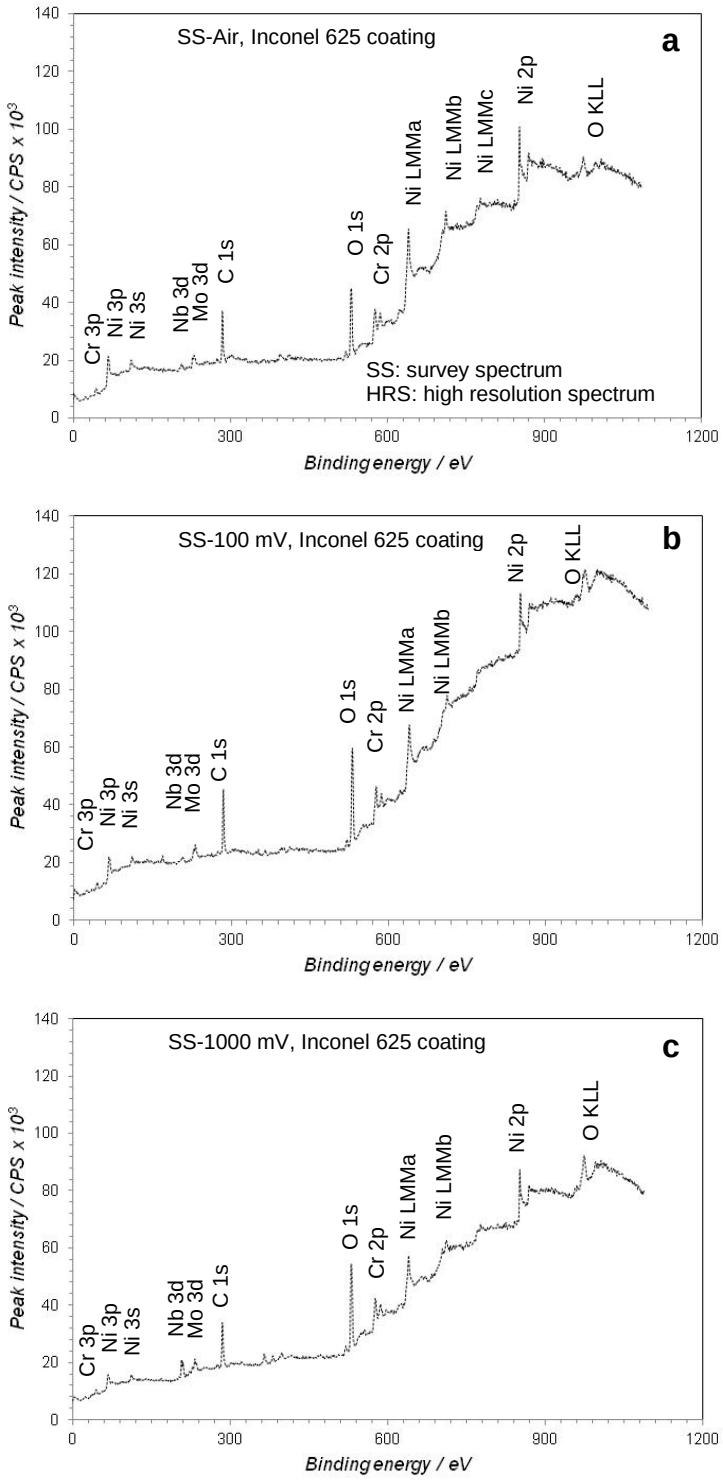

Figure 5-28: XP survey spectrum at polished 1 cm^{2}Inconel 625 coating samples, a) after air exposure for 24 hours, b) after polarizing the sample to 100 mV vs. E_{oc}, c) after polarizing the sample to 1000mV vs. E_{oc}. Samples were stabilized in 0.5M H_2SO_4 before polarization to different constant potentials for 5 minutes. After polarization samples were washed with de-ionized water and dried before inserting in XPS vacuum chamber for scan.

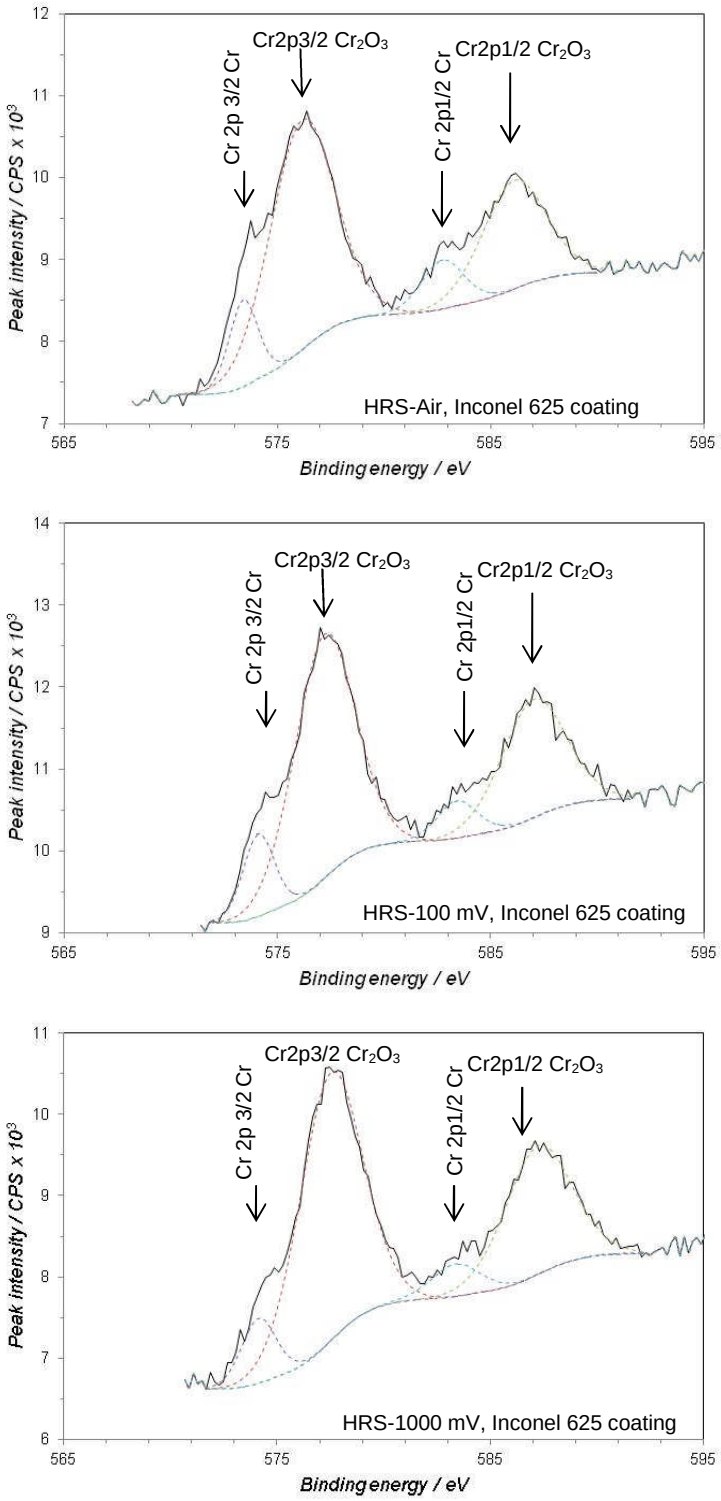

Figure 5-29: XP high resolution spectrum of Cr2p at polished 1 cm^{2}Inconel 625 coating samples, a) after air exposure for 24 hours, b) after polarizing the sample to 100 mV vs. E_{oc}, c) after polarizing the sample to 1000mV vs. E_{oc}. Samples were stabilized in 0.5M H_2SO_4 before polarization to different constant potentials for 5 minutes. After polarization samples were washed with de-ionized water and dried before inserting in XPS vacuum chamber for scan.

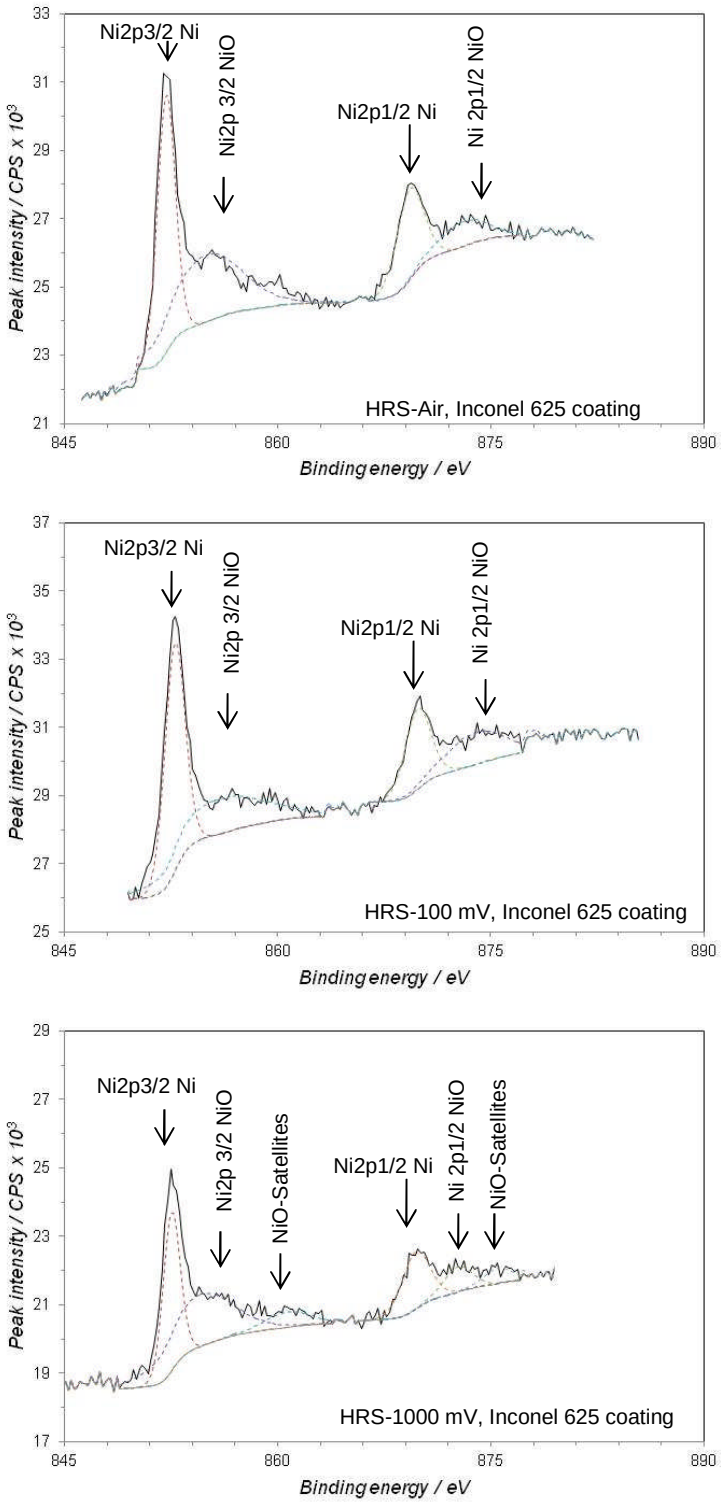

Figure 5-30: XP high resolution spectrum of Ni2p at polished 1 cm^{2}Inconel 625 coating samples, a) after air exposure for 24 hours, b) after polarizing the sample to 100 mV vs. E_{oc}, c) after polarizing the sample to 1000mV vs. E_{oc}. Samples were stabilized in 0.5M H_2SO_4 before polarization to different constant potentials for 5 minutes. After polarization samples were washed with de-ionized water and dried before inserting in XPS vacuum chamber for scan.

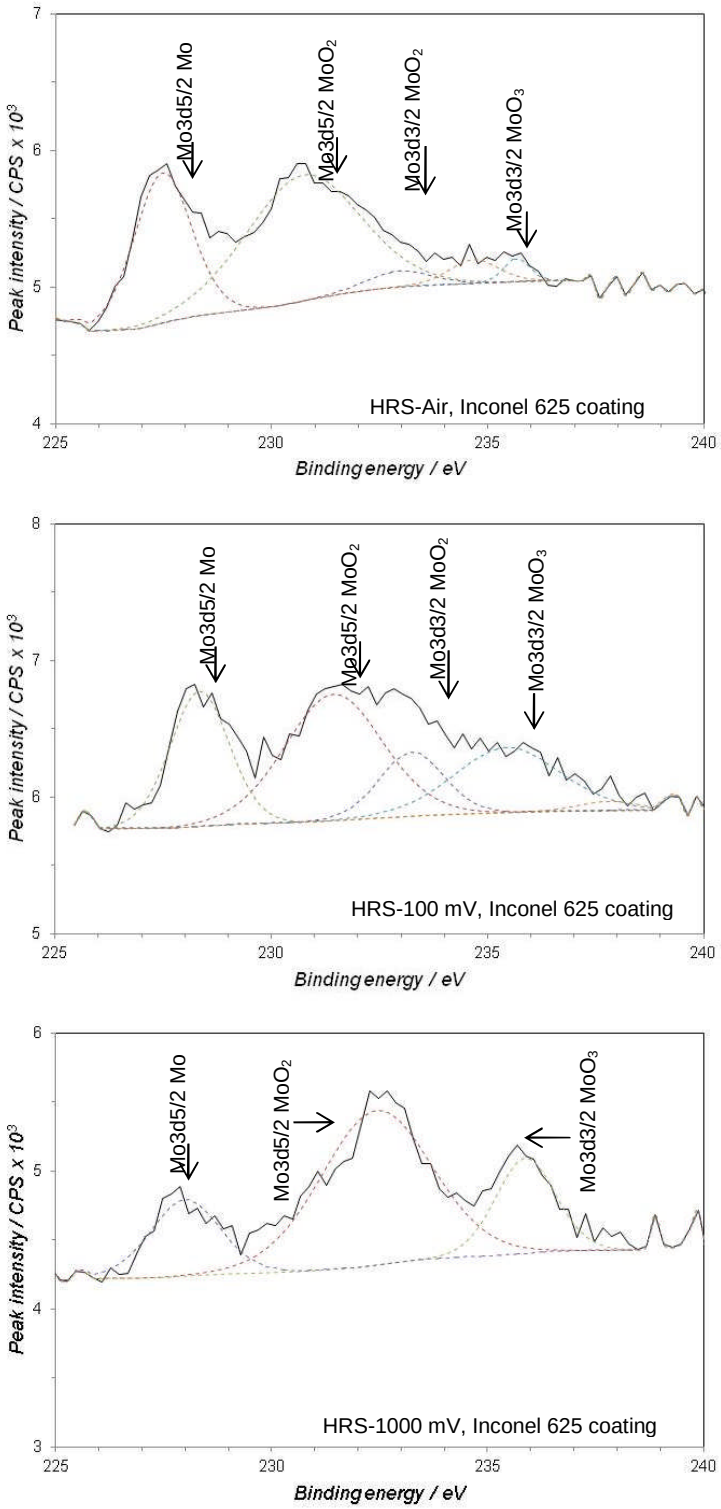

Figure 5-31: XP high resolution spectrum of Mo3d at polished 1 cm^{2}Inconel 625 coating samples, a) after air exposure for 24 hours, b) after polarizing the sample to 100 mV vs. E_{oc}, c) after polarizing the sample to 1000mV vs. E_{oc}. Samples were stabilized in 0.5M H_2SO_4 before polarization to different constant potentials for 5 minutes. After polarization samples were washed with de-ionized water and dried before inserting in XPS vacuum chamber for scan.

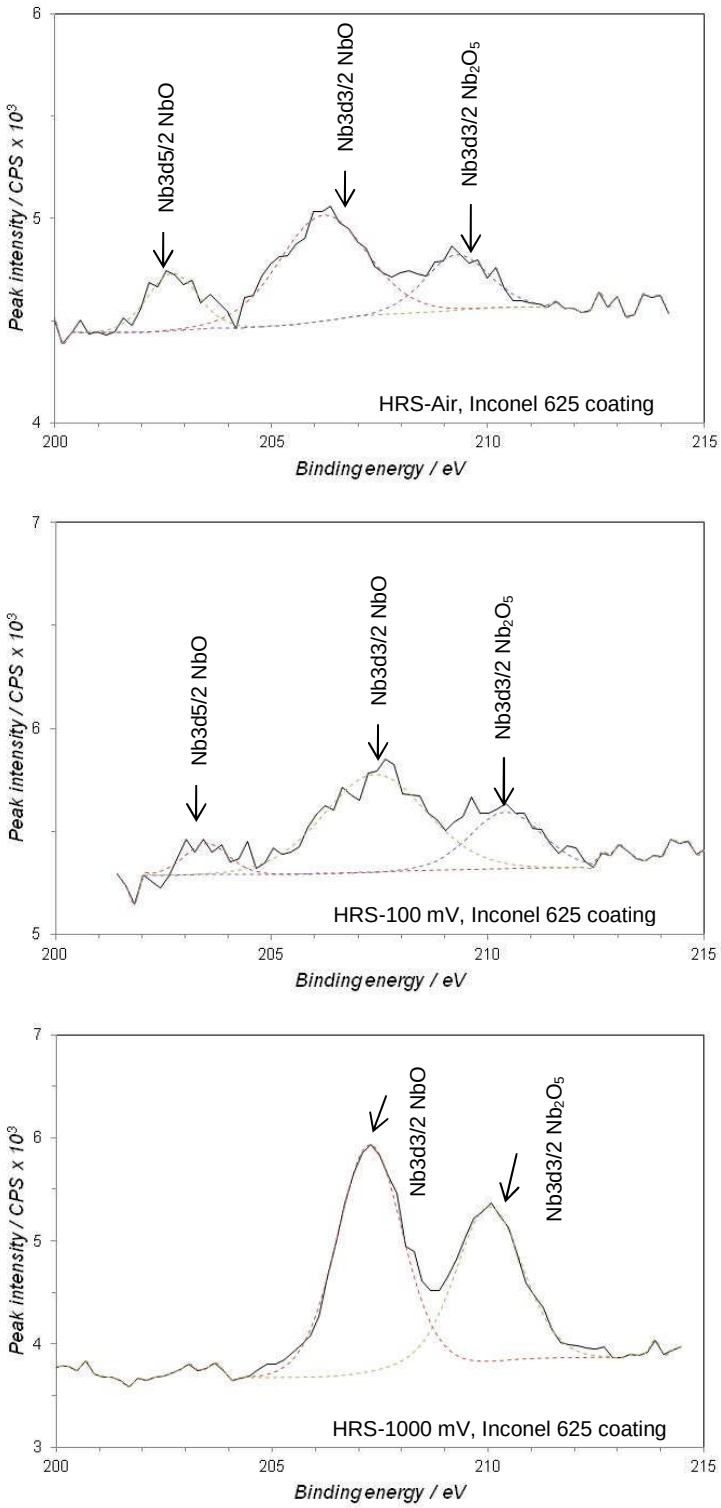

Figure 5-32: XP high resolution spectrum of Nb3d at polished 1 cm^{2}Inconel 625 coating samples, a) after air exposure for 24 hours, b) after polarizing the sample to 100 mV vs. E_{oc}, c) after polarizing the sample to 1000mV vs. E_{oc}. Samples were stabilized in 0.5M H_2SO_4 before polarization to different constant potentials for 5 minutes. After polarization samples were washed with de-ionized water and dried before inserting in XPS vacuum chamber for scan.

5.7.2 XPS of CoNiCrAlY coating

The quantification of the surface elements was carried out from the photoelectron peaks of O 1s, Ni 2p and Co 2p and Al 2s. The peak position of O 1s, Ni 2p, Co 2p and Al 2s were 531, 853, 778 and 120 eV were consistent with NIST XPS data base [187]. The % of the peak area for O 1s, Ni 2p, and Co 2p and, Al 2s was 71, 3.5, 8.1 and 11 % when sample was exposed in air for 24 hours. The amount of O 1s changes from 83 to 76% when polarized from 100 mV to 1000 mV. The % peak area for Ni 2p, Co2p and Al 2s also changes with polarization.

The high resolution spectrum Ni 2p doublet consists of both elemental and oxide peak of Ni $2p_{3/2}$ and Ni $2p_{1/2}$. The peak positions were 852, 855 eV for Ni $2p_{3/2}$ elemental-Ni and NiO-oxide and 869, 872 eV for Ni $2p_{1/2}$ elemental-Ni and NiO-oxide peaks. The NiO-oxide satellite peak was also visible in the spectrum at 1000 mV polarization. The sample exposed in air shows 45% of elemental Ni and 55% NiO. The peak area for NiO changed to 16% for the sample polarized to 100 mV and 31% for the sample polarized to 1000 mV.

The high resolution peaks of Co 2p shows the amount of elemental Co decreased at higher potentiostatic polarization. The Co2p was further resolved into Co $2p_{3/2}$ and $Co2p_{1/2}$ peaks. The Co_2O_3 was identified as main oxide and the peak area was 27% for air exposed sample, 14% for 100 mV polarized and 22% for 1000 mV polarized samples. The elemental to oxide peak area was highest for the 100 mV polarized sample. Both elemental and oxide peak were identified from the Cr 2p. The peak position were identified as 574, 577 eV for Cr $2p_{3/2}$ elemental-Cr and Cr_2O_3 - oxide and 583, 587 eV for Cr $2p_{1/2}$

elemental-Cr and Cr_2O_3-oxide peaks. The elemental-Cr was 17 % for the sample exposed in air and changed to 4% when polarized to 100 mV. The elemental-Cr increased to 20% for the sample polarized to 1000 mV.

The oxidation of CoNiCrAlY in air starts with instantaneous formation of Al_2O_3, followed by oxidation of Al from beta phase [48, 49]. Once beta phase get fully oxidized the oxidation of Cr and Co occurred to form spinel oxide [114]. The formation of Al-oxide can be related to the Gibbs free energy of oxidation of the constituents present in the CoNiCrAlY coating i.e.-1690.46 kJ mol^{-1} for Al_2O_3, -1153.88 kJ mol^{-1} for Cr_2O_3, -251 kJ mol^{-1} for NiO and -254 kJ mol^{-1} for CaO [260]. The Gibbs free energy to form oxide was least for Al therefore Al will oxidize first before proceeding to oxidation of other elements of the coating.

The area under the curve for all metallic peaks decreased with the polarization. The lower height of the high resolution peaks of Ni 2p and Co 2p also indicates the oxidation of the elements increases with the potentiostatic polarization. The oxidation of the CoNiCrAlY was found to be a maximum at 100 mV which was the activation region polarization curves for the CoNiCrAlY coating. It is also possible that the driving force established due to preferential oxidation of some elements cause the vigorous oxidation of elements like Co and Ni at lower potential [50]. The high resolution peaks of the Co 2p and Ni 2p are highly distorted; it is possible some of the element quantification also include errors due to peak fittings. The errors in the energy position are 10% and intensities in high resolution spectra around 20% [261].

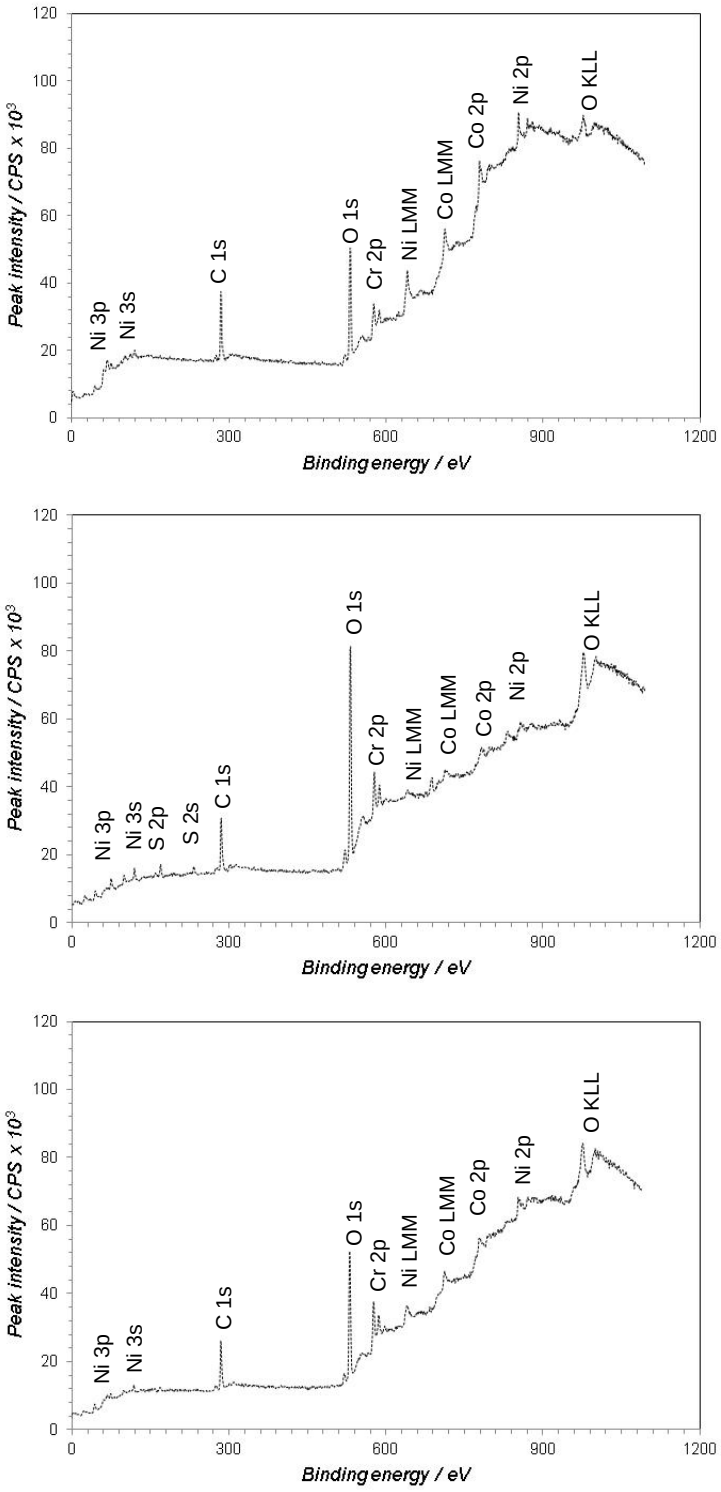

Figure 5-33: XP survey spectrum at polished 1 cm^2 CoNiCrAlY coating samples, a) after air exposure for 24 hours, b) after polarizing the sample to 100 mV vs. E_{oc}, c) after polarizing the sample to 1000mV vs. E_{oc}. Samples were stabilized in 0.5M H_2SO_4 before polarization to different constant potentials for 5 minutes. After polarization samples were washed with de-ionized water and dried before inserting in XPS vacuum chamber for scan.

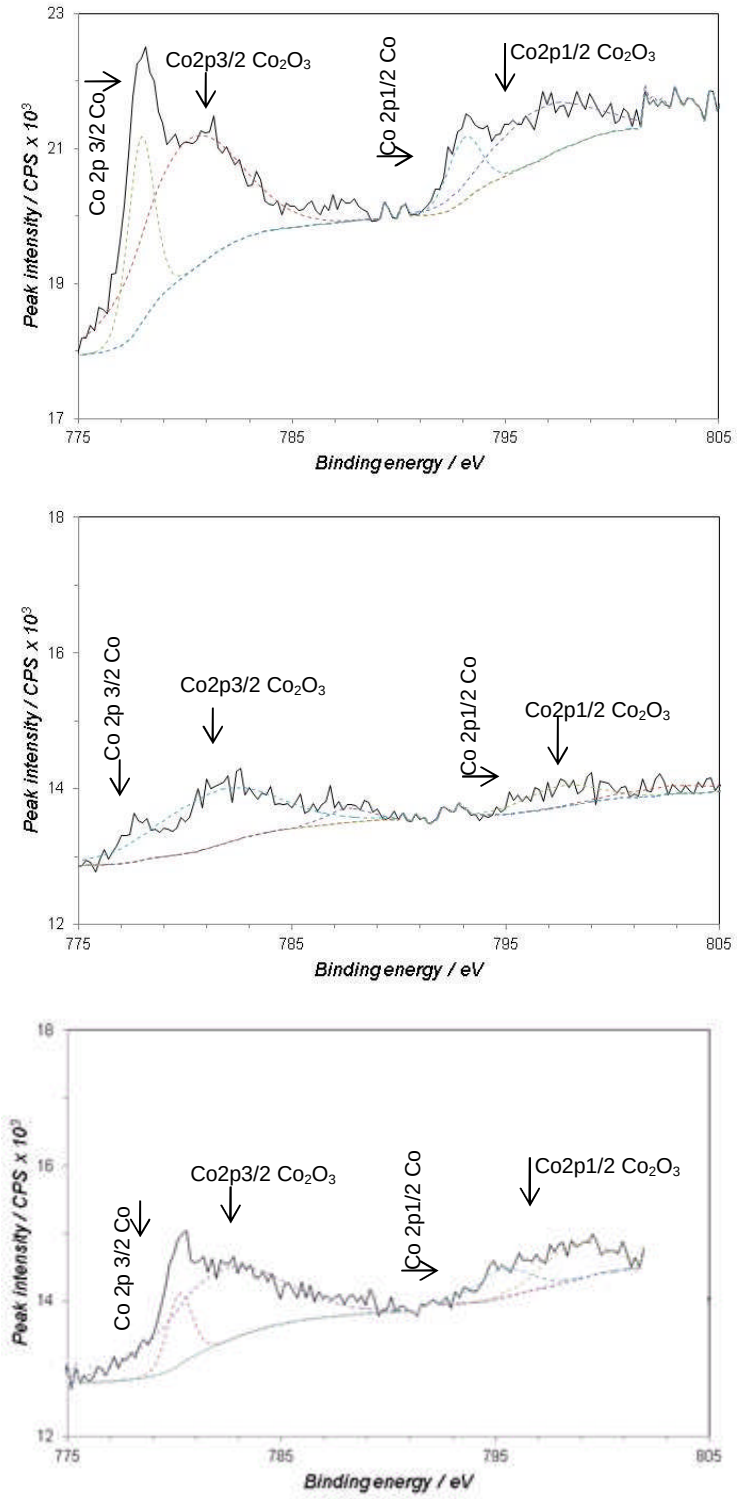

Figure 5-34: XP high resolution spectrum of Co2p at polished 1 cm^{2}CoNiCrAlY coating samples, a) after air exposure for 24 hours, b) after polarizing the sample to 100 mV vs. E_{oc}, c) after polarizing the sample to 1000mV vs. E_{oc}. Samples were stabilized in 0.5M H_2SO_4 before polarization to different constant potentials for 5 minutes. After polarization samples were washed with de-ionized water and dried before inserting in XPS vacuum chamber for scan.

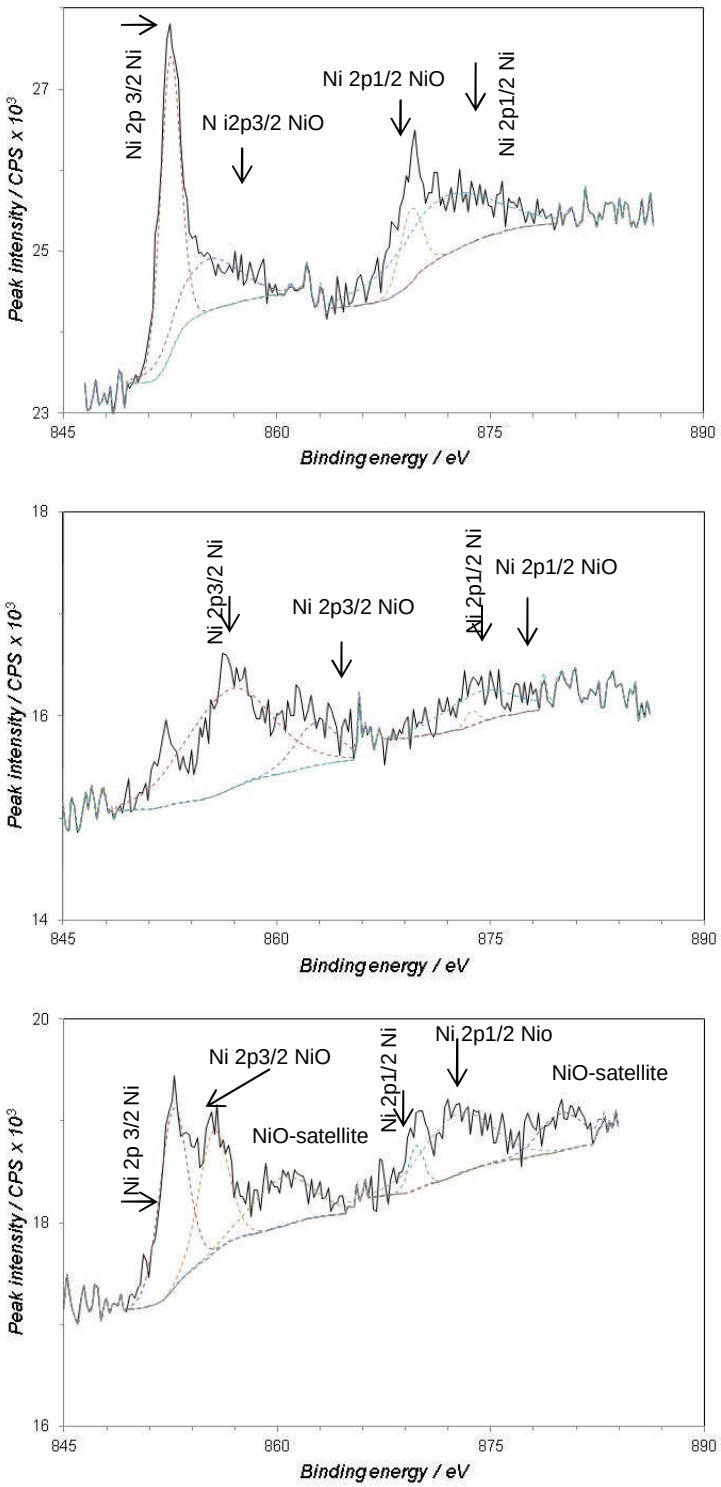

Figure 5-35: XP high resolution spectrum of Ni2p at polished 1 cm^{2}CoNiCrAlY coating samples, a) after air exposure for 24 hours, b) after polarizing the sample to 100 mV vs. E_{oc}, c) after polarizing the sample to 1000mV vs. E_{oc}. Samples were stabilized in 0.5M H_2SO_4 before polarization to different constant potentials for 5 minutes. After polarization samples were washed with de-ionized water and dried before inserting in XPS vacuum chamber for scan.

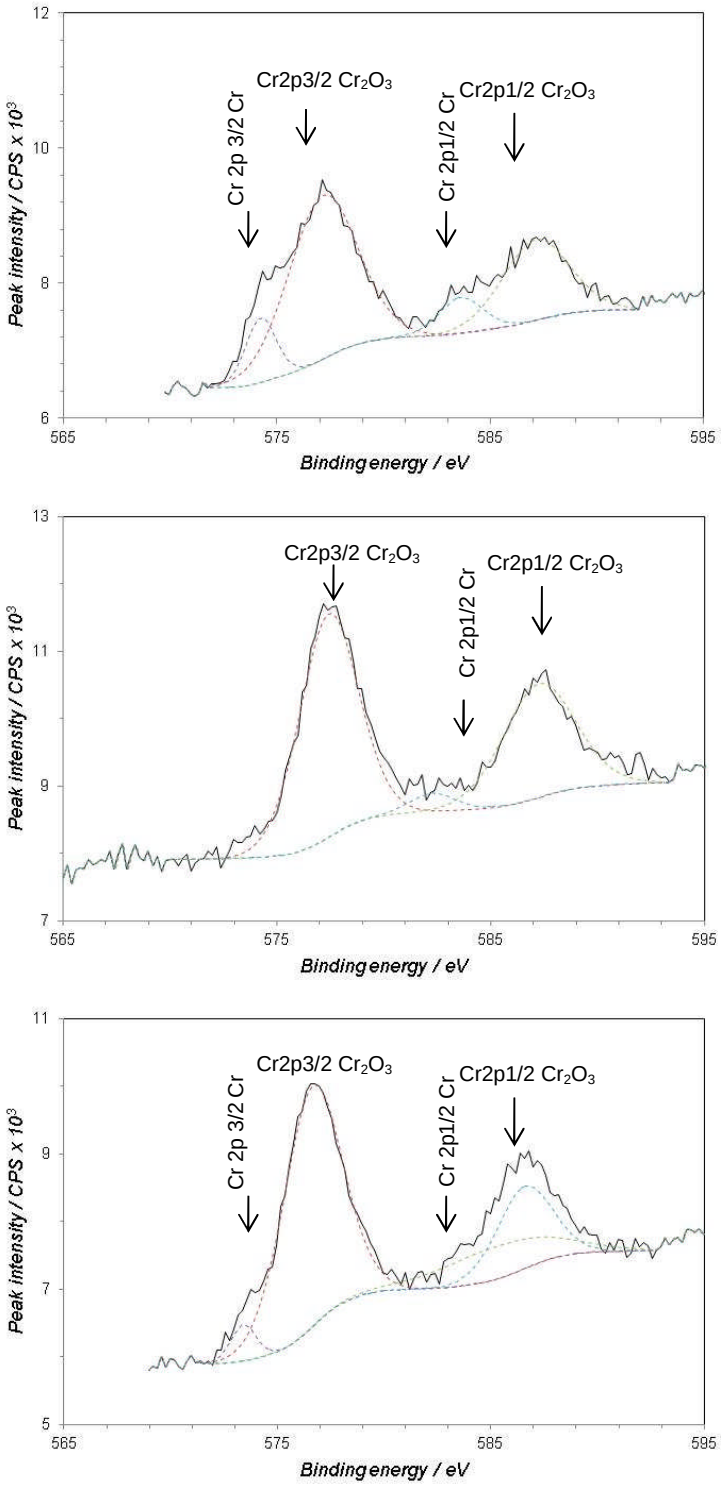

Figure 5-36: XP high resolution spectrum of Cr2p at polished 1 cm^{2}CoNiCrAlY coating samples, a) after air exposure for 24 hours, b) after polarizing the sample to 100 mV vs. E_{oc}, c) after polarizing the sample to 1000mV vs. E_{oc}. Samples were stabilized in 0.5M H_2SO_4 before polarization to different constant potentials for 5 minutes. After polarization samples were washed with de-ionized water and dried before inserting in XPS vacuum chamber for scan.

Table 5-15: XPS survey and high resolution results of CoNiCrAlY coating

XP survey spectrum results after different constant potential polarizations for 5 min						
Constituent	Binding energy (eV)	Air for 24 h % peak area	100 mV % peak area	200 mV % peak area	500 mV % peak area	1000 mV %peak area
O 1s	531.49	71.7	83.1	79.4	76.7	75.8
Ni 2p	853.49	3.5	0.4	2.1	3.1	0.2
Co 2p	778.49	8.1	2.1	3.6	3.8	2.8
Al 2s	120.49	11.4	9.9	8.1	11	8.1
High resolution XP spectrum results of Cr 2p						
2p3/2 Co	777.9	19.1	7.9	26.4	24.7	-
2p3/2Co_2O_3	780.07	52.5	69	34.7	46	-
2p1/2 Co	793.05	8	6.7	21.2	11.2	-
2p1/2Co_2O_3	796.6	20.3	16.5	17.8	18.1	-
High resolution XP spectrum results of Ni 2p						
2p3/2 Ni	852.48	35	14.2	30.2	31	27.7
2p 3/2 NiO	855.09	19.7	66.3	35.7	30.9	19.7
2p1/2 Ni	869.41	9.6	1.5	14.6	19.4	3.6
2p1/2 NiO	872.51	35.6	18	19.5	18.7	32.8
2p3/2NiOsat	860.33	-	-	-	-	16.3
High resolution XP spectrum results of Mo 3d						
2p3/2 Cr	574.25	9.7	-	6.8	10.6	3.9
2p3/2 Cr_2O_3	577.14	55.7	56.8	54.3	55.3	60.6
Cr 2p1/2 Cr	583.6	7.9	3.6	5.7	9.4	16
2p1/2 Cr_2O_3	587.1	26.7	35.5	33.2	24.7	19.5

5.7.3 XPS of WCCoCr cermet coating

The quantification of the surface elements in WCCoCr coating was carried out from the photoelectron peaks of O 1s, C 1s, W 4d and Co 2p. The peak position of O 1s, C 1s, W 4d and Co 2p were 531, 285, 243 and 778 eV, which were consistent with previous reported work [74, 262] and XPS data base [187]. The percentages of the peak area for O 1s, C 1s, W 4d and Co 2p was 29, 58, 7 and 5 % when sample was exposed in air for 24 hours. The amount of O 1s changes from 30 to 48% when polarized to 100 mV and 1000 mV constant potential for 5 min. The W 4d and W 4f peak were identified as WC peaks rather the W-elemental peaks. The % peak area of other elemental peaks also change with polarization to higher applied potentials.

The main oxide peaks were identified as WO_2 and W_3O_2 from the high resolution spectrum of W 4d. The peak positions were 244, 256 and 259 eV

for W $4d_{5/2}$ WC and W $4d_{5/2}$ WO_2. The constant potential polarization to 500 mV in 0.5M H_2SO_4 for 5 min did not change the oxide amount too much. The significant change in the passive oxide layer due to polarization at small potential for longer time in 3.5 % NaCl has been reported by some authors [263]. The area of the peaks labelled for W-oxide was 41% for air exposed, 40% for 100 mV and 95% for 1000 mV polarized sample. The main oxide peak was identified as WO_3. The high resolution peaks identified as 4f 5/2 WC, 4f 3/2 WC, 4f 7/2 WO_3 and 4f 5/2 WO_3 at 31, 34, 35 and 8 eV from high resolution spectrum of W 4d. The peak area of the oxide for air exposed sample was 35%, 32% for the sample polarized to 100 mV and 46 for the sample polarized to 1000 mV.

The WCCoCr coating was highly corrosion resistant in acidic environment hence the percentage of surface oxygen was less as compared to other materials. The amount of oxygen was less than 50% for all samples. The sample exposed in air for 24 hours shows the minimum amount of oxygen indicating the lower extent of oxidation. The amount of oxidation increases with higher potentiostatic polarization. The amount of carbon also reduces with polarization probably due to preferential oxidation of the WC-phase and leaving the carbon in solution [5, 227]. The peak shapes of the WCCoCr coatings also shows that shape was significantly changed due to higher potentiostatic polarization [5].

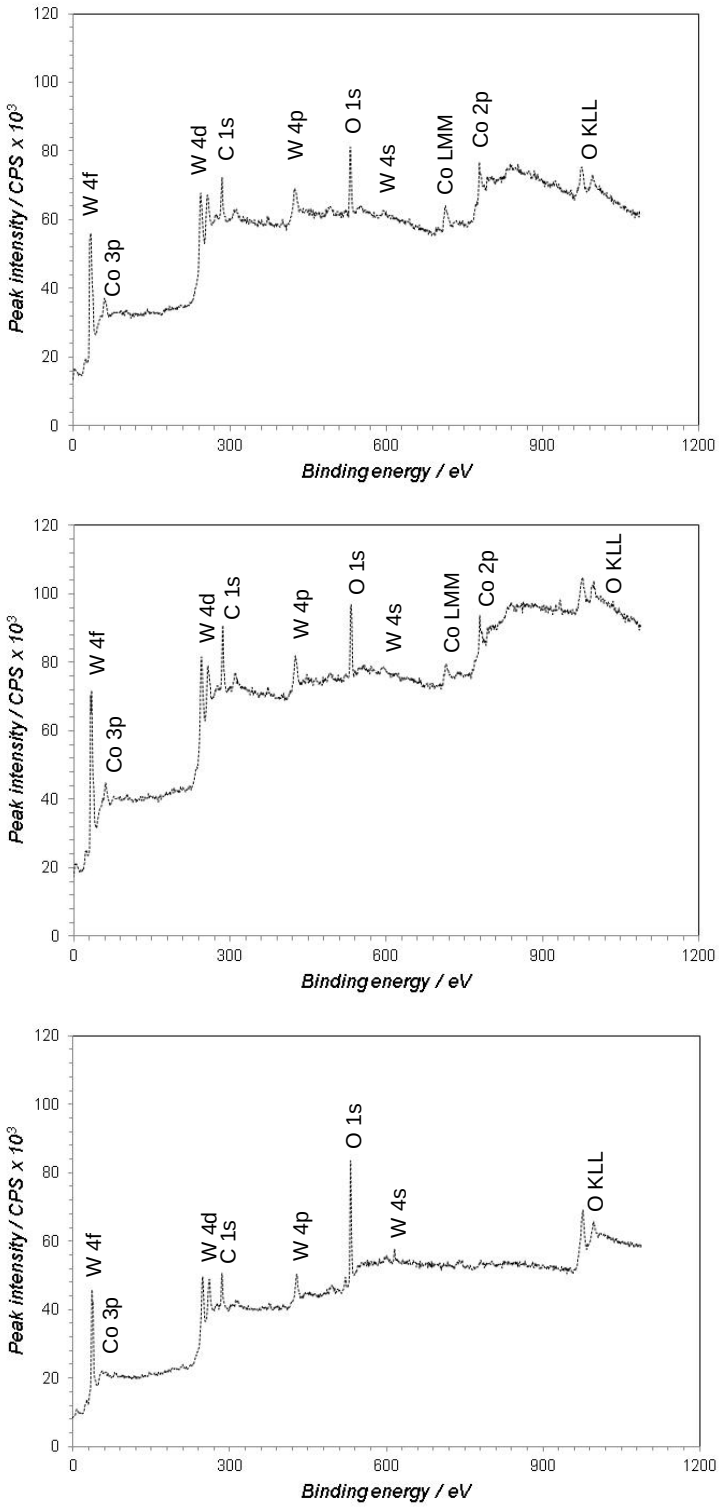

Figure 5-37: XP survey spectrum at polished 1 cm^2 WCCoCr coating samples, a) after air exposure for 24 hours, b) after polarizing the sample to 100 mV vs. E_{oc}, c) after polarizing the sample to 1000mV vs. E_{oc}. Samples were stabilized in 0.5M H_2SO_4 before polarization to different constant potentials for 5 minutes. After polarization samples were washed with de-ionized water and dried before inserting in XPS vacuum chamber for scan.

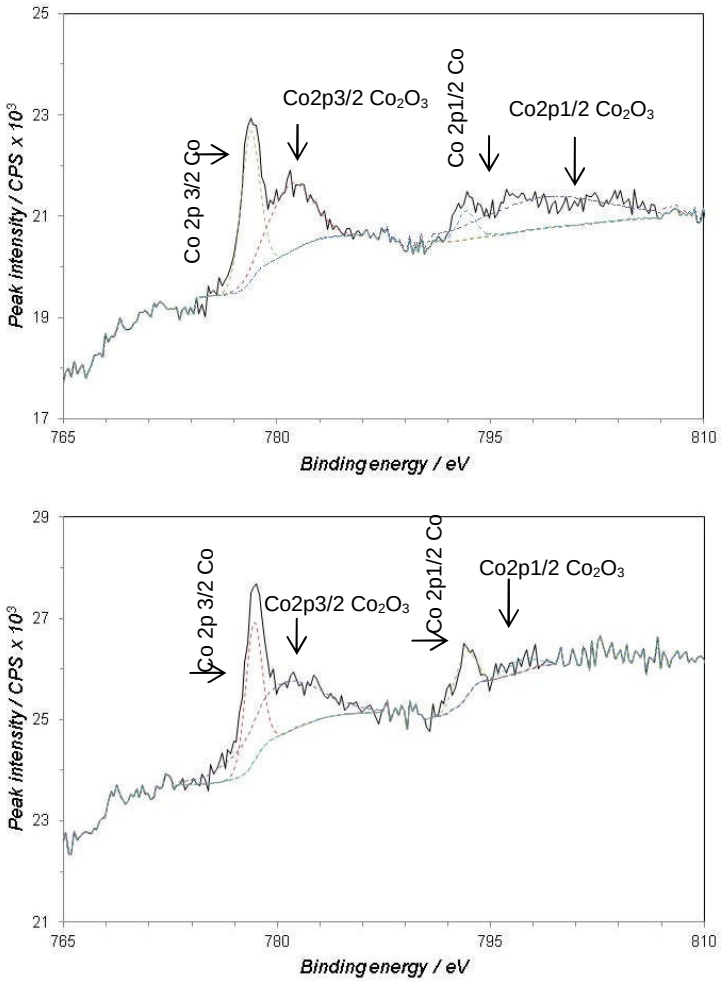

Figure 5-38: XP high resolution spectrum of Co2p at polished 1 cm^2 WCCoCr coating samples, a) after air exposure for 24 hours, b) after polarizing the sample to 100 mV vs. E_{oc}, c) after polarizing the sample to 1000mV vs. E_{oc}. Samples were stabilized in 0.5M H_2SO_4 before polarization to different constant potentials for 5 minutes. After polarization samples were washed with de-ionized water and dried before inserting in XPS vacuum chamber for scan.

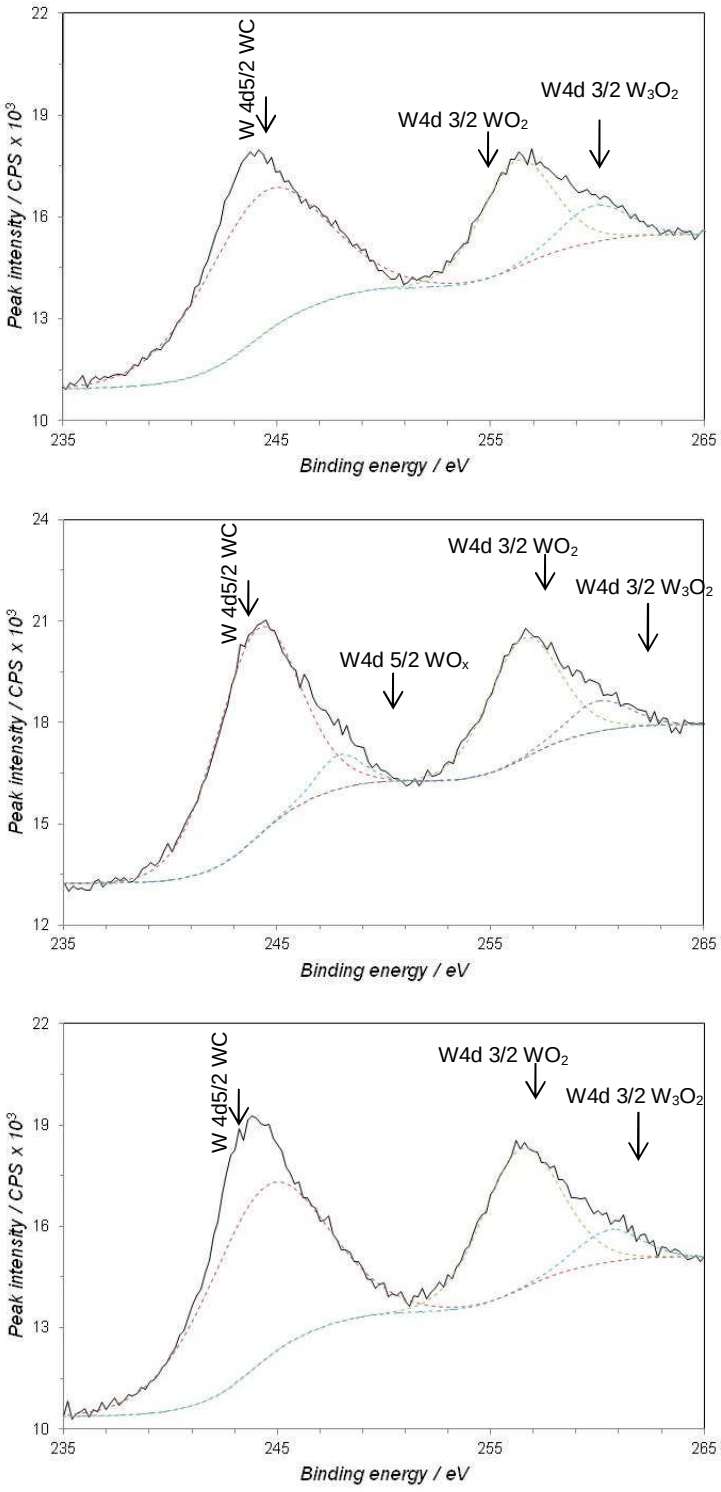

Figure 5-39: XP high resolution spectrum of W4d at polished 1 cm^2 WCCoCr coating samples, a) after air exposure for 24 hours, b) after polarizing the sample to 100 mV vs. E_{oc}, c) after polarizing the sample to 1000mV vs. E_{oc}. Samples were stabilized in 0.5M H_2SO_4 before polarization to different constant potentials for 5 minutes. After polarization samples were washed with de-ionized water and dried before inserting in XPS vacuum chamber for scan.

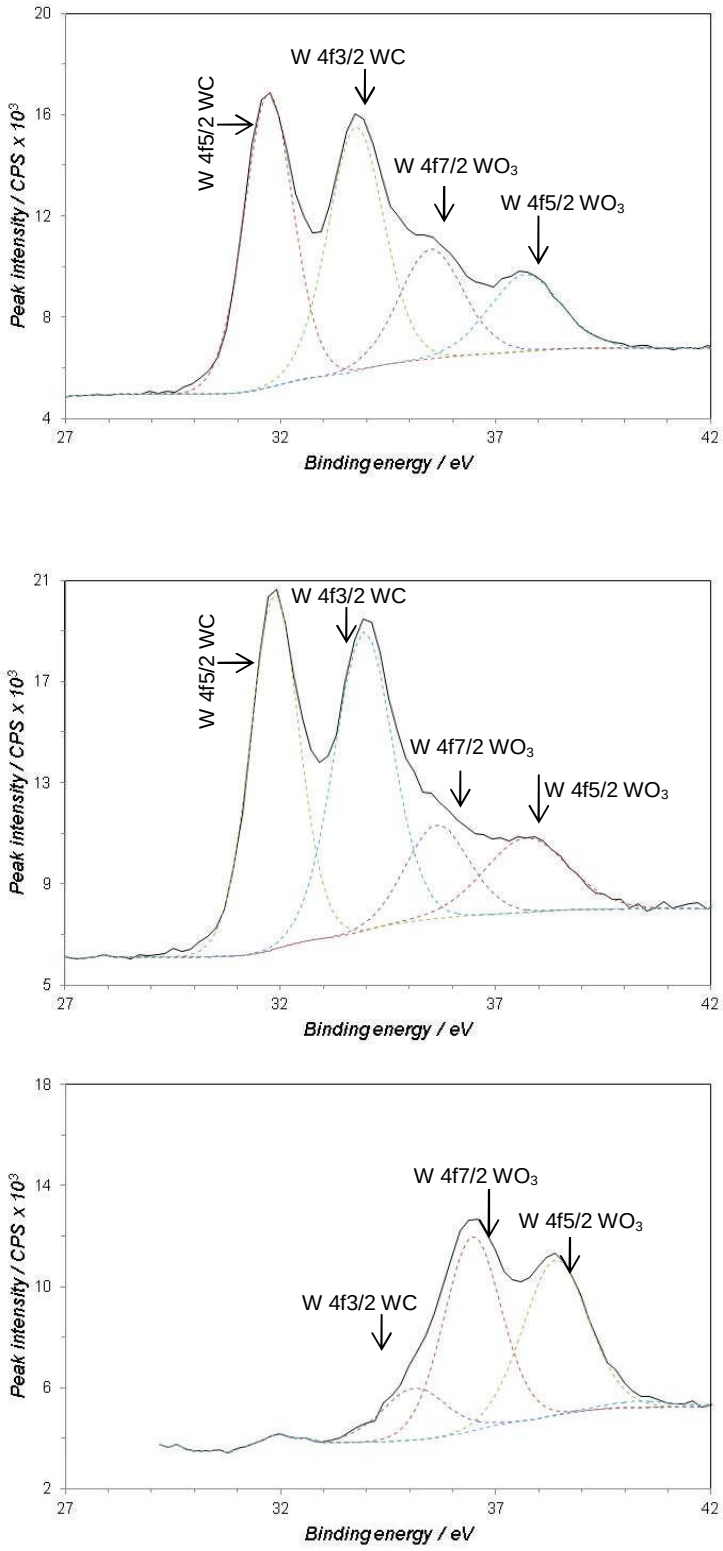

Figure 5-40: XP high resolution spectrum of W4f at polished 1 cm^2 WCCoCr coating samples, a) after air exposure for 24 hours, b) after polarizing the sample to 100 mV vs. E_{oc}, c) after polarizing the sample to 1000mV vs. E_{oc}. Samples were stabilized in 0.5M H_2SO_4 before polarization to different constant potentials for 5 minutes. After polarization samples were washed with de-ionized water and dried before inserting in XPS vacuum chamber for scan.

Table 5-16: XPS survey and high resolution results of WCCoCr coating

XP survey spectrum results after different constant potential polarizations for 5 min						
Constituent	Binding energy (eV)	Air for 24 h % peak area	100 mV % peak area	200 mV % peak area	500 mV % peak area	1000 mV % peak area
O 1s	531.43	29.5	30.2	30.8	30.5	48.5
C 1s	285.43	58	59.7	58.7	57.1	44.8
W 4d	243.43	7.5	7.5	8.1	8.9	6.5
Co 2p	778.43	5.1	2.6	2.4	3.5	0.1
High resolution XP spectrum results of Co 2p						
2p3/2 Co	778.11	27.1	30.7	29.1	25.5	-
2p3/2 Co_2O_3	780.94	29.3	51.6	45.2	50.2	-
2p1/2 Co	793.3	5.1	4.9	11.4	9.2	-
2p1/2 Co_2O_3	798.74	38.5	12.9	14.2	15.1	-
High resolution XP spectrum results of W 4d						
4d5/2 WC	243.41	57.8	58.7	58.1	54.2	5.2
4 d3/2W_3O_2	256.19	35.1	29.6	36.8	34.5	39.5
4d3/2 WO_x	259.87	8.1	5.3	5.1	11.3	55.4
4d5/2 WO_x	244.27		6.3			
High resolution XP spectrum results of W 4f						
4f5/2 WC	31.71	35.6	36.9	27.9	32.8	-
4f3/2 WC	33.74	33.5	37.2	9.7	18.6	20.6
4f7/2 WO_3	35.49	17.3	12.6	53.1	41.8	64.3
4f5/2 WO_3	37.68	13.6	13.2	9.3	6.7	15.1

5.7.4 XPS of the bulk Inconel 625

The quantification of the surface elements in Inconel 625 coating was done from the photoelectron peaks of O 1s, Ni 2p, Cr 2p and Mo 3d. The peak position of O 1s, Ni 2p, Cr 2p and Mo 3d were 531, 852, 576 and 230 eV which were consistent with the previous work and XPS data base [187]. The % of the peak area for O 1s, Ni 2p, Cr 2p and Mo 3d was 78, 10, 7 and 4 % when sample was exposed in air for 24 hours. The amount of O 1s for the sample polarized to 100 and 1000 mV potential show the oxygen % as 89 and 87. The peak area for Ni 2p, Cr 2p and Mo 3d also changes with the polarization. Both elemental and oxide peak were identified from the Cr 2p sub peaks, approximately around the same peak position as that of Inconel 625 coating. The peak positions were 575, 577 eV for Cr $2p_{3/2}$ elemental and Cr_2O_3 - oxide and 584, 587 eV for $Cr2p_{1/2}$ elemental and Cr_2O_3-oxide peaks. The

amount of elemental-Cr was 18% for air exposed sample, 11% for 100 mV polarized sample. There was not any elemental peak for Cr for the sample polarized to 1000 mV constant potential. The high resolution spectrum Ni 2p doublet consists of elemental and oxide peak of $Ni2p_{3/2}$ and $Ni2p_{1/2}$. The peak position were 854, 856 eV for $Ni2p_{3/2}$ elemental-Ni and NiO-oxide and 871, 876 eV for Ni $2p_{1/2}$ elemental-Ni and NiO-oxide peaks. The NiO-oxide satellite peak was also visible around 876 eV in the spectrum of the sample polarized to 1000 mV. The sample exposed in air shows 44% of Ni into elemental form and 56 into oxide form. After peak fitting the % area for the elemental Ni 2p was 17% and 29% for the sample polarized to 100 and 1000 mV potentials.

The only elemental peak was identified at 227 eV for molybdenum. The oxide peaks of Mo $3d_{5/2}$ MoO_2, Mo $3d_{3/2}$ MoO_2 and Mo $3d_{3/2}$ MoO_3 were identified at 231, 232 and 235 eV. The peak position of elemental and oxide position were consistent with the NIST database [187]. The peak area for the elemental Mo was 27% for air exposed spectrum and changed to 2% and 19 % for 100 and 1000 mV polarization. No elemental peak was identified in any sample of Nb 3d spectrum. The Nb $3d_{5/2}$ NbO, $Nb3d_{3/2}$NbO and $Nb3d_{3/2}$ Nb_2O_5 peak were identified from high resolution spectrum at 203, 206 and 209 eV which were consistent with the Inconel 625 coating sample [8]. The Nb 3d3/2NbO increase with polarization at higher potentials. The amount of Nb_2O_5 also increases with the polarization at higher potentials. The percentage peak area of Nb_2O_5 was 22 % after air exposure and 33, 32% after constant potential

exposure at 100 mV and 1000 mV. The change in shape of the spectrum was also consistent with the change in polarization potentials.

The constituent present in bulk Inconel 625 show approximately same trend as that of Inconel 625 coating sample. There was not any visible elemental peak for Nb same as the coating sample. The oxygen at the bulk alloy surface was higher than coating probably due to higher oxidation. The high resolution peaks for the bulk Inconel 625 further evident that Cr 2p, Ni 2p and Mo 3d peak consist of higher amount of oxides than coating sample. We suggest from our XPS results that passive oxide layer formed on the bulk Inconel 625 was more uniform than the Inconel 625 coating, therefore was more protective

Table 5-17: XPS survey and high resolution spectrum results of bulk Inconel

XP survey spectrum results after different constant potential polarizations for 5 min						
Constituent	Binding energy (eV)	Air for 24 h % peak area	100 mV % peak area	200 mV % peak area	500 mV % peak area	1000 mV %peak area
O 1s	531.21	78.5	88.9	75.2	78.5	87
Ni 2p	852.21	10.4	1.0	6	6.9	3.3
Cr 2p	576.21	6.8	7.5	15.3	9.6	6.9
Mo 3d	230.21	4.3	2.6	3.5	5	2.9
High resolution XP spectrum results of Cr 2p						
2p3/2 Cr	575.33	16.1	-	7.4	4.9	-
2p3/2Cr_2O_3	577.95	58.2	51.8	51.7	55.7	61.3
Cr 2p1/2 Cr	584.62	2.3	11	12.4	7.3	-
2p1/2Cr_2O_3	587.59	23.4	37.3	28.6	32.1	38.7
High resolution XP spectrum results of Ni 2p						
2p3/2 Ni	854.03	28.1	11.3	40.7	35.6	4
2p3/2 NiO	856.55	43.9	48.8	29.1	33.6	46.7
2p1/2 Ni	871.13	16.5	6.1	14.5	21.3	25.4
2p 1/2 NiO	874.98	11.5	33.7	15.7	9.4	11.7
2p1/2 NiO_x	875.65	-	-	-	-	12.3
High resolution XP spectrum results of Mo 3d						
3d5/2 Mo	227.76	26.6	1.4	27.2	19.7	18.3
3d5/2MoO_2	232.69	3.3	65.7	1.3	6.9	61.5
3d3/2MoO_2	231.14	46.2	20.6	57.9	46.7	-
3d3/2MoO_3	235.34	23.8	12.2	13.6	26.7	20.2
High resolution XP spectrum results of Nb 3d						
3d5/2 NbO	202.72	15.8	12.3	37.2	15.4	15.9
3d3/2 NbO	206.29	61.7	54.9	53.3	60.4	52.1
3d3/2Nb_2O_5	209.07	22.5	32.8	9.5	24.2	32

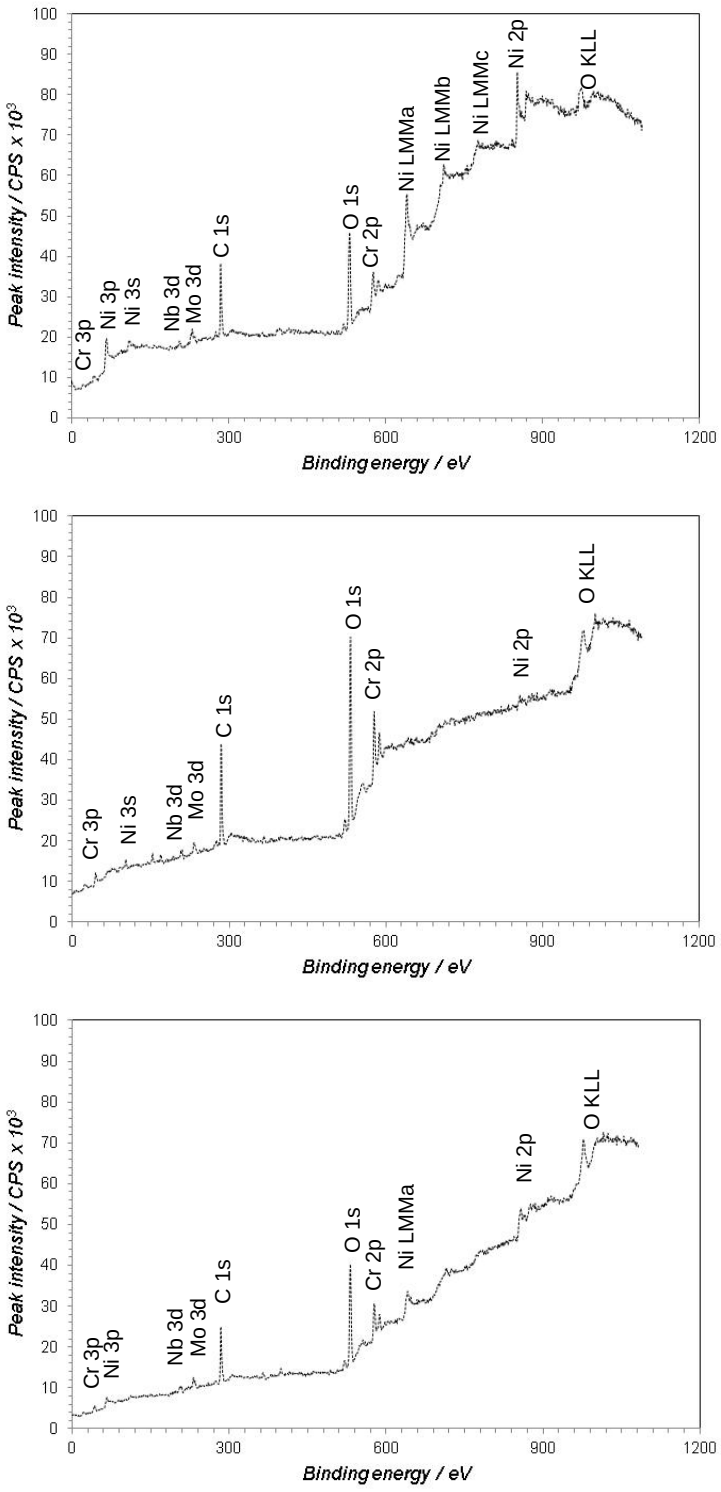

Figure 5-41: XP survey spectrum at polished 1 cm2 bulk Inconel 625 coating samples, a) after air exposure for 24 hours, b) after polarizing the sample to 100 mV vs. E_{oc}, c) after polarizing the sample to 1000mV vs. E_{oc}. Samples were stabilized in 0.5M H_2SO_4 before polarization to different constant potentials for 5 minutes. After polarization samples were washed with de-ionized water and dried before inserting in XPS vacuum chamber for scan.

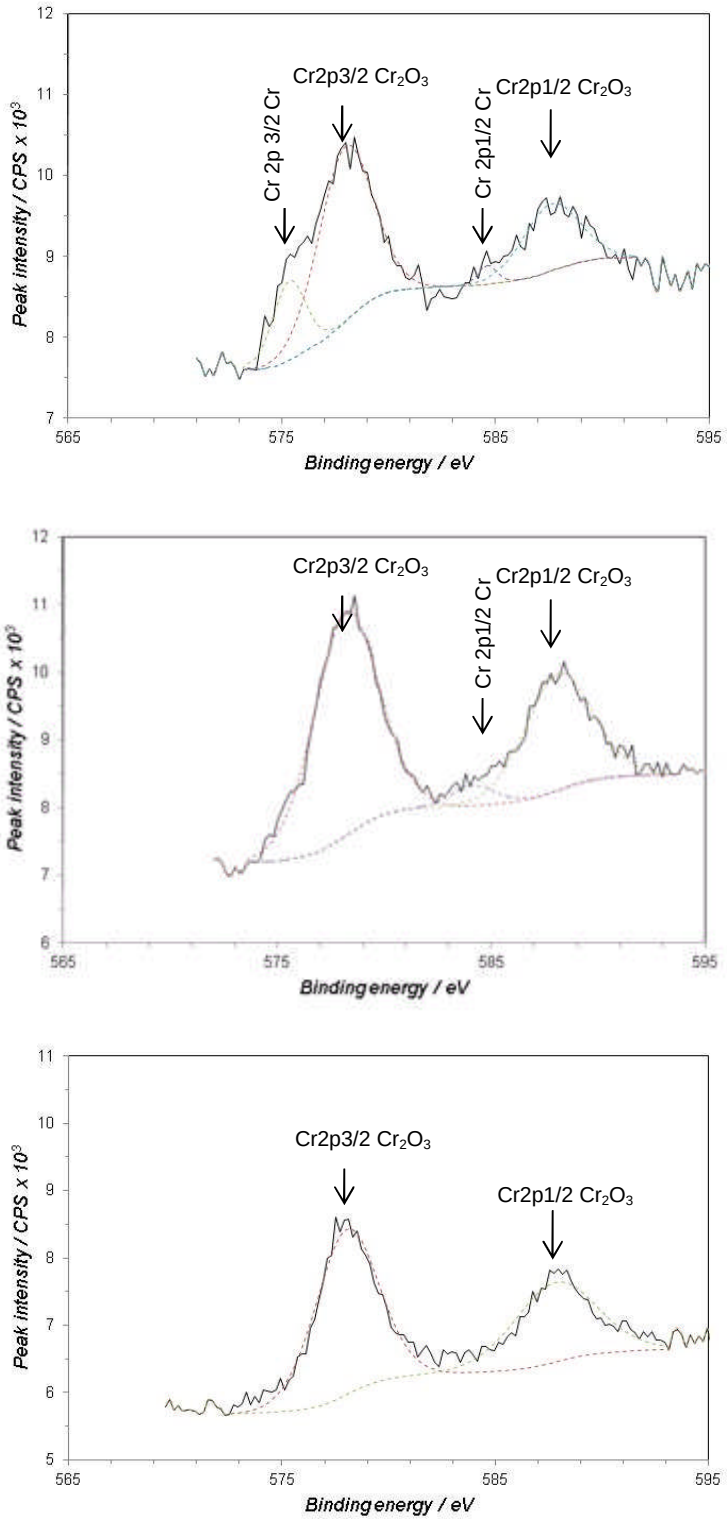

Figure 5-42: XP high resolution spectrum of Cr2p at polished 1 cm^2 bulk Inconel 625 samples, a) after air exposure for 24 hours, b) after polarizing the sample to 100 mV vs. E_{oc}, c) after polarizing the sample to 1000mV vs. E_{oc}. Samples were stabilized in 0.5M H_2SO_4 before polarization to different constant potentials for 5 minutes. After polarization samples were washed with de-ionized water and dried before inserting in XPS vacuum chamber for scan.

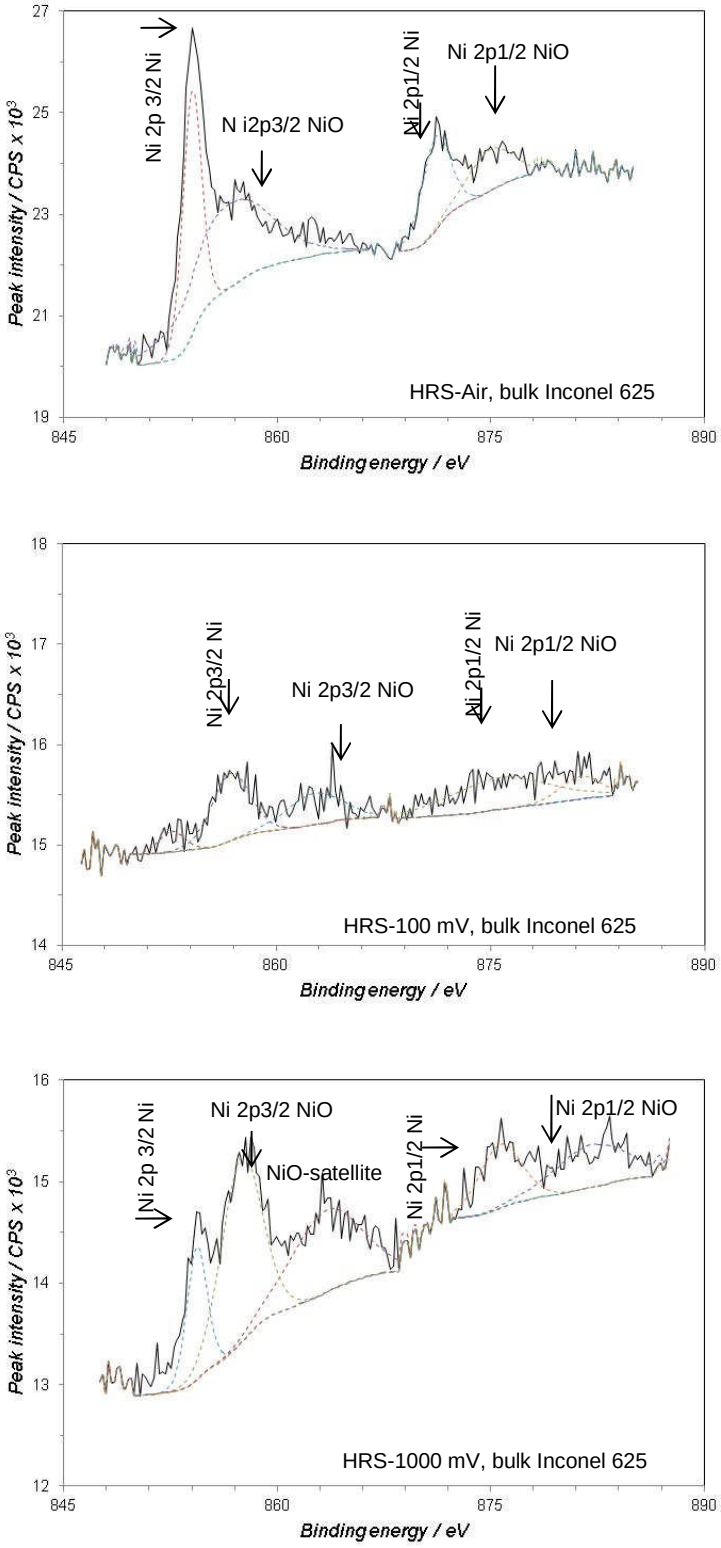

Figure 5-43: XP high resolution spectrum of Ni2p at polished 1 cm^2 bulk Inconel 625 samples, a) after air exposure for 24 hours, b) after polarizing the sample to 100 mV vs. E_{oc}, c) after polarizing the sample to 1000mV vs. E_{oc}. Samples were stabilized in 0.5M H_2SO_4 before polarization to different constant potentials for 5 minutes. After polarization samples were washed with de-ionized water and dried before inserting in XPS vacuum chamber for scan.

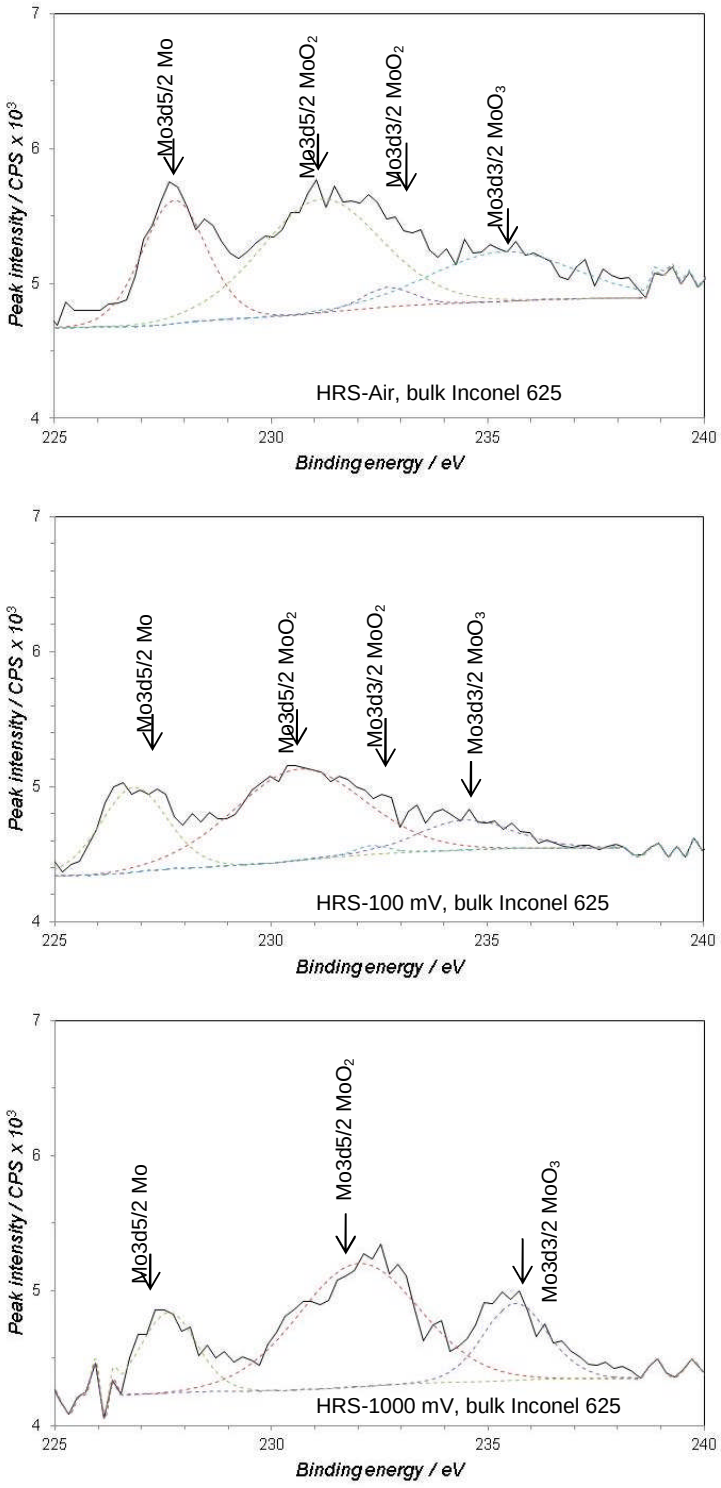

Figure 5-44: XP high resolution spectrum of Mp3d at polished 1 cm^2 bulk Inconel 625 samples, a) after air exposure for 24 hours, b) after polarizing the sample to 100 mV vs. E_{oc}, c) after polarizing the sample to 1000mV vs. E_{oc}. Samples were stabilized in 0.5M H_2SO_4 before polarization to different constant potentials for 5 minutes. After polarization samples were washed with de-ionized water and dried before inserting in XPS vacuum chamber for scan.

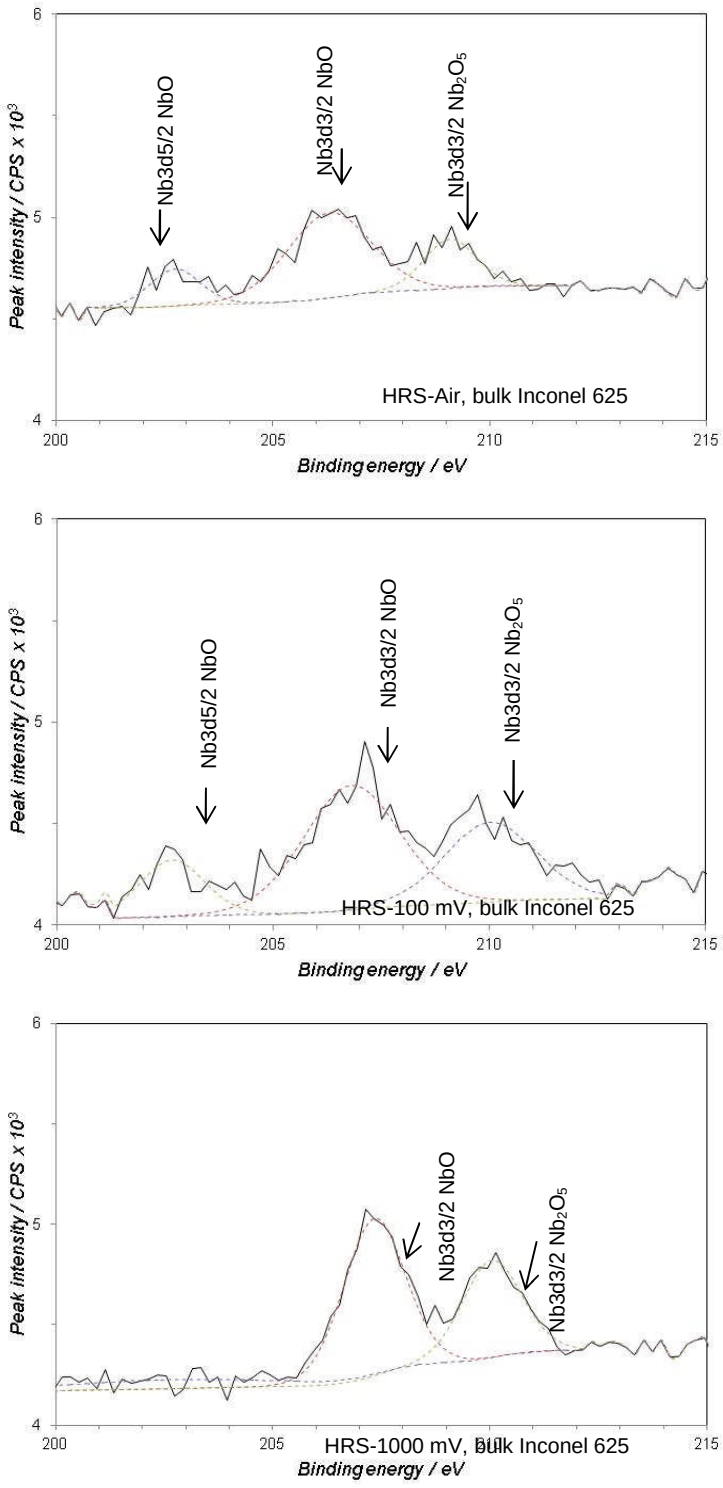

Figure 5-45 XP high resolution spectrum of Nb3d at polished 1 cm^2 bulk Inconel 625 samples, a) after air exposure for 24 hours, b) after polarizing the sample to 100 mV vs. E_{oc}, c) after polarizing the sample to 1000mV vs. E_{oc}. Samples were stabilized in 0.5M H_2SO_4 before polarization to different constant potentials for 5 minutes. After polarization samples were washed with de-ionized water and dried before inserting in XPS vacuum chamber for scan.

5.7.5 XPS results for stainless steel sample

The peak positions of O 1s, Ni 2p, Co 2p and Al 2s were 530, 575 and 710 eV in stainless steel sample were consistent NIST XPS data base [187]. The % of the peak area for O 1s, Cr 2p, and Fe 2p was 86, 9 and 5% when sample was exposed to air for 24 hours. The amount of O 1s changes from 88 to 80% when polarized from 100 mV to 1000 mV. The % peak area for Cr 2p and Fe 2p also changes with polarization.

The amount of elemental Cr was less in the stainless steel than other samples. The amount of elemental Cr was 11% for air exposed sample and 6%, 5% for the sample polarized to 100 and 1000 mV constant potentials. The disappearance of the elemental peak was also evident from the high resolution spectrum of the respective photoelectron peaks. The Fe 2p was appeared as a doublet with both elemental and oxide part. The peak positions of $Fe2p_{3/2}$ Fe, $Fe2p_{3/2}$ Fe_2O_3 were 706, 710 eV and $Fe2p_{1/2}$ Fe, $Fe2p_{1/2}$ Fe_2O_3 around 720 and 724 eV. The amount of elemental Fe 2p was 34% for air exposed sample, 18% when sample was polarized to 100 mV and 26% at 1000 mV.

Chromium forms a passive oxide layer on the stainless steel which protects the surface from further oxidation [264, 265]. The active-passive materials like stainless steel oxidize very fast and form passive layer as soon as they exposed in air. The typical air formed oxide film on stainless steel is in the order of few nanometers [35, 265]. The thickness of the oxide layer increases with exposure time and potentiostatic polarization in solution. Although dilute sulfuric acid is a reducing acid and thins the air formed film due to hydrogen evolution reaction, still when stainless steel samples are polarized to positive potentials

the oxide starts thickening again. The increase in the amount of oxide at the surface is evident from the higher oxygen peak of the sample polarized to 100 mV. The 1000 mV potentiostatic potential also produced higher amounts of oxides because there was no protective layer and more positive potential was used to oxidize the elements present at the surface.

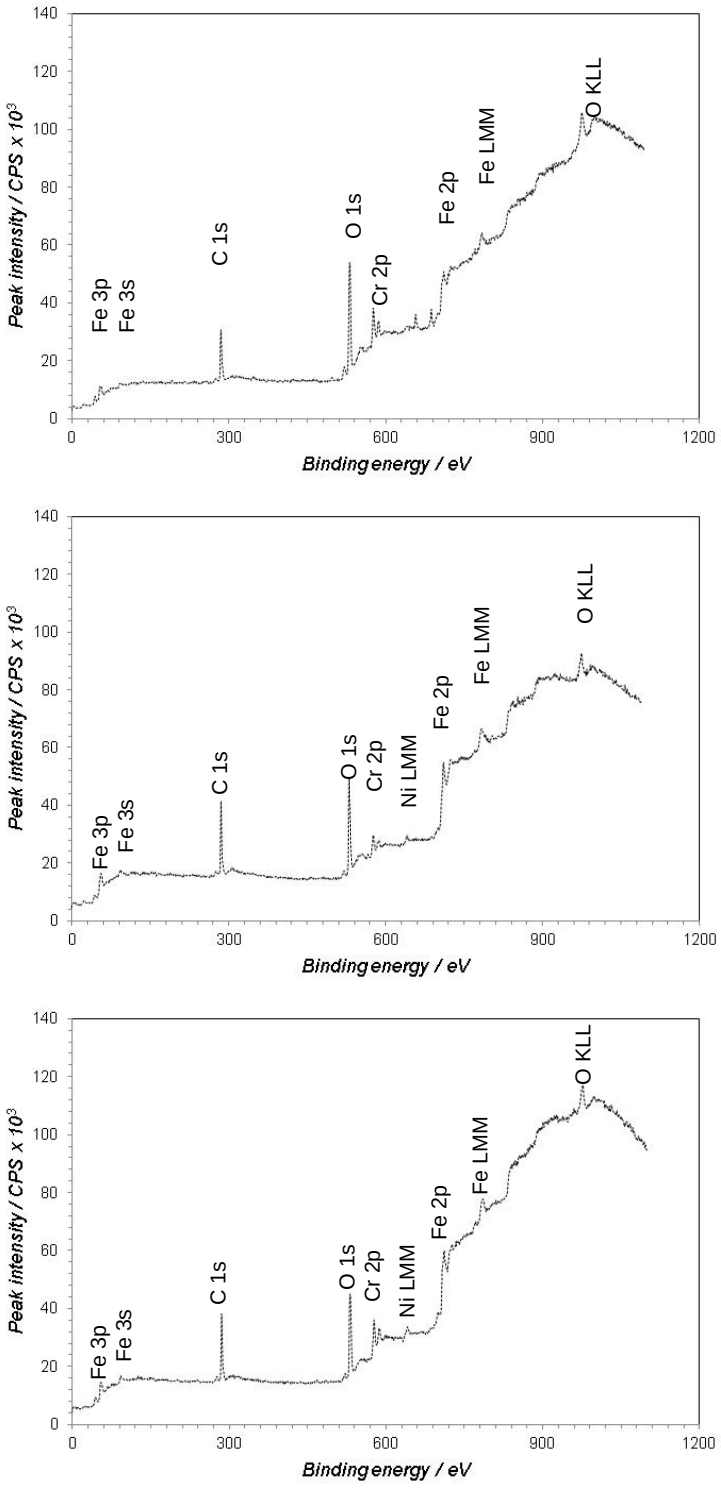

Figure 5-46: XP survey spectrum at polished 1 cm^2 stainless steel samples, a) after air exposure for 24 hours, b) after polarizing the sample to 100 mV vs. E_{oc}, c) after polarizing the sample to 1000mV vs. E_{oc}. Samples were stabilized in 0.5M H_2SO_4 before polarization to different constant potentials for 5 minutes. After polarization samples were washed with de-ionized water and dried before inserting in XPS vacuum chamber for scan.

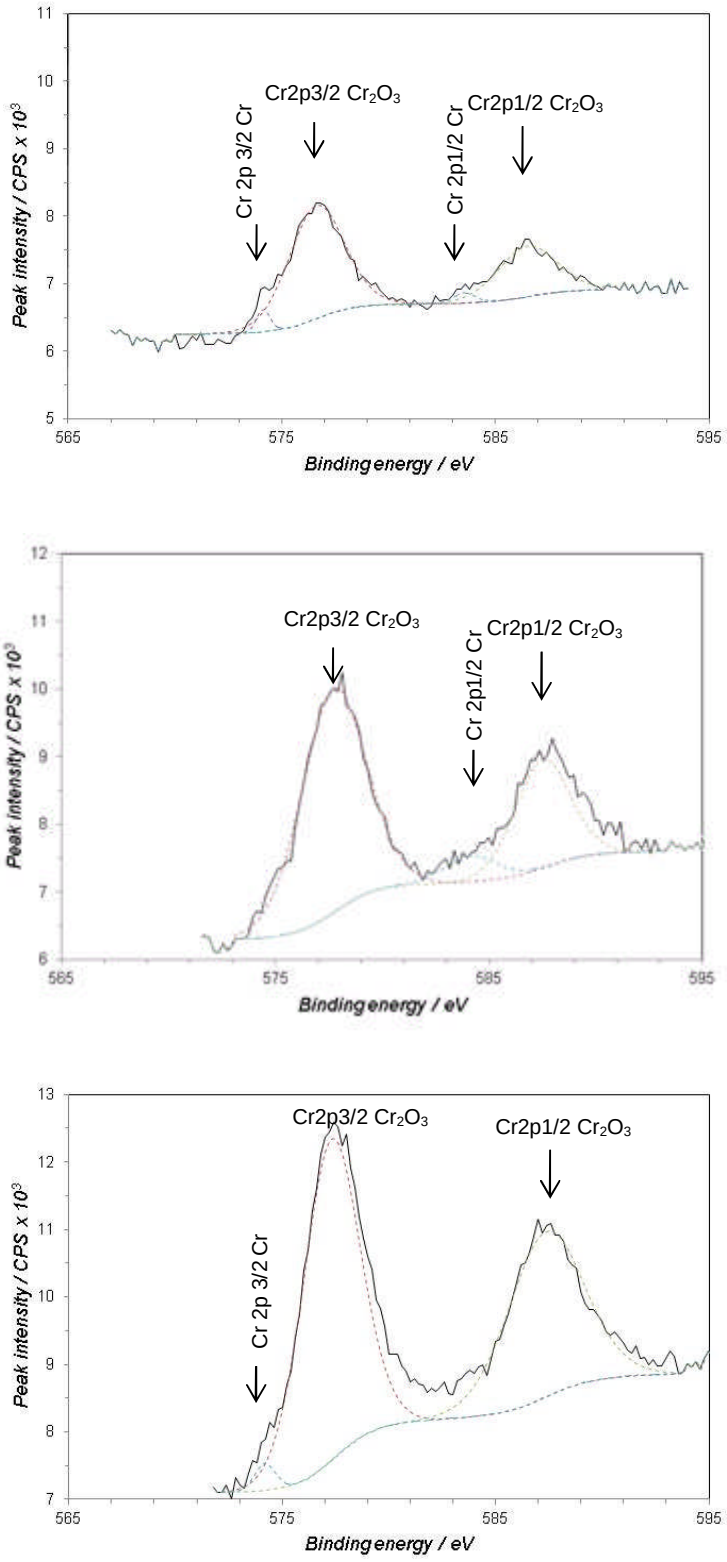

Figure 5-47: XP high resolution spectrum of Cr2p at polished 1 cm^2 stainless steel samples, a) after air exposure for 24 hours, b) after polarizing the sample to 100 mV vs. E_{oc}, c) after polarizing the sample to 1000mV vs. E_{oc}. Samples were stabilized in 0.5M H_2SO_4 before polarization to different constant potentials for 5 minutes. After polarization samples were washed with de-ionized water and dried before inserting in XPS vacuum chamber for scan.

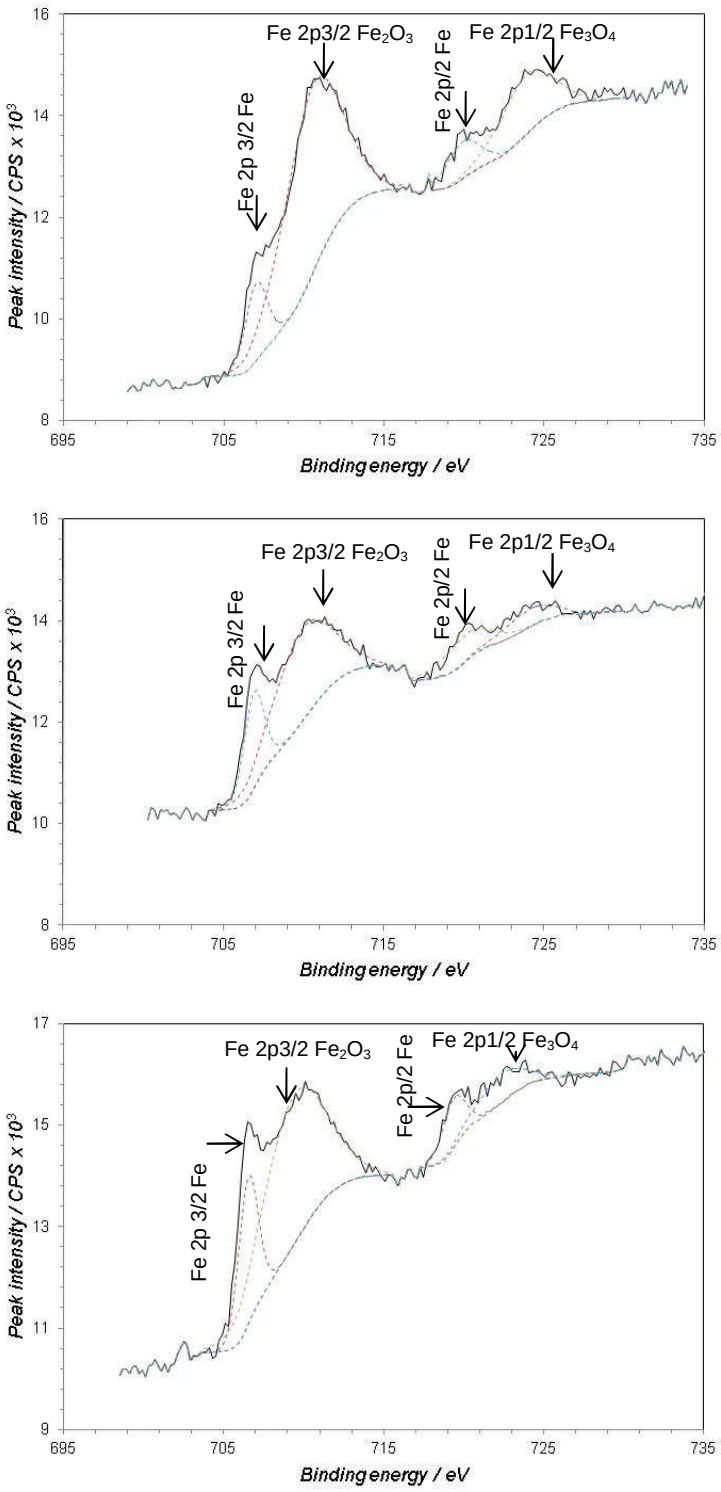

Figure 5-48: XP high resolution spectrum of Fe2p at polished 1 cm^2 stainless steel samples, a) after air exposure for 24 hours, b) after polarizing the sample to 100 mV vs. E_{oc}, c) after polarizing the sample to 1000mV vs. E_{oc}. Samples were stabilized in 0.5M H_2SO_4 before polarization to different constant potentials for 5 minutes. After polarization samples were washed with de-ionized water and dried before inserting in XPS vacuum chamber for scan.

Table 5-18: XPS survey and high resolution results of stainless steel

XP survey spectrum results after different constant potential polarizations for 5 min						
Constituent	Binding energy (eV)	Air for 24 h % peak area	100 mV % peak area	200 mV % peak area	500 mV % peak area	1000 mV % peak area
O 1s	529.67	86	88.3	86.9	85.5	80.9
Fe 2p	709.67	9	4.7	4.5	7.1	10.4
Cr 2p	575.67	5	7	8.6	7.4	8.7
High resolution XP spectrum results of Cr 2p						
2p3/2 Cr	574.12	5.9	-	4.9	1.6	5.4
2p3/2Cr_2O_3	576.58	62.1	64	56.2	52.2	58.5
2p1/2 Cr	583.52	6.2	5.6	11.6	10.2	-
2p1/2Cr_2O_3	586.46	25.9	30.4	27.3	36	36.1
High resolution XP spectrum results of W 4d						
2p3/2 Fe	706.99	20.2	10.3	16.4	12.9	19.9
2p3/2Fe_2O_3	710.53	56.7	62.9	64.8	70.6	63.3
2p1/2 Fe	719.94	13.8	7.6	8.6	8.5	7.8
2p1/2Fe_3O_4	723.91	9.3	19.2	10.2	8	9

5.7.6 Summary of all XPS results and discussion

The surface analysis of all tested materials reveals that oxidation occurs in air and extent of oxidation depends on the elements present and their microstructures. The oxygen peak area measured from survey spectrum was higher for the stainless steel and bulk Inconel than the coatings. This indicates that the bulk/cast material oxidizes more in air than the coating. The microstructure of the bulk Inconel 625 was homogenous and has higher amount of Mo and Nb at the surface than Inconel 625 coating, this was also evident from SEM/EDS analysis. The Nb and Mo are easily oxidizing constituents of the Inconel 625; hence their higher percentages at the surface allow greater extent of surface oxidation. The readily available oxidizing elements may allow forming uniform oxide layer for bulk alloy.

XPS is highly surface sensitive technique and is used to measure the composition to a surface depth of 10 nm which is approximately 20 atomic layers [187]. The oxide formed on the metals is of conductive nature which

allows the easy passage of electron and ions across the passive layer. The dilute sulfuric acid is a reducing acid. There is large availability of H^+ ions and electrons easily travel through air-formed oxide layer. The availability of hydrogen ions and electron favours hydrogen evolution and the oxide reduction at the air-formed oxide/solution interface. The more the time sample stays in the solution, the more the surface oxide layer thins. Therefore careful monitoring of time in solution before applying constant potential is important in this kind of oxide formation study. In our experiments the time was kept at 30 minutes before polarizing the samples to constant potential for 5 minutes.

The polarization to higher constant over potentials increases the oxide content in the sampled volume. In our experimentation after polarization of the sample to different overpotentials samples were removed from the epoxy and washed/dried for an hour before inserting into XPS high vacuum chamber. The time span between polarization and inserting into vacuum chamber was 1-2 hours. It was assumed that the oxidation of the surfaces by polarization is generally more than the air, so short exposure time is not contributing too much towards oxidation in air but this time interval may allow some air-formed film formation. In an attempt to observe changes due to negative applied potential and to more accurately measure the oxidation due to positive applied potential it is more appropriate to minimize the time interval between polarization and XPS analysis or to keep polarized samples in air-removed environment. The oxidation of the bulk Inconel 625 shows the similar trend where the oxygen content increases with polarization to higher potentials. From three different coatings, WCCoCr coating show the minimum oxygen

percentage in XPS survey spectra. This was probably due to presence of WC-phase which has a redox potential of +189 mV vs. Ag/AgCl in 0.5M H_2SO_4 solution [266].

The peak area for oxygen generally increases with polarization to higher potentials but the rate of oxidation was higher at lower positive potentials. This was the active region for the material where overall corrosion takes place at faster rate. The 2p 1/2Cr elemental peak fully disappears in the CoNiCrAlY coating stainless steel and bulk Inconel 625 spectra at 100 mV potential polarization. The higher oxidation rate at 100 mV was true for all materials except WCCoCr coating. This was probably due to higher positive potential required for oxidation of WC-phase [266]. The WCCoCr coating analysis at higher potential shows decrease in the carbon content probably due to de-carbonization of WC-phase [263], where tungsten oxide is formed and carbon goes in solution.

The nature of oxide and its quantity also changes with higher potentials. The amount of Nb_2O_5 in Inconel 625 coating and bulk Inconel increased when samples were polarized to higher positive potential. The amount of MoO_3 also increased in both bulk and coating Inconel 625 at higher positive potentials. The Ni-satellite peak also appeared at higher positive potentials in both Inconel and CoNiCrAlY coatings.

The oxidation of material increases with the higher potential polarization and elemental form decreases. The XPS analyses of HVOF coatings showed for some higher potential the extent of oxidation decreased. The decreased oxidation was probably due to variations in the surface composition or error in

the peak fitting e.g. the survey spectrum of Inconel 625 coating show 8% Cr in air exposed sample and 16% when sample was polarized to 500 mV potential (***see Table 5-14***).

The higher oxides percentages in the X-ray spectrum at 1000 mV constant potential were due to higher oxidation rate and probably entering the transpassive regime. In the transpassive regions break down of the oxide film along with higher oxygen evolution occurs (water molecule breaking). The breakage of the oxide film exposes fresh surface and the bulk availability of oxygen at the surface causes this fresh surface to quickly oxidize. The availability of the fresh surface and oxygen were the main reasons for higher oxides contents in their relative X-ray spectrums.

The main oxides identified on the Inconel 625 coating and the bulk Inconel 625 alloy surface were Cr_2O_3, NiO, NiO-satellite, MoO_2, MoO_3, NbO and Nb_2O_5. The previously reported less protective $Ni(OH)_2$ for Inconel 625 coating was not identified here probably due to less time for polarization [8]. The higher performance of the bulk Inconel 625 alloy was attributed to more homogeneous oxidation of the surface than coating. The oxides present on the WCCoCr coating were identified as Co_2O_3, W_2O_3 and some non-stoichiometric oxides. The formation of W_2O_5 due to secondary oxidation at higher temperature was not seen in our results [263, 267]. The formation of W_2O_5 may only be restricted to high temperature oxidation. The CoNiCrAlY coating surface contained Co_2O_3, Cr_2O_3 and NiO. The main oxides on the stainless steel surface were identified as Cr_2O_3, Fe_2O_3 and Fe_3O_4.

5.8 Summary

- The potentiodynamic polarization results showed the passive current density for the Inconel 625 coating was a factor of 10 higher than the bulk Inconel 625 alloy. The higher passive current density for Inconel 625 coating was attributed to microstructural changes due to HVOF process.
- The polarization curve results for different materials showed overall shift in E_{corr}, passive current density, and breakdown potential. Amongst all HVOF coating tested for corrosion the E_{corr} was most negative for CoNiCrAlY and most positive for Inconel 625. The breakdown potential was approximately same for CoNiCrAlY, WCCoCr coatings and more positive for Inconel 625 coating. The passive current density was approximately same for WCCoCr, Inconel 625 coatings and slightly lower for CoNiCrAlY coating.
- The pitting propensity of the Inconel 625 coating exposed in 3.5% NaCl solution for 10 days was also confirmed by the polarization curves produced in 3.5% sodium chloride and coating microstructural study before and after potentiodynamic polarization test. The CoNiCrAlY coating aggressively corrodes all over the surface in 3.5% NaCl while WCCoCr coating did not show any sign of pitting.
- The heterogeneous ET rate constant obtained for bulk Inconel 625 was a factor of 100 lower than the Inconel 625 coating indicating corrosion reaction is taking place at slower rate at bulk alloy. The higher rate

constant for CoNiCrAlY and WCCoCr coating prove that these two coating are corroding at fast rate.

- The effect of potential scan rate, potential scan direction, stabilisation time before starting polarization curve, potential scan starting point and applied potential before polarization experiment shift the position of polarization curves was found different for different coatings. The main findings by changing the testing parameters are given below:

    - Increasing the stabilization time from 1h to 15h before starting polarization test decreased the E_{oc} change from 13-50 mV h^{-1} to 1-6 mV h^{-1}. The greater stabilization of E_{oc} increased accuracy of the polarization test as current voltage correlation defining polarization curve reflects the same corrosion phenomena of the curve. The higher E_{oc} change adversely effect in passive systems where slight polarization upset the electrochemical process enough that the generated curve did not pass through the origin, this mean applied current will be observed at zero volt relative to the starting E_{oc}.
    - The shift in E_{corr} to more negative value by applying prior negative potential was 17-41 mV for bulk alloys and 1-16 mV for the coatings. The shift in E_{corr} to more positive value by applying prior positive potential was 2-4 mV for bulk alloys and 5-18 mV for the coatings. The more negative shift in E_{corr} value for the bulk alloys by prior negative applied potential was attributed to partial removal of the oxide layer. The more

positive shift in E_{corr} value by prior positive applied potential for the coatings was probably due to increased positive potential drive in the coating, which causes the oxidation of active spots. In bulk alloys the surface oxide has to grow more uniformly hence the applied potential distributed more evenly on the surface, therefore the shift in E_{corr} value by positive applied potential was lower for bulk alloys. We suggest from our results that microstructure, constituent materials and their percentage contribute to the E_{corr} shift by prior potential.

- It was noticed that the higher scan rate shifted E_{corr} to more negative potential from starting E_{oc} and increased the charging current contribution in net current. Charging current was increased with scan rate for all coatings but comparing the bulk and coating samples, the charging current was a factor of 10 to 100 lower for the bulk Inconel 625 than that of the Inconel 625 coating samples. So the sprayed microstructure has changed the magnitude of the charging current. The higher value of faradaic current can be attributed to faster corrosion reaction. At all scan rates the faradaic and charging currents were highest for CoNiCrAlY coating and lowest for bulk Inconel 625, this indicates that the CoNiCrAlY coating is least and bulk Inconel 625 is most corrosion resistant material under the used experimental conditions.
- The shift in E_{corr} value from the starting E_{oc} value was 2-22 mV for the partial anodic and cathodic curves and 30-176 mV for

the continuous polarization curves at 10, 20, 60 and 180 mV min^{-1}. The shift in E_{corr} value from the partial scan was 21 mV for bulk Inconel 625, 22 mV for stainless steel, 8 mV for Inconel 625 coating, 9 mV for CoNiCrAlY coating and 2 mV for the WCCoCr coating for the same set of scan rates. In the continuous polarization curves the shift in E_{corr} value was 109 mV for the bulk Inconel 625, 176 mV for stainless, -32 mV for the Inconel 625 coating, -35 mV for the CoNiCrAlY coating and -30 mV for the WCCoCr coating. The small E_{corr} shift in the partial polarization curves is attributed to lower charging current.

- The heterogeneous ET rate constant values were 6.59×10^{-12} cm s^{-1} for bulk Inconel 625 and 3.17×10^{-10} cm s^{-1} for Inconel 625 in 0.5M H_2SO_4. The electron transfer rate constant value from potentiodynamic polarization is the resultant of all surface reactions plus the errors due to adsorption and charging current.

- The XPS results show that all tested materials have oxides of their constituents when they were exposed in air and polarized in 0.5 M H_2SO_4 solution. The percentage of surface oxygen was 5-10% higher for the bulk alloys than the HVOF coatings both for air formed and applied potential induced oxides. The percentage of oxygen was also increased when samples were polarized to higher potentials.
- The main oxides identified on the Inconel 625 coating and the bulk Inconel 625 alloy surface were Cr_2O_3, NiO, MoO_2, MoO_3, NbO and

Nb_2O_5. The presence of $Ni(OH)_2$ in the Inconel 625 coating was not evident from our results probably due to short time of polarization in the electrolyte. The oxides present on the WCCoCr coating were Co_2O_3, W_2O_3 and some non-stoichiometric oxides. Oxides formed on the CoNiCrAlY coating surface were Co_2O_3, Cr_2O_3 and NiO. The main oxides on the stainless steel surface were Cr_2O_3, Fe_2O_3 and Fe_3O_4.

6 Electrochemical impedance spectroscopy

6.1 Introduction

In this chapter the electrochemical impedance spectroscopy results are presented for Inconel 625, CoNiCrAlY and WCCoCr coatings. In first part of the testing the physical features of the Inconel 625 coating microstructure are correlated with their electrochemical response by equivalent circuit modelling. The time evolution changes in impedance spectra due to corrosion process are presented for Inconel 625, CoNiCrAlY and WCCoCr coatings by recording EIS data for 72 hours. The changes in impedance spectra by polarizing coating samples to active and passive stage are presented in the last section.

6.2 EIS at Inconel 625 coating sample

Figure 6-1 shows the Nyquist plot, Bode impedance and Bode theta plot for Inconel 625 coating. The Nyquist plot showed three humps in the spectra encircled with 1, 2 and 3 at approximately 50, 150 and 450 Ω cm^{-2} respectively. These regions are also marked on Bode impedance and theta plots. A uniform half circle in the Nyquist plot represents one time constant (RC), consistent with an equivalent circuit containing of a resistor and capacitor. The Nyquist plot for Inconel 625 did not show such a response, the resultant spectra is complex and contains more than one time constant. It should be noted that the Nyquist plot does not show the frequency axis but the impedance values around origin are related to the higher frequency response and frequency decreases away from the origin.

The small humps seen from the Nyquist plot were obstructed due to the log frequency axis in the Bode impedance plot. The Bode impedance spectra showed the characteristic electrical response of the tested material and spectra can be divided into different parts over the tested frequency range. The plateau in the Bode impedance plot represent dominant resistive behaviour and increase in impedance with increase in frequency represent the capacitative behaviour [94, 149]. An impedance plateau was visible around the higher frequency end indicating predominant resistive response. The impedance at higher frequency was related with solution resistance/physical defects (pores, cracks, inclusion) and lower related with corrosion processes [95].

The Bode theta plot show the angle started from -20° at lower frequency and reached to 60° around 100 Hz. The value of theta remains constant at 60° before decreasing to lower values again. The phase angle shift between the applied potential and response current also gives the characteristic information about the electrical response which can be correlated with physical features [96, 136]. The +90° shift in the phase angle is characteristic property of capacitor and -90 is the characteristic property of inductor [144]. The applied potential and response current stay in phase for a resistor.

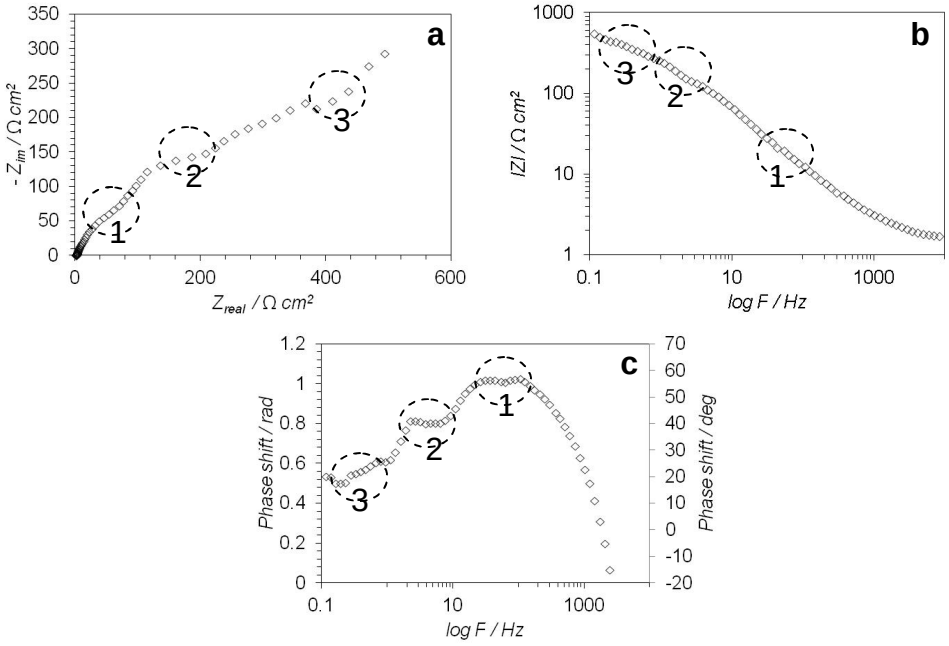

Figure 6-1: Electrochemical impedance spectra recorded for Inconel 625 coating in 0.5 M H_2SO_4 by applying a 10 mV AC signal over a frequency range of 0.1 to 10000 Hz, a) Nyquist plot, b) Bode impedance plot, c) Bode theta plot.

The impedance response at Inconel 625 coating over a frequency range is complex and requires analysis/synthesis into simpler function for results interpretation and understanding. One of the analysis processes is equivalent circuit modelling (ECM) extensively reported in the literature. In ECM an electrical circuit model is used to compare and quantify the impedance

response of the corrosion system. The detail about the equivalent circuit modelling for the HVOF Inconel 625 coating is given in the next section.

6.3 Modulation of EC to follow corrosion process in HVOF Inconel 625 coating

In this section microstructure features of the Inconel 625 coating and their corrosion processes are presented with electrical circuit component. These circuit components are later connected into logical circuitry to build an equivalent circuit model (ECM). The proposed ECM for Inconel 625 coating was fitted with experimental impedance data and compared with the previously reported ECM for Inconel 625 coating.

6.3.1 Reported equivalent circuit for HVOF coating

The ECM reported for the polished surfaces of Ni-Ti, and iron based amorphous HVOF coatings are shown in ***Figure 6-2*** [268-270]. The simple Randles model with a Warburg diffusion element is also reported for bulk Inconel 625 alloy [271]. In the reported model the constituents of the oxidation product i.e. oxides formed during HVOF coating process and formed in air/electrolyte exposure were neither considered independently nor their differential electrochemical activity. The time constants of oxides of Ni, Cr, Mo, Nb were not identified in the impedance spectra hence only one time constant was used in the equivalent circuit. The HVOF Inconel 625 coating is very dense, having a porosity of 2-3% [2] so pore resistance was ignored. The capacitance of the whole system was considered as C_{coat} and the charge transfer resistance across this layer as R_p. All of the resistance within the pore,

due to corrosion product accumulation were combined with single Warburg diffusion W_{diff} element.

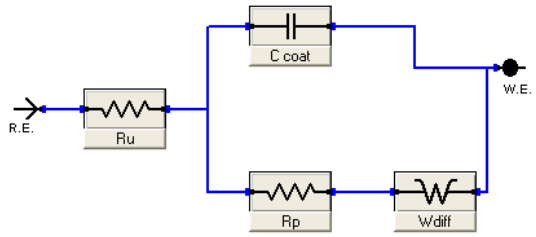

Figure 6-2: Reported ECM for HVOF coatings

6.3.2 Proposed ECM for HVOF Inconel 625 coating

Based on coating microstructural features and experimental impedance spectra results the ECM in ***Figure 6-3***c was proposed for the HVOF Inconel 625 coatings. The HVOF Inconel 625 coatings was compact [2, 56], yet the coating have some pores on the surface within the lamellae connecting boundaries and where particles meet each other. The surface pores can be seen in ***Figure 6-3***a, b plan and cross-section view micrograph of Inconel 625 coating. The resistance due to pores was represented by R_{pore} in the ECM. The capacitance at the coating was represented by CPE_{coat}. Inconel 625 consists of Ni, Cr, Mo, and Nb which may be oxidised during polarization. The XPS results showed that oxides of Mo and Nb were also present but their percentage in overall oxide layer was less than the Ni and Cr (see ***section 4.2.1***and ***5.7.1***).

Hydro-oxides of Ni and Cr may be present [8] but there percentage may not be enough to show appearance in impedance spectra. The XPS results also confirmed that there was not any hydroxide of Ni or Cr present in the passive layer (***see section 5.7.1***). The oxide layer formed on the melted and non-melted regions were considered for modelling. The oxide formed in the Cr-depleted

regions was considered as oxide 1 and oxide formed on the non-melted region was considered as oxide 2. The oxide layer formed in the non melted regions was more stable than the one formed in Cr-depleted regions in splat boundaries [63, 272].

The low electrochemical stability of the oxide layer formed in Cr-depleted regions ($CPE_{oxide1,}$ R_{oxide1}) was later confirmed with SECM where positive feedback was recorded at splat boundaries and high k^0 from kinetic of ET study (***see section 7.10.6***). The oxide layer on the non-melted region (R_{oxide2}, R_{oxide2}) was electrochemically more stable than the Cr-depleted regions. The non-melted particles gave negative feedback and k^0 value was also lower than the active sites we suggest that the ECM for the HVOF coating cannot be configured by stringent series or parallel circuitry due to embedded and layered structure of the oxides, so mixed parallel setup was used.

The oxide growth in Inconel 625 alloy was predominantly reported as layered structure [273, 274] hence oxides were assumed in series. There were pores in the coating but not too many to allow seepage of electrolyte to the substrate [2, 7], so the coating capacitance was dominant. Pores allow the separate current path and hence were considered in parallel with the oxide layer. The solution resistance R_u, is always in series with rest of the circuit while L is the inductance involved in the coating. The induction effect was probably the current induced from the surrounding equipment as well as the instrument/cables itself [96, 275].

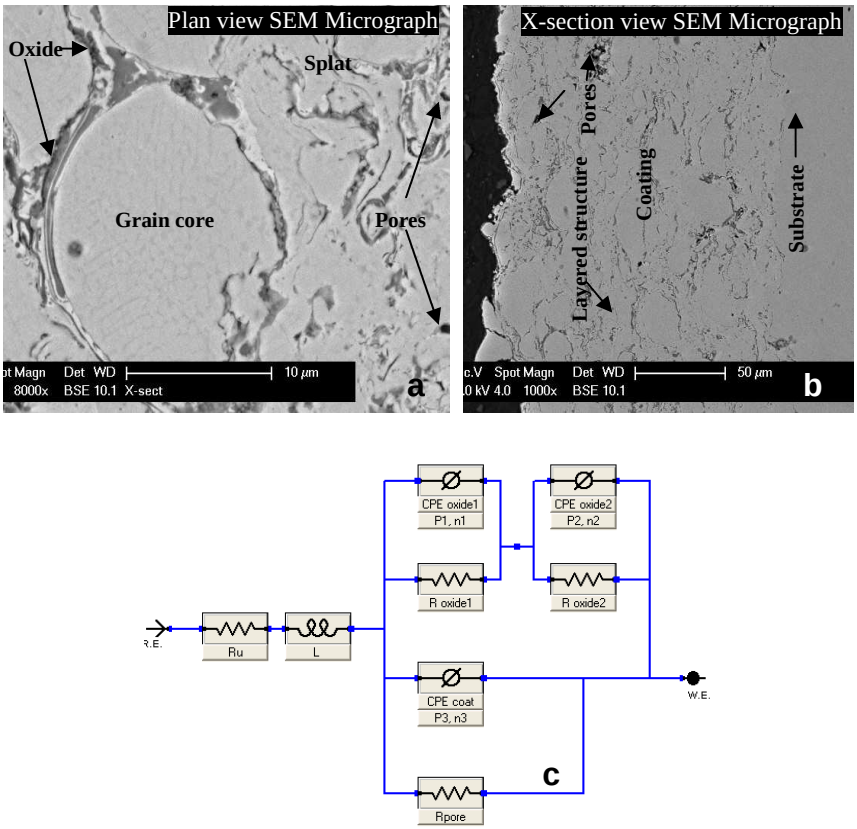

Figure 6-3: Proposed ECM for HVOF coatings

6.3.3 EIS results after fitting experimental results with previously reported and proposed ECM at E_{oc}

To check the quality of fit and quantify the values of the circuit elements, the experimental EIS spectra were fitted with reported and proposed equivalent circuit model. ***Figure 6-4*** and ***Figure 6-5*** show the curve fitting of EIS spectra for Inconel 625 coating. The EIS results after fitting experimental spectra with previously reported and proposed ECM models are summarised in ***Table 6-1*** and ***Table 6-2***.

In most of the EIS data analysis the initial values of the circuit component were adjusted before starting analysis. The values can be estimated from the shape of impedance spectra e.g. the plateau of impedance over a frequency

range is resistive behaviour and inclined line at an angle > 60° with the base line is the capacitative behaviour. The impedance values for resistor can be read from the impedance spectra while capacitance values can be calculated from the impedance formulae of the capacitor ($Z_c = 1 / 2\pi f C$ where Z_c impedance of capacitor, f is frequency and C is capacitance). The EIS-analyser software used for the analysis automatically finds these seed values and fit with the experimental data therefore it was not necessary to estimate these values for different components.

The reported equivalent and proposed ECM have different circuit elements so their quantitative values were not comparable with each other. Only overall fitting quality and their error can be correlated with the relevant circuit elements (Error is the % difference between each element of ECM and experimental impedance spectra). The experimental impedance spectra fitting with the reported ECM produce smaller errors in results than the fitting with proposed ECM. In the first case only R_u was found higher than the acceptable limit of error, all other circuit element have an error below 10%.

In both model fittings (reported and proposed model) the simulated graph (solid line) did not fully overlap the all experimental data points this is attributed to the complexity due to heterogeneity and electrochemical instability of the coating system. The proposed model fitting shows some additional effects have been omitted. The data validity tests in the experimental section (***see section 4.7.3.3.1***) also prove that the residual errors (difference between actual and calculated values) for the Inconel 625 coating were much higher than the recommended (1-2%). The change was more pronounced in the

Bode theta plot around lower frequencies (1-10 Hz). Although both models did not fully fit with the experimental data, still the visual appearance of fitting of the proposed model was improved as compared to reported model, particularly for the higher frequency results.

It should be noted that capacitance values extracted from the fitting of experimental spectra with ECM for both reported and proposed models were approximately same as reported in the literature (i.e. 10^{-5} – 10^{-7} μF/cm^2) [276-279]. We suggested from our results that the variation in the capacitance was due to defective nature of the passive layer. As revealed from the XPS results a number of different oxides were present in the passive layer. The passive layer also changes with time and applied potential (see ***section 5.3.1***and ***5.7.1***). It can be summarized that considering microstructure features of the coatings i.e., porosity, phases and electrochemical processes in corrosion, we can construct a representative equivalent circuit. Furthermore, it was found from our EIS model fitting that reasonable good fit can be produced if coating microstructure features are included in the ECM.

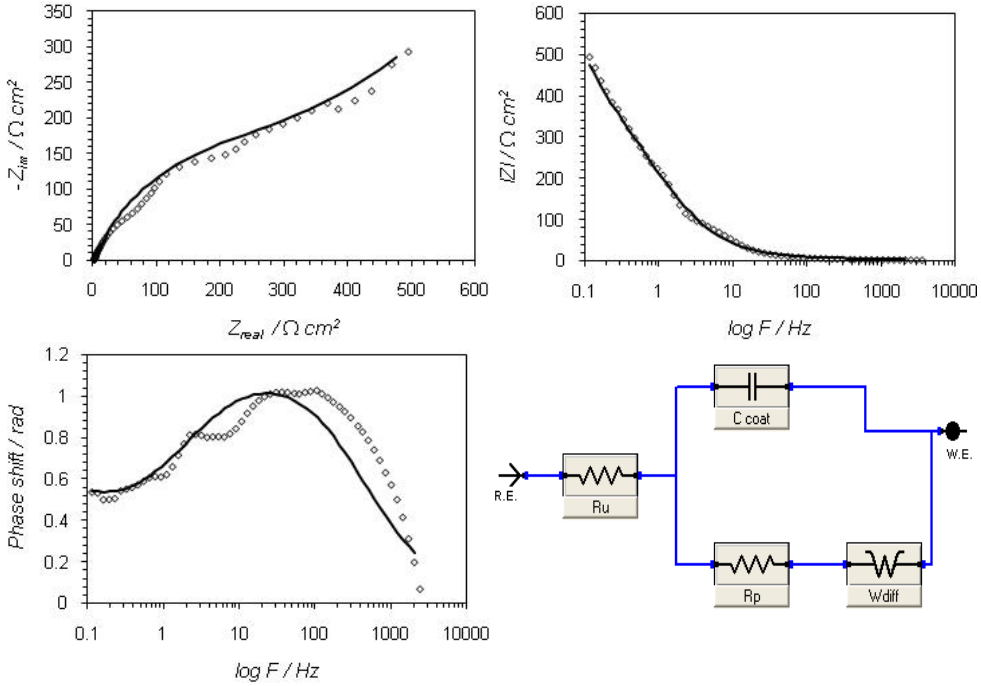

Figure 6-4: ECM fitting with experimental data (reported model)

Table 6-1: EIS results after fitting with reported ECM for HVOF coating

Parameter		Seed values	Fitted values	Error %
R_u (Ω cm^2)		10.0	4.6	-
R_p (Ω cm^2)		300	3.0×10^2	3.2
W (Ω cm^2)		100	2.1×10^2	6.8
CPE	P	5.0×10^4	5.0×10^{-4}	5.9
	n	1.0	7.7×10^{-1}	2.0

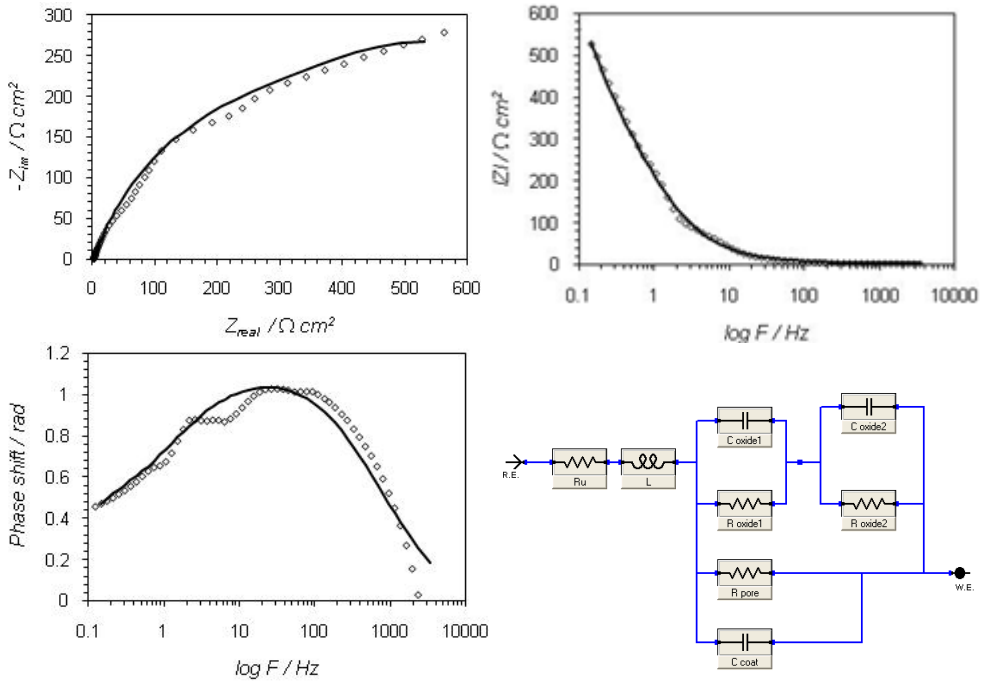

Figure 6-5: ECM fitting with experimental data (proposed model)

Table 6-2: EIS results after fitting with proposed ECM for HVOF coating

Parameter	*Seed values*	*Fitted values*	*Error%*
R_u	10	3.1	-
R_{pore}	50	9.7×10^{2}	3.8
R_{oxide1}	150	5.2×10^{2}	3.0
R_{oxide2}	450	8.5×10^{2}	-
P_{oxide1}	5.0×10^{-4}	5.0×10^{-4}	1.2
n_{oxide1}	1.0	8.2×10^{-1}	5.1
P_{oxide2}	5.0×10^{-4}	4.2×10^{-4}	3.1
n_{oxide2}	1.0	8.4×10^{-1}	1.1
P_{coat}	5.0×10^{-4}	5.0×10^{-4}	7.2
n_{coat}	1.0	6.0×10^{-1}	4.4
L	1.0×10^{-5}	5.3×10^{-7}	-

6.4 EIS results after polarizing to different potentials

Figure 6-6 shows the Bode impedance and the Nyquist plots for bulk Inconel 625, Inconel 625 coating, CoNiCrAlY and WCCoCr coating when samples were potentiodynamically polarized to different potentials before recording the EIS data. After stabilizing in 0.5 M H_2SO_4 for one hour samples all samples were polarized to 100 mV (active corrosion) and 500 mV (passive film formation) with respect to E_{oc}. The EIS data after one hour of stabilizing time, after 100 and 500 mV polarizations were carried out on the same sample. The polarization to different potentials was carried out to correlate the fast surface changes due to corrosion process and their display in the impedance spectra. The experimental impedance spectra were fitted with the ECM in ***Figure 6-2*** and results extracted are summarized in ***Table 6-3.***

The bulk Inconel 625 shows the highest impedance and the CoNiCrAlY coating show the least impedance amongst all tested materials. This was probably due to their different oxidation in acidic media. The bulk Inconel 625

alloy forms a protective oxide layer which protects the surface from further oxidation while the CoNiCrAlY coating severely oxidized in acidic solution. This was also visible from the surface as most of the CoNiCrAlY coating surface where shiny surface turned black and with progressive damage was eaten away by the electrolyte, i.e. actively corroded without forming a protective oxide layer. The XPS analysis showed the corrosion product predominantly consists of Co_2O_3, Cr_2O_3 and NiO (***see section 5.7.2***). The impedance of both bulk Inconel 625 and Inconel 625 coating increases with polarization while decreases for CoNiCrAlY and the WCCoCr coating.

The Bode impedance plots for all tested materials except CoNiCrAlY at E_{oc} and active stage approximately overlap each other indicating that the lower positive potential was not altering the surface to change their impedance value. The Bode impedance and the Nyquist plot for the CoNiCrAlY coating showed the decrease in impedance at E_{oc} and polarization to 100 mV. The decrease in impedance spectra for the CoNiCrAlY coating shows that surface was corroding and hence showing low impedance. Polarizing to 500 mV increases the impedance for bulk Inconel 625 and Inconel 625 coating and decreases for the CoNiCrAlY coating. The decrease in impedance for CoNiCrAlY is attributed to non-adherent mixed oxides at the surface. The Oxide formed at 100 mV was not protective to slow down the corrosion reaction, the higher oxidation rate was also clear from the XPS results (***see section 5.7.2***). We suggested that once the surface is covered with non-protective mixed oxide it did not passivate at 500 mV rather corrode actively. It is also possible that

complete passivation may not be reached for CoNiCrAlY sample, therefore return to active corrosion once the positive potential was removed.

Nyquist plots also showed the same trend, where the capacitive loop of the Nyquist plot at E_{oc} and active stage overlapped for Inconel 625. The Bode impedance plot shows that the impedance of the Inconel 625 coating largely increased when samples were polarized to 500 mV. The impedance of the WCCoCr also decreases by polarizing to 500 mV but decreasing impedance trend with higher positive potential was more pronounced for the CoNiCrAlY coating.

The Nyquist plots for the CoNiCrAlY coating showed a small inverted semi-circle with the graph lifting end at further lower impedance values. This was probably due to inductive behaviour [94]or fast corrosion process at lower frequencies which influx the AC-response signal and lowers the impedance values. The WCCoCr coating also showed some inductance behaviour at higher frequencies probably due to higher porosity of the coatings. The impedance of the WCCoCr coating at passive stage was increased until 0.1 Hz indicating the surface layer was more resistive in this region but the higher side of the impedance overlaps with the impedance spectra at E_{oc} and active stage.

The data was also compared with equivalent circuit model to quantify the results. The small features of the impedance spectra were not considered to avoid complexity and make their parameters comparable with other materials. The ECM model in ***Figure 6-2*** was used for WCCoCr coating, Inconel 625 bulk and coating sample. The Warburg diffusion element was removed for the CoNiCrAlY coating modelling as the Nyquist plot showed the regular half

circle in impedance spectra. The results extracted by comparing the experimental spectra with ECM are summarized in ***Table 6-3.***

The impedance values of the coatings after fitting ECM with experimental data show the R_p value is highest for the Inconel 625 coating and lowest for the CoNiCrAlY coating at E_{oc}. The polarization of the samples to 100 mV before taking EIS data slightly decrease the R_p value of Inconel 625 and WCCoCr coating but decreased to approximately half for the CoNiCrAlY coating. The polarization of the sample to 500 mV before taking EIS data increases the R_p values for Inconel 625 coating but decreases for the CoNiCrAlY coating.

The value of the diffusion impedance *W* also shows the higher value for Inconel 625 as compared to WCCoCr coating. Both parameter *P* and exponent *n* of CPE increase with the polarization for Inconel 625 coating but do not changes for WCCoCr and CoNiCrAlY coatings. This is probably due to less surface change with polarization for WCCoCr coating and continues corrosion of the CoNiCrAlY coating. The less surface change for WCCoCr coating and continuous corrosion for CoNiCrAlY were also evident from potentiodynamic polarization results (see ***section 5.3.2***) and XPS analysis (see ***sections 5.7.3*** and ***5.7.2***). Comparing the bulk Inconel 625 and Inconel 625 coating impedance values are a factor of 10 to 100 higher for bulk Inconel 625, the trend was also consistent with the potentiodynamic polarization results (see ***section 5.2.4***). The corrosion performance parameters by EIS in terms of R_p, *W* and *CPE* were in-line with the potentiodynamic polarization results of E_{corr}, j_{pass} and E_{break} for three coatings and bulk Inconel 625 alloy.

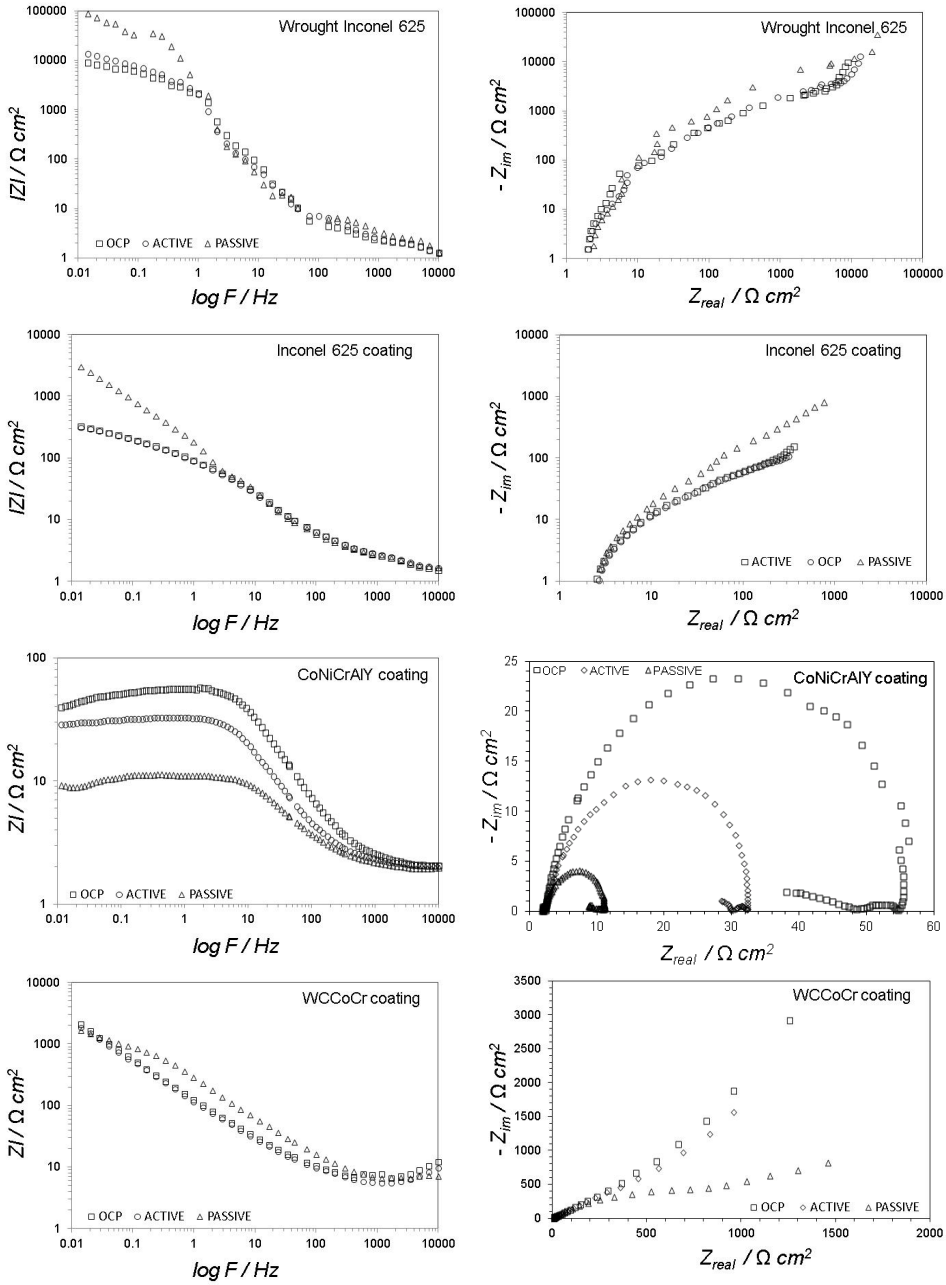

Figure 6-6: Bode impedance and Nyquist plot for bulk Inconel 625, Inconel 625 coating, CoNiCrAlY coating and WCCoCr coating. EIS are recorded at E_{oc}, active (polarized to 100 mV > E_{oc}) and passive (500 mV > E_{oc}) state for all samples.

Table 6-3: EIS results for different materials after fitting with reported ECM

Wrought Inconel 625					Inconel 625 coating		
Parameters		*EIS-OCP*	*EIS-Active*	*EIS-Passive*	*EIS-OCP*	*EIS-Active*	*EIS-Passive*
R_u ($\Omega\ cm^{-2}$)		1.9	1.5	2.0	4.6	6.5	1.3
R_p ($\Omega\ cm^{-2}$)		1.0×10^{4}	6.3×10^{3}	1.8×10^{4}	3.6×10^{2}	4.8×10^{2}	1.7×10^{3}
W ($\Omega\ cm^{-2}$)		5.4×10^{3}	3.3×10^{3}	1.4×10^{4}	2.1×10^{2}	1.8×10^{2}	2.7×10^{2}
CPE	*P*	3.44×10^{-5}	5.03×10^{-5}	2.7×10^{-5}	5.0×10^{-4}	5.0×10^{-4}	5.0×10^{-4}
	n	1.0	9.8×10^{-1}	9.9×10^{-1}	7.7×10^{-1}	8.0×10^{-1}	8.7×10^{-1}
WCCoCr coating					CoNiCrAlY coating		
R_u ($\Omega\ cm^{-2}$)		8.9	7.0	7.0	3.4	2.1	1.4
R_p ($\Omega\ cm^{-2}$)		5.2×10^{2}	3.3×10^{2}	2.7×10^{2}	4.8×10^{1}	2.9×10^{1}	8.9
W ($\Omega\ cm^{-2}$)		3.3×10^{2}	3.2×10^{2}	3.3×10^{2}	-	-	-
CPE	*P*	5.0×10^{-4}	5.0×10^{-4}	5.0×10^{-4}	3.0×10^{-4}	5.0×10^{-4}	5.0×10^{-4}
	n	9.5×10^{-1}	1.0	1.0	1.0	1.0	1.0
The error between ECM and experimental data is below 10% with exception of few elements >10%							

6.5 Evolution processes in HVOF coatings and their EIS response

The HVOF coatings in an electrolyte changes with time due to different physical, chemical and electrochemical processes taking place at the surface. The processes include pore sealing or localized corrosion in pores, change in nature of passive layer or thickness, galvanic corrosion between the substrate-coating if electrolyte penetrates to the surface [277, 278]. The sealing of the pore or oxide thickness growth appears as rise in impedance of the circuit [268, 270, 279]. New time constants can appear in the impedance spectra if substrate corrosion process occurs or nature of the passive layer significantly changes with time [280, 281]. The extent of changes due to corrosion processes depends on the nature of material, environment and time. EIS can be used as a tool to study processes, and extent of change due to different processes can be quantified by fitting the experimental data with equivalent circuit model.

Figure 6-8 shows a set of the Bode impedance and the Nyquist plots for the bulk Inconel 625, Inconel 625 coating, CoNiCrAlY coating and WCCoCr coating. The impedance spectra were gathered by conducting EIS tests after set intervals of times i.e., from 30 min, 1hr, 2hrs, 3hrs, 4hrs 5hrs and 6hrs for every 3 readings. The time was plotted on the third axis of the Bode impedance and the Nyquist plot to see the changes with time. Impedance at high frequencies represent the solution resistance and impedance at low frequencies represent the polarization resistance in the Bode Impedance plot [282].

The Bode impedance plots for the bulk Inconel 625 showed that at lower frequencies the impedance was increased for first 5-7 hours before reaching to approximately constant value. The maximum impedance was 10000 Ω cm^2 around 0.1 Hz frequency. The increase in impedance with time correlate well with results for E_{oc} vs. time (see ***section 5.3.1***) where E_{oc} shifts to more positive values with the time for first 10 hours indicated oxide layer growth. A slight hump can be seen around 1 Hz, this was probably due to an oxide of higher resistance. The impedance data in the Nyquist plot also showed the vertical lift at the higher impedance side of the real axis. The impedance spectra after 20 hours were approximately similar indicating no change was occurring after 20 hours and surface was probably covered with oxide layer.

The Bode impedance spectra for Inconel 625 coating showed the gradual increase in impedance from 300 to 500 Ω cm^2 after 0.5 to 11 hrs. The minimum impedance was around 200 Ω cm^2 after 72 hrs. The initial rise in the impedance was probably due to formation of the oxide which covers the surface and slow down further oxidation. Due to extended time in reactive

electrolyte and presence of surface defects on the coating, other types of less protective oxide may formed which decreases the overall impedance of the coating [8]. The time evolution results for the Inconel 625 coating correlate with the E_{oc} -time graphs except for first 2-3 h where coating E_{oc} shifts towards negative potential. This could probably due to slightly different exposed surface as it is largely believed that 10 mV potential and EIS test do not change the exposed surface [95, 147, 148].

The CoNiCrAlY coating showed the least polarization resistance at lower frequencies than rest of the materials. The progressive degradation was also faster in CoNiCrAlY coating where the highest impedance decreased from 50 Ω cm^2 to 5 Ω cm^2 after 72 hours. The size of the semi-circle in the Nyquist plot clearly shows the progressive degradation. We suggest from our results after 5 hours the coating was fully damaged and possibly electrolyte penetrated to the substrate. The cross section micrographs of CoNiCrAlY coating in ***Figure 6-7*** after 72 hours also showed significant loss in the coating thickness. The progressive decrease in the E_{oc} vs. time (see ***section 5.3.1***), intensive oxidation with polarization and XPS results also proof the severe corrosion of the CoNiCrAlY coating in 0.5M H_2SO_4

The progressive degradation of the WCCoCr coating was also apparent from the Bode impedance and the Nyquist plots. The highest impedance was measured at the start and lowest after 72 hours. The Nyquist plots also show the bigger curvature at start than the end.

It can be concluded from above results that bulk Inconel 625, Inconel 625 coating, CoNiCrAlY and WCCoCr coatings degrade progressively in 0.5 M

H_2SO_4. The degradation of Inconel 625 and WCCoCr coatings with time was slower than the CoNiCrAlY coating. The degrading only display change in the impedance and do not change the shape of impedance spectra.

The corrosion performance ranking of the three different coatings and bulk Inconel 625 alloy was same from the time evolution EIS as that for the EIS-polarization and potentiodynamic polarization testing. The impedance values were a approximately a factor of 100 higher the bulk Inconel 625 alloy as compared to Inconel 625 coating. Amongst the three coating samples the Inconel 625 coating has the highest impedance values and the CoNiCrAlY has the lowest impedance values over all intervals of times.

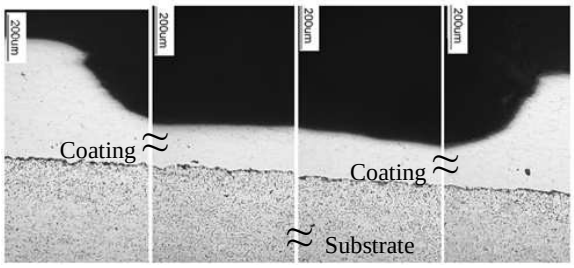

Figure 6-7: Cross section view of CoNiCrAlY coating after 72 hours in 0.5 M H_2SO_4

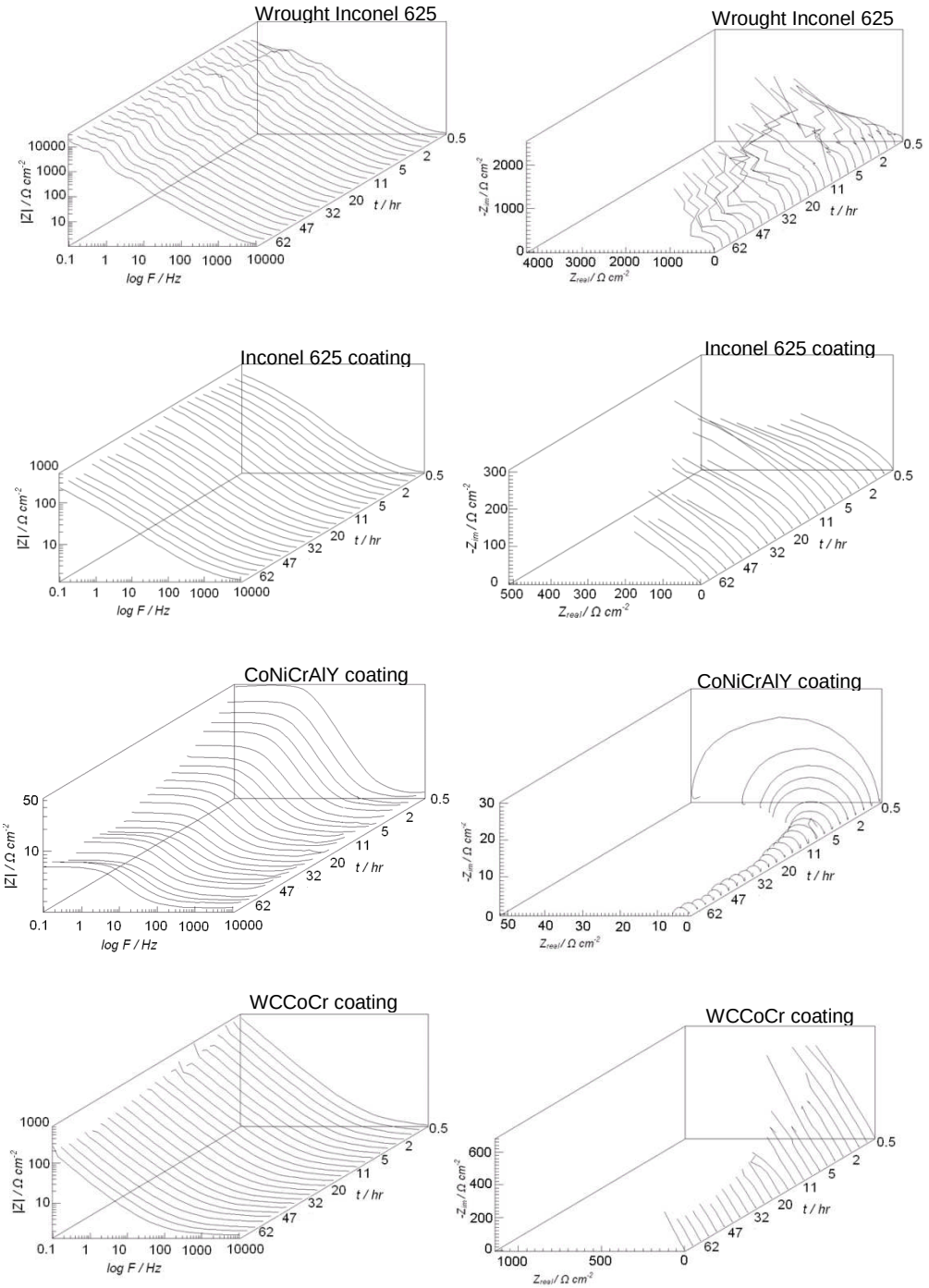

Figure 6-8: Bode and Nyquist plots for bulk Inconel 625, Inconel 625 coating, CoNiCrAlY coating and WCCoCr coating for 0.5 to 72 hours in 0.5 M H_2SO_4.

6.6 ET kinetic rate constant from EIS results

The R_p value obtained at E_{oc} from electrochemical impedance spectroscopy data shown in ***Table 6-3*** is used to calculate the kinetic of heterogeneous ET rate constant for bulk Inconel 625, Inconel 625 coating, CoNiCrAlY coating

and WCCoCr coating. The procedure described in ***section 0*** is used to obtain the ET rate constants.

The ET rate constant for different materials were found in the same ranking as the one obtained from potentiodynamic polarization data i.e. highest for the WCCoCr coating and lowest for the Inconel 625 coating. The rate constant for the bulk Inconel 625 was a factor of 100 lower than that of the Inconel 625 coating. The rate constant obtained for all materials from EIS data was a factor of 10 higher than the one obtained from polarization data. The high rate constant in EIS is attributed to elimination of solution resistance and capacitance. The heterogeneous ET rate constants calculated from potentiodynamic polarization and EIS were in corrosive environment i.e. 0.5M H_2SO_4 solution. No particular reaction was identified in potentiodynamic polarization and EIS technique therefore the estimation of the rate constant is to get general idea how fast or slow reactions are taking place. The rate constant calculated from SECM is the one for the reduction and oxidation of FcOH across electrode/electrolyte interface hence the rate constant values from SECM is real and more accurate than other methods

Table 6-4: ET rate constant obtained from the EIS data

Material	R_P / Ω cm^2	i_0 / A cm^{-2}	k^0 / cm s^{-1}
Wrought Inconel	1.00×10^{4}	2.57×10^{-6}	5.32×10^{-11}
Inconel coat	3.60×10^{2}	7.13×10^{-5}	1.48×10^{-9}
CoNiCrAlY coat	5.20×10^{5}	4.94×10^{-5}	1.02×10^{-9}
WCCoCr coat	4.80×10^{1}	5.35×10^{-4}	1.11×10^{-8}

6.7 Summary

- Some of the microstructure features of HVOF coating can be correlated to EIS results by electrochemical equivalent circuit modelling but full compliance between ECM and microstructure is difficult to establish due to complex microstructure of the HVOF coating.
- The electrochemical and physical features of the HVOF coatings display their partial appearance as rise or fall in impedance spectra at different frequencies. The corrosion process changes the overall impedance spectra but change in the ECM is only required when impedance spectra significantly changed from original values.
- The corrosion performance of the materials ranking by EIS parameter, $R_{p,}$ W and CPE was in-line with corrosion performance ranking by potentiodynamic polarization testing where $E_{corr,}$ j_{pass} and E_{break} are the main corrosion performance ranking parameters.
- The impedance values for the bulk Inconel 625 at E_{oc} were a factor of 10 to 100 higher than the Inconel 625 coating. The impedance values after 100 and 500 mV polarizations were also higher for the bulk alloy than the coating.
- Impedance for the Inconel 625 and WCCoCr coatings were slightly decreased when polarized to 100 mV but for the CoNiCrAlY coating impedance decreased to approximately half as compared to E_{oc}.
- The impedance values for the Inconel 625 were increased but decreased for the WCCoCr and CoNiCrAlY coatings when polarized to 500 mV.

- The time evolution results were consistent with the E_{oc} vs. time results. The ranking of the different materials by EIS was also in-line with the potentiodynamic polarization testing and XPS analysis.
- The heterogeneous ET rate constant obtained for different materials was in the same ranking as the one obtained from polarization data. The rate constant by a factor 10 from EIS data is attributed to elimination of solution resistance and capacitance.

7 Scanning electrochemical microscopy

7.1 Introduction

In this chapter the electrochemical activity at the stainless steel, bulk Inconel 625 and Inconel 625 coating is quantified by measuring standard heterogeneous ET reaction rate constant (k^0) across substrate electrolyte interface. The microelectrode tip potential was kept at 0.6 V to drive oxidation of ferrocenemethanol (FcOH) and substrate potential was systematically changed to drive oxidation and reduction at the substrate. Before recording the kinetic data the electrochemical activity at the substrate was also visualized by SECM imaging and confirmed by SECM feedback approach curves. The chapter also includes the cyclic voltammograms (CV) of different materials as well as the steady and non-steady CV to extract the electrochemical reaction information.

7.2 Cyclic Voltammetry at Platinum, Inconel 625 and stainless steel electrodes

Figure 7-1a, b, c and d show the cyclic voltammograms for platinum disc, bulk Inconel 625, Inconel 625 coating and stainless steel samples at a scan rates of 10, 20, 30, 40, 50, 60 and 70 mV s^{-1}. All CVs were recorded in 1M K_2SO_4 containing 1mM FcOH solution. The oxidation of FcOH takes place in forward scan and reduction in the reverse scan. The redox peak potentials and currents of FcOH extracted from the cyclic voltammograms at different scan rates of all materials are summarized in ***Table 7-1***. The cyclic voltammograms were analysed to extract characteristic information about the reactions taking place at the substrate surfaces. At the Pt substrate, the response was essentially reversible; the ratio of the anodic and cathodic peak currents ($i_{p,a}/i_{p,c}$) was approximately 1, the peak-to-peak separation (ΔE_p) was approximately 60 mV, the anodic ($E_{p,a}$) and cathodic ($E_{p,c}$) peak potentials were independent of the scan rate (υ) and peak current (i_p) was proportional to square root of scan rate ($\upsilon^{1/2}$) [106]. However, the CVs obtained at the bulk Inconel 625 substrate, the Inconel 625 coating and at the stainless steel surface were all markedly different to that obtained at Pt.

ΔE_p for FcOH oxidation and reduction was greater than 60 mV in each case and increased with the scan rate, as expected for kinetically controlled heterogeneous ET reactions. In case of the stainless steel surface, the reduction peak of $FcOH^+$ was observed at approximately -100 mV and the oxidation peak for FcOH was at approximately 700 mV. The oxidation peak

of FcOH at stainless steel was obscured by the presence of a large peak at approximately 1100 mV. Unlike the peaks due to FcOH oxidation and reduction observed at each substrate surface, i_p for this peak was proportional to υ, suggesting that it was due to a surface oxidation process. To confirm that this was a surface oxidation peak, a CV was recorded at the stainless steel surface in blank K_2SO_4, shown by the solid line of the innermost CV in ***Figure 7-1***d. The presence of this peak in the CV obtained in the blank electrolyte clearly shows that the peak was due to oxidation of the stainless steel surface.

Figure 7-2 show the i_p vs. $\upsilon^{1/2}$ for oxidation of FcOH at platinum, bulk Inconel 625 and Inconel 625 coating and i_p vs. υ for stainless steel. The plot shows straight line with higher gradient of the line for platinum than bulk Inconel 625 and Inconel 625 coating. The gradient of line is lower for the bulk Inconel 625 than the Inconel 625 coating sample.

The oxidation of FcOH was not clear at the stainless steel sample and peak fully disappeared in the reverse scan, therefore it was not possible to plot the i_p vs. $\upsilon^{1/2}$ for stainless less steel. The suppression/disappearance of the reverse peak is probably due to formation of the oxide layer at the stainless steel surface which limits the ET reaction. The passivation of stainless steel in sulphate containing environments is well reported in the literature [239, 283]. The plot between i_p vs. υ showed a straight line for the stainless steel, indicating the surface oxidation stainless steel. From the above peak current vs. scan rate relationship, one can suggest that ET rate at Pt substrate is faster compared to the other samples.

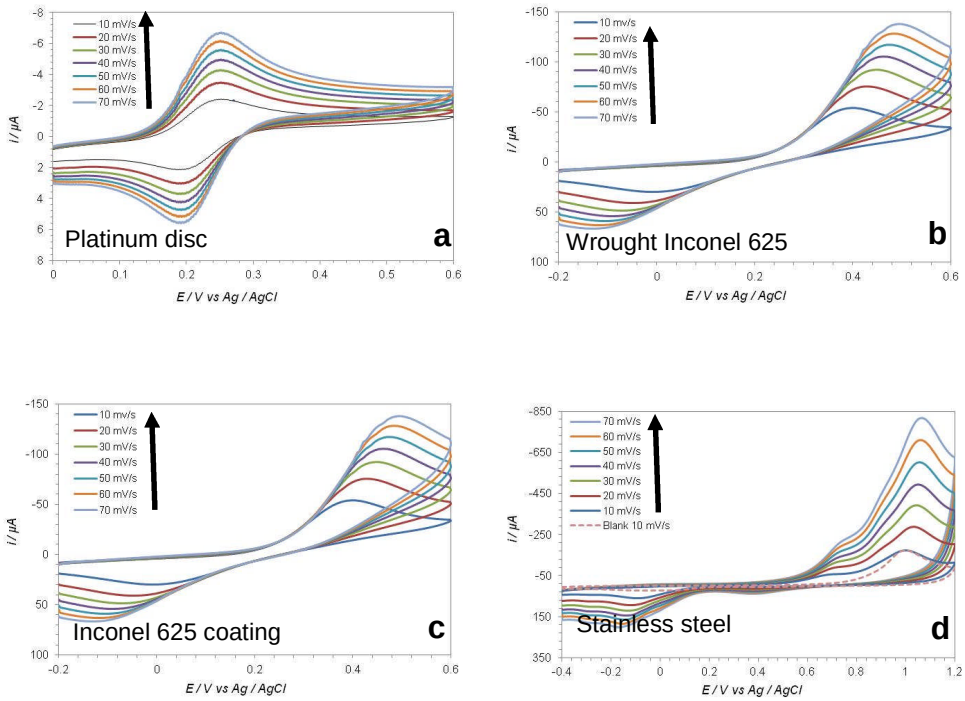

Figure 7-1: Cyclic voltammograms of a) 2mm Platinum electrode, b) bulk Inconel 625, c) Inconel 625 coating, d) stainless steel obtained in 1mM FcOH in 0.1M K_2SO_4. All CVs were recorded at a scan rate of 10, 20, 40, 50, 60 and 70 mV s^{-1} and potential limits were a) 0.0 to 0.6 V, b) -0.2 to 0.6 V, c) -0.2 to 0.6 V and d) -0.4 to 1.2 V respectively. The solid line 10 mV s^{-1} in d shows the voltammogram obtained at stainless steel in blank 0.1 M K_2SO_4 solution.

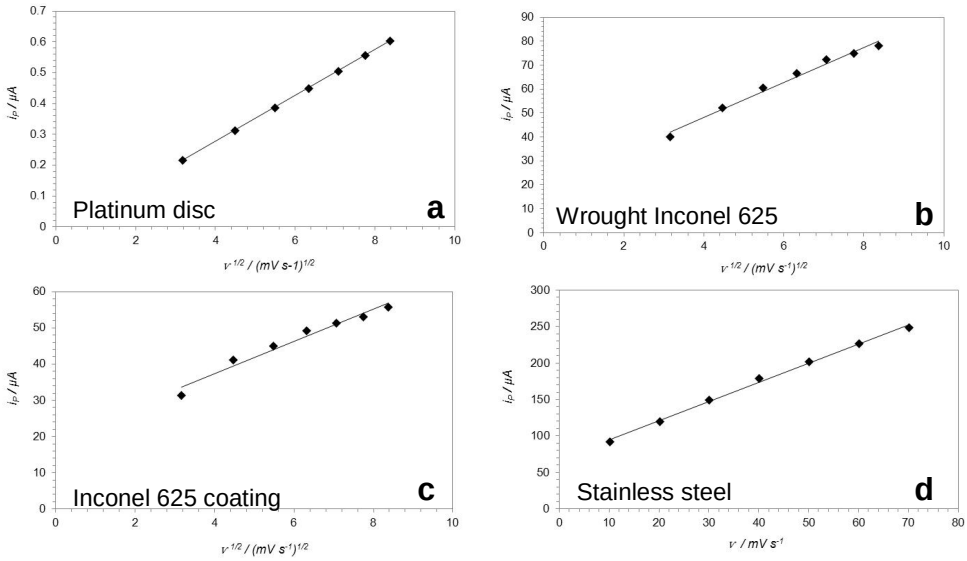

Figure 7-2: Peak current vs. square root of the scan rate trend for a) Pt-disc electrode, b) bulk Inconel 625, c) Inconel 625 coating and d) current vs. scan rate for stainless steel.

Table 7-1: Results extracted from cyclic voltammograms of different materials

Platinum								
Scan rate mV s^{-1}	*E_{pa} / mV*	*E_{pc} / mV*	*i_{pa} / µA*	*i_{pc} / µA*	*ΔE_p / mV*	*$E_p - E^{0\prime}$*	*E_{po} / mV*	*i_{po} / µA*
10.0	252.0	192.0	2.2	-2.5	60.0	30.0	-	-
20.0	252.0	192.0	3.1	-3.4	60.0	30.0	-	-
30.0	252.0	192.0	3.9	-4.1	60.0	30.0	-	-
40.0	252.0	192.0	4.5	-4.8	60.0	30.0	-	-
50.0	252.0	192.0	5.0	-5.3	60.0	30.0	-	-
60.0	252.0	192.0	5.6	-5.8	60.0	30.0	-	-
70.0	252.0	192.0	6.0	-6.3	60.0	30.0	-	-
Wrought Inconel 625								
10.0	399.0	5.0	40.1	-30.0	394.0	197.0	-	-
20.0	428.0	46.8	52.2	-41.1	381.2	190.6	-	-
30.0	450.0	70.3	60.6	-48.4	379.7	189.9	-	-
40.0	464.0	82.1	66.4	-54.4	381.9	191.0	-	-
50.0	471.0	104.3	72.1	-59.6	366.7	183.4	-	-
60.0	485.0	106.9	74.9	-63.5	378.1	189.1	-	-
70.0	493.0	129.0	78.1	-66.7	364.0	182.0	-	-
Inconel 625 coating								
10.0	417.0	33.7	31.3	-28.1	383.3	191.7	-	-
20.0	446.0	88.6	41.1	-39.0	357.4	178.7	-	-
30.0	464.0	106.9	44.9	-46.6	357.1	178.6	-	-
40.0	475.0	142.2	49.2	-52.5	332.8	166.4	-	-
50.0	490.0	165.8	51.3	-57.7	324.2	162.1	-	-
60.0	500.0	178.8	53.0	-61.7	321.2	160.6	-	-
70.0	504.0	186.7	55.7	-66.2	317.3	158.7	-	-
Stainless steel								
10.0	701.0	-91.0	55.4	-30.5	792.0	396	1001.0	91.6
20.0	722.1	-121.0	91.7	-33.0	843.1	421.5	1030.0	119.2
30.0	730.0	-130.0	119.3	-28.6	860.0	430	1041.0	149.2
40.0	737.7	-139.0	143.9	-21.4	876.7	438.3	1048.0	178.2
50.0	748.2	-139.0	173.1	-21.4	887.2	443.6	1055.0	201.9
60.0	753.5	-151.0	202.1	-185.5	904.5	452.2	1058.0	226.5
70.0	763.9	-161.5	232.5	-205.0	925.4	462.7	1066.0	248.2

E_{pa} = anodic peak potential, E_{pc} = cathodic peak potential, i_{pa} = anodic peak current, i_{pc} = cathodic peak current, ΔE_p = difference in peak potential, $E^{0\prime}$ = Formal potential, E_{po} = oxide peak potential, i_{po} = oxide peak current

7.3 ET rate constant calculation from CV data

The data obtained from CV of different materials given in ***Table 7-1*** was used to calculate the ET rate constant. The value E_p was used to find the charge transfer coefficient (α) by sing ***equation 7.1*** [105]. The quasi-reversible kinetic equations were not applicable as the ΔE_p was greater than 212 mV [284, 285] .

$$\propto = \frac{47.7}{(E_p - E_{\frac{p}{2}})} \qquad \textbf{7.1}$$

$$k^0 = 2.18\left(\frac{\propto DnF\upsilon}{RT}\right)^{\frac{1}{2}} \times e^{\propto nF(E^0 - E_p)/RT} \qquad \textbf{7.2}$$

The values of α were later used in ***equation 7.2*** to calculate the heterogeneous ET rate constant for different materials. In ***equation 7.2***, D is diffusion coefficient which is 7.80×10^{-6} cm^2 s^{-1} for aqueous solution, $E^{0'}$ formal potential a value of 0.22 V was used in our calculations [105]. The kinetic values obtained from the CVs of different materials are summarized in ***Table 7-2***.

It can be seen from results in ***Table 7-2*** that the rate constants for the Inconel 625 both in coating and bulk form were higher than the stainless steel. The small rate constants indicating slow electron transfer reaction for stainless steel. The slow electron transfer at stainless steel also correlates well with the potentiodynamic and XPS results, where polarization curve for stainless steel show low passivation current and XPS spectra show predominantly uniform Cr_2O_3 layer on the surface. (***see section 5.2.1 and 5.7.5***). As expected from the results the k^0 value also increases with the scan rate for all materials.

Table 7-2: Kinetic data extracted from cyclic voltammogram data

Scan rate	Stainless steel		Bulk Inconel 625		Inconel 625 coating	
υ / mV s^{-1}	α	k^0 cm s^{-1}	α	k^0 cm s^{-1}	α	k^0 cm s^{-1}
10	1.56×10^{-1}	4.61×10^{-5}	2.36×10^{-1}	3.73×10^{-4}	2.12×10^{-1}	4.55×10^{-4}
20	1.59×10^{-1}	4.55×10^{-5}	2.01×10^{-1}	6.82×10^{-4}	1.78×10^{-1}	8.74×10^{-4}
30	1.59×10^{-1}	4.99×10^{-5}	1.83×10^{-1}	9.01×10^{-4}	1.67×10^{-1}	1.10×10^{-3}
40	1.59×10^{-1}	5.16×10^{-5}	1.75×10^{-1}	1.06×10^{-3}	1.55×10^{-1}	1.52×10^{-3}
50	1.57×10^{-1}	5.75×10^{-5}	1.66×10^{-1}	1.34×10^{-3}	1.45×10^{-1}	1.80×10^{-3}
60	1.58×10^{-1}	5.44×10^{-5}	1.61×10^{-1}	1.38×10^{-3}	1.41×10^{-1}	2.01×10^{-3}
70	1.58×10^{-1}	5.16×10^{-5}	1.53×10^{-1}	1.67×10^{-3}	1.38×10^{-1}	2.21×10^{-3}

7.4 Steady and non-steady state CV

Figure 7-3 shows the CVs for a 3mm platinum disc electrode (dotted line) and 25µm platinum UME (solid line). Both experiments were carried out in 1M K_2SO_4 solution containing 1mM FcOH as a redox mediator. The CVs were recorded within the applied potential limits of 0 to 0.6 V at a scan rate of 20 mV s^{-1}. The right to left current axis in ***Figure 7-3*** show for 25 µm microelectrode and 3mm macroelectrode.

The CV for the 3mm Pt-disc electrode shows oxidation current peak around 0.252 V and reduction current peak around 0.192 V when applied potential was ramped from 0 to 0.6 V. The peaks occur due to predominant linear diffusion at the 3mm Pt-disc electrode. The CV for the 25µm microelectrode does not show oxidation or reduction peaks instead a plateau of current around 1nA and -3nA. The microelectrode allows predominant radial diffusion to form hemispherical shape diffusion layer which extends out into solution. The hemispherical shape diffusion layer at microelectrode eliminates the current peak.

The area between forward and reverse scan curves was also decreased for the microelectrode CV indicating lower charging current at the microelectrode [166]. The charging current during potentiodynamic testing depends on the surface area; the decrease in the charging current was attributed to lower surface area of the microelectrode [105]. The current increased at higher rate from 0.20 V to 0.35 V, the region is called activation region. In activation region the reaction rate is controlled by ET reaction between redox mediator and the electrode. The rate of exchange of electron between the electrode and redox mediator was comparable with the diffusion of analyte. The reaction was diffusion controlled from 0.35 V to 0.6 V and shows the steady current value. In diffusion controlled reaction, the rate of exchange of the electron was faster than the diffusion of redox mediator to the electrode hence rate of reaction rate is governed by analyte availability to the electrode surface. The magnitude of the current was much lower for the microelectrode than the disc electrode due to smaller electrode area [105, 172, 286].

The electro-active area of microelectrode is very small therefore the time required to charge the double layer is very short. The charging of the double layer decays with $R_u\ C_{dl}$, also called as time constant (τ). The τ for the double layer charging is given by the equation $a\ C^0/4\kappa$, where 'a' is tip radius and κ is solution conductivity and C^0 is the capacitance per unit area. The 95% of the double layer charging completes by the time equal to 3 τ. The meaningful results (faradaic current) can only be obtain after $t > 5\ \tau$, where convolution of the charging current is minimum [105]. The decrease in the τ is the result of decreasing radius of the microelectrode, hence the small C_{dl} facilitates the

rapid changes in the electrode potential (fast response time) and almost eliminates the charging current effect.

When current flows through electrochemical cell an ohmic drop occurs which causes the true potential to differ from applied potential by an offset of iR_u ($E_{true} = E_{applied} - iR_u$), where i is net current and R_u is uncompensated solution resistance between *RE* & *WE* [130]. The bigger the value of iR_u, the higher will be difference between applied and actual potential. The higher iR_u can cause separation of the peak potential and distort the current response of the CV at macroelectrode [214, 287]. The net current decreases with the radius of the electrode. ***Figure 7-3*** shows that the current decreased to 1000 times by decreasing the radius of the electrode from 1.5 mm to 12.5 µm. The low current flow at microelectrode almost eliminates the *iR* losses and make it possible to carry out electrochemistry in highly resistive electrolytes [130].

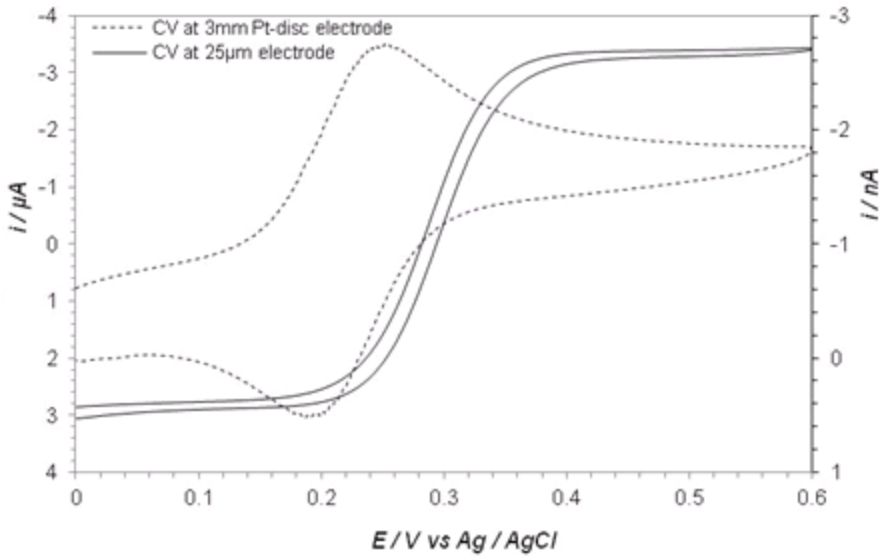

Figure 7-3: Cyclic voltammogram at 3mm platinum disc (dotted line) and 25µm microelectrode (solid line) in 1mM FcOH in 0.1M K_2SO_4 at a scan rate of 20 mV s^{-1}. The current axis from right to left shows for 25µm and 3mm diameter electrodes.

7.5 SECM imaging and SECM feedback approach curves at stainless steel

Before recording SECM imaging working stage should be fully aligned. The problem arises due to improper bevelling of the microelectrode tip or uneven substrate surface which allows the glass sheath of the microelectrode to touch the substrate surface instead of metal part (in ***Figure 7-4***A). The left side of the ***Figure 7-4***A also shows the redox reaction between the tip substrate. The oxidation for the FcOH occurs at the SECM tip (tip potential at 0.6V) and form $FcOH^+$. In case of conductive surface $FcOH^+$ get reduced at the substrate surface while no reduction occurs in case of insulting surface.

The stage was aligned horizontally by adjusting the micro-screws of the working stage before SECM imaging. The flatness of the substrate surface relative to the tip of the microelectrode was achieved by recording SECM feedback approach curves on the four connecting points of the 500×500 µm square. The SECM current distance feedback curves were carried out on four points a, b, c, d as shown in ***Figure 7-4***B until all points give maximum feedback at same height. When the surface became approximately flat another SECM feedback approach curve was carried out to keep the microelectrode tip in the current feedback region. This was done by crashing the tip to maximum current feedback from the substrate surface, than lift up the tip to 4 µm. The SECM imaging was carried out by raster scanning of the microelectrode tip.

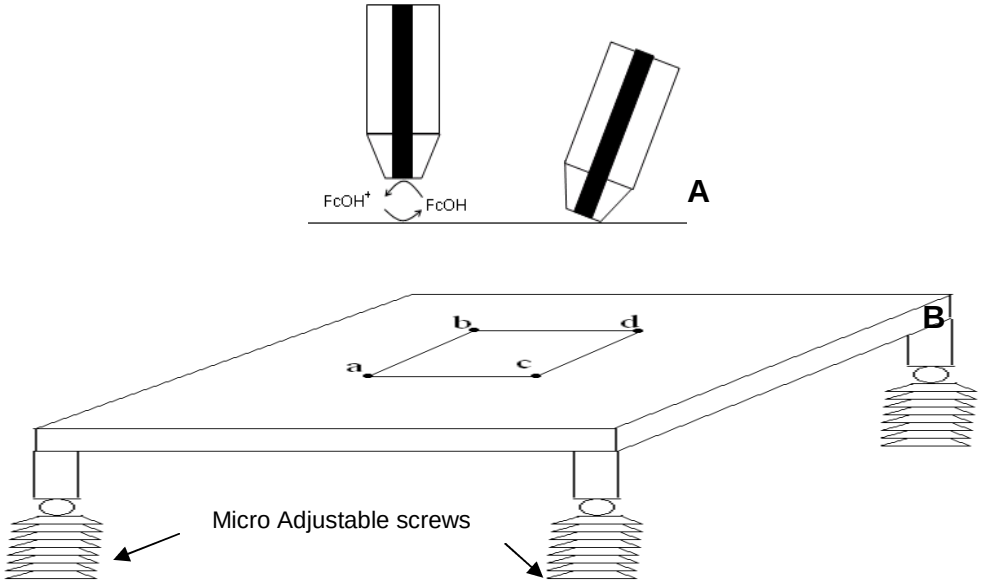

Figure 7-4: Schematic of SECM table levelling for SECM imaging

The SECM image and SECM feedback approach curves at different regions of the stainless steel sample are shown in ***Figure 7-5***. The substrate was kept at E_{oc} during SECM imaging and recording SECM feedback approach curves. The current feedback at the surface was -3.42nA to -3.67nA over the image area. The green region of the surface shows the lowest current and brown region the highest. The different colour contrast regions are separated in the SECM image by dotted lines.

The SECM feedback approach curves were recorded at the regions of different colour contrast. It is general practise to normalize the tip current against steady state tip current and tip-substrate distance normalized with radius of the tip. The thin solid lines in ***Figure 7-5***B are normalized experimental SECM feedback approach curves and open circles are pure negative feedback generated from theoretical approximation equation (***see section 4.6***). For each SECM feedback approach curve the tip of the microelectrode was lifted to 6*L* i.e. approximately 80 µm and moved to the different black spots shown in

Figure 7-5A one by one. The tip potential was kept at 0.6 V during recording SECM feedback approach curves. The tip was scanned downward until it touched the substrate surface to record the feedback from substrate. The SECM feedback approach curves not fully overlap the theoretical curves around *1L* to *2L* and the minimum current did not reach to 0 for all six curves.

The stainless steel forms a protective oxide layer in air which stops or slowdown the further oxidation of the surface [239, 283]. The XPS results (***see section 5.7.5***) also indicated that stainless surface was predominantly covered with Cr_2O_3. The SECM image was taken in electrolyte containing redox mediator showed slight variation of current over the surface which was probably due to different electrochemical activity at the surface or slight tilt in the sample. To check if the different colours of the image are due to electrochemical activity or surface tilt, SECM feedback approach curves were done on different regions of image. For all six spots, the current decreases as the tip of the microelectrode reached to the substrate, this indicates that the surface is behaving as insulator and not allowing reduction of $FcOH^+$ at the substrate surface.

The lower end (*L* less than 1) of the SECM feedback approach curves becomes approximately horizontal. This was probably due to slightly uneven surface geometry of the microelectrode tip which allowed the edge of the glass shield of the tip to touch the substrate leaving the Pt-wire at non zero *L* [178, 180]. The schematic in right side of ***Figure 7-5***A show the same situation where Pt-wire stayed at some distance although the tip of the microelectrode tip was at zero tip-substrate distance. The experimental SECM feedback approach curves

did not fully overlap the theoretical curves, indicating the feedback was not pure negative and allowed some ET across the stainless steel electrolyte interface [82, 288].

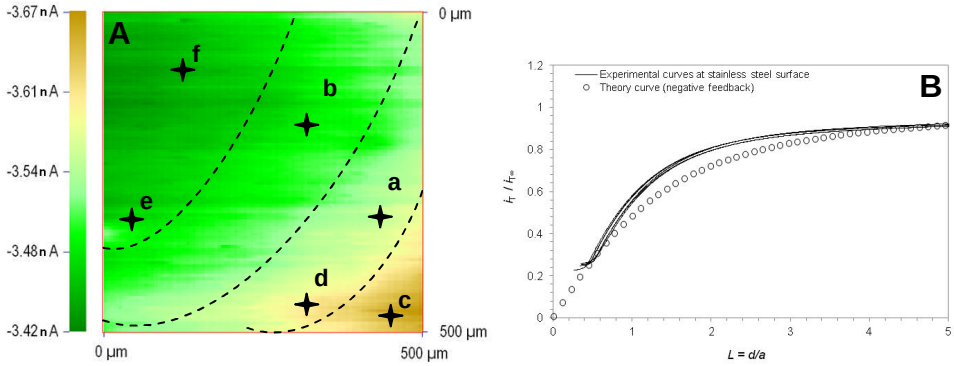

Figure 7-5: SECM image (a) and current distance SECM feedback approach curves (b) for stainless steel in 1mM FcOH in 0.1M K_2SO_4 by using 25µm diameter disc shaped platinum electrode with a R_g value ≈ 10. The tip was held at 0.6 V to drive the oxidation of FcOH at diffusion limited rate, the substrate was at E_{oc}. The SECM image was obtained by measuring i_T at a constant vertical tip-substrate distance of ≈ 4µm = 0.3L. The tip was scanned laterally at 250µm s^{-1} in x-plane and increasing step of 5µm in y-plane. The SECM feedback approach curves a-f, were obtained from the sites indicated in fig 1-4a by vertically scanning the tip from finite distance to the maximum current feedback at the substrate. The tip vertical downward speed was kept at 2µm s^{-1}.

7.6 SECM imaging and SECM feedback approach curves at bulk Inconel 625

Figure 7-6A and B show a 500×500 µm SECM image and normalized SECM feedback approach curves for bulk Inconel 625. The adjustment of the tip substrate flatness and height of the tip was done as previously for other materials. The two colour image display different regions of lower and higher feedback current. The feedback current was within the limit of -3.31nA to -3.51nA. The regions of different colour are separated by dotted lines to check the difference of electrochemical activity. The XPS results have showed (***see section 5.7.4***) that oxide layer at the bulk Inconel 625 alloy contained Cr_2O_3,

NiO, MoO and Nb_2O_5. To check the current variation was either due to presence of different oxides on the surface or surface tilt, SECM feedback approach curves were recorded at different regions of the surface.

All SECM feedback approach curves at different regions gave the negative feedback. The experimental curves were fitted with the theoretical curves and the data fit well with theoretical curves. This indicates that there was not significant electrochemical variation of different regions at the surface. The bulk Inconel 625 alloy form protective oxide layer which works as a barrier between redox mediator and metallic surface, preventing ET and hence not allowing reduction of the $FcOH^+$. The different regions marked on the SECM image show slight variation in the current, this is probably due to the surface tilt from left to right. The surface tilt caused the SECM feedback to record at different tip-substrate heights.

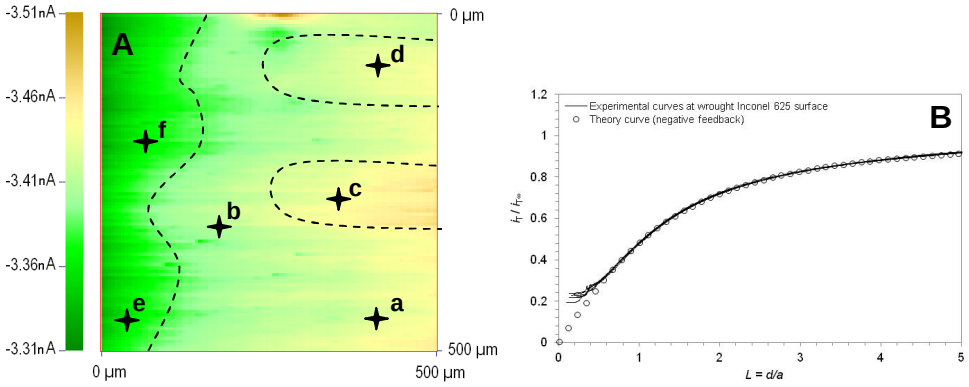

Figure 7-6: SECM image and current distance SECM feedback approach curves for bulk Inconel 625 in 1mM FcOH in 0.1M K_2SO_4 by using 25µm diameter disc shaped Pt-electrode with a R_g value of ≈ 10. The tip was held at 0.6 V to drive the oxidation of FcOH at diffusion limited rate, the substrate was at E_{oc}. The SECM image was obtained by measuring i_T at a constant vertical tip-substrate distance of ≈ 4µm = 0.3L. The tip was scanned laterally at 250µm s^{-1} in x-plane and increasing step of 5µm in y-plane. The SECM feedback approach curves at black spots were obtained by vertically scanning the tip from finite distance to the maximum current feedback at the substrate. The tip vertical downward speed was kept at 2µm s^{-1}.

7.7 Repeatability of SECM imaging on heterogeneous materials

Figure 7-7A, B, C shows the SECM images taken consecutively at the same 500×500 µm area for Inconel 625 coating. The scan time for each run was approximately 5 minutes. The experimental parameters were kept same to visualize the changes occurred with time. The minimum and maximum current measured was -1.40 nA to -5.15 nA for the first scan, -1.37 nA to -4.94 nA for the second scan and -1.34 to -3.17 nA for the third scan. This indicates that the minimum value of feedback current did not change but the maximum feedback current values change. This was probably due to decrease of electrochemical activity of the highly active site at the start of experiment. The surface features can be more clearly seen in ***Figure 7-7***A and fade off in the later scans.

Three clearly defined regions a, b and c are marked with dotted lines in three SECM images. The high feedback current region “a” appear around 5nA in ***Figure 7-7***A. The value of the feedback current decreased and features of SECM image fade off in ***Figure 7-7***B and C. In first SECM image the region was allowing the effective ET reaction across the electrode electrolyte interface, which may be slow down due to formation of partial oxide layer in B and C image. The region “b” in ***Figure 7-7***A also show features of low and high current disappeared in ***Figure 7-7***C. In the region “c” of ***Figure 7-7***A the predominant colour was green some light green and brown features. The visibility of these features decreased in ***Figure 7-7***B and disappeared in ***Figure 7-7***C. It can be established from the results that the electrochemical

activity at the surface is slightly changed with the time which caused the SECM features to disappear with repeated scans.

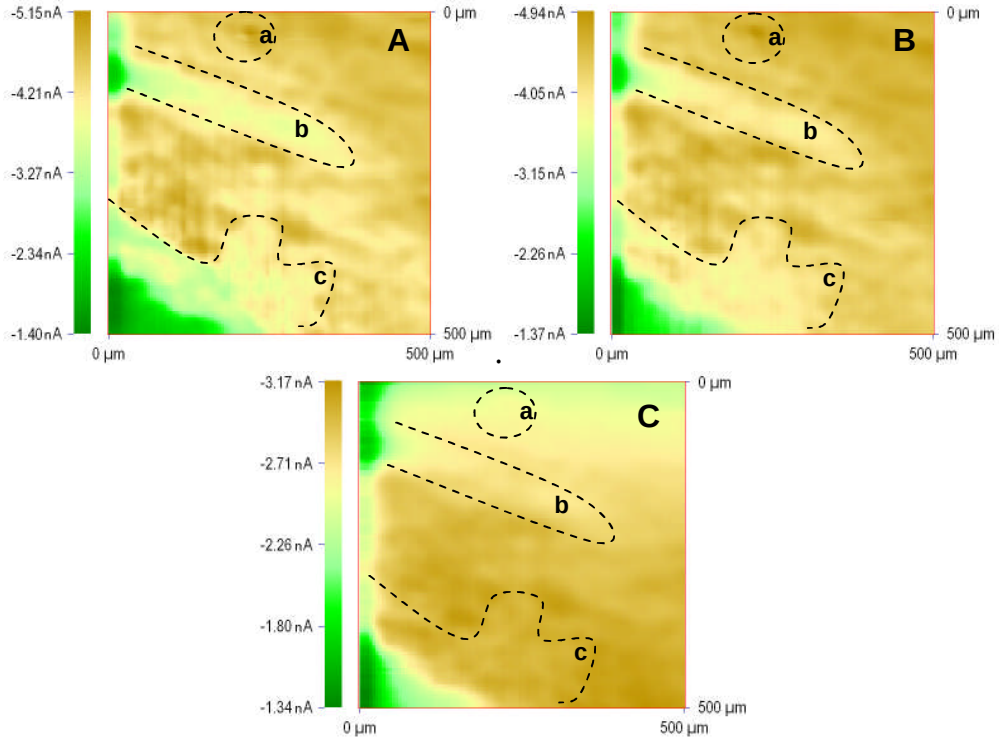

Figure 7-7: Same spot imaging for Inconel 625 coating to observe the surface changes

7.8 SECM imaging and SECM feedback approach curves at Inconel 625 coating

Figure 7-8A, B show the SECM image for Inconel 625 coating and SECM feedback approach curves at regions of different electrochemical activity. The 500×500 µm SECM image show the regions of different electrochemical activity spread all over the surface. The feedback current at constant tip height was within the limit of -4.57nA to -6.32 nA. The current feedback variation over the Inconel 625 coating sample was higher than stainless steel and bulk Inconel 625 alloys.

The surface oxide layer of the Inconel 625 coating has the same constituents as that for the bulk Inconel 625. It was clear from the SECM imaging of the bulk alloy that different oxide were not making the difference in the feedback current. To see if the microstructure of the Inconel 625 coating was contributing to the change of the feedback current, SECM feedback approach curves were recorded at the spot of different electrochemical activity. The spots a, b, c and d sites gave the positive feedback i.e. current increases as the tip of the microelectrode approaching the substrate. The SEM/EDS analysis revealed that splat boundaries around the partially melted zone have largely different compositions (***see section 5.2.2***). The region of splat boundaries was approximately 20-50 μm wider with some part extending the size by overlapping adjacent active regions. It is suggested by us that the splat boundaries region were electrochemically more active than rest of the coating and gave the positive feedback. The SECM feedback approach curves recorded at e and f sites show negative feedback. The negative feedback was probably from the regions have the oxide layer which did not allow the reduction of $FcOH^+$. The normalized experimental SECM feedback approach curves (a - f) fitted with the theoretical curves (open circles) are shown in ***Figure 7-8***B. The experimental curves show positive and negative feedback but do not fully overlay the theoretical curves.

The SECM image also showed different intensity of the colour for the Inconel 625 coating sample. The dark green region showed the lowest feedback current coming from the oxides formed on the non-melted regions of the coating which were enriched in Cr therefore formed stable oxide and allowed the least

reduction of the $FcOH^+$ at the coating surface. The small isolated round regions marked with arrows were probably the pores. The region within the pore and around the region provided the sites for $FcOH^+$ reduction hence gave the positive feedback. The small circles on the SECM image are the partially melted particles, where centre of the particle oxidized and surrounding splat boundary was electrochemical active. The SEM and EDS analysis of different regions of the Inconel 625 coating also proved that the regions of different compositions exists within the microstructure (***see section Figure 5-1***).

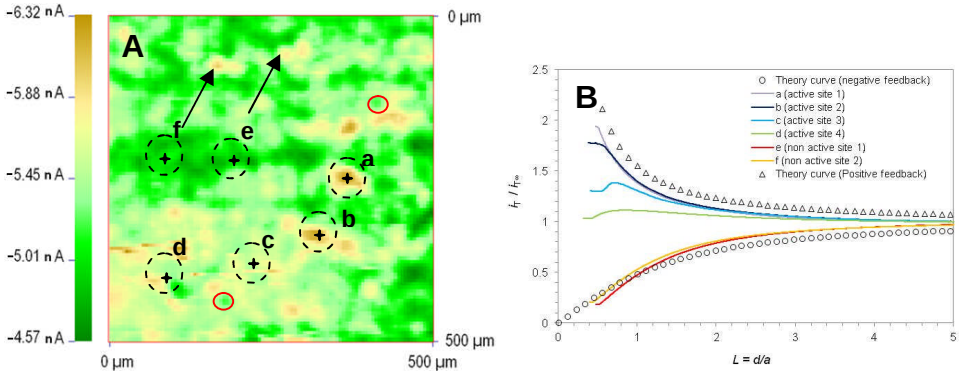

Figure 7-8: SECM image (a) and current distance SECM feedback approach curves (b) for Inconel 625 coating in 1mM FcOH in 0.1M K_2SO_4 by using 25µm diameter disc shaped Pt-electrode with a R_g value of ≈ 10. The tip was held at 0.6 V to drive the oxidation of FcOH at diffusion limited rate, the substrate was at E_{oc}. The SECM image was obtained by measuring i_T at a constant vertical tip-substrate distance of ≈ 4µm = 0.3L. The tip was scanned laterally at 250µm s^{-1} in x-plane and increasing step of 5µm in y-plane. The SECM feedback approach curves at black spots were obtained by vertically scanning the tip from finite distance to the maximum current feedback at the substrate. The tip vertical downward speed was kept at 2µm s^{-1}.

7.8.1 Comparing SECM image with microscopy image

SECM image and SECM feedback approach curves in the previous section clearly show that regions of different electrochemical activity exist at the Inconel 625 coating surface. An attempt was made to correlate the microstructure features of the Inconel 625 coating to SECM image by using

12.5µm radius platinum microelectrode. The features were not well resolved by using 12.5µm radius microelectrode. However, L. Johnson [81], carried out SECM imaging with 2 µm tip and was able to compare the microstructure features with SECM image.

Figure 7-9A, B and C show SECM image, microscopy image and an overlay of SECM and microscopy image respectively to correlate the electrochemical activity of the different microstructure features with SECM image. The ring like features were observed in the SECM image, the same features can be seen on the micrograph. The comparison of the optical image of the HVOF Inconel 625 coating surface 6A with 6B clearly illustrates that the ring-link features observed in the SECM imaging corresponded to the splat boundaries observed by the using optical microscopy. The further confirmation was made by overlaying the SECM image on top of the microscopy image. The high current features of the SECM image correspond to the splat boundaries and low current features to the centre of the particles.

The high current regions (brown features) are the regions of higher electrochemical activity and low current (green features) are the regions of low electrochemical activity. The features of different electrochemical activity are marked a, b, c, d in 6A. It can be seen the round green features are the unmelted powder particles size 20-50 µm and the brown features of 10-15µm are splat boundaries. Therefore, from our comparison of the SECM and microscopy imaging we can establish the splat boundaries are the most active regions in the HVOF Inconel 625 coating for FcOH reduction.

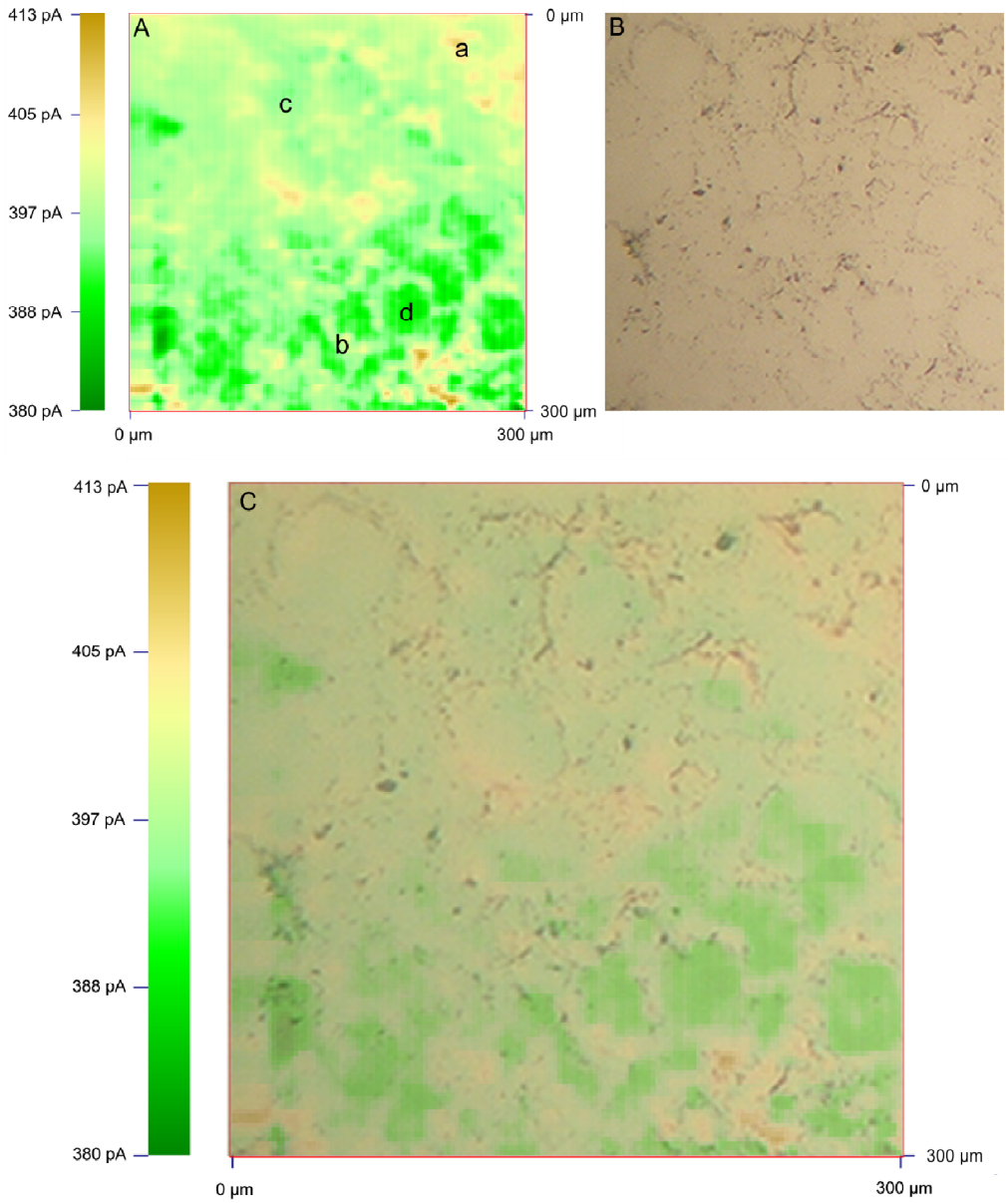

Figure 7-9: SECM image obtained at a HVOF-sprayed Inconel 625 coating on mild steel by recording i_T as a 2 µm radius Pt SECM tip was scanned in x-y plane at 100 µm s^{-1}. The tip was held at 0.6 V to drive the oxidation of FcOH at a diffusion-controlled rate, the substrate was at open circuit potential and the tip-substrate distance was 3 µm (1.5 L). The electrolyte was 0.1 M K_2SO_4, which contained 1 mM FcOH. (A) and (B) show an SECM and optical image of the same region, respectively. (C) Shows a composite image of the SECM image overlaid on the optical image. Labels a-d indicates positions at which experimental SECM feedback approach curves were obtained.

7.9 SECM imaging and SECM feedback approach curves at CoNiCrAlY

Figure 7-10A and B show the SECM image and SECM feedback approach curves for the CoNiCrAlY coating. The feedback current at constant tip height over 500 × 500 µm surface was -1.78nA to -2.47 nA. The feedback current variation between minimum and maximum value was for the CoNiCrAlY coating higher than stainless steel and bulk Inconel 625. The SECM image was taken using the same process parameters as for the other materials. The colour contrast of the image was almost uniform except the top edge showed the green colour.

The HVOF CoNiCrAlY coating have the same microstructure features like pores, splats and regions of different electrochemical activity but these features were probably obscured due to overall electrochemically active surface. Furthermore the CoNiCrAlY coating has smaller sizes of splats and pores (***see section 5.2***) than Inconel 625 coating which may not be resolvable by the 25 µm size microelectrode. The nature of the different region of the image was further checked by SECM feedback approach curves at different spots. All normalized current distance SECM feedback approach curves show the positive feedback indicating that the CoNiCrAlY coating was electrochemically active all over the surface. The highest feedback end of the SECM feedback approach curves were distorted due the partial penetration of the tip to the coating or glass sheath touching the substrate surface.

The CoNiCrAlY coating is a bond coat for thermal barrier coating and designed to grow oxide during service when heated to elevated temperatures [49, 50]. The oxide formed at room temperature may not be enough protective to block the ET across interface and stop reduction of $FcOH^+$. ***Figure 7-11*** shows the SECM feedback approach curves obtained for the CoNiCrAlY coating after heating in the furnace at 1000^0 C for 1, 2, 5, 20 and 40 hours respectively. The heat treatment was done to deliberately grow the Al_2O_3 at the surface. The oxide layer at the surface may block the reduction of $FcOH^+$ at the surface and give negative feedback. The experimental SECM feedback approach curves after heat treatment showed negative feedback all over the surface, indicating predominantly insulating response.

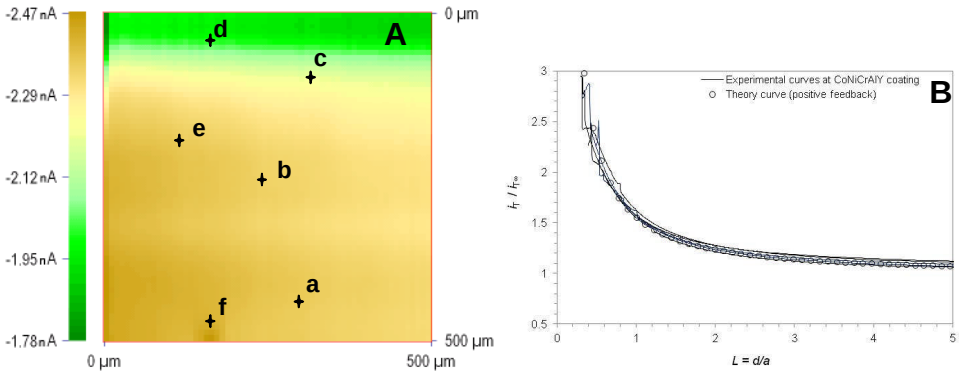

Figure 7-10: SECM image and current distance SECM feedback approach curves for CoNiCrAlY coating in 1mM FcOH in 0.1M K_2SO_4 by using 25µm diameter disc shaped Pt-electrode with a R_g value of ≈ 10. The tip was held at 0.6 V to drive the oxidation of FcOH at diffusion limited rate, the substrate was at E_{oc}. The SECM image was obtained by measuring i_T at a constant vertical tip-substrate distance of ≈ 4µm = 0.3L. The tip was scanned laterally at 250µm s^{-1} in x-plane and increasing step of 5µm in y-plane. The SECM feedback approach curves at black spots were obtained by vertically scanning the tip from finite distance to the maximum current feedback at the substrate. The tip vertical downward speed was kept at 2µm s^{-1}.

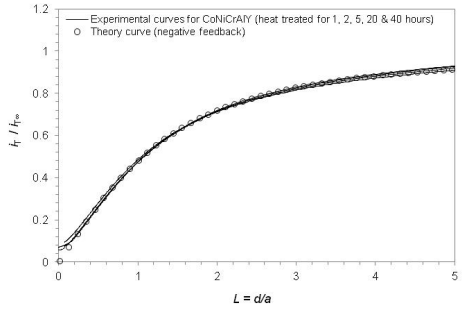

Figure 7-11: SECM feedback approach curves fitted with theoretical curves for the CoNiCrAlY coating after heating at 1000°C for 1, 2, 5, 20 and 40 hours. The procedure for recording SECM feedback approach curves was same as for other materials

7.10 Quantification of electrochemical activity

It is established from the results of previous sections that Inconel 625 coating microstructure was electrochemically more heterogeneous than bulk Inconel 625 and stainless steel. In this section the electrochemical activity of the Inconel 625 coating, bulk Inconel 625 and stainless steel is quantified by measuring the kinetics of heterogeneous ET across electrode electrolyte interface.

7.10.1 Kinetics of heterogeneous ET study by SECM

The kinetics of heterogeneous ET rate constant measured by SECM method eliminates the errors due to charging current and solution resistance [105]. The first step in the kinetic measurement is to obtain the SECM feedback approach curves while keep the tip process at diffusion limited. In our study 1mM FcOH was used as redox mediator in 0.1M K_2SO_4 solution, the tip was kept at 0.6 V to drive diffusion limited oxidation at the tip. The substrate potential was systematically changed from negative to positive potential around the formal potential to drive $FcOH^+$ reduction and FcOH oxidation at the substrate.

The tip measured the kinetically controlled current at the substrate as a function of overpotential by SECM feedback approach curves. The tip current and the tip-substrate distance were converted into normalized tip current (Ni_T) and normalize tip-substrate distance L. The experimental data for Ni_T and L were fitted with the theoretical curves plotted from the analysis of the old [86, 164, 173] and new [178-181] analytical equations to extract the dimensionless rate constant for ET (κ).

7.10.2 Curve fitting by using Bard and Mirkin theory

The fitting procedure is based on SECM theory for the finite substrate heterogeneous kinetics [173], using the following equation to extract the first order rate constant (only concentration of one reactant e.g. FcOH involved in reaction with one ET).

$$I_T^k = I_S^k\left(1 - I_T^{ins}/I_T^c\right) + I_T^{ins} \qquad \textbf{7.3}$$

Where I_T^c, I_T^k and I_T^{ins} describe the normalised tip currents for diffusion controlled regeneration of redox mediator, finite substrate kinetics and insulating kinetics respectively, and I_S^k is the kinetically controlled substrate current given below [162]. The above currents can be calculated by using the following analytical approximation equations.

$$I_T^c = \frac{0.78377}{L} + 0.3315\, exp(\frac{-1.0672}{L}) + 0.68 \qquad \textbf{7.4}$$

$$I_T^{ins} = 1/[0.15 + \frac{1.5358}{L} + 0.58\, exp(\frac{-1.14}{L}) + 0.0908\, exp(\frac{L-6.3}{1.017L})] \qquad \textbf{7.5}$$

$$I_S^k = \frac{0.78377}{L(1+1/\kappa)} + [0.68 + 0.3315\, exp\left(\frac{-1.0672}{L}\right)]/[1 + \frac{7.3+11/L\,\kappa}{110-40\,\kappa}] \quad \textbf{7.6}$$

L is the normalised tip-substrate distance and $\kappa = kd/D$, where k is the heterogeneous rate constant (cm s^{-1}). Tafel graph were plotted from the log of the reaction rate constant vs. over potential (i.e. *log k vs. (E - $E^{0\prime}$)*). The extrapolation of the Tafel plots to zero overpotential give the heterogeneous ET rate constant k^0. The accuracy of the ***equation 7.3*** is claimed by the authors as 1-2% for $0.1 < L < 1.5$ and $0.01\ k < 1000$ for a disk microelectrode with $R_g = 10$ [86, 158, 162].

7.10.3 Curve fitting by using Cornut and Lefrou theory

The ***equation 7.3*** has been used for some research group for their experimental data fitting, ignoring the exact R_g value. A new analytical procedure was proposed by Cornut and Lefrou in 2008 [179, 180] for the kinetic information extraction of SECM steady state feedback experiment data. The authors address the errors in Ni_T to difference of the steady state current from infinite distance, validity of the equation for all R_g and errors in the tip-substrate distance due to irregular tip geometry, which were not covered in the Bard et al. theory. The accuracy of the results were claimed by the authors as within the ±2.5% for any kinetics in conditions $L > 0.1$ for a disk type microelectrode with $R_g < 20$ [178, 179].

$$Ni_T(L,\kappa,R_g) = Ni_T^c\left(L+\frac{1}{\kappa},R_g\right) + \frac{Ni_T^{ins}(L,R_g)-1}{\left(1+2.47R_g^{0.31}L\kappa\right)\left(1+L^{R_g-0.113}\kappa^{-0.0236R_g-0.91}\right)} \quad \textbf{7.7}$$

$$Ni_T^{ins}(L, R_g) \quad \textbf{7.8}$$

$$= \frac{\frac{2.08}{R_g^{0.358}}\left(L - \frac{0.145}{R_g}\right) + 1.585}{\frac{2.08}{R_g^{0.358}}(L + 0.0023R_g) + 1.57 + \frac{LnR_g}{L} + \frac{2}{\pi R_g} Ln\left(1 + \frac{\pi R_g}{2L}\right)}$$

$$Ni_T^c(L, R_g) = \alpha(R_g) + \frac{\pi}{4\beta(R_g)ArcTan(L)} \quad \textbf{7.9}$$

$$+ \left(1 - \alpha(R_g) - \frac{1}{2\beta(R_g)}\right)\frac{2}{\pi} ArcTan(L)$$

$$\alpha(R_g) = Ln2 + Ln2\left(1 - \frac{2}{\pi} ArcCos\left(\frac{1}{R_g}\right)\right) - Ln\left(1 - \left(\frac{2}{\pi} ArcCos\left(\frac{1}{R_g}\right)\right)^2\right) \quad \textbf{7.10}$$

$$\beta(R_g) = 1 + 0.639\left(1 - \frac{2}{\pi} ArcCos\left(\frac{1}{R_g}\right)\right) \quad \textbf{7.11}$$

$$- 0.186\left(1 - \left(\frac{2}{\pi} ArcCos\left(\frac{1}{R_g}\right)\right)^2\right)$$

The definition of the parameters κ, k, k^0, and L were consistent with the Bard et al. equations except $\alpha(R_g)$ and $\beta(R_g)$ values which can were calculated by using e***quation 7.10*** and ***7.11***. The term normalized tip current used differently in the Bard equations. The normalized tip currents in the Bard equations were not corrected for small R_g values. The $i_{T\infty}$ for the R_g < 1.1 can add approximately 10% errors in the normalized tip current. An error factor of the zero distance from the tip-substrate distance and errors in the steady state current as compared to the SECM feedback approach curve starting point should also be included while fitting the experimental data with theoretical curves extracted from the analysis of the approximation curves.

Fitting of the experimental curves with variable values of $R_{g,}$ L and Ni_T lead to more accurate values of κ. The heterogeneous ET rate constant (k) can be calculate from $k = \kappa D/a,$ where D is diffusion coefficient and a is the radius of the tip. Tafel graphs were plotted between *log* of the reaction rate constant vs. overpotential (i.e. *log k* vs. (E-$E^{0'}$)). The extrapolation of the Tafel plats to the zero overpotential give heterogeneous ET reaction rate constant k^0 [178, 180, 181].

7.10.4 Measuring kinetics of heterogeneous ET at random sites for stainless steel

Figure 7-12 and ***Figure 7-13*** show three sets of data for stainless steel at three random sites. As shown in ***Figure 7-5*** the SECM image of stainless steel did not show variation in electrochemical activity hence sites for obtaining kinetic data were selected randomly. The data acquisition and analysis were carried out in the same way as for Inconel 625 coating. The graph is plotted between *lnk* vs. η in ***Figure 7-13***a also known as Tafel plot. The extrapolation of the Tafel plot to zero overpotential yield the heterogeneous ET rate constant at equilibrium k^0 the analysis the kinetic data produce the k^0 value 4.9×10^{-5} cm s^{-1}. The rate constant was also measured by using analytical equation proposed by Cornut for exact values of R_g and corrected Ni_T. The values of k^0 were approximately same and summarized in ***Table 7-3***.

The SECM image did not show the features of different electrochemical activity as for Inconel 625 coating indicating the surface is homogeneous. The SECM feedback approach curves at random sites confirm that surface is

predominantly acting as insulator and giving negative feedback. The variation in current is probably due to slight tilt of the substrate surface.

The analysis of the kinetic data produces the k^0 values for stainless steel a factor of 10 lower than that of the Inconel 625 coating and a factor of 100 lower than that of the bulk Inconel 625. The lower k^0 value for stainless steel is due to slow ET and presence of passive oxide layer on the stainless steel. The analysis of the kinetic data at different site of the stainless steel surface produces the k^0 value slightly different from each other this is probably due to variation of the oxide layer formed on the surface. The area with thin oxide layer produced slightly higher k^0 value than the area with thick oxide layer. The Tafel data for two of the sites were not fully linear especially from the higher ends of the positive and negative potential.

The transfer coefficient "α" calculated from the slope of the lnk vs. η plot where reduction slope = $-\alpha F / 2.3 R T$ and oxidation slope = $(1-\alpha) F / 2.3 R T$. The value of α was 0.20 for the stainless steel which is significant lower than simple outer-sphere ET reaction, generally taken as α = 0.5 [95].

Table 7-3: Kinetic data (k, k^0) extracted for stainless steel

E / V	*k (site1)cm s^{-1}*	*k (site2) cm s^{-1}*	*k (site3) cm s^{-1}*
5.0×10^{-2}	2.0×10^{-4}	6.0×10^{-4}	5.0×10^{-4}
0.0×10^{0}	5.8×10^{-4}	1.0×10^{-3}	8.0×10^{-4}
-5.0×10^{-2}	1.6×10^{-3}	1.7×10^{-3}	1.3×10^{-3}
-1.0×10^{-1}	3.2×10^{-3}	3.0×10^{-3}	2.2×10^{-3}
-1.5×10^{-1}	5.3×10^{-3}	4.5×10^{-3}	3.6×10^{-3}
-2.0×10^{-1}	7.8×10^{-3}	6.5×10^{-3}	5.4×10^{-3}
-2.5×10^{-1}	1.1×10^{-2}	9.1×10^{-3}	7.5×10^{-3}
-3.0×10^{-1}	1.8×10^{-2}	1.3×10^{-2}	1.0×10^{-2}
-3.5×10^{-1}	3.0×10^{-2}	1.7×10^{-2}	1.3×10^{-2}
-4.0×10^{-1}	4.5×10^{-2}	1.9×10^{-2}	1.4×10^{-2}
Heterogeneous ET reaction rate constant at equilibrium k^0			
$(k^0)_{Bard}$ *cm* s^{-1}	**4.9×10^{-5}**	**1.7×10^{-5}**	**7.3×10^{-5}**
$(k^0)_{Cornut}$ *cm* s^{-}	**3.4×10^{-5}**	**1.3×10^{-5}**	**5.5×10^{-5}**
k = rate constant, k^0 = rate constant at equilibrium			

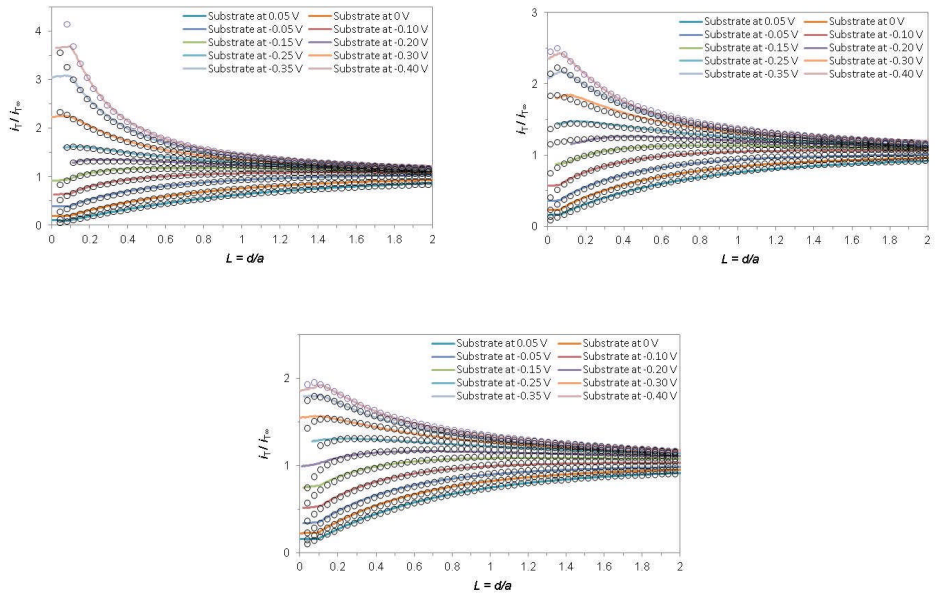

Figure 7-12: SECM feedback approach curves for kinetic study at three different spots for stainless steel. The tip potential was 0.6 V and substrate potential was kept at -0.40,-0.35, -0.30, -0.25, -0.20, -0.15, -0.10, 0.00 and 0.05 V vs. Ag/AgCl for different SECM feedback approach curves. The solid lines represent the normalized experimental curves and open circles show the points generated from theatrical equations.

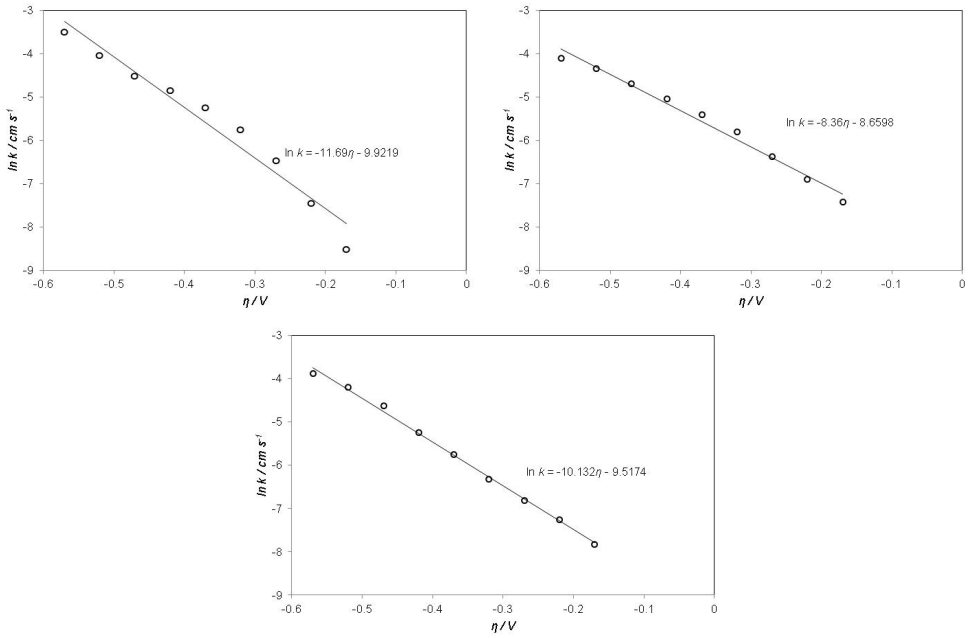

Figure 7-13: Tafel plots of lnk vs. overpotential (η) for stainless steel at three different spots obtained from the fitting of the SECM feedback approach curves at substrate potentials of -0.40,-0.35, -0.30, -0.25, -0.20, -0.15, -0.10, 0.00 and 0.05 V

7.10.5 Heterogeneous ET transfer study at random sites for a period for 5-days for bulk Inconel 625

The heterogeneous ET rate constant measured on random sites of the bulk Inconel 625 was approximately the same. This indicates that the electrochemical activity for the bulk Inconel 625 is not changing from site to site over the surface. The XPS results of bulk Inconel 625 have shown that there were different oxides present in the passive layer (***see section 5.7.1***) but from SECM imaging and k^0 values, we suggested that oxides present in the passive layer were approximately same electrochemically at least under the used testing conditions. The SECM feedback approach curve gives negative feedback when substrate was at E_{oc} and produces approximately same k^0 for different sites. The data was analysed by using the analytical equation

proposed by Bard and Cornut group. The extracted values by fitting the experimental data with theoretical curves extracted from analytical equations are summarized in ***Table 7-4*** and ***Table 7-5***. The k^0 values from both methods were close to each other, indicating the higher R_g value did not effect the value too much as it can effect for the lower R_g values.

The kinetic data measured for five consecutive days on the same sample shows the k^0 changed a factor of 10 over the period of five days. The sample was cleaned in the sonicator and dried before/after recording SECM data for each day. The value of k^0 after day one was approximately the same as the one recorded at the beginning, indicating that the surface did not change during 24 hours of exposure. After 5 days the k^0 value became considerably lower than the one measured at the start, indicating the surface of the bulk Inconel 625 alloy has been altered. It is suggested the lower k^0 value is either due to exposure in the air or repeated runs on the same sample which grew the protective oxide layer thick enough to slow down the ET across electrode electrolyte interface. The transfer coefficient calculated from the Tafel slope for bulk Inconel produces and α value of 0.33.

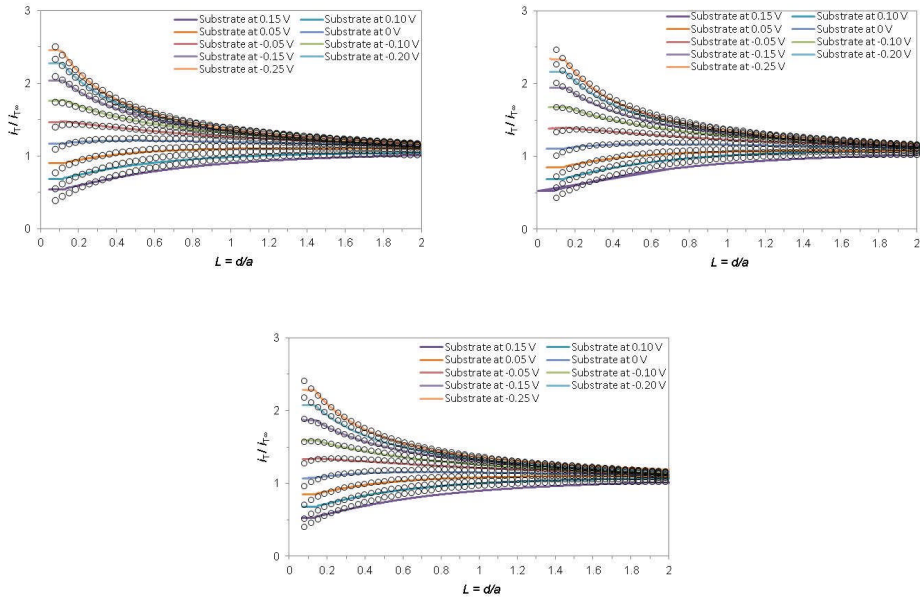

Figure 7-14: SECM feedback approach curves for kinetic study at three different spots for bulk Inconel 625. The tip potential was 0.6 V and substrate potential was kept at -0.25, -0.20, -0.15, -0.10, 0.00, 0.05, 0.10 and 0.15 V vs. Ag/AgCl for different SECM feedback approach curves. The solid lines represent the normalized experimental curves and open circles show the ones generated from theoretical equation.

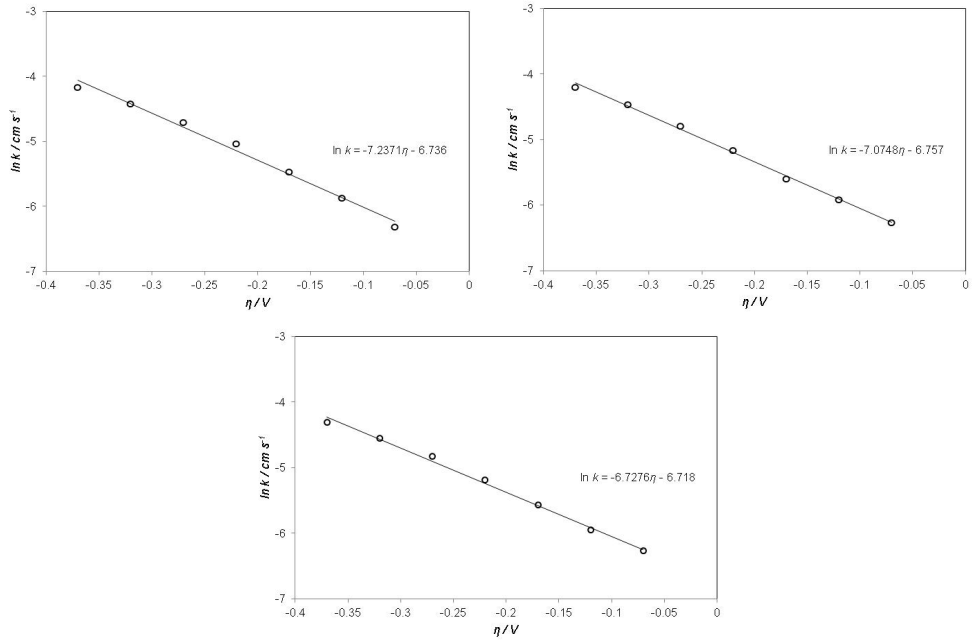

Figure 7-15: Tafel plots of lnk vs. overpotential (η) for bulk Inconel 625 at three different spots obtained from the fitting of the SECM feedback approach curves at substrate potentials of -0.25, -0.20, -0.15, -0.10, 0.00, 0.05, 0.10 and 0.15 V

Table 7-4: Kinetic data (k, k^0) extracted for bulk Inconel 625

E / V	*k (site1) cm s^{-1}*	*k (site2) cm s^{-1}*	*k (site3) cm s^{-1}*	*k (site4) cm s^{-1}*	*k (site5) cm s^{-1}*
1.5×10^{-1}	1.8×10^{-3}	1.9×10^{-3}	1.9×10^{-3}	1.9×10^{-3}	2.0×10^{-3}
1.0×10^{-1}	2.8×10^{-3}	2.7×10^{-3}	2.6×10^{-3}	2.6×10^{-3}	2.6×10^{-3}
5.0×10^{-2}	4.2×10^{-3}	3.7×10^{-3}	3.8×10^{-3}	3.7×10^{-3}	3.6×10^{-3}
0.0×10^{0}	6.5×10^{-3}	5.7×10^{-3}	5.6×10^{-3}	5.3×10^{-3}	4.3×10^{-3}
-5.0×10^{-2}	9.0×10^{-3}	8.3×10^{-3}	8.0×10^{-3}	7.5×10^{-3}	5.7×10^{-3}
-1.0×10^{-1}	1.2×10^{-2}	1.2×10^{-2}	1.1×10^{-2}	9.5×10^{-3}	7.7×10^{-3}
-1.5×10^{-1}	1.6×10^{-2}	1.5×10^{-2}	1.4×10^{-2}	1.2×10^{-2}	9.7×10^{-3}
-2.0×10^{-1}	1.8×10^{-2}	1.8×10^{-2}	1.7×10^{-2}	1.4×10^{-2}	1.2×10^{-2}
$-2.5 \times 10^{--1}$	2.0×10^{-2}	2.1×10^{-2}	1.9×10^{-2}	1.6×10^{-2}	1.4×10^{-2}
Heterogeneous ET reaction rate at equilibrium k^0					
$(k^0)_{Bard}$ *cm s^{-1}*	**1.2×10^{-3}**	**1.2×10^{-3}**	**1.2×10^{-3}**	**1.3×10^{-3}**	**1.4×10^{-3}**
$(k^0)_{Cornut}$ *cm s^{-1}*	**2.2×10^{-3}**	**2.2×10^{-3}**	**1.0×10^{-3}**	**1.7×10^{-3}**	**1.5×10^{-3}**

Table 7-5: Kinetic data as a function of time for bulk Inconel 625

E / V	*k (day1) three sites / cm s^{-1}*			*k (day2) three sites / cm s^{-1}*		
1.0×10^{-1}	2.0×10^{-3}	2.3×10^{-3}	2.3×10^{-3}	1.4×10^{-3}	1.6×10^{-3}	1.5×10^{-3}
5.0×10^{-2}	2.8×10^{-3}	3.2×10^{-3}	3.1×10^{-3}	2.0×10^{-3}	2.7×10^{-3}	2.3×10^{-3}
0.0×10^{0}	4.0×10^{-3}	4.8×10^{-3}	5.0×10^{-3}	3.0×10^{-3}	3.8×10^{-3}	3.5×10^{-3}
-5.0×10^{-2}	7.0×10^{-3}	1.1×10^{-2}	1.1×10^{-2}	4.5×10^{-3}	7.0×10^{-3}	6.0×10^{-3}
-1.0×10^{-1}	1.2×10^{-2}	1.3×10^{-2}	1.4×10^{-2}	8.2×10^{-3}	1.2×10^{-2}	1.0×10^{-2}
-1.5×10^{-1}	1.6×10^{-2}	1.6×10^{-2}	1.7×10^{-2}	1.3×10^{-2}	1.6×10^{-2}	1.3×10^{-2}
-2.0×10^{-1}	2.0×10^{-2}	2.0×10^{-2}	2.1×10^{-2}	1.8×10^{-2}	2.1×10^{-2}	1.9×10^{-2}
$-2.5 \times 10^{--1}$	2.4×10^{-2}	2.6×10^{-2}	2.5×10^{-2}	2.5×10^{-2}	2.9×10^{-2}	2.4×10^{-2}
Heterogeneous ET reaction rate at equilibrium k^0						
$(k^0)_{Bard}$ *cm s^{-1}*	**8.3×10^{-4}**	**1.1×10^{-3}**	**1.1×10^{-3}**	**4.8×10^{-4}**	**6.5×10^{-4}**	**6.1×10^{-4}**
$(k^0)_{Cornut}$ *cm s^{-1}*	**7.5×10^{-4}**	**1.4×10^{-3}**	**1.4×10^{-3}**	**3.2×10^{-4}**	**8.9×10^{-4}**	**8.0×10^{-4}**
E / V	*k (day3) three sites / cm s^{-1}*			*k (day5) three sites / cm s^{-1}*		
1.0×10^{-1}	1.8×10^{-3}	1.8×10^{-3}	2.0×10^{-3}	1.5×10^{-3}	1.8×10^{-3}	1.9×10^{-3}
5.0×10^{-2}	2.6×10^{-3}	2.5×10^{-3}	2.9×10^{-3}	2.1×10^{-3}	2.6×10^{-3}	2.7×10^{-3}
0.0×10^{0}	4.0×10^{-3}	4.0×10^{-3}	4.2×10^{-3}	2.9×10^{-3}	3.5×10^{-3}	3.8×10^{-3}
-5.0×10^{-2}	6.0×10^{-3}	7.5×10^{-3}	6.5×10^{-3}	4.0×10^{-3}	4.9×10^{-3}	6.0×10^{-3}
-1.0×10^{-1}	1.1×10^{-2}	1.1×10^{-2}	9.5×10^{-3}	5.6×10^{-3}	6.6×10^{-3}	9.0×10^{-3}
-1.5×10^{-1}	1.5×10^{-2}	1.6×10^{-2}	1.4×10^{-2}	8.3×10^{-3}	8.8×10^{-3}	1.9×10^{-2}
-2.0×10^{-1}	1.9×10^{-2}	2.2×10^{-2}	1.9×10^{-2}	1.2×10^{-2}	1.2×10^{-2}	2.9×10^{-2}
$-2.5 \times 10^{--1}$	2.6×10^{-2}	2.5×10^{-2}	2.4×10^{-2}	1.5×10^{-2}	1.5×10^{-2}	4.0×10^{-2}
Heterogeneous ET reaction rate constant at equilibrium k^0						
$(k^0)_{Bard}$ *cm s^{-1}*	**7.2×10^{-4}**	**7.2×10^{-4}**	**8.7×10^{-4}**	**6.6×10^{-4}**	**9.1×10^{-4}**	**9.7×10^{-4}**
$(k^0)_{Cornut}$ *cm s^{-}*	**8.0×10^{-4}**	**6.8×10^{-4}**	**6.2×10^{-4}**	**8.0×10^{-4}**	**9.2×10^{-4}**	**9.5×10^{-4}**

7.10.6 Measuring kinetics of heterogeneous ET at Inconel 625 coating

The suitability of the kinetic experiments on substrate by SECM depends on the radius of the substrate taking part in the feedback loop and size of the different electrochemical active regions. The radius of the area of the substrate that participates in the feedback loop during SECM experiments is $r \approx a + 1.5d$ where 'a' is tip radius and 'd' is the tip-substrate separation [105]. Thus the substrate for a tip-substrate distance of $L \leq 2$, a large substrate behaves as UME compared to the tip of the electrode (where $L = a/d$). Hence the kinetic experiments can be performed by SECM on Inconel 625 coating. The regions of higher electrochemical activity were approximately 50µm, which is twice the size of the SECM tip used in experiments. Therefore based on the relative tip and active/non-active sites dimensions it should be possible to perform the kinetic measurement on the regions of different electrochemical activity at the coating surface.

Figure 7-16 shows the SECM image for the Inconel 625 coating, recorded by using the same procedure as for stainless steel and bulk Inconel 625 coating. The feedback current at constant tip height was -3.91nA to -6.75nA when substrate was kept at E_{oc}. The SECM image shows regions of lower and higher current indicating different electrochemical activity. The SECM feedback approach curves were recorded on these regions to check the electrochemical activity before recording kinetic data. The feedback response was same as shown in ***section 7.8***. The measurement of heterogeneous ET at the substrate was carried out by keeping UME at constant positive potential i.e. 0.6V to get

diffusion limited mass transfer at the tip and kinetics controlled process at the substrate.

The process of oxidation and reduction were driven at the substrate by providing small positive and negative potentials around the formal potential i.e. -0.25 V to 0.10 V with an increment step of 50mV. After analysis of the kinetically controlled experimental data with theoretical curves, representing data in Tafel plots and extrapolating of the Tafel plot the standard heterogeneous rate constant k^0 was measured at regions of heterogeneity. The regions of high electrochemical activity are probably the splat boundaries i.e., the regions deficient in chromium. The regions of lower electrochemical activity are attributed to protective oxides or covered with insulating layers which do not allow the electron flow to cause reduction at the surface. The k^0 value measured at a, b, c sites were higher than those measured at d, e and f sites indicating the electrochemical activity is higher on brown sites. The lowest k^0 value at active sites was 2.01×10^{-4} cm s^{-1} and the highest value of k^0 was 5.25×10^{-4} cm s^{-1} which indicates that corrosion reaction was faster at active sites and slower at non-active sites. The SECM feedback approach curves at different potential were also analysed by Cornut analytical equation. The rate constant values extracted after fitting with both analytical equations are summarized in ***Table 7-6***.

The overall electrochemical activity in terms of k^0 value at the Inconel coating surface was lower than the bulk Inconel 625. The lower electrochemical activity of the Inconel 625 coating surface towards $FcOH^+$ reduction than that of the bulk alloy does not correlate with the poorer corrosion resistance of the

sprayed material. However, it is very unlikely that a simple correlation between the electrochemical activity of a thermal sprayed coating for $FcOH^+$ reduction and its corrosion resistance under normal operating conditions is possible but our results give quantitative information about the electrochemical activity by measuring k^0 at regions of heterogeneity. The lower k^0 value for Inconel 625 coating surface compared to the bulk Inconel 625 surface may be due to formation of localised oxides during thermal spraying, which differ from those formed on the bulk alloy's surface.

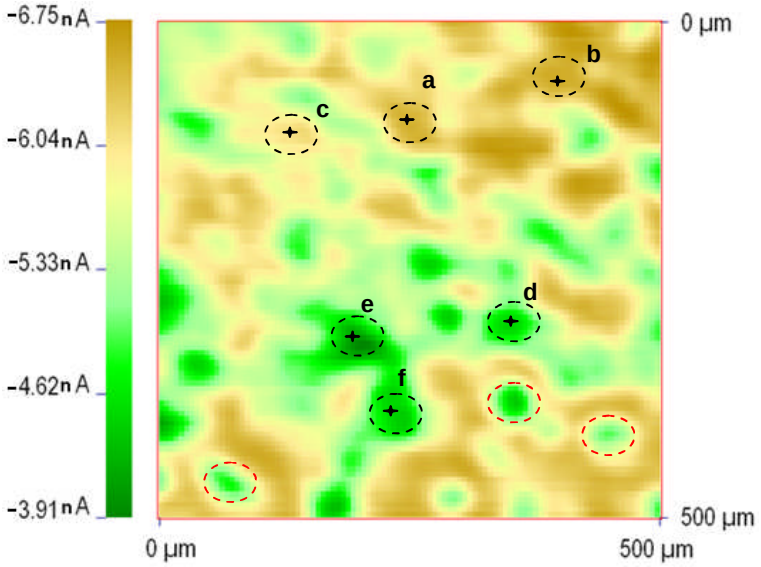

Figure 7-16: SECM image for Inconel 625 coating in 1mM FcOH in 0.1M K_2SO_4 by using 25µm diameter disc shaped Pt-electrode with a R_g value of ≈ 10. The tip was held at 0.6 V to drive the oxidation of FcOH at diffusion limited rate, the substrate was at E_{oc}. The SECM image was obtained by measuring i_T at a constant vertical tip-substrate distance ≈ 4µm = 0.3L. The tip was scanned laterally at 250µm s^{-1} in x-plane and increasing step of 5µm in y-plane.

Table 7-6: The kinetic data (k, k^0) extracted for Inconel 625 coating

E / V	*k (a) cm s^{-1}*	*k (b) cm s^{-1}*	*k (c) cm s^{-1}*	*k (d) cm s^{-1}*	*k (e) cm s^{-1}*	*k (f) cm s^{-1}*
1.5×10^{-1}	1.0×10^{-3}	7.0×10^{-3}	9.0×10^{-4}	3.0×10^{-4}	5.0×10^{-4}	5.0×10^{-4}
1.0×10^{-1}	2.0×10^{-3}	1.6×10^{-3}	1.9×10^{-3}	9.0×10^{-4}	1.0×10^{-3}	1.0×10^{-3}
5.0×10^{-2}	3.0×10^{-3}	2.3×10^{-3}	3.2×10^{-3}	1.6×10^{-3}	2.0×10^{-3}	1.6×10^{-3}
0	5.5×10^{-3}	3.7×10^{-3}	5.6×10^{-3}	2.4×10^{-3}	3.5×10^{-3}	2.2×10^{-3}
-5.0×10^{-2}	8.5×10^{-3}	6.0×10^{-3}	9.0×10^{-3}	4.0×10^{-3}	6.0×10^{-3}	3.5×10^{-3}
-1.0×10^{-2}	1.5×10^{-2}	9.0×10^{-3}	1.4×10^{-2}	6.5×10^{-3}	9.0×10^{-3}	4.9×10^{-3}
-1.5×10^{-2}	2.4×10^{-2}	1.4×10^{-2}	2.0×10^{-2}	9.5×10^{-3}	1.4×10^{-2}	6.8×10^{-3}
-2.0×10^{-2}	4.0×10^{-2}	2.0×10^{-2}	2.6×10^{-2}	1.4×10^{-2}	1.9×10^{-2}	8.8×10^{-3}
-2.5×10^{-2}	6.5×10^{-2}	2.6×10^{-2}	3.3×10^{-2}	1.9×10^{-2}	2.2×10^{-2}	1.2×10^{-2}
Heterogeneous ET reaction rate constant at equilibrium k^0						
$(k^0)_{Bard}$ *cm s^{-1}*	**5.2×10^{-4}**	**5.2×10^{-4}**	**4.3×10^{-4}**	**2.0×10^{-4}**	**2.7×10^{-4}**	**3.5×10^{-4}**
$(k^0)_{Cornut}$ *cm s^{-}*	**6.2×10^{-4}**	**5.7×10^{-4}**	**7.5×10^{-4}**	**3.7×10^{-4}**	**4.5×10^{-4}**	**3.8×10^{-4}**
E = applied potential, k = rate constant, k^0 = rate constant at equilibrium, a, b, c, d, e, f = different sites						

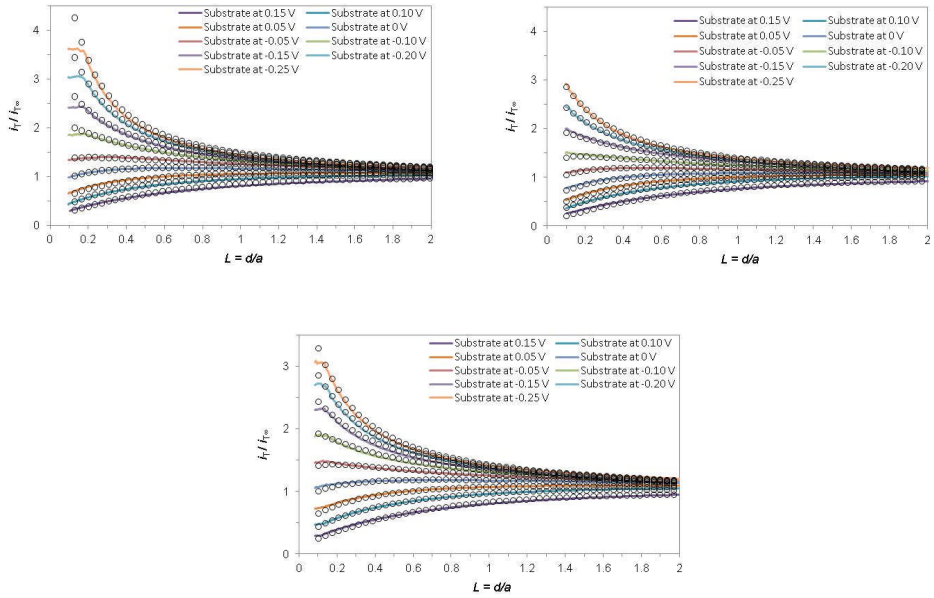

Figure 7-17: SECM feedback approach curves for kinetic study at different active spots a, b and c in Figure 7-16 for Inconel 625 coating. The tip potential was 0.6 V and substrate potential was kept at -0.25, -0.20, -0.15, -0.10, 0.00 and 0.05, 0.10, 0.15 V vs. Ag/AgCl for different SECM feedback approach curves. The solid lines represent the experimental curves and open circles show theoretical curves generated from the equation in the literature survey chapter.

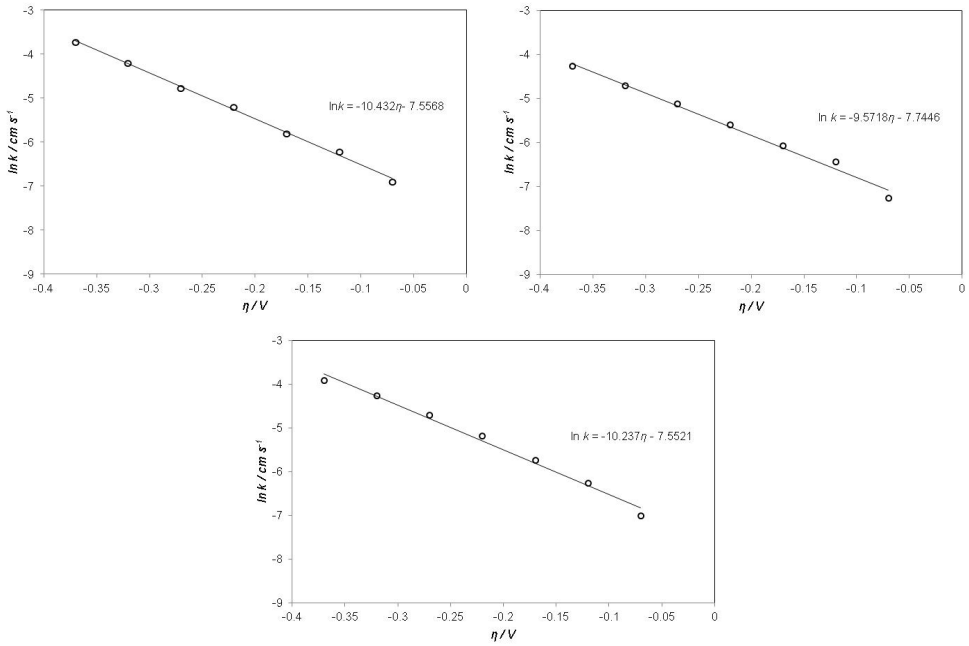

Figure 7-18: Tafel plots of lnk vs. overpotential (η) for Inconel 625 coating on active spots obtained from the fitting of the SECM feedback approach curves at substrate potentials of -0.25, -0.20, -0.15, -0.10, 0.00 and 0.05, 0.10, 0.15 V.

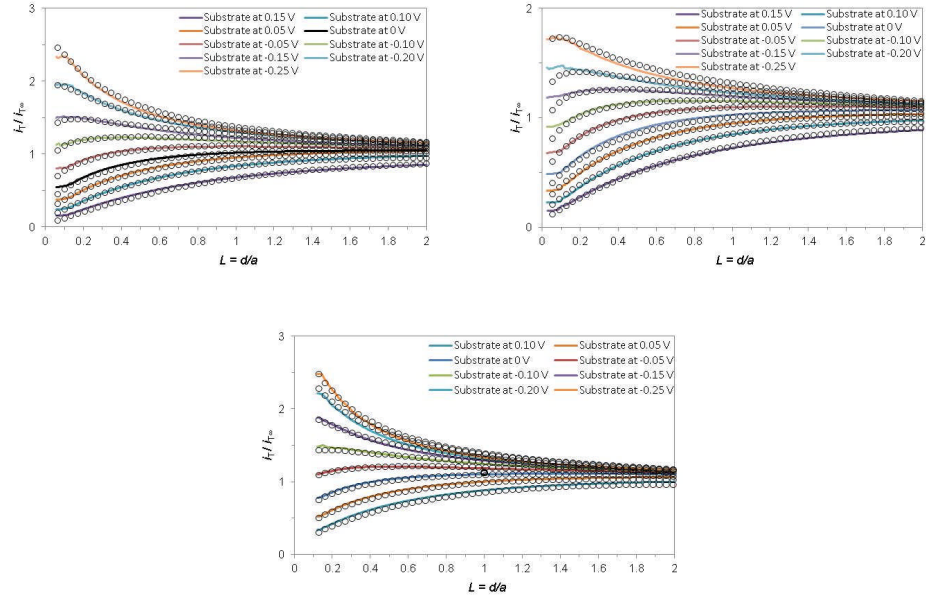

Figure 7-19: SECM feedback approach curves for kinetic study at different non-active spots d, e and f in Figure 7-16 for Inconel 625 coating. The tip potential was 0.6 V and substrate potential was kept at -0.25, -0.20, -0.15, -0.10, 0.00 and 0.05, 0.10, 0.15 V vs. Ag/AgCl for different SECM feedback approach curves. The solid lines represent the normalized experimental curves and open circles show theoretical curves generated from the equation in the literature survey chapter.

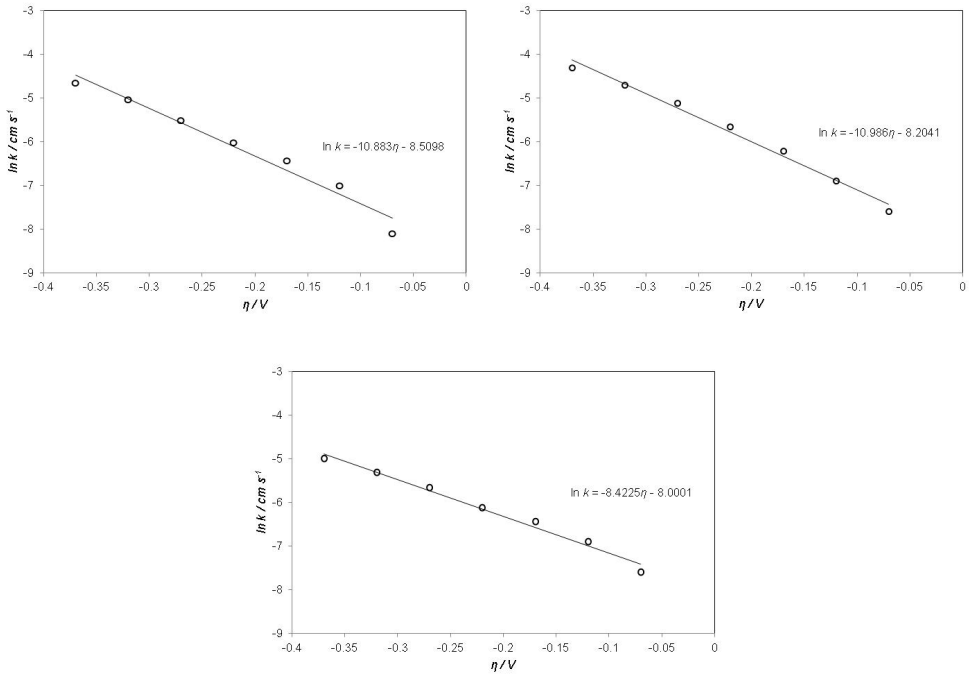

Figure 7-20: Tafel plots of lnk vs. overpotential (η) for Inconel 625 coating on non-active spots obtained from the fitting of the SECM feedback approach curves at substrate potentials of at -0.25, -0.20, -0.15, -0.10, 0.00 and 0.05, 0.10, 0.15 V.

7.11 Summary

- The cyclic voltammograms results showed the reaction at Pt-electrode is essentially reversible and quasi reversible at Inconel 625 coating, bulk Inconel 625 and stainless steel. The CV at the microelectrode tip did not show any current peak due to predominantly radial diffusion which allowed the microelectrode to acquire fast steady state.
- The ET rate constants obtained from CV data were representative of overall redox reaction ($FcOH^+$/FcOH) at the substrate. The k^0 values for CV include the errors due to ohmic drop and charging current. The k^0 values from CV increases with the scan rate.
- SECM was effectively used to visualize the electrochemical activity of the heterogeneous surfaces. The heterogeneity in terms of feedback current difference at E_{oc} between lowest and highest feedback values was 0.21nA for bulk alloy and 1.75nA for Inconel 625 coating. The electrochemical activity of different regions was confirmed by SECM feedback approach curves i.e. the active sites give positive feedback and non-active site give negative feedback. The stainless steel and bulk Inconel 625 gave negative feedback all over the surface while Inconel 625 coating both positive and negative feedback on different regions.
- The comparison between SECM and microscopy images at HVOF Inconel 625 coating surface clearly illustrate that the splat boundaries regions were electrochemically more active than rest of the coating.
- The quantification of electrochemical activity was done by monitoring the rate of heterogeneous ET rate constant across electrode-electrolyte

interface. This was effectively measured for stainless steel, bulk Inconel 625 and Inconel 625 coating samples by SECM feedback approach curves and fitting with theoretical curves. The k^0 value was 4.9×10^{-5} cm s^{-1} for stainless steel, 1.2×10^{-3} cm s^{-1} and 2.0 to 5.2×10^{-4} cm s^{-1} for the Inconel 625 coating samples.

- The heterogeneous ET rate constant was also calculated by the new analytical approximation procedure proposed by Cornut and Lefrou. The values of the k^0 were approximately same as with Bard curve fitting method.
- The heterogeneous ET rate constant at equilibrium for the Inconel 625 coating was approximately a factor of 10 higher than stainless steel and a factor of 10 lower than bulk Inconel 625 alloy. The lower heterogeneous ET rate constant at Inconel 625 coating surface was probably due to formation of some stable oxides during the HVOF process. The kinetic data acquired from the stable oxides regions will allow less ET therefore the rate constant may decrease. The bulk Inconel 625 sample need some time to establish this oxide. The rate constant data at bulk Inconel 625 also show progressive increase in the k^0 values.
- The correlation between the electrochemical activity of a thermal sprayed coating for $FcOH^+$ reduction and its corrosion resistance under normal operating conditions was not possible but our analysis did show that SECM can be used to quantify the electrochemical activity in terms of standard heterogeneous ET rate constant.

8 Summary, conclusions and future work

8.1 Introduction

This chapter includes the main results come from potentiodynamic polarization, electrochemical impedance spectroscopy and scanning electrochemical microscopy. The comparison of the different results from one technique to other is also made in summary section. The outcome of the project is concluded with some future recommendations.

8.2 Summary of results

In this research work potentiodynamic polarization testing, electrochemical impedance spectroscopy and scanning electrochemical microscopy were used to get the broader picture of corrosion processes taking place at the HVOF Inconel 625, WCCoCr and CoNiCrAlY coatings. The three HVOF coatings electrochemically tested corrode mildly to severely in 0.5M sulfuric acid. The three electrochemical testing methods used in the project gave general to more advanced information about the corrosion processes.

8.2.1 Potentiodynamic polarization

The passive current density (j_{corr}) was a factor of 10 higher for the Inconel 625 coating than that of the bulk Inconel 625. The higher passive current density for the Inconel 625 coating was attributed to HVOF process. The heterogeneous ET rate constant obtained for bulk Inconel 625 was a factor of 100 lower than the Inconel 625 coating indicating corrosion reaction is taking place at slower rate at bulk alloy.

The polarization curves analysis revealed that among three coatings, Inconel 625 was most, WCCoCr was moderate and CoNiCrAlY was least corrosion resistant in 0.5M H_2SO_4 solution. The corrosion potential (E_{corr}) for the WCCoCr and CoNiCrAlY was 30 and 50 mV more negative than E_{corr} of the Inconel 625 coating. The j_{corr} was a factor of 10 higher for the CoNiCrAlY coating than the Inconel 625 and WCCoCr coating. The breakdown potential (E_{break}) and j_{pass} were approximately same for the three coatings. The different corrosion resistance of the three coating was attributed to the constituents of

the coating materials and testing solution. The higher ET rate constant for CoNiCrAlY and WCCoCr coating prove that these two coating are corroding at fast rate.

The propensity of pitting in 3.5% NaCl solution and attack on the Cr-depleted regions was more pronounced in Inconel 625 coating than that of the WCCoCr coating. Pits were all over the surface for the CoNiCrAlY coating in 3.5% NaCl and 0.5M sulfuric acid solution containing 50 ppm of KSCN. The corrosion performance gap between the bulk Inconel 625 coating and HVOF Inconel 625 coating was also evident from pitting corrosion results.

The systematic experimental errors associated with potentiodynamic polarization results were addressed by deliberately changing the scan rate, potential scan direction, increasing stabilizing time and applied potential before testing.

- Increasing the stabilization time from 1h to 15h before starting polarization test decreased the E_{oc} change from 13-50 mV h^{-1} to 1-6 mV h^{-1}. The greater stabilization of E_{oc} increased accuracy of the polarization test as current voltage correlation defining polarization curve reflects the same corrosion phenomena of the curve. The higher E_{oc} change adversely effect in passive systems where slight polarization upset the electrochemical process enough that the generated curve did not pass through the origin, this mean applied current will be observed at zero volt relative to the starting E_{oc}.
- The shift in E_{corr} to more negative value by applying prior negative potential was 17-41 mV for bulk alloys and 1-16 mV for the coatings.

The shift in E_{corr} to more positive value by applying prior positive potential was 2-4 mV for bulk alloys and 5-18 mV for the coatings. The more negative shift in E_{corr} value for the bulk alloys by prior negative applied potential was attributed to partial removal of the oxide layer. This occurs as native (air-formed) oxide film decreases in thickness due to hydrogen evolution. The thickness of the native oxide is in the order of a few angstroms, insufficient to impede the flow of electron/ions across the interface. The excess availability of hydrogen ions and electrons to creates a reducing environment by hydrogen evolution at the interface. This hydrogen evolution decreases the thickness of oxide and further eases in/out diffusion of electro-active species across the interface. The thickness decreases more and more as the potential becomes more and more negative than the E_{oc}. The more positive shift in E_{corr} value by prior positive applied potential for the coatings was probably due to increased positive potential drive in the coating, which causes the oxidation of active spots. In bulk alloys the surface oxide has to grow more uniformly hence the applied potential distributed more evenly on the surface, therefore the shift in E_{corr} value by positive applied potential was lower for bulk alloys. We suggest from our results that microstructure, constituent materials and their percentage contribute to the E_{corr} shift by prior potential.

- It was noticed that the higher scan rate shifted E_{corr} to more negative potential from starting E_{oc} and increased the charging current contribution in net current. Charging current was increased with scan rate for all coatings but comparing the bulk and coating samples, the

charging current was a factor of 10 to 100 lower for the bulk Inconel 625 than that of the Inconel 625 coating samples. So the sprayed microstructure has changed the magnitude of the charging current. The higher value of faradaic current can be attributed to faster corrosion reaction. At all scan rates the faradaic and charging currents were highest for CoNiCrAlY coating and lowest for bulk Inconel 625, this indicates that the CoNiCrAlY coating is least and bulk Inconel 625 is most corrosion resistant material under the used experimental conditions.

- The shift in E_{corr} value from the starting E_{oc} value was 2-22 mV for the partial anodic and cathodic curves and 30-176 mV for the continuous polarization curves at 10, 20, 60 and 180 mV min^{-1}. The shift in E_{corr} value from the partial scan was 21 mV for bulk Inconel 625, 22 mV for stainless steel, 8 mV for Inconel 625 coating, 9 mV for CoNiCrAlY coating and 2 mV for the WCCoCr coating for the same set of scan rates. In the continuous polarization curves the shift in E_{corr} value was 109 mV for the bulk Inconel 625, 176 mV for stainless, -32 mV for the Inconel 625 coating, -35 mV for the CoNiCrAlY coating and -30 mV for the WCCoCr coating. The small E_{corr} shift in the partial polarization curves is attributed to lower charging current.
- Combining 10 hours stabilization time and potential scan starting from E_{oc} at 20 mV min^{-1} the E_{corr} shift was 200-240 mV for bulk alloys and 20-40 mV for HVOF coating from starting E_{oc} value, hence stabilizing time and potential scan direction greatly effect the E_{corr} value. The shift

in E_{corr} value was attributed to surface change and charging current flow due to potential scan direction.

8.2.2 X-ray photoelectron spectroscopy results

To see what oxides were present on the surface before and after electrochemical testing the oxide films formed in air and 0.5 M H_2SO_4 solution were analysed by X-ray photoelectron spectroscopy. The analysis revealed that all tested materials oxidize in air and 0.5 M H_2SO_4 solution. The percentage of oxygen and oxidation state of the elements increased with the applied potential. The stainless steel and bulk Inconel 625 alloys showed more extensive oxidation than HVOF coatings. There was not any difference between the oxides formed on bulk Inconel 625 and Inconel 625 coating samples. The amount of oxygen was 2-10% higher in air exposed and polarized samples of the bulk Inconel 625 as compared to coating sample, hence the better corrosion performance of the bulk alloy may attributed to uniform oxidation of the surface. The main oxides identified on the Inconel 625 coating and the bulk Inconel 625 alloy surface were Cr_2O_3, NiO, MoO_2, MoO_3, NbO and Nb_2O_5. The less protective $Ni(OH)_2$ responsible for low corrosion resistance of the Inconel 625 coating, reported by a member of the same group Bakere at el was not seen in our results probably due to short time for polarization. The oxides present on the WCCoCr coating were Co_2O_3, W_2O_3 and some non-stoichiometric oxides. Oxides formed on the CoNiCrAlY coating surface were Co_2O_3, Cr_2O_3 and NiO.

In our experiments XPS analysis was carried out to investigate the oxides formed during potentiodynamic polarization testing, so samples were polarized

to constant potential rather constant current. If it is desirable to test oxide thickness growth with time it is more appropriate to use the galvanostatic approach where constant current is applied and potential is measured. The time gap between oxide thinning experiments (cathodic applied currents) and inserting the samples to vacuum chamber for XPS testing should be carefully watched to avoid distortion to results due to oxidation in air.

8.2.3 Electrochemical impedance spectroscopy

- The EIS has diagnosed the three dominant electrical responses approximately at 50, 150 and 450 Ω cm^2 for HVOF Inconel 625 coating. The impedance values were correlated with *pores*, $oxide_1$ of low impedance and $oxide_2$ of high impedance. The equivalent circuit model was configured for Inconel 625 coating and correlated with the microstructural features. The impedance values of the circuit components fitted well with the experimental data therefore EIS can be used to identify microstructural features and quantify by the equivalent circuit model.
- The corrosion ranking of three coatings by EIS was analogous to the potentiodynamic results at E_{oc}, active-passive polarization and time based-EIS study. The Inconel 625 was highly corrosion resistant and CoNiCrAlY was least corrosion resistant, hence the EIS results clarify the potentiodynamic results.
- The heterogeneous ET rate constant obtained for different materials was in the same ranking as the one obtained from polarization data. The ET rate constant from EIS was a factor of 10 lower than the one

calculated from potentiodynamic polarization curves, the lower rate constant from EIS is attributed to elimination of solution resistance and capacitance.

- The exchange current density calculated from EIS for all materials was different from the corrosion current obtained from potentiodynamic polarization curves but the ranking of the materials was in same order for both sets of results. Therefore it is worth using EIS to complement the results from potentiodynamic polarization method. The exchange current was a factor of 10 lower for the bulk Inconel 625 then the Inconel 625 coating. The CoNiCrAlY and WCCoCr coatings were less corrosion resistant in terms of i_{corr} values than bulk Inconel 625 and Inconel 625 coating samples.

8.2.4 Scanning electrochemical microscopy

- The SECM images of bulk Inconel 625 and stainless did not show any features. The SECM feedback approach curves on both bulk alloys gave negative feedback all over the surface. The heterogeneous electron transfer rate constant across electrode electrolyte was 1.2×10^{-3} cm s^{-1} for bulk Inconel 625 and 4.9×10^{-5} cm s^{-1} for stainless steel. The lower electron transfer rate constant value for the stainless steel attributed to higher insulating nature of surface oxide than bulk alloy. The value of electron transfer rate constant for bulk Inconel 625 decreased to 9.7×10^{-4} cm s^{-1} after 5-days indicating progressive growth of surface oxide layer.

- The SECM image of Inconel 625 coating showed regions of different electrochemical activity. The current distance approach curves gave positive feedback on brown regions and negative feedback at green regions of the SECM image. The heterogeneous electron transfer rate constant was 2.0×10^{-4} to 5.2×10^{-4} cm s^{-1} from regions of high to low electrochemical activity. The higher values of electron transfer rate constant confirm that the splat boundaries were more active than the rest of the coating.
- The heterogeneous ET rate constants calculated from potentiodynamic polarization and EIS were in corrosive environment i.e. 0.5M H_2SO_4 solution. No particular reaction was identified in potentiodynamic polarization and EIS technique therefore the estimation of the rate constant is to get general idea how fast or slow reactions are taking place. The rate constant calculated from SECM is the one for the reduction and oxidation of FcOH across electrode/electrolyte interface hence the rate constant values from SECM is real and more accurate than other methods.

8.3 Conclusions

It has been established from this research that combined use of three electrochemical techniques enhances the understanding of corrosion processes at HVOF coating. The potentiodynamic polarization results gave overall corrosion behaviour of the coating and EIS established the correlation between microstructural features and their electrochemical response. The spatially resolved more sophisticated SECM imaging with heterogeneous ET rate

constant study in feedback mode spotted and identified electrochemical activity at microstructural level.

The higher corrosion resistance in terms of low passive current density from potentiodynamic polarization for the bulk Inconel 625 as compared to Inconel 625 coating was consistent with the higher impedance values from the EIS results. The ET rate constant obtained from SECM for the bulk Inconel 625 was higher than that measured at the Inconel 625 coating but the rate constant for bulk Inconel 625 progressively decreased to a low value than coating. The quantitative results from three techniques prove that oxidation of the bulk Inconel 625 takes place at a slower rate than at the Inconel 625 coating.

We proved from our results that without careful consideration of experimental details significant errors can be introduced in the potentiodynamic polarization results. The common practise of potentiodynamic polarization test with the one suggested for ten hours of stabilization time and starting potential scan from E_{oc} shits the E_{corr} to 200-240 mV for bulk alloys and 20-40 mV for HVOF coating from starting E_{oc} was noticed.

The ET rate constant measured from potentiodynamic polarization and EIS were related to overall reactions in the corrosive media with errors due to non steady state. The rate constants measured from CV in redox mediator containing electrolyte include the errors due to ohmic drop and charging current. The ET rate constants obtained from SECM were true electron kinetics values across substrate electrolyte interface.

The spatially resolved SECM imaging combined with heterogeneous ET rate constant study in feedback mode was used for the first time to identify the electrochemical activity of different regions for Inconel 625 coating. The splat boundaries seen from SEM images correlated well with the regions of higher electrochemical activity. This study opens the new window of SECM applications to study localized corrosion in complex microstructural systems.

8.4 Recommendations for future work

The combination of three technique yielded enormous amount of information about the corrosion processes taking place and HVOF coating surfaces but still there is a scope of future work, the recommendations for the future work are given below:

- The quantification of the EIS data need improvement, this can be done by developing standard defects in the samples and recording their impact on the impedance spectra. The samples containing standard defects can be tested by three different techniques to see how the results of one technique correlate with each other.
- The kinetics of electron transfer rate constant study for the CoNiCrAlY was problematic due to redox mediator reaction with the surface at E_{oc}. The electrolyte in the presence of ferrocenemethanol and Ru-hex made the CoNiCrAlY surface black at E_{oc} and this became more extensive with negative and positive applied potential. The hard surface of the WCCoCr coating was not smooth enough to conduct the SECM study. Further research is needed to find the suitable redox mediator or modification of the experimental setup to avoid oxidation.

- In this project we have used the SECM tip as chloride injection tip to study the pitting propensity of the regions of different electrochemical activity but the amount of chloride ions and tip-substrate distance were unable to control. Further research is needed to overcome these problems.
- The localized impedance measurement at regions of different electrochemical reactivity combined with SECM can further enhance the understanding of corrosion processes at HVOF coatings.
- The SECM combined with tensile testing can be used to explore the material stress corrosion behaviour.

9 References

1. A. Neville, J.M. Perry, T. Hodgkiess, and H.P. Chua, *Wrought and high-velocity oxy fuel sprayed Inconel 625 - examination of corrosion aspects.* IMechE, 2000. 214: p. 41-48.
2. D. Zhang, S.J. Harris, and D.G. McCartney, *Microstructure formation and corrosion behaviour in HVOF-sprayed Inconel 625 coatings.* Mater. Sci. Eng., A, 2003. 344(1-2): p. 45-56.
3. J.M. Guilemany, J. Fernandez, J. Delgado, A.V. Benedetti, and F. Climent, *Effects of thickness coating on the electrochemical behaviour of thermal spray Cr3C2-NiCr coatings.* Surf. Coat. Technol., 2002. 153(2-3): p. 107-113.
4. M. Magnani, P.H. Suegama, N. Espallargas, S. Dosta, C.S. Fugivara, J.M. Guilemany, and A.V. Benedetti, *Influence of HVOF parameters on the corrosion and wear resistance of WC-Co coatings sprayed on AA7050 T7.* Surf. Coat. Technol., 2008. 202(19): p. 4746-4757.
5. V.A.D. Souza and A. Neville, *Linking electrochemical corrosion behaviour and corrosion mechanisms of thermal spray cermet coatings (WC-CrNi and WC/CrC-CoCr).* Mater. Sci. Eng., A, 2003. 352(1-2): p. 202-211.
6. P.H. Suegama, C.S. Fugivara, A.V. Benedetti, J. Fernandez, J. Delgado, and J.M. Guilemany, *Electrochemical behavior of thermally sprayed stainless steel coatings in 3.4% NaCl solution.* Corros. Sci., 2005. 47(3): p. 605-620.
7. N. Ahmed, M.S. Bakare, D.G. McCartney, and K.T. Voisey, *The effects of microstructural features on the performance gap in corrosion resistance between bulk and HVOF sprayed Inconel 625.* Surf. Coat. Technol., 2010. 204(14): p. 2294-2301.
8. M.S. Bakare, K.T. Voisey, M.J. Roe, and D.G. McCartney, *X-ray photoelectron spectroscopy study of the passive films formed on thermally sprayed and wrought Inconel 625.* Appl. Surf. Sci., 2010. 257(3): p. 786-794.
9. M.M. Verdian, K. Raeissi, and M. Salehi, *Corrosion performance of HVOF and APS thermally sprayed NiTi intermetallic coatings in 3.5% NaCl solution.* Corros. Sci., 2010. 52(3): p. 1052-1059.
10. M. Kendig, F. Mansfeld, and S. Tsai, *Determination of the Long term Corrosion Behavior of Coated steel with A.C. Impedance Measurements.* Corros. Sci., 1983. 23(4): p. 317-329.
11. M.S. Ali, S. Song, and P. Xiao, *Evaluation of degradation of thermal barrier coatings using impedance spectroscopy.* J. Eur. Ceram. Soc., 2002. 22(1): p. 101-107.
12. M.G. Fontana and N.D. Greene, *Corrosion Engineering*. 1978: McGraw-Hill. 39-50.
13. D.A. Jones, *Principles and prevention of corrosion*. 2nd ed. 1996: Prentice Hall. 3-15.
14. L.L. Shreir, G.T. Burstein, and R.A. Jarman, *Corrosion*. 1998: Butterworth-Heinemann. 17:3-17:40.
15. R.D. Angal, *Principles and Prevention of Corrosion*. 2010: Alpha Science International. 17-28.
16. R.W. Revie, *Uhlig's Corrosion Handbook. 2nd ed.* 2000: John Wiley & Sons. 137-153, 165-171.
17. R.G. Kelly, J.R. Scully, D.W. Shoesmith, and R.G. Buchheit, *Electrochemical Techniques in Corrosion Science and Engineering*. 2002: Marcel Dekker. 35-56, 63-88.

18. N. Perez, *Electrochemistry and Corrosion Science*. 2004: Kluwer Academic.
19. K.E. Heusler, D. Landolt, and S. Trasatti, *Electrochemical Corrosion Nomenclature.* Pure & Appl. Chem, 1989. 61(1): p. 19-22.
20. R.W. Revie, *Uhlig's Corrosion Handbook. 2nd Ed.* 2000: John Wiley & Sons.
21. P.R. Roberge, *Handbook of Corrosion Engineering*. 1999: McGraw-Hill.
22. E. Mccafferty, *Introduction to Corrosion Science*. 2010: Springer. 9-16.
23. S.L. Chawla and R.K. Gupta, *Materials Selection for Corrosion Control*. 1993: ASM International. 334, 389.
24. S.D. Cramer and B.S. Covino, *ASM Handbook, Volume 13A - Corrosion Fundamentals*. 1987: ASM International. 18-24, 2442-2443.
25. M.V. Veazey, *Corrosion Cost and Preventive Strategies in the United State.* Mater. Perform., 2002: p. 1-10.
26. S.D. Cramer and B.S. Covino, *ASM Handbook, Volume 13B - Corrosion Testing and Protections*, ASM International.
27. CIA, *The world fact book - Country comparision of GDP*. 2009.
28. G. Schmitt, *Global needs for knowledge dissemination, research, and development in material deterioration and corrosion control.* World Corrosion Organization, 2009(July): p. 1-40.
29. J.L. Villalobos, *Corrosion Risk Revised.* Risk Management, 2005. 52(6): p. 36-41.
30. A.W. Peabody, *Control of Pipeline Corrosion*. 1967: National Association of Corrosion Engineers. 5-15.
31. M.E. Parker and E.G. Peattie, *Pipe line Corrosion and Cathodic Protection: A Practical Manual for Corrosion Engineers, Technicians, and Field Personnel*. 1984: Gulf Pub.
32. M. Samples, *Introduction to Corrosin Monitoring Systems.* Metal Samples.
33. R.B. Eckert, *Advanced Procedures for Analysis of Coupons used for Evaluating and Monitoring Internal Corrosion.* CC Technologies Inc., 2002: p. 1-17.
34. B. Marple, M. Hyland, and Y. Lau, *Thermal Spray 2006: Building on 100 Years of Success* 2006: ASM International.
35. K. Dobler, H. Kreye, and R. Schwetzke, *Oxidation of Stainless Steel in the High Velocity Oxy-fuel Process.* J. Therm. Spray Technol., 2000. 9(3): p. 407-413.
36. L. Xie, X. Ma, E.H. Jordan, N.P. Padture, D.T. Xiao, and M. Gell, *Deposition Mechanisms of Thermal Barrier Coatings in the Solution Precursor Plasma Spray Process.* Surf. Coat. Technol., 2004: p. 103-107.
37. J.R. Davis, *Handbook of Thermal Spray Technology*. 2004: ASM International.
38. J.A.L. Dobbelaar, *The Use of Impedance Measurements in Corrosion Research*. 1990, Deflt University. p. 1-28.
39. M. Li, D. Shi, and P.D. Christofides, *Model-based estimation and control of particle velocity and melting in HVOF thermal spray.* Chem. Eng. Sci., 2004. 59(22–23): p. 5647-5656.
40. S. Metco, *Hybrid HVOF spray system to produce tougher coatings.* Metal Powder Report, 1996. 51(9): p. 6.
41. A.L. Mohd Tobi, P.H. Shipway, and S.B. Leen, *Finite element modelling of brittle fracture of thick coatings under normal and tangential loading.* Tribology International, 2013. 58(0): p. 29-39.
42. S. Shrestha and A.J. Sturgeon, *Use of Advanced Thermal Spray Processes for Corrosion Protection in Marine Environments.* Surf. Eng., 2004. 20(4): p. 237-243.

43. R. Molins, B. Normand, G. Rannou, B. Hannoyer, and H. Liao, *Interlamellar Boundary Characterization in Ni-based alloy Thermally Sprayed Coating.* Mater. Sci. Eng., A, 2003. 351(1): p. 325-333.
44. M. Takeda, N. Mohrihiro, and R. Ebara, *Diamond Jet Hybrid HVOF Thermal Spray: Rule-Based Modeling of Coating Microstructure.* Mater. Trans., 2002. 11(2860-2865).
45. M.L. Dan Shi, and Panagiotis D. Christofides, *Diamond Jet Hybrid HVOF Thermal Spray: Rule-Based Modeling of Coating Microstructure.* Ind. Eng. Chem. Res., 2004. 43: p. 3653-3665.
46. H.Y. Al-Fadhli, J. Stokes, S. Hashmi, and B.S. Yilbas, *Post Test Analysis of Inconel-625 (HVOF) Coating Using SEM and EDS after Exposure to Erosion-Corrosion Test.* Microsc. Microanal., 2005. 11: p. 1996-1997.
47. E. Klar and ASM, *ASM Handbook Volume 7: Powder Metallurgy*. 1984: ASM International.
48. S. Saeidi, *Microstructure, oxidation and mechanical properties of as sprayed and annealed HVOF and VPS CoNiCrAlY coatings*, in *Mechanical, Manufacturing and Materials Engineering*. 2010, University of Nottingham: Nottingham.
49. P. Richer, M. Yandouzi, L. Beauvais, and B. Jodoin, *Oxidation behaviour of CoNiCrAlY bond coats produced by plasma, HVOF and cold gas dynamic spraying.* Surf. Coat. Technol., 2010. 204(24): p. 3962-3974.
50. F. Tang, G.E. Kim, V. Provenzano, and J.M. Schoenung, *Effects of surface oxidation during HVOF processing on the primary stage oxidation of a CoNiCrAlY coating.* Surf. Coat. Technol., 2004. 185(3): p. 228-233.
51. M. Oksa, E. Turnen, and T. Suhonen, *Optimization and charactrization of high velocity oxy-fuel sprayed coatings*. 2011, Technical Research Centre of Finland. p. 17-52.
52. D. Zhang, S.J. Harris, and D.G. McCartney, *Microstructure formation and corrosion behaviour in HVOF-sprayed Inconel 625 coatings.* Mater. Sci. Eng., A, 2003. 344(1-2): p. 45-56.
53. G.H. Aydogdu and M.K. Aydinol, *Determination of susceptibility to intergranular corrosion and electrochemical reactivation behaviour of AISI 316L type stainless steel.* Corros. Sci., 2006. 48(11): p. 3565-3583.
54. T. Amadou, H. Sidhom, and C. Braham, *Double loop electrochemical potentiokinetic reactivation test optimization in checking of duplex stainless steel intergranular corrosion susceptibility.* Metall. Mater. Trans. A, 2004. 35(11): p. 3499-3513.
55. V. Shankar, K. Bhanu Sankara Rao, and S.L. Mannan, *Microstructure and mechanical properties of Inconel 625 superalloy.* J. Nucl. Mater., 2001. 288(2-3): p. 222-232.
56. N. Ahmed, M.S. Bakare, D.G. McCartney, and K.T. Voisey, *The effects of microstructural features on the performance gap in corrosion resistance between bulk and HVOF sprayed Inconel 625.* Surf. Coat. Technol., 2010. 204(14): p. 2294-2301.
57. P.H. Suegama, C.S. Fugivara, A.V. Benedetti, J. Fernández, J. Delgado, and J.M. Guilemany, *Electrochemical behavior of thermally sprayed stainless steel coatings in 3.4% NaCl solution.* Corrosion Science, 2005. 47(3): p. 605-620.
58. N. Ahmed, M.S. Bakare, D.G. McCartney, and K.T. Voisey, *The effects of microstructural features on the performance gap in corrosion resistance between bulk and HVOF sprayed Inconel 625.* Surf. Coat. Technol., 2010. 204(14): p. 2294-2301.

59. A.J. Sturgeon, *Microstructural characterization of high velocity oxy-fuel sprayed coatings of Inconel 625.* J. Mater. Sci., 1997. 32: p. 863 - 872.
60. Z. Liu, J. Cabrero, S. Niang, and Z.Y. Al-Taha, *Improving corrosion and wear performance of HVOF-sprayed Inconel 625 and WC-Inconel 625 coatings by high power diode laser treatments.* Surf. Coat. Technol., 2007. 201(16–17): p. 7149-7158.
61. P. Poza, C.J. Munez, M.A. Garrido, S. Vezzu, S. Rech, and A. Trentin, *Effect of laser remelting on the mechanical behaviour of Inconel 625 cold-sprayed coatings.* Procedia Engineering, 2011. 10: p. 3799-3804.
62. A.A. Boudi, M.S.J. Hashmi, and B.S. Yilbas, *HVOF coating of Inconel 625 onto stainless and carbon steel surfaces: corrosion and bond testing.* J. Mater. Process. Technol., 2004. 155–156(0): p. 2051-2055.
63. W. Tsung-Feng and T. Wen-Ta, *Effect of KSCN and its concentration on the reactivation behavior of sensitized alloy 600 in sulfuric acid solution.* Corros. Sci., 2003. 45(2): p. 267-280.
64. K.P. Cooper, P. Slebodnick, and E.D. Thomas, *Seawater corrosion behavior of laser surface modified Inconel 625 alloy.* Mater. Sci. Eng., A, 1996. 206(1): p. 138-149.
65. P.H. Suegama, C.S. Fugivara, A.V. Benedetti, J.M. Guilemany, J. Fernández, and J. Delgado, *The influence of gun transverse speed on electrochemical behaviour of thermally sprayed Cr3C2-NiCr coatings in 0.5 M H2SO4 solution.* Electrochimica Acta, 2004. 49(4): p. 627-634.
66. P.H. Suegama, C.S. Fugivara, A.V. Benedetti, J.M. Guilemany, J. Fernandez, and J. Delgado, *The influence of gun transverse speed on electrochemical behaviour of thermally sprayed Cr_3C_2-NiCr coatings in 0.5 M H_2SO_4 solution.* Electrochim. Acta, 2004. 49(4): p. 627-634.
67. S. Ahmaniemi, P. Vuoristo, T. Mantyla, C. Gualco, A. Bonadei, and R. Di Maggio, *Thermal cycling resistance of modified thick thermal barrier coatings.* Surf. Coat. Technol., 2005. 190(3): p. 378-387.
68. W.R. Chen, X. Wu, D. Dudzinski, and P.C. Patnaik, *Modification of oxide layer in plasma-sprayed thermal barrier coatings.* Surf. Coat. Technol., 2006. 200(21): p. 5863-5868.
69. A.N. Khan and J. Lu, *Behavior of air plasma sprayed thermal barrier coatings, subject to intense thermal cycling.* Surf. Coat. Technol., 2003. 166(1): p. 37-43.
70. G. Newaz and X. Chen, *Progressive damage assessment in thermal barrier coatings using thermal wave imaging technique.* Surf. Coat. Technol., 2005. 190(1): p. 7-14.
71. F. Tang, L. Ajdelsztajn, and J.M. Schoenung, *Characterization of oxide scales formed on HVOF NiCrAlY coatings with various oxygen contents introduced during thermal spraying.* Scripta Materialia, 2004. 51(1): p. 25-29.
72. B.V. Krishna, V.N. Misra, P.S. Mukherjee, and P. Sharma, *Microstructure and properties of flame sprayed tungsten carbide coatings.* International Journal of Refractory Metals and Hard Materials, 2002. 20(6): p. 355-374.
73. N. Espallargas, J. Berget, J.M. Guilemany, A.V. Benedetti, and P.H. Suegama, *Cr_3C_2-NiCr and WC-Ni thermal spray coatings as alternatives to hard chromium for erosion-corrosion resistance.* Surf. Coat. Technol., 2008. 202(8): p. 1405-1417.
74. M. Takeda, N. Morihiro, and R. Ebara, *Corrosion Behavior of Thermally Sprayed WC Coating in Na_2SO_4* Mater. Trans., 2002. 43(11): p. 2860-2865.

75. L. Fedrizzi, S. Rossi, R. Cristel, and P.L. Bonora, *Corrosion and wear behaviour of HVOF cermet coatings used to replace hard chromium.* Electrochimica Acta, 2004. 49(17-18): p. 2803-2814.
76. D. Walsh, E. Lisa, M.S. Bakare, and K.T. Voisey, *Visualisation of the local electrochemical activity of thermal sprayed anti-corrosion coatings using scanning electrochemical microscopy*. Electrochim. Acta, 2009. 54(20): p. 4647-4654.
77. V. Edgar, I.C. Gonzalez, and C. Ernesto, *Scanning electrochemical microscopy measurement of ferrous ion fluxes during localized corrosion of steel.* Electrochem. Commun., 2006. 8(1): p. 179-183.
78. C. Gabrielli, S. Joiret, M. Keddam, H. Perrot, N. Portail, P. Rousseau, and V. Vivier, *A SECM assisted EQCM study of iron pitting.* Electrochim. Acta, 2007. 52(27): p. 7706-7714.
79. A.K. Neufeld and A.P. OMullane, *Effect of the mediator in feedback mode-based SECM interrogation of indium tin-oxide and boron-doped diamond electrodes.* J. Solid State Electrochem., 2006(10): p. 808–816.
80. A.M. Simoes, D. Battocchi, D.E. Tallman, and G.P. Bierwagen, *SVET and SECM imaging of cathodic protection of aluminium by a Mg-rich coating.* Corros. Sci., 2007. 49(10): p. 3838-3849.
81. L. Johnson, A. Niaz, A. Boatwright, K.T. Voisey, and D.A. Walsh, *Scanning Electrochemical Microscopy at Thermal Sprayed Anti-Corrosion Coatings: Effect of Thermal Spraying on Heterogeneous Electron Transfer Kinetics.* J. Electroanal. Chem. In Press, Accepted Manuscript.
82. P. Sun, Z. Liu, H. Yu, and M.V. Mirkin, *Effect of Mechanical Stress on the Kinetics of Heterogeneous Electron Transfer*. Langmuir, 2008. 24(18): p. 9941-9944.
83. H.S. White and S. Irina, *Scanning Electrochemical Microscopy of Electroactive Defect Sites in the Native Oxide Film on Aluminum.* Electrochem. Solid-State Lett., 2001. 4(1): p. B4-B6.
84. S. B. Basame and H.S. White, *Scanning Electrochemical Microscopy of Metal/Metal Oxide Electrodes. Analysis of Spatially Localized Electron-Transfer Reactions during Oxide Growth.* Anal. Chem., 1999. 71(15): p. 3166-3170
85. M.B. Jensen, A. Guerard, D.E. Tallman, and G.P. Bierwagenb, *Studies of Electron Transfer at Aluminum Alloy Surfaces by Scanning Electrochemical Microscopy*. J. Electrochem. Soc., 2008. 155(7): p. C324-C332.
86. Z.L. Peng Sun, Honghui Yu, and Michael V. Mirkin, *Effect of Mechanical Stress on the Kinetics of Heterogeneous Electron Transfer.* Langmuir, 2008. 24: p. 9941-9944.
87. F. Falkenberg, K. Fushimi, and M. Seo, *Study on initiation of localised corrosion on copper thin film electrode by combinational use of an EQCM with a liquid-phase ion gun.* Corros. Sci., 2003. 45(11): p. 2657-2670.
88. J.W. Still and D.O. Wipf, *Breakdown of the Iron Passive Layer by Use of the Scanning Electrochemical Microscope.* J. Electrochem. Soc., 1997. 144(8): p. 2657-2665.
89. K. Fushimi and M. Seo, *Initiation of a Local Breakdown of Passive Film on Iron due to Chloride Ions Generated by a Liquid-Phase Ion Gun.* J. Electrochem. Soc., 2001. 148(11): p. B450-B456.
90. I. Serebrennikova and H.S. White, *Scanning Electrochemical Microscopy of Electroactive Defect Sites in the Native Oxide Film on Aluminum.* Electrochem. Solid-State Lett., 2001. 4(1): p. B4-B6.

91. X.L. Zhang, Z.H. Jiang, Z.P. Yao, Y. Song, and Z.D. Wu, *Effects of scan rate on the potentiodynamic polarization curve obtained to determine the Tafel slopes and corrosion current density.* Corros. Sci., 2009. 51(3): p. 581-587.
92. G. Rocchini, *The determination of tafel slopes by the successive approximation method.* Corros. Sci., 1995. 37(6): p. 987-1003.
93. D.P. Schweinsberg and H.J. Flitt, *Reproducibility of corrosion parameters for the acidic dissolution of pure iron: potentiostatic polarisation.* Corros. Sci., 2005. 47(6): p. 1520-1533.
94. J.R. Macdonald, *Impedance Spectroscopy: Theory, Experiment, and Applications*. 2005: Willy
95. L. Andrzej, *Electrochemical Impedance Spectroscopy and its Applications*, in *Modern Aspects of Electrochemistry*. 2002, Springer US. p. 143-248.
96. J. Fleig, J. Jamnik, J. Maier, and J. Ludvig, *Inductive Loops in Impedance Spectroscopy Caused by Electrical Shielding.* J. Electrochem. Soc., 1996. 143(11): p. 3636-3641.
97. V. Otieno-Alego, G.A. Hope, H.J. Flitt, G.A. Cash, and D.P. Schweinsberg, *The effect of potential scan rate on the parameters used to synthesize anodic polarization curves.* Corros. Sci., 1992. 33(11): p. 1719-1734.
98. G.S. Frankel and M. Rohwerder, *Electrochemical Techniques for Corrosion*, in *Encyclopedia of Electrochemistry*. 2007, Wiley-VCH Verlag GmbH & Co. KGaA.
99. R. Baboian, *Corrosion Tests and Standards: Application and Interpretation*. 2005: ASTM International.
100. ASTM, *Standard Reference Test Method for Making Potentiostatic and Potentiodynamic Anodic Polarization Measurements (G5 - 94)*. 1999: ASTM International.
101. A. Legat, *Monitoring of steel corrosion in concrete by electrode arrays and electrical resistance probes.* Electrochim. Acta, 2007. 52(27): p. 7590-7598.
102. D.G. Enos, *The Potentiodynamic Polarization Scan.* solartron Instruments, January 1997(2): p. 14.
103. R.I. Holland, *Use of potentiodynamic polarization technique for corrosion testing of dental alloys.* European Journal of Oral Sciences, 1991. 99(1): p. 75-85.
104. D.C. Silverman and S. Inc, *Tutorial on Cyclic Potentiodynamic Polarization Technique.* Corros. Sci., 1998: p. 1-21.
105. C.G. Zoski, A.J. Bard, J. Leddy, and L.R. Faulkner, *Electrochemical methods. 2nd Ed*. 2002: John Wiley & Sons Inc.
106. J. Wang, *Analytical electrochemistry 2nd ed*. 2006: Wiley & Sons Inc.
107. S. Rossi, M. Fedel, F. Deflorian, and M. del Carmen Vadillo, *Localized Electrochemical Techniques: Theory and Practical Examples in Corrosion Studies.* C. R. Chim., 2008. 11(9): p. 984-994.
108. M.A. Ibrahim, S. Abd El Rehim, and M. Hamza, *Corrosion Behavior of some Austenitic Stainless Steels in Chloride Environments.* Mater. Chem. Phys., 2009. 115(1): p. 80-85.
109. N. Parvathavarthini, R.K. Gupta, A. Vinod Kumar, S. Ramya, and U. Kamachi Mudali, *Interpretation of Electrochemical Potentiokinetic Reactivation data in the presence of sulphide/oxysulphide inclusions in 316LN stainless steel.* Corros. Sci., 2011. 53(10): p. 3202-3214.
110. C. Andrade and C. Alonso, *Corrosion rate monitoring in the laboratory and on-site.* Construction and Building Materials, 1996. 10(5): p. 315-328.

111. A. Sergio, L.D. Wolynec, and S. Costa, *Corrosion Characterization of Titanium alloys by Electrochemical Techniques.* Electrochim. Acta, 2006. 51(9): p. 1815-1819.
112. G. Bolelli, L. Lusvarghi, and R. Giovanardi, *A Comparison Between the Corrosion Resistances of some HVOF-Sprayed metal alloy Coatings.* Surf. Coat. Technol., 2008. 202(19): p. 4793-4809.
113. Y.Y. Chen, L.B. Chou, and H.C. Shih, *Factors Affecting the Electrochemical Behavior and Stress Corrosion Cracking of Alloy 690 in Chloride Environments.* Mater. Chem. Phys., 2006. 97(1): p. 37-49.
114. A.W.E. Hodgson, S. Kurz, S. Virtanen, V. Fervel, C.O.A. Olsson, and S. Mischler, *Passive and transpassive behaviour of CoCrMo in simulated biological solutions.* Electrochim. Acta, 2004. 49(13): p. 2167-2178.
115. ASTM, *Standard practice for preparing, cleaning, and evaluating corrosion test specimens (G1 - 03)*. 1995: ASTM International.
116. ASTM, *Standard practice for laboratory immersion corrosion testing of metals (G31 - 72)*. 2004: ASTM International.
117. ASTM, *Standard Practice for Conventions Applicable to Electrochemical Measurements in Corrosion Testing (G3 - 89)*. 2010: ASTM International.
118. ASTM, *Standard Test Method for Conducting Potentiodynamic Polarization Resistance Measurements (G59 - 97)*. 2009: ASTM International.
119. ASTM, *Standard Practice for Calculation of Corrosion Rates and Related Information from Electrochemical Measurements (G102 - 89)*. 2010: ASTM International.
120. ASTM, *Standard Test Method for Conducting Cyclic Potentiodynamic Polarization Measurements for Localized Corrosion Susceptibility of Iron-, Nickel-, or Cobalt-Based Alloys (G61-86)*. 2009: ASTM International.
121. Y. Tsutsumi, A. Nishikata, and T. Tsuru, *Pitting corrosion mechanism of Type 304 stainless steel under a droplet of chloride solutions.* Corros. Sci., 2007. 49(3): p. 1394-1407.
122. O. Martin, P. De Tiedra, C. Garcia, F. Martín, and M. Lopez, *Comparative study between large-scale and small-scale electrochemical potentiokinetic reactivation performed on AISI 316L austenitic stainless steel.* Corros. Sci., 2012. 54(0): p. 119-126.
123. M. Prohaska, H. Kanduth, G. Mori, R. Grill, and G. Tischler, *On the substitution of conventional corrosion tests by an electrochemical potentiokinetic reactivation test.* Corros. Sci., 2010. 52(5): p. 1582-1592.
124. J.M. Aquino, C.A. Della Rovere, and S.E. Kuri, *Intergranular corrosion susceptibility in supermartensitic stainless steel weldments.* Corros. Sci., 2009. 51(10): p. 2316-2323.
125. ASTM, *Standard Test Method for Electrochemical Reactivation (EPR) for Detecting Sensitization of AISI Type 304 and 304L Stainless Steels (G108-98)*. 2010: ASTM International.
126. H. Tan, Y. Jiang, B. Deng, W. Gao, and J. Li, *Evaluation of aged Incoloy 800 alloy sensitization to intergranular corrosion by means of double loop electrochemical methods and image analysis.* Nucl. Eng. Des., 2011. 241(5): p. 1421-1429.
127. M.F. Maday, A. Mignone, and M. Vittori, *The application of the electrochemical potentiokinetic reactivation method for detecting sensitization in inconel 600. The influence of some testing parameters.* Corros. Sci., 1988. 28(9): p. 887-900.

128. BSI, *Corrosion of metals and alloys. Electrochemical test methods. Guidelines for conducting potentiostatic and potentiodynamic polarization measurements (BS EN ISO 17475:2008)*. 2006: British Standards Institute.
129. V.S. Bagotosky, *Fundamentals of electrochemistry*. 2006: Wiley-Interscience.
130. C.G. Zoski, ed. *Handbook of Electrochemistry*. 1st ed. 2007, Elsevier.
131. A.J. Bard and L.R. Faulkner, *Electrochemical methods: fundamentals and applications*. 1980: Wiley.
132. C.H. Kim, S.-I. Pyun, and H.-C. Shin, *Kinetics of Double-Layer Charging/Discharging of Activated Carbon Electrodes: Role of Surface Acidic Functional Groups.* Journal of The Electrochemical Society, 2002. 149(2): p. A93-A98.
133. A.J. Bard, G. Inzelt, and F. Scholz, *Electrochemical Dictionary*. 2010: Springer.
134. V.O. Alego, G.A. Hope, H.J. Flitt, G.A. Cash, and D.P. Schweinsberg, *The effect of potential scan rate on the parameters used to synthesize anodic polarization curves.* Corros. Sci., 1992. 33(11): p. 1719-1734.
135. P.P. David Loveday, and Bob Rodgers, *Evaluation of Organic Coatings with Electrochemical Impedance Spectroscopy (Paper 2).* J. Coat. Technol., 2004. August 2004: p. 46-52.
136. G. Song, *Equivalent circuit model for AC electrochemical impedance spectroscopy of concrete.* Cem. Concr. Res., 2000. 30(11): p. 1723-1730.
137. A. Miszczyk, M. Szocinski, and K. Darowicki, *Interlayer defect evolution in an organic coating system on steel under hydromechanical loading.* J. Appl. Electrochem., 2007. 37(3): p. 353-358.
138. K.E. Jeffers. *Electrochemical impedance spectroscopy for the characterization of corrosion and cathodic protection of buried pipelines*. 1999.
139. J. Oijerholm, J. Pan, Q. Lu, and C. Leygraf, *In-situ Impedence Spectroscopy Study of Electrical Conductivity and Ionic Transport in Thermally Grown Oxide Scales on a Commercial FeCrAl Alloy.* Oxid. Met., 2007. 68(5): p. 253-269.
140. T.A. Strivens and C.C. Taylor, *An Assessment of A/C Impedance as a Basic Research and Routine Testing Method for Studying Corrosion of Metals under Paint films.* Mater. Chem. Phys., 1982. 7(2): p. 199-220.
141. M.E.P. Souza, E. Ariza, M. Ballester, I.V.P. Yoshida, L.A. Rocha, and C.M.A. Freire, *Characterization of organic-inorganic hybrid coatings for corrosion protection of galvanized steel and electroplated ZnFe steel.* Materials Research, 2006. 9: p. 59-64.
142. G.P. Bierwagen, L. He, J. Li, L. Ellingson, and D.E. Tallman, *Studies of a new accelerated evaluation method for coating corrosion resistance - thermal cycling testing.* Prog. Org. Coat., 2000. 39(1): p. 67-78.
143. P.P. David Loveday, and Bob Rodgers, *Evaluation of Organic Coatings with Electrochemical Impedance Spectroscopy (Paper 1).* J. Coat. Technol., 2004(1): p. 88-93.
144. P.P. David Loveday, and Bob Rodgers, *Evaluation of Organic Coatings with Electrochemical Impedance Spectroscopy (Paper 3).* J. Coat. Technol., 2005: p. 22-27.
145. J.J. Senkevich, D.A. Jones, and I. Chatterjee, *Measuring the growth of oxide films on low carbon steel at 500°C by impedance spectroscopy.* Corros. Sci., 2000. 42(2): p. 201-210.
146. Autolab, *Electrochemical Impdance Spectroscopy Data Analysis.* Autolab Instruments.

147. C. A. Schiller, F. Richter, and E.G.a.N. Wagner, *Validation and evaluation of electrochemical impedance spectra of systems with states that change with time.* Phys. Chem. 2001(3): p. 374-378.
148. V.D. Jovic, *Determination of the correct value of Cdl from impedance results fitted by the commercially available software.* Gamry Instruments, 2003.
149. C.R. Magana-Zavala, M.E. Angeles-San Martın, and F.J. Rodrıguez-Gomez, *Electrochemical impedance spectroscopy (EIS) modelling of different behaviours of Ni and Ni oxide thin films for corrosion prevention in sour media.* Anti-Corrosion Methods and Materials, 2010. 57: p. 118–125.
150. B. Jayaraj, V.H. Desai, C.K. Lee, and Y.H. Sohn, *Electrochemical impedance spectroscopy of porous ZrO_2-8 wt.% Y_2O_3 and thermally grown oxide on nickel aluminide.* Mater. Sci. Eng., A, 2004. 372(2): p. 278-286.
151. C. A. Schiller, F. Richter, and E.G.a.N. Wagner, *Validation and evaluation of electrochemical impedance spectra of systems with states that change with time.* Phys. Chem., 2000. 2001(3): p. 374-378.
152. B.A. Boukamp, *Practical application of the Kramers-Kronig transformation on impedance measurements in solid state electrochemistry.* Solid State Ionics, 1993. 62(2): p. 131-141.
153. J.L. Polo, E. Cano, and J.M. Bastidas, *An impedance study on the influence of molybdenum in stainless steel pitting corrosion.* J. Electroanal. Chem., 2002. 537(2): p. 183-187.
154. J. Kwak and A.J. Bard, *Scanning electrochemical microscopy. Apparatus and two-dimensional scans of conductive and insulating substrates.* Anal. Chem., 1989. 61(17): p. 1794-1799.
155. R.C. Engstrom and C.M. Pharr, *Scanning electrochemical microscopy.* Anal. Chem., 1989. 61(19): p. 1099A-1104A.
156. J.S. Newman and K.E. Thomas-Alyea, *Electrochemical Systems*. 2004: J. Wiley.
157. C. Instruments. *Model 920D Scanning Electrochemical Microscope*. 2012; Available from: http://www.chinstruments.com/chi900.shtml.
158. P.S. Franc, O. Laforge, and M.V. Mirkin, *Scanning electrochemical microscopy in the 21st century.* Phys. Chem. Chem. Phys., 2006. 2007(9): p. 802–823.
159. A.A. Gewirth and B.K. Niece, *Electrochemical Applications of in Situ Scanning Probe Microscopy.* Chem. Rev., 1997. 97(4): p. 1129-1162.
160. E. Bakker, *Electrochemical Sensors.* Anal. Chem., 2004. 76(12): p. 3285-3298.
161. B.J. Privett, J.H. Shin, and M.H. Schoenfisch, *Electrochemical Sensors.* Anal. Chem., 2010. 82(12): p. 4723-4741.
162. M.V. Mirkin, F.F. Fu-Ren, and A.J. Bard, *Scanning electrochemical microscopy part 13. Evaluation of the tip shapes of nanometer size microelectrodes.* J. Electroanal. Chem., 1992. 328(1-2): p. 47-62.
163. A.J. Bard and M.V. Mirkin, eds. *Scanning Electrochemical Microscopy*. SECM, ed. Bard A.J. 2001, Marcel Dekker Inc: Austin Texas.
164. A.J. Bard, M.V. Mirkin, P.R. Unwin, and D.O. Wipf, *Scanning electrochemical microscopy. 12. Theory and experiment of the feedback mode with finite heterogeneous electron-transfer kinetics and arbitrary substrate size.* J. Phys. Chem., 1992 96(4): p. 1861-1868
165. C.M. Sanchez, F.J. Vidal-Iglesias, J. Solla-Gullon, V. Montiel, A. Aldaz, J.M. Feliu, and E. Herrero, *Scanning electrochemical microscopy for studying electrocatalysis on shape-controlled gold nanoparticles and nanorods.* Electrochim. Acta, 2010. 55(27): p. 8252-8257.

166. X. Lu, Q. Wang, and X. Liu, *Review: Recent applications of scanning electrochemical microscopy to the study of charge transfer kinetics.* Anal. Chim. Acta, 2007. 601(1): p. 10-25.
167. M. Arca, M.V. Mirkin, and A.J. Bard, *Polymer Films on Electrodes. 26. Study of Ion Transport and Electron Transfer at Polypyrrole Films by Scanning Electrochemical Microscopy*. J. Phys. Chem., 1995. 99(14): p. 5040-5050
168. A.K.N.A.P. O'Mullane, *Effect of the mediator in feedback mode-based SECM interrogation of indium tin-oxide and boron-doped diamond electrodes.* J. Solid State Electrochem., 2006. (2006)(10): p. 808–816.
169. A.M. Simões, D. Battocchi, D.E. Tallman, and G.P. Bierwagen, *SVET and SECM imaging of cathodic protection of aluminium by a Mg-rich coating.* Corros. Sci., 2007. 49(10): p. 3838-3849.
170. E. Volker, C.G. Inchauspe, and E.J. Calvo, *Scanning electrochemical microscopy measurement of ferrous ion fluxes during localized corrosion of steel*. Electrochem. Commun., 2006. 8(1): p. 179-183.
171. A.K. Neufeld and O.A. Mullane, *Effect of the mediator in feedback mode-based SECM interrogation of indium tin-oxide and boron doped diamond electrodes.* J. Solid State Electrochem., 2006(10): p. 808-816.
172. K. Lovelock, F. Cowling, A. Taylor, P. Licence, and D. Walsh, *Effect of Viscosity on Steady-State Voltammetry and Scanning Electrochemical Microscopy in Room Temperature Ionic Liquids*. J. Phys. Chem., 2010. 13(114): p. 4442-4450.
173. M.V. Mirkin, M. Arca, and A.J. Bard, *Scanning electrochemical microscopy. 22. Examination of thin solid silver(I) bromide films: ion diffusion in the film and heterogeneous kinetics at the film/solution interface.* J. Phys. Chem., 1993. 97(41): p. 10790-10795
174. R. Cornut, P. Hapiot, and C. Lefrou, *Enzyme-mediator kinetics studies with SECM: Numerical results and procedures to determine kinetics constants.* J. Electroanal. Chem., 2009. 633(1): p. 221-227.
175. R. Cornut and C. Lefrou, *Studying permeable films with scanning electrochemical microscopy (SECM): Quantitative determination of permeability parameter.* J. Electroanal. Chem., 2008. 623(2): p. 197-203.
176. S. Griveau, S. Aroua, D. Bediwy, R. Cornut, C. Lefrou, and F. Bedioui, *Spontaneous adsorbed layers of 4-nitrobenzenediazonium salt on gold and glassy carbon: Local characterization by SECM and electron-transfer kinetics evaluation.* J. Electroanal. Chem., 2010. 647(1): p. 93-96.
177. P.G. Nicholson, S. Zhou, G. Hinds, A.J. Wain, and A. Turnbull, *Electrocatalytic activity mapping of model fuel cell catalyst films using scanning electrochemical microscopy*. Electrochim. Acta, 2009. 54(19): p. 4525-4533.
178. R. Cornut, S. Griveau, and C. Lefrou, *Accuracy study on fitting procedure of kinetics SECM feedback experiments.* J. Electroanal. Chem., 2010. 650(1): p. 55-61.
179. R. Cornut and C. Lefrou, *New analytical approximation of feedback approach curves with a microdisk SECM tip and irreversible kinetic reaction at the substrate.* J. Electroanal. Chem., 2008. 621(2): p. 178-184.
180. R. Cornut and C. Lefrou, *A unified new analytical approximation for negative feedback currents with a microdisk SECM tip.* J. Electroanal. Chem., 2007. 608(1): p. 59-66.
181. R. Cornut and C. Lefrou, *New analytical approximations for negative feedback currents with a microdisk SECM tip.* J. Electroanal. Chem., 2007. 604(2): p. 91-100.

182. S. Metco. *Publications on HVOF*. Advanced technology solution and services 2008; Available from: http://www.sulzer.com/en/Products-and-Services/Coating-Equipment/Thermal-Spray/Processes/HVOF-Liquid-Fuel.
183. G.D. Jonathan L. Amphlett and, *Scanning Electrochemical Microscopy (SECM): An Investigation of the Effects of Tip Geometry on Amperometric Tip Response*. J. Phys. Chem. B, 1998. 102((49)): p. 9946-9951.
184. S. Instruments. *P-2000 Laser Based Micropipette Puller* Available from: http://www.sutter.com/products/sell_sheets/P-2000.pdf.
185. S. Instruments. *BV-10 Microelectrode Beveler* Available from: http://www.sutter.com/products/product_sheets/bv10.html.
186. J.L. Polo, E. Cano, and J.M. Bastidas, *An impedance study on the influence of molybdenum in stainless steel pitting corrosion.* J. Electroanal. Chem., 2002. 537(1-2): p. 183-187.
187. J.F. Moulder and J. Chastain, *Handbook of X-Ray Photoelectron Spectroscopy: A Reference Book of Standard Spectra for Identification and Interpretation of XPS Data*. 1992: Physical Electronics Division, Perkin-Elmer Corporation.
188. F. Karcı, R. Kacar, and S. Gunduz, *The effect of process parameter on the properties of spot welded cold deformed AISI304 grade austenitic stainless steel.* J. Mater. Process. Technol., 2009. 209(8): p. 4011-4019.
189. N. Karimi, F. Riffard, F. Rabaste, S. Perrier, R. Cueff, C. Issartel, and H. Buscail, *Characterization of the oxides formed at 1000 °C on the AISI 304 stainless steel by X-ray diffraction and infrared spectroscopy*. Appl. Surf. Sci., 2008. 254(8): p. 2292-2299.
190. N. Ahmed, M.S. Bakare, D.G. McCartney, and K.T. Voisey, *The effects of microstructural features on the performance gap in corrosion resistance between bulk and HVOF sprayed Inconel 625*. Surf. Coat. Technol. 204(14): p. 2294-2301.
191. G.P. Dinda, A.K. Dasgupta, and J. Mazumder, *Laser aided direct metal deposition of Inconel 625 superalloy: Microstructural evolution and thermal stability*. Mater. Sci. Eng., A, 2009. 509(1–2): p. 98-104.
192. V. Shankar, K. Bhanu Sankara Rao, and S.L. Mannan, *Microstructure and mechanical properties of Inconel 625 superalloy*. J. Nucl. Mater., 2001. 288(3): p. 222-232.
193. A.A. Lebedev and V.V. Kosarchuk, *Influence of phase transformations on the mechanical properties of austenitic stainless steels.* Int. J. Plast., 2000. 16(7–8): p. 749-767.
194. M. Martin, S. Weber, C. Izawa, S. Wagner, A. Pundt, and W. Theisen, *Influence of machining-induced martensite on hydrogen-assisted fracture of AISI type 304 austenitic stainless steel.* Int. J. Hydrogen Energy, 2011. 36(17): p. 11195-11206.
195. R.G. Vardiman and I.L. Singer, *Transformation of stress-induced martensite in 304 stainless steel by ion implantation.* Mater. Lett., 1983. 2(2): p. 150-154.
196. F. Tang, L. Ajdelsztajn, G.E. Kim, V. Provenzano, and J.M. Schoenung, *Effects of surface oxidation during HVOF processing on the primary stage oxidation of a CoNiCrAlY coating.* Surf. Coat. Technol., 2004. 185(2–3): p. 228-233.
197. S. Saeidi, *Microstructure, oxidation & mechanical properties of as-sprayed and annealed HVOF & VPS CoNiCrAlY coatings*, in *Mechanical, materials and manufacturing engineering*. 2011, University of Nottingham.
198. A. Aguero, F. Camon, J. Garcıa de Blas, J.C. del Hoyo, R. Muelas, A. Santaballa, S. Ulargui, and a.P. Valles, *HVOF-Deposited WCCoCr as*

Replacement for Hard Cr in Landing Gear Actuators. J. Therm. Spray Technol., 2011. 20(6): p. 1292-308.
199. S.H. Avner, *Introduction to physical metallurgy*. 1974: McGraw-Hill.
200. L. Kumar, R. Venkataramani, M. Sundararaman, P. Mukhopadhyay, and S.P. Garg, *Studies on the oxidation behavior of Inconel 625 between 873 and 1523 K.* Oxid. Met., 1996. 45(1): p. 221-244.
201. G. Bolelli, R. Giovanardi, L. Lusvarghi, and T. Manfredini, *Corrosion resistance of HVOF-sprayed coatings for hard chrome replacement.* Corros. Sci., 2006. 48(11): p. 3375-3397.
202. L. Gil and M.H. Staia, *Influence of HVOF parameters on the corrosion resistance of NiWCrBSi coatings.* Thin Solid Films, 2002. 420–421: p. 446-454.
203. J. Kawakita, S. Kuroda, T. Fukushima, and T. Kodama, *Development of dense corrosion resistant coatings by an improved HVOF spraying process.* Science and Technology of Advanced Materials, 2003. 4(4): p. 281-289.
204. N. Boshkov, *Galvanic Zn–Mn alloys electrodeposition, phase composition, corrosion behaviour and protective ability*. Surf. Coat. Technol., 2003. 172(2–3): p. 217-226.
205. J. Idrac, G. Mankowski, G. Thompson, P. Skeldon, Y. Kihn, and C. Blanc, *Galvanic corrosion of aluminium copper model alloys.* Electrochim. Acta, 2007. 52(27): p. 7626-7633.
206. W.T. Tsai and J.-R. Chen, *Galvanic corrosion between the constituent phases in duplex stainless steel.* Corros. Sci., 2007. 49(9): p. 3659-3668.
207. S.P. Jeng, P.H. Holloway, and C.D. Batich, *Surface passivation of Ni/Cr alloy at room temperature*. Surf. Sci., 1990. 227(3): p. 278-290.
208. N. Parvathavarthini, R. Subbarao, R. Dayal, H. Khatak, and S. Kumar, *Elimination of intergranular corrosion susceptibility of cold-worked and sensitized AlSl 316 SS by laser surface melting.* J. Mater. Eng. Perform., 2001. 10(1): p. 5-13.
209. C. Piehl, Z. Toekei, and H.J. Grabke, *Influence of chromium diffusion and different surface finishes on the oxidation behaviour of chromium steels.* Materials at High Temperatures, 2000. 17(2): p. 243-246.
210. I.N. Gladkii and Y.P. Chmyrev, *Corrosion resistance of aluminum and its alloys in sodium chloride media.* Chemical and Petroleum Engineering, 1969. 5(8): p. 619-622.
211. B. Beverskog and I. Puigdomenech, *Revised Pourbaix diagrams for nickel at 25–300 °C.* Corros. Sci., 1997. 39(5): p. 969-980.
212. M.J. Munoz Portero, J. Garcia Anton, J.L. Guinon, and V. Perez Herranz, *Pourbaix diagrams for chromium in concentrated aqueous lithium bromide solutions at 25°C.* Corros. Sci., 2009. 51(4): p. 807-819.
213. S. Hiromoto, A.P. Tsai, M. Sumita, and T. Hanawa, *Effects of surface finishing and dissolved oxygen on the polarization behavior of Zr65Al7.5Ni10Cu17.5 amorphous alloy in phosphate buffered solution.* Corros. Sci., 2000. 42(12): p. 2167-2185.
214. K.I. Popov, N.D. Nikolic, P.M. Zivkovic, and G. Brankovic, *The effect of the electrode surface roughness at low level of coarseness on the polarization characteristics of electrochemical processes.* Electrochim. Acta, 2010. 55(6): p. 1919-1925.
215. Y. Wang, S.L. Jiang, Y.G. Zheng, W. Ke, W.H. Sun, and J.Q. Wang, *Effect of porosity sealing treatments on the corrosion resistance of high-velocity oxy-fuel (HVOF)-sprayed Fe-based amorphous metallic coatings.* Surf. Coat. Technol., 2011. 206(6): p. 1307-1318.

216. S.M. Morsy, M.R. El-Sourougy, and H. Diab, *Effect of surface roughness on anodic protection parameters of 316 stainless steel in sulphuric acid.* J. Mater. Sci. Lett., 1989. 8(8): p. 887-890.
217. B. Yoo, K.R. Shin, D.Y. Hwang, D.H. Lee, and D.H. Shin, *Effect of surface roughness on leakage current and corrosion resistance of oxide layer on AZ91 Mg alloy prepared by plasma electrolytic oxidation.* Appl. Surf. Sci., 2010. 256(22): p. 6667-6672.
218. S. Cisse, L. Laffont, B. Tanguy, M.-C. Lafont, and E. Andrieu, *Effect of surface preparation on the corrosion of austenitic stainless steel 304L in high temperature steam and simulated PWR primary water.* Corros. Sci., 2012. 56(0): p. 209-216.
219. L. Fedrizzi, S. Rossi, R. Cristel, and P.L. Bonora, *Corrosion and wear behaviour of HVOF cermet coatings used to replace hard chromium.* Electrochim. Acta, 2004. 49(18): p. 2803-2814.
220. T. Laitinen, *Localized corrosion of stainless steel in chloride, sulfate and thiosulfate containing environments.* Corros. Sci., 2000. 42: p. 421-441.
221. J. Kawakita, S. Kuroda, T. Fukushima, and T. Kodama, *Corrosion resistance of HVOF sprayed HastelloyC nickel base alloy in seawater.* Corros. Sci., 2003. 45(12): p. 2819-2835.
222. Y.Y. Chen, L.B. Chou, and H.C. Shih, *Effect of solution pH on the electrochemical polarization and stress corrosion cracking of Alloy 690 in 5 M NaCl at room temperature.* Mater. Sci. Eng., A, 2005. 396(1–2): p. 129-137.
223. Y. Miyata, T. Handa, and H. Takazawa, *An analysis of current fluctuations during passive film breakdown and repassivation in stainless alloys.* Corros. Sci., 1990. 31(0): p. 465-470.
224. Y.M. Tang, Y. Zuo, and X.H. Zhao, *The metastable pitting behaviors of mild steel in bicarbonate and nitrite solutions containing Cl^-.* Corros. Sci., 2008. 50(4): p. 989-994.
225. Y. Tang, Y. Zuo, and H. Zhao, *The current fluctuations and accumulated pitting damage of mild steel in $NaNO_2$–NaCl solution.* Appl. Surf. Sci., 2005. 243(1–4): p. 82-88.
226. T. Suter, E.G. Webb, H. Bahni, and R.C. Alkire, *Pit Initiation on Stainless Steels in 1 M NaCl With and Without Mechanical Stress.* J. Electrochem. Soc., 2001. 148(5): p. B174-B185.
227. V.A.D. Souza and A. Neville, *Corrosion and erosion damage mechanisms during erosion–corrosion of WC–Co–Cr cermet coatings.* Wear, 2003. 255(1–6): p. 146-156.
228. I.J. Yang, *Effect of sulphate and chloride ions on the crevice chemistry and stress corrosion cracking of alloy 600 in high temperature aqueous solutions.* Corros. Sci., 1992. 33(1): p. 25-37.
229. S. Shigeng, Frank, P., *Investigation on initial oxidation kinetics of Al, Ni and Hf metal film surfaces.* Chinese Optics Letters, 2009. 8(2010): p. 87-90.
230. K.B. Hallberg, B.M. Grail, C.A.d. Plessis, and D.B. Johnson, *Reductive dissolution of ferric iron minerals: A new approach for bio-processing nickel laterites.* Miner. Eng., 2011. 24(7): p. 620-624.
231. G.B. Reartes, P.J. Morando, M.A. Blesa, P.B. Hewlett, and E. Matijevic, *Reactivity of Chromium Oxide in Aqueous Solutions. 2. Acid Dissolution.* Langmuir, 1995. 11(6): p. 2277-2284.
232. G.P. Power and I.M. Ritchie, *Mixed potential measurements in the elucidation of corrosion mechanismsâ€" 1. Introductory theory.* Electrochim. Acta, 1981. 26(8): p. 1073-1078.

233. A. Anderko and J.A.R. Editor-in-Chief:A A Tony, *2.38 - Modeling of Aqueous Corrosion*, in *Shreir's Corrosion*. 2010, Elsevier: Oxford. p. 1585-1629.
234. M. Tachibana, K. Ishida, Y. Wada, R. Shimizu, N. Ota, and N. Hara, *Cathodic polarization curves of the oxygen reduction reaction on various structural materials of boiling water reactors in high temperature–high purity water*. J. Nucl. Sci. Technol., 2012. 49(5): p. 551-561.
235. A. Aguero, F. Camon, J.G. de Blas, J.C. del Hoyo, R. Muelas, A. Santaballa, S. Ulargui, and P. Valles, *HVOF-Deposited WCCoCr as Replacement for Hard Cr in Landing Gear Actuators.* J. Therm. Spray Technol., 2011. 20(6): p. 1292-1309.
236. J. Kawakita, S. Kuroda, and T. Kodama, *Evaluation of through-porosity of HVOF sprayed coating.* Surf. Coat. Technol., 2003. 166(1): p. 17-23.
237. A.S. Luiz, W. Stephan, and C. Isolda, *Corrosion Characterization of Titanium alloys by Electrochemical Techniques.* Electrochim. Acta., 2006. 51(8-9): p. 1815-1819.
238. K.R. Trethewey and J. Chamberlain, *Corrosion for students of science and engineering*. 1988: Longman Scientific & Technical.
239. M. Kuczynska-Wydorska and J. Flis, *Corrosion and passivation of low-temperature nitrided AISI 304L and 316L stainless steels in acidified sodium sulphate solution.* Corros. Sci., 2008. 50(2): p. 523-533.
240. C. Bessing, M. Bergman, and A. Thorén, *Potentiodynamic polarization analysis of low-gold and silver-palladium alloys in three different media.* Dent. Mater., 1987. 3(3): p. 153-159.
241. A. Dhawan, K. Sachdev, S. Roychowdhury, P.K. De, and S.K. Sharma, *Potentiodynamic polarization studies on amorphous Zr 46.75 Ti 8.25 Cu 7.5 Ni 10 Be 27.5, Zr 65 Cu17.5 Ni10 Al 7.5, Zr 67 Ni 33 and Ti 60 Ni 40 in aqueous HNO_3 solutions.* J. Non-Cryst. Solids, 2007. 353(27): p. 2619-2623.
242. A.M.M. Ibrahim, S.S. Abd El Rehim, and M.M. Hamza, *Corrosion behavior of some austenitic stainless steels in chloride environments.* Mater. Chem. Phys., 2009. 115(1): p. 80-85.
243. D. Sun, P. Monaghan, W.A. Brantley, and W.M. Johnston, *Potentiodynamic polarization study of the in vitro corrosion behavior of 3 high-palladium alloys and a gold-palladium alloy in 5 media.* J. of Prosthet. Dent. , 2002. 87(1): p. 86-93.
244. K.V. Rybalka, L.A. Beketaeva, N.G. Bukhan'ko, and A.D. Davydov, *Electrochemical behavior and the rate of general corrosion of NiAl intermetallic compound in the unbuffered sodium chloride solutions.* Corros. Sci., 2011. 53(2): p. 630-636.
245. X.L. Zhang, Z.H. Jiang, Z.P. Yao, and Z.D. Wu, *Electrochemical study of growth behaviour of plasma electrolytic oxidation coating on Ti6Al4V: Effects of the additive.* Corros. Sci., 2010. 52(10): p. 3465-3473.
246. T. Ohtsuka, A. Hyono, and Y. Sasaki, *Potential modulation reflectance of passivated type 304 stainless steel in sulfuric acid solution.* Electrochim. Acta, 2012. 60(0): p. 384-391.
247. E.J. Sutow, W.A. Maillet, and G.C. Hall, *Corrosion potential variation of aged dental amalgam restorations over time.* Dent. Mater. , 2006. 22(4): p. 325-329.
248. Abdel-Gaber, A. M. Khamis, E. Abo-Eldahab, and S. H. Adeel, *Novel package for inhibition of aluminium corrosion in alkaline solutions.* Mater. Chem. Phys., 2010. 124(1): p. 773-779.

249. G.E. Badea, A. Caraban, M. Hyland, and S. Dzitac, *Polarisation Measurements Used for Corrosion Rates Determination.* Journal of sustenable energy, 2010. 1(1): p. 1-14.
250. M. Gamero, F. Pariente, E. Lorenzo, and C. Alonso, *Nanostructured rough gold electrodes for the development of lactate oxidase-based biosensors.* Biosensors and Bioelectronics, 2010. 25(9): p. 2038-2044.
251. M. Gamero, M. Sosna, F. Pariente, E. Lorenzo, P.N. Bartlett, and C. Alonso, *Influence of macroporous gold support and its functionalization on lactate oxidase-based biosensors response.* Talanta, 2012. 94(0): p. 328-334.
252. B.-W. Park, D.-Y. Yoon, and D.-S. Kim, *Formation and modification of a binary self-assembled monolayer on a nano-structured gold electrode and its structural characterization by electrochemical impedance spectroscopy*. J. Electroanal. Chem., 2011. 661(2): p. 329-335.
253. D.D. Gorhe, K.S. Raja, S.A. Namjoshi, and D.A. Jones, *Development of an electrochemical reactivation test procedure for detecting microstructural heterogeneity in Ni-Cr-Mo-W alloy welds.* J. Mater. Sci., 2004. 39(6): p. 2257-2261.
254. L.H. Wang, C.H. Tsai, and J.J. Kai, *Effect of prior thermal treatment on the microchemistry and crack propagation of proton-irradiated AISI 304 stainless steels.* J. Nucl. Mater., 2004. 328(1): p. 11-20.
255. S. Frangini and A. Mignone, *Modified Electrochemical Potentiokinetic Reactivation Method for Detecting Sensitization in 12 wt% Cr Ferritic Stainless Steels.* Corrosion, 1992. 48(9): p. 715-726.
256. V. Chial and S. Lasek, *Trends in the electrochemical polarization potentiodynamic reactivation method EPR.* Chem. Biochem. Engg., 2007. 21(1): p. 47-54.
257. L. Tan, X. Ren, K. Sridharan, and T.R. Allen, *Corrosion behavior of Ni-base alloys for advanced high temperature water-cooled nuclear plants.* Corros. Sci., 2008. 50(11): p. 3056-3062.
258. H. Edris, D. McCartney, and A. Sturgeon, *Microstructural characterization of high velocity oxy-fuel sprayed coatings of Inconel 625.* J. Mater. Sci., 1997. 32(4): p. 863-872.
259. K.S.K. Danadurai, T.M. Sridhar, S.V. Narasimhan, and S. Rajeswari, *Surface characterisation and crevice corrosion behaviour of nickel-based alloys in the paper industry*. J. Solid State Electrochem., 2000. 4(3): p. 159-167.
260. J. Jiang, H. Zhao, X. Zhou, S. Tao, and C. Ding, *The effect of ion implantation on the oxidation resistance of vacuum plasma sprayed CoNiCrAlY coatings.* Appl. Surf. Sci., (0).
261. M.P. Seah and M.T. Brown, *Validation and accuracy of peak synthesis software for XPS.* Appl. Surf. Sci., 1999. 144–145(0): p. 183-187.
262. M.M. Stack and T.M. Abd El-Badia, *Mapping erosion-corrosion of WC/Co-Cr based composite coatings: Particle velocity and applied potential effects.* Surf. Coat. Technol., 2006. 201(Article): p. 1335-1347.
263. V. Souza and A. Neville, *Mechanisms and kinetics of WC-Co−Cr high velocity oxy-fuel thermal spray coating degradation in corrosive environments.* J. Therm. Spray Technol., 2006. 15(1): p. 106-117.
264. T. Hryniewicz, K. Rokosz, and R. Rokicki, *Electrochemical and XPS studies of AISI 316L stainless steel after electropolishing in a magnetic field.* Corros. Sci., 2008. 50(9): p. 2676-2681.
265. R.-H. Jung, H. Tsuchiya, and S. Fujimoto, *XPS characterization of passive films formed on Type 304 stainless steel in humid atmosphere.* Corros. Sci., 2012. 58: p. 62-68.

266. B. Bozzini, G. Pietro De Gaudenzi, A. Fanigliulo, and C. Mele, *Electrochemical oxidation of WC in acidic sulphate solution.* Corros. Sci., 2004. 46(2): p. 453-469.
267. J.W. Johnson and C.L. Wu, *The Anodic Dissolution of Tungsten.* J. Electrochem. Soc., 1971. 118(12): p. 1909-1912.
268. M.M. Verdian, K. Raeissi, and M. Salehi, *Corrosion performance of HVOF and APS thermally sprayed NiTi intermetallic coatings in 3.5% NaCl solution.* Corros. Sci., 2010. 52(3): p. 1052-1059.
269. R.Q. Guo, C. Zhang, Q. Chen, Y. Yang, N. Li, and L. Liu, *Study of Structure and Corrosion resistance of Fe-based amorphous coatings prepared by HVAF and HVOF*. Corros. Sci. 53(7): p. 2351-2356
270. M.M. Verdian, K. Raeissi, and M. Salehi, *Electrochemical impedance spectroscopy of HVOF-sprayed NiTi intermetallic coatings deposited on AISI 1045 steel.* J. Alloys Compd., 2010. 507(1): p. 42-46.
271. Z.F. Yin, W.Z. Zhao, W.Y. Lai, and X.H. Zhao, *Electrochemical behaviour of Ni-base alloys exposed under oil/gas field environments.* Corros. Sci., 2009. 51(8): p. 1702-1706.
272. Y. Lim, H. Kim, J. Kim, and H. Kwon, *Double loop electrochemical potentiokinetic reactivation test of Nickel-base Alloy 600* Met. & Matr. Intl., 2001. 7(1): p. 61-65.
273. M. Sun, X. Wu, Z. Zhang, and E.-H. Han, *Analyses of oxide films grown on Alloy 625 in oxidizing supercritical water.* The Journal of Supercritical Fluids, 2008. 47(2): p. 309-317.
274. L.E. Fratila-Apachitei, H. Terryn, P. Skeldon, G.E. Thompson, J. Duszczyk, and L. Katgerman, *Influence of substrate microstructure on the growth of anodic oxide layers.* Electrochim. Acta, 2004. 49(7): p. 1127-1140.
275. G. Fafilek, *The use of voltage probes in impedance spectroscopy.* Solid State Ionics, 2005. 176(25–28): p. 2023-2029.
276. M. Da Cunha Belo, N.E. Hakiki, and M.G.S. Ferreira, *Semiconducting properties of passive films formed on nickel-base alloys type Alloy 600: influence of the alloying elements.* Electrochim. Acta, 1999. 44(14): p. 2473-2481.
277. B. Huiping and F. WANG, *Protective Properties of High Temperature Oxide Films on Ni-based Superalloys in 3.5% NaCl Solution.* J. Mater. Sci. Technol, 2007. 23(4).
278. Y. Zhang, H. Feng, X. Wu, L. Wang, A. Zhang, T. Xia, H. Dong, X. Li, and L. Zhang, *Progress of electrochemical capacitor electrode materials.* Int. J. Hydrogen Energy, 2009. 34(11): p. 4889-4899.
279. A. Lloydis, J. Noel, D. Shoesmith, and N. McIntyre, *The open-circuit ennoblement of alloy C-22 and other Ni-Cr-Mo alloys.* J. Min. Met. Mat Soc., 2005. 57(1): p. 31-35.
280. A. Lasia, B.E. Conway, J.O.M. Bockris, and R.E. White, *Electrochemical Impedance Spectroscopy and its Applications*, in *Modern Aspects of Electrochemistry*. 2002, Springer US. p. 143-248.
281. P. Agarwal and B.A. Boukamp, *Electrochemical Corrosion Measurement* in *Application notes*. 2010.
282. P.P. David Loveday, and Bob Rodgers, *Evaluation of Organic Coatings with Electrochemical Impedance Spectroscopy.* J. Coat. Technol., 2004(1): p. 88-93.
283. J. Zhang, J. Yuan, Y. Qiao, C. Cao, J. Zhang, and G. Zhou, *The corrosion and passivation of SS304 stainless steel under square wave electric field.* Mater. Chem. Phys., 2003. 79(1): p. 43-48.

284. S. Bollo, S. Finger, J.C. Sturm, L.J. Nunez Vergara, and J.A. Squella, *Cyclic voltammetry and scanning electrochemical microscopy studies of the heterogeneous electron transfer reaction of some nitrosoaromatic compounds.* Electrochim. Acta, 2007. 52(15): p. 4892-4898.
285. C. Cannes, F. Kanoufi, and A.J. Bard, *Cyclic voltammetry and scanning electrochemical microscopy of ferrocenemethanol at monolayer and bilayer-modified gold electrodes.* J. Electroanal. Chem., 2003. 547(1): p. 83-91.
286. A.J. Bard and L.R. Faulkner, *Electrochemical Methods: Fundamentals and Applications*. 2001. 572.
287. C. Amatore, L. Thouin, and M. Fatima Bento, *Steady state voltammetry at low electrolyte/reactant concentration ratios: what it means and what it does not mean.* J. Electroanal. Chem., 1999. 463(1): p. 45-52.
288. D.O. Wipf, *Initiation and study of localized corrosion by scanning electrochemical microscopy.* Colloids and Surfaces A: Physicochemical and Engineering Aspects, 1994. 93: p. 251-261.